Titre: Title:	Numerical study of the effects of particle's geometric properties on the critical shear strength of granular materials.
Auteur: Author:	Sergio Carrasco Cisterna
Date:	2024
Type:	Mémoire ou thèse / Dissertation or Thesis
Référence: Citation:	Carrasco Cisterna, S. (2024). Numerical study of the effects of particle's geometric properties on the critical shear strength of granular materials. [Thèse de doctorat, Polytechnique Montréal]. PolyPublie. https://publications.polymtl.ca/59181/

URL de PolyPublie: PolyPublie URL:	https://publications.polymtl.ca/59181/
Directeurs de recherche: Advisors:	Carlos Ovalle, & David Cantor
Programme: Program:	Génie minéral

POLYTECHNIQUE MONTRÉAL
affiliée à l'Université de Montréal

Numerical study of the effects of particle's geometric properties on the critical shear strength of granular materials.

SERGIO CARRASCO CISTERNA
Département de génies civil, géologique et des mines

Thèse présentée en vue de l'obtention du diplôme de *Philosophiæ Doctor* Génie mineral

Août 2024

POLYTECHNIQUE MONTRÉAL
affiliée à l'Université de Montréal

Cette thèse intitulée :

Numerical study of the effects of particle's geometric properties on the critical shear strength of granular materials.

présentée par **Sergio CARRASCO CISTERNA**
en vue de l'obtention du diplôme de *Philosophiæ Doctor*
a été dûment acceptée par le jury d'examen constitué de :

Pooneh MAGHOUL, présidente
Carlos OVALLE, membre et directeur de recherche
David CANTOR, membre et codirecteur de recherche
Pedro CACCIARI, membre
Francois NICOT, membre externe

DEDICATION

À ma partenaire de vie Nicole,
et à ma famille…

ACKNOWLEDGEMENTS

Vivir la vida y aceptar el reto,
recuperar la risa, ensayar el canto,
bajar la guardia y extender las manos,
desplegar las alas e intentar de nuevo,
celebrar la vida y retomar los cielos.

— *Mario Benedetti*

These words perfectly capture the spirit of this journey—one filled with challenges, laughter and the courage to try again. I believe that making this decision, both risky and courageous, was one of the most important moments that led me to where I am today, writing these words. This choice, along with the great efforts behind it, allowed me to meet wonderful people, travel a bit around the world, learn new languages, laugh in ways I never imagined and ultimately finish a thesis. Of course, I couldn't have done it alone. Many people helped, supported and advised me along the way. Now is the time to say thank you to them.

First of all, I would like to express my deep gratitude to all the members of the jury! Thank you Professor Pooneh Maghoul for honoring me by presiding over this jury and Professors Francois Nicot and Pedro Cacciari for taking on this heavy task. It was an honor for me to have such a prestigious jury to present my work.

I find it difficult to express my gratitude to my co-supervisor, David Cantor. The outcome of this thesis is largely due to his enthusiasm and the considerable time he dedicated to teaching me micromechanics. I am deeply thankful for your immense support in the technical work of this thesis, but what I appreciate even more is that you shared with me your love for science and teaching, your curiosity and your endless good humor. I have deep gratitude in both my heart and mind towards my supervisor, Carlos Ovalle. Thank you for your patience, kindness and invaluable teaching. You have been a mentor to me and I will never find the words to express how grateful I am. Your passion and rigor in both research and life are something I will always carry with me. Meeting both of you has been a true upheaval in my scientific and personal life.

I would also like to extend my gratitude to Professor Emilien Azéma for his support and for always being available to discuss ideas. I also extend my thanks to Frédéric Dubois and Rémi Mozul for all their support and assistance in the numerical developments and implementations carried out for this thesis. Thank you for always being willing to discuss and engage in conversations about mathematical algorithms.

I would also like to thank my lab mates who accompanied me throughout this journey: Kasra, Gilbert, Florian, Quyen, Madison, Khawla, Cristian and Yuyu. In particular, I would like to express my gratitude to my friends with whom I worked more closely, discussing and philosophizing about life and science. Thank you, Tristan, for helping me take my first steps in Canada and Paula, for always caring about everyone (you never forgot a birthday). I also extend my thanks to those who joined later, like Carolina, who puts her heart into her work and Manuel, who made the last few months of writing this document so much more enjoyable. I want to give special thanks to Monica Monzon, who has been like a second mother to me here in the cold north. Thank you for always motivating us to participate in extracurricular activities and for your positive energy. I will truly miss you all.

Thanks to the Research Institute on Mines and the Environment (RIME) UQAT-Polytechnique and their industrial partners, also the financial support of the Natural Sciences and Engineering Research Council of Canada (NSERC) [Ref. RGPIN-2019-06118], the Fonds de recherche du Québec — Nature et technologies (FRQNT) through the 'Programme de recherche en partenariat sur le développement durable du secteur minier-II' [Ref. 2020-MN-281267]. This research was also partially enabled by Calcul Quebec (calculquebec.ca) and Compute Canada (computecanada.ca) support.

When I left Chile for Canada, it was the first time I had ever taken a plane and left my country. I am infinitely grateful that since the moment I met my life partner, Nicole, she has always supported me in everything. She traveled with me on this adventure to the cold north of the world. Finding the right words to thank life itself is complex. Still, I want to thank you deeply for all your support, the philosophical discussions about science and education and especially for your love and care. To my family, thank you for your love and encouragement, especially during the times when I needed it most. A special thanks to my parents, Silvia and Sergio, for their unwavering support.

To my great friends, both new and old, who have accompanied me on this incredible journey. I am grateful to have crossed paths in Montreal with Rodrigo Victoriano. Thank you for your tremendous support and for being part of the small Latin family. Thanks as well to Arturo and Mali. I also want to thank David Aponte. I truly enjoyed my short time in Montpellier with you and your little son, Santiago. I extend my gratitude to all my friends in Chile, those I met throughout each stage of my life and who, despite being far away, always gave me their full support. Thank you, Humberto, Felipe, David, Eduardo, Victoria, Benjamin, Norman, Arlette and Pablo. I am grateful for the support from my old professors in Chile, especially Matias Silva, who has always had a great sense of humor and supported me throughout the years. I also want to thank Marcos Valdevenito, whose encouraging words motivated me to take on this challenge.

This thesis would not have been possible without the contributions, guidance and sacrifices of all those mentioned above. Thank you for your belief in me and for the role you played in making this project a reality.

ABSTRACT

Transitioning to more sustainable energy systems and improved energy storage is crucial for mitigating climate change. Still, it requires a substantial and growing increase in mineral production. Therefore, the mining industry is fundamental in providing the resources for these technology developments, while upholding rigorous safety requirements and minimizing environmental impacts. Mining operations manage large volumes of uneconomic waste rock (WR) that must be excavated to access ore-rich layers. Once extracted, WR is stored in massive waste rock piles (WRPs), which are among the largest geotechnical structures worldwide. WRPs pose significant technical and environmental challenges due to their chemical, hydrogeological and mechanical instability. WR material often consists of loose, uncompacted coarse-blasted rocks with a wide particle size distribution (psd), including large angular rock fragments, gravel, sand and silt. Slope stability analyses of these loose granular fills is mainly influenced by the critical friction angle (ϕ_c), which is the crucial material parameter to measure in order to perform safe designs.

Particle oversizing limits the methods for mechanical characterization of coarse granular material such as gravelly fluvial soils, rockfill and WRs, since often the coarsest material fraction does not fit in standard laboratory sample sizes. To be able to characterize these materials, small-scaling techniques, like truncated, scalping or parallel grading, are widely applied. These methods modify the psd in order to fit a fine fraction of the field material in a standard laboratory device. The maximum particle size ($d_{\max}$) should meet international engineering standards, which specify aspect ratios of $D/d_{\max}$ between 5 and 10 (where D is the characteristic sample dimension), depending on the type of shear test. This constraint limits a comprehensive understanding of the behavior of coarse materials. Furthermore, many results on small-scaling tests are apparently contradictory, namely, as $d_{\max}$ of the material increases, a number of studies have concluded that the shear strength increases, while many others have indicated the opposite trend.

The critical state of granular materials is influenced by several factors. It is well known that a better graded material will present a lower critical void ratio, meaning that the location of the critical state line (CSL) is strongly affected by the psd. However, several studies have shown that critical shear strength (i.e., ϕ_c) does not depend on the psd, given that particle shape and roughness remain constant along with grain sizes. On the other hand, particle shape has a significant impact on ϕ_c; materials having angular or elongated grains present higher values of critical shear strength than samples with rounded grains. Notably, recent research

had demonstrated correlations between the size and shape of particles in certain granular materials, including sand, rockfill and WR. This suggests that when the psd is adjusted to scale down a sample, the distribution of particle shapes may also be altered, resulting in variations in the mechanical behavior observed across different scales. Therefore, the scaled material might not be representative of the original coarser one, since their characteristic particle shapes might differ. Among other factors, this could be a source of the apparently contradictory results observed in small-scaling techniques. To address this gap, this thesis numerically investigates the coupled effects of the geometric properties of particles (i.e., size and shape) on the critical shear strength of granular materials.

The primary objective of this project is to quantify the influence of particle size and shape distributions on the critical shear strength of granular materials. In doing so, we aim evaluating the reliability of small-scaling techniques for coarse granular material. To achieve this, we employ two and three-dimensional discrete element method (DEM) simulations to model granular assemblies with controlled variations in particle size and shape. DEM is a numerical technique that simulates the behavior of a collection of particles by tracking their interactions and movements. The particle shapes studied include circular, elongated and angular polygonal shapes in 2D scenarios and their analogous shapes in 3D models. We conduct a series of drained shearing tests in dry material with a defined grain size-shape correlation and varying particle size dispersion. The macroscopic behavior is studied through the stress-strain response and critical state parameters, such as ϕ_c and critical void ratio. Additionally, a microscopic study of particle coordination, force transmission and fabric anisotropies is computed within the granular assembly. Understanding these micro-mechanical mechanisms provide insights into how particle geometric properties influence shear strength.

Our series of DEM simulations involves three 2D studies, including (i) diverse elongated and circular grains, (ii) regular polygons with varied sharpness and (iii) pentagons with multiple irregularities. Moreover, 3D assemblies are composed of spheres and angular polyhedral grains. Each systematic study covers two inverse grain size-shape correlations. The overall results show that, on the one hand, in assemblies composed of fine rounded particles and coarse angular or elongated particles, the critical shear strength decreases as the grain size span increases due to the ineffective interlocking promoted for the fine rounded fraction. On the other hand, in assemblies with fine angular or elongated particles and coarse rounded grains, the critical shear strength increases as the dispersion on particle size increases, due to elongated and angular shapes promoting interlocking and sliding between grains. Furthermore, related to the micromechanical behavior, these variations in the critical shear strength are mainly associated with the anisotropy of normal forces in cases composed of angular and rounded particles and the anisotropy of tangential forces in cases with elongated and rounded

grains.

These findings highlight the importance of considering size-shape correlations when small-scaling techniques are used to test oversized granular materials. After re-analyzing several results on small-scale samples reported by researchers over the last 60 years, it can be noted that some materials presented a grain size-shape correlation that could explain the changes in shear strength as different fine fractions of the field material were tested. Moreover, our numerical results prove that, if particle size and shape are correlated, small-scaling techniques fail to replicate the mechanical behavior of in situ materials. Nevertheless, these numerical observations need to be validated through experimental tests. In order to address this gap, future research should focus on experimental validation and numerical models should incorporate more realistic particle shapes [1].

Keywords: critical shear strength, particle shape distribution, particle size distribution, discrete-element modeling, granular materials

---

[1] Subsequent chapters of this thesis elaborate on the detailed examination and outcomes of the simulations, accompanied by specific numerical data, graphs and further micro-mechanical analyses. This abstract offers a concise summary of the research scope, methodology and key findings.

RÉSUMÉ

La transition vers des systèmes énergétiques plus durables et un meilleur stockage de l'énergie est cruciale pour atténuer le changement climatique. Cela nécessite néanmoins une augmentation substantielle et croissante de la production minérale. Par conséquent, l'industrie minière joue un rôle fondamental en fournissant les ressources nécessaires à ces développements technologiques, tout en respectant des exigences de sécurité rigoureuses et en minimisant les impacts environnementaux. Les opérations minières gèrent de grands volumes de roches stériles sans aucune valeur économique qui doivent être excavés pour accéder aux couches riches en minerai. Une fois extraites, les stériles sont stockés dans des haldes, qui comptent parmi les plus grandes structures géotechniques au monde. Les haldes à stériles posent d'importants défis techniques et environnementaux en raison de leur instabilité chimique, hydrogéologique et mécanique. Les matériaux stériles sont souvent constitués de clastes de roches dynamitées à l'état lâche, non compactées et avec une large distribution granulométrique, comprenant de gros fragments de roches angulaires, du gravier, du sable et du silt. Les analyses de stabilité des pentes de ces remblais granulaires lâches sont principalement influencées par l'angle de frottement critique (ϕ_c), qui est le paramètre du matériau déterminant à mesurer afin de réaliser des designs sûrs.

Le surdimensionnement des particules limite les méthodes de caractérisation mécanique des matériaux granulaires grossiers tels que les sols fluviaux graveleux, les enrochements et les roches stériles, car souvent la fraction de matériau la plus grossière ne rentre pas dans les tailles d'échantillons de laboratoire standard. Pour pouvoir caractériser ces matériaux, des techniques à petite échelle, telles que la granulométrie tronquée, scalpée ou parallèle, sont largement appliquées. Ces méthodes modifient la granulométrie afin d'adapter une fraction fine du matériau de terrain dans un appareil de laboratoire standard. La taille maximale des particules ($d_{\max}$) doit répondre aux normes d'ingénierie internationales, qui spécifient des rapports d'aspect de $D/d_{\max}$ entre 5 et 10 (où D est la dimension caractéristique de l'échantillon), en fonction sur le type d'essai de cisaillement. Cette contrainte limite une compréhension globale du comportement des matériaux grossiers. De plus, de nombreux résultats d'essais à petite échelle sont apparemment contradictoires, à savoir qu'à mesure que $d_{\max}$ du matériau augmente, un certain nombre d'études ont conclu que la résistance au cisaillement augmente, tandis que de nombreuses autres ont indiqué la tendance opposée.

L'état critique des matériaux granulaires est influencé par plusieurs facteurs. Il est bien connu qu'un matériau avec une granulométries plus étalée présentera un indice de vide cri-

tique plus faible, ce qui signifie que l'emplacement de la ligne d'état critique est fortement affecté par la granulométrie. Cependant, plusieurs études ont montré que la résistance critique au cisaillement (c'est-à-dire, ϕ_c) ne dépend pas de la granulométrie, étant donné que la forme et la rugosité des particules restent constantes pour les diverses tailles des grains. D'un autre côté, la forme des particules a un impact significatif sur ϕ_c ; les matériaux ayant des grains angulaires ou allongés présentent des valeurs de résistance critique au cisaillement plus élevées que les échantillons à grains arrondis. Des recherches récentes ont notamment démontré des corrélations entre la taille et la forme des particules dans certains matériaux granulaires, notamment des sables, des enrochements et des WR. Cela suggère que lorsque la granulométrie est ajustée pour réduire un échantillon, la distribution des formes de particules peut également être modifiée, entraînant des variations du comportement mécanique observé à différentes échelles. Par conséquent, le matériau à l'échelle réduite pourrait ne pas être représentatif du matériau original plus grossier, puisque la forme caractéristique de ses particules pourrait différer. Entre autres facteurs, cela pourrait être à l'origine des résultats apparemment contradictoires observés dans les techniques à petite échelle. Pour combler cette lacune, cette thèse étudie numériquement les effets couplés des propriétés géométriques des particules (c'est-à-dire la taille et la forme) sur la résistance critique au cisaillement des matériaux granulaires.

L'objectif principal de ce projet est de quantifier l'influence de la distribution de la taille et de la forme des particules sur la résistance critique au cisaillement des matériaux granulaires. Ce faisant, nous visons à évaluer la fiabilité des techniques à petite échelle pour les matériaux granulaires grossiers. Pour y parvenir, nous utilisons des simulations par la méthode des éléments discrets (DEM) en deux et trois dimensions pour modéliser des assemblages granulaires avec des variations contrôlées de la taille et de la forme des particules. DEM est une technique numérique qui simule le comportement d'un ensemble de particules en suivant leurs interactions et leurs mouvements. Les formes de particules étudiées comprennent des formes polygonales circulaires, allongées et angulaires dans des scénarios 2D, ainsi que leurs formes analogues dans des modèles 3D. Nous effectuons une série d'essais de cisaillement drainés sur des matériaux secs avec une corrélation taille-forme des grains définie et une dispersion granulométrique variable. Le comportement macroscopique est étudié à travers la réponse contrainte-déformation et les paramètres d'état critique, tels que ϕ_c et l'indice de vide critique. De plus, on présente une étude microscopique de la coordination des particules, de la transmission des forces et des anisotropies. La compréhension de ces mécanismes micromécaniques permet de mieux comprendre comment les propriétés géométriques des particules influencent la résistance au cisaillement.

Notre série de simulations DEM implique trois études 2D, comprenant (i) divers grains allon-

gés et circulaires, (ii) des polygones réguliers avec une netteté variée et (iii) des pentagones avec de multiples irrégularités. De plus, les assemblages 3D sont composés de sphères et de grains polyédriques angulaires. Chaque étude systématique couvre deux corrélations inverses taille-forme des grains. Les résultats globaux montrent que, d'une part, dans les assemblages composés de particules fines arrondies et de particules grossières angulaires ou allongées, la résistance critique au cisaillement diminue à mesure que l'étendue granulométrique augmente en raison de l'emboîtement inefficace favorisé pour la fraction fine arrondie. En revanche, dans les assemblages comportant des particules fines anguleuses ou allongées et des grains grossiers arrondis, la résistance critique au cisaillement augmente à mesure que la dispersion sur la granulométrie augmente, du fait des formes allongées et angulaires favorisant l'emboîtement et le glissement entre les grains. De plus, liées au comportement micromécanique, ces variations de la résistance critique au cisaillement sont principalement associées à l'anisotropie des forces normales dans les cas composés de particules angulaires et arrondies, et à l'anisotropie des forces tangentielles dans les cas à grains allongés et arrondis.

Ces résultats soulignent l'importance de prendre en compte les corrélations taille-forme lorsque des techniques à petite échelle sont utilisées pour tester des matériaux granulaires surdimensionnés. Après avoir réanalysé plusieurs résultats sur des échantillons à petite échelle rapportés par des chercheurs au cours des 60 dernières années, on peut noter que certains matériaux présentaient une corrélation taille-forme de grain qui pourrait expliquer les changements de résistance au cisaillement en fonction des différentes fractions fines du matériau de terrain qui ont été testées. De plus, nos résultats numériques prouvent que, si la taille et la forme des particules sont corrélées, les techniques à petite échelle ne parviennent pas à reproduire le comportement mécanique des matériaux in situ. Néanmoins, ces observations numériques nécessitent d'être validées par des tests expérimentaux. Afin de combler cette lacune, les recherches futures devraient se concentrer sur la validation expérimentale et les modèles numériques devraient incorporer des formes de particules plus réalistes [2].

Mots clés : résistance critique au cisaillement, distribution de la forme des particules, distribution granulométrique, modélisation par éléments discrets, matériaux granulaires

---

[2] Les chapitres suivants de cette thèse détaillent l'examen détaillé et les résultats des simulations, accompagnés de données numériques spécifiques, de graphiques et d'autres analyses micromécaniques. Ce résumé offre un résumé concis de la portée de la recherche, de la méthodologie et des principales conclusions.

TABLE OF CONTENTS

DEDICATION . . . iii

ACKNOWLEDGEMENTS . . . iv

ABSTRACT . . . vii

RÉSUMÉ . . . x

TABLE OF CONTENTS . . . xiii

LIST OF TABLES . . . xvi

LIST OF FIGURES . . . xvii

LIST OF SYMBOLS AND ACRONYMS . . . xxvi

CHAPTER 1 INTRODUCTION . . . 1

CHAPTER 2 LITERATURE REVIEW . . . 5
- 2.1 Context . . . 5
- 2.2 Waste rock piles (WRPs) . . . 6
  - 2.2.1 Types of waste rock piles . . . 7
  - 2.2.2 Factors affecting mechanical stability . . . 8
  - 2.2.3 Waste rock material properties . . . 10
  - 2.2.4 Failures and stability acceptance criteria . . . 15
- 2.3 Shear strength of coarse granular materials . . . 17
  - 2.3.1 Mechanical testing of granular materials . . . 20
  - 2.3.2 Material and sample geometric properties affecting the shear strength of granular materials . . . 25
  - 2.3.3 Small-scaling methods for coarse granular materials . . . 36
  - 2.3.4 Remarks on small-scaling methods . . . 42
- 2.4 Discrete element method in geomechanics . . . 44
  - 2.4.1 Smooth-DEM . . . 46
  - 2.4.2 Contact Dynamics (CD) — Non Smooth-DEM . . . 48
  - 2.4.3 Remarks on the choice of the numerical method . . . 49
- 2.5 Concluding remarks . . . 50

CHAPTER 3 METHODOLOGY 52
3.1 Research approach and design 52
3.2 Numerical test series 52
3.2.1 Modeled material in 2D 53
3.2.2 Sample preparation and 2D shear tests 55
3.2.3 Modeled material in 3D 58
3.2.4 Sample preparation and 3D shear tests 59
3.3 Data analysis 61
3.3.1 Macroscopic descriptors 61
3.3.2 Microscopic behavior 62
3.4 Validation of the numerical method 65
3.4.1 Numerical simulations 65
3.4.2 Experimental tests 69
3.4.3 Comparison of numerical and experimental results 70
3.4.4 Limitations of using DEM in shearing tests for soil mechanics 72

CHAPTER 4 ARTICLE 1: Effects of particle size-shape correlations on steady shear strength of granular materials: The case of particle elongation 73
4.1 Introduction 74
4.2 Model material and numerical simulation 75
4.3 Macroscopic behavior 79
4.4 Microscopic descriptors 82
4.5 Micromechanical contributions to strength 86
4.6 Conclusions 95

Bibliography 103

CHAPTER 5 ARTICLE 2: Shear strength of angular granular materials with size and shape polydispersity 108
5.1 Introduction 109
5.2 Model material and numerical simulation 110
5.2.1 Grain shape size correlations 110
5.2.2 Granular sample generation 112
5.2.3 DEM simulation 114
5.3 Macroscopic behavior 116
5.4 Microscopic behavior 120
5.4.1 Connectivity 120

- 5.4.2 Influence of the type of contact between grains 123
- 5.4.3 Contributions to shear strength by shape class 126

5.5 Conclusion 128

Bibliography 130

CHAPTER 6 ARTICLE 3: Particle shape distribution effects on the critical strength of granular materials 137

6.1 Introduction 138

6.2 Numerical Model 139

- 6.2.1 Dispersity of grain size and shape 139
- 6.2.2 Particle simulation 142
- 6.2.3 Sample generation 144

6.3 Macroscopic mechanical behavior 145

6.4 Characterization at the microscale 148

- 6.4.1 Connectivity 148
- 6.4.2 Force network 149
- 6.4.3 Fabric and contact and force anisotropies 151

6.5 Conclusions 155

Bibliography 158

CHAPTER 7 DISCUSSION 164

7.1 Rethinking the main findings 164

7.2 Comparison with previous studies 166

7.3 A recent implication of the study 170

7.4 Limitations 171

7.5 Future research directions 173

CHAPTER 8 CONCLUSION 175

REFERENCES 178

LIST OF TABLES

2.1 Standards of direct shear tests regarding the maximum allowed particle size ($d_{\max}$), specimen width (W), thickness (T), and diameter (D) [1]. 25

2.2 Materials and specimen sizes used in direct shear tests by Cerato and Lutenegger [2] (modified from [1]). 26

2.3 Specimen sizes, $d_{\max}$, and aspect ratios for WR1 and WR2 [3]. 27

2.4 Most used shape descriptors [4]. 31

2.5 Rockfill materials: $d_{\max}$ of tested material, specimen dimensions, and aspect ratios [5]. 37

2.6 Crushed ballast material: $d_{\max}$ of tested materials, D and aspect ratio, modified from [6]. 38

2.7 Pyramid rockfill, crushed basalt, Oroville and Venato sandstone materials: $d_{\max}$, D, and aspect ratio [7]. 40

2.8 $d_{\max}$ for materials CP and STV, D and aspect ratios [8]. 40

2.9 Scalping and parallel gradation: $d_{\max}$ and aspect ratio by W and T [9]. 41

2.10 Apparently contradicting result of grain sizes effect on shear strength reported. 44

5.1 Parameters $d_{\max}$, $d_{\min}$, R_D, D_{50} and C_u for different values of S. . . . 114

6.1 Geometrical characteristics of grains $P1$ to $P6$. n_v is the number of vertices, n_f is the number of faces, V_P/V_s is the ratio between the volume of particle and the corresponding circumscribing sphere, A_P/A_s is the ratio between the particle surface area and that of the circumscribing sphere, and $\mathcal{S}$ is the sphericity, which denotes the ratio of the surface area of a sphere with equivalent volume to that of the given particle [10].140

LIST OF FIGURES

2.1 Large waste rock pile constructed with benches at the Canadian Malartic Mine, Québec [11]. 6

2.2 East WRP of the Antamina mine in Peru [12]. 7

2.3 Diagram of WRPs and stockpile stability rating and hazard classification system [12]. 9

2.4 Data compilation of psd of WR materials, modified from [13]. 10

2.5 Typical psd ranges for WR materials (a) Hawley & Cunning [12], (b) Bard *et al.* [14] and (c) Linero *et al.* [15]. 11

2.6 Particles' roundness and smoothness from different sources [16]. . . . 12

2.7 Iron mine waste rock: (a) Characteristic dimensions of the particles, L=Length, I=Breath, and S= Thickness [17]. (b) Variability of elongation ratio and flatness ratio calculated from the form dimensions L and I for the different size fractions [18]. 12

2.8 Shale rockfill: (a) Characteristic dimensions of the particles, a=largest, c=shortest dimension. (b) particle shape-size correlation [19]. 13

2.9 Particle crushing strength of different rock aggregates [13]. 13

2.10 Evolution of the dry density with WRP height, estimated from oedometric and compression triaxial tests [14]. 14

2.11 View of NAR of 50 m high WRP, modified from [12]. 15

2.12 Failures of WRPs: (a) failure of a 515 m high WRP in a copper mine in Chile [20] and (b) Aberfan coal WR failure, October 21st 1966 [12]. 16

2.13 WRP stability rating and hazard: (a) class chart, and (b) chart illustrating the results of the 1991 and 2013 surveys [12]. 17

2.14 Illustrative diagram of the phenomena affecting shear strength in granular materials [21]. 18

2.15 Illustrative diagram of the critical state line and its protection on $e-p'$ and $q-p'$ spaces [22]. 19

2.16 Stress-strain (a) and void ratio (b) paths in the failure surface of a sheared granular material until critical state; dense case in blue and loose case in red; the normal effective stress σ'_n on the surface is the same in both cases. 19

2.17 Maximum friction angle for compiled sands, ballasts, and rockfill [legend: material name/$d_{\max}$ (mm) (Ref.)] (modified form [13]). 21

2.18 General arrangement and free-body diagram of the conventional DS test [23]. 22

2.19 (a) Loading mode setup, distances in mm; g = gap size; x = shear displacement; and (b) the large direct shear (LDS) equipment [18]. . . 22

2.20 Schematic diagram of triaxial apparatus [24]. 23

2.21 Large diameter triaxial cells (≈1000mm) (h, ϕ: max. height and diameter of the sample, respectively) [25]. 24

2.22 Variation of the friction angle in terms of specimen width and thickness to d_{max} ratios for specimens with different relative densities (data taken from [2]): (a) Ottawa sand, (b) FHWA (brown mortar), (c) Morie [1]. 26

2.23 Waste rock material: (a) Psd for cases WR1 and WR2, and (b) friction angle variations as function of W/d_{max} for WR2 [3]. 27

2.24 Fujian sand: (a) psd curves of four fractions, (b) critical states in stress space [26]. 28

2.25 Views of tested granular systems: (a1) monodisperse, (a2) bidisperse and (a3) polydisperse samples; (b) critical friction angle as a function of the size span $\lambda = d_{\text{max}}/d_{\text{min}}$; dashed line shows the mean value for all experiments, and vertical bars indicate the maximum and minimum values between repetitions [27]. 28

2.26 Psd for various grading of samples composed of circular discs for DEM analysis [28]. 29

2.27 Stress-strain response of 2D DEM simulations of grain assemblies with different psd: (a) dense samples; (b) loose samples [28]. 29

2.28 Average macroscopic coefficient of friction, error bars represent the standard deviation of the data (mod., from [29,30]). 30

2.29 (a) Microphotographs showing various grain shapes encountered in Cho's study, (b) Effect of particle shape on critical state friction angle [31]. 32

2.30 Ballotini Glass Bead: (a) correlation between particle shape descriptors, and (b) $q - p'$ shearing plane [32]. 32

2.31 DEM 2D elongated particles: (a) Initial packing configurations for different particle elongation (η) [33], (b) and normalized shear strength as a function of η. 33

2.32 DEM polyhedral particles: (a) Initial packing configurations for different particle angularity (α), and (b) normalized shear strength as a function $\langle\alpha\rangle$ [33]. 34

2.33 Mixture between Ottawa and blasting sand, critical state friction angle based on the angle of repose as a function of the mass fraction of angular particles [34]. 34
2.34 (a) Initial psd of parallel graded STV samples, and (b) peak friction angle as a function of confining pressure for a Shale rockfill [19]. . . . 35
2.35 Screenshots of 2D DEM samples: (a) assemblies composed of disks and (b) assemblies composed of particles with size-shape correlation based on elongation [35]. 36
2.36 Comparison between critical friction angles as a function of S for both study cases [35]. 36
2.37 Rockfill materials: (a) field psd and scalped psds (modified from [1]), and (b) evolution of friction angle as a function of $d_{\max}$ for different porosities (all test at confining pressure of 88 kPa) (modified from [5]). 37
2.38 Triaxial tests on crushed ballast material: (a) scalping psd and (b) friction angle as a function of $d_{\max}$ for medium-dense material (modified from [6]). 38
2.39 Pyramid rockfill material: (a) parallel gradations and (b) friction angle as a function of confining pressure [36] (data from [7]). 39
2.40 Parallel grading psd for: (a) calcareous rock and (b) quartzite rock material [8]. 40
2.41 Calcareous rock (CP) and quartzite rock (STV) material: evolution of maximum friction angle as a function of confining pressure [8]. 41
2.42 Waste rock material: (a) scalped psds, (b) parallel psds, and (c) evolution of friction angle as a function of $d_{\max}$ for both small-scale techniques. 42
2.43 Particle size and shape of rockfill material: (a) Ranjit Sagar dam site and (b) Purulia dam site [37]. 43
2.44 Stress-strain behavior from (a) Ranjit Sagar dam site and (b) Purulia dam site, (c) friction angle as a function of $d_{\max}$ for both materials [37]. 43
2.45 DEM: (a) Simulations of assemblies of discs [38], (b) annual rate of discrete element modeling publications [39] 45
2.46 Schematic diagram of approach used to model contact interactions in smooth-DEM methods [40]. 46
2.47 Diagram of disk to disk contact geometry [40]. 47
2.48 Diagram of normal and shear contact force models [40]. 47
2.49 Inelastic shock and Coulomb graphs [41] 49

3.1 Scheme of 2D elongated particles: (a) Scheme presenting the inner and outer circles of an elongated particle, and (b) examples of particles with elongation equal to 1, 3 and 5. 53

3.2 Scheme presenting the evolution of corner sharpness, being n_s the number of sides of regular polygons. 54

3.3 Scheme presenting the evolution of grain geometric irregularity as a function of parameter δ, based on [42] 55

3.4 Screenshots of 2D DEM samples with size-shape correlation based on elongation (left), angularity (center) and irregularity (right). Cases A are in the upper part and Cases B are the lower part. 56

3.5 Particle size distributions for all modeled materials as a function of particle size span S, where each particle diameter d is normalized by the maximum particle diameter $d_{\max}$. 57

3.6 Illustration of potential-based deposition method [43]. 57

3.7 Scheme of simple shearing conditions on granular samples; red dashed lines represent the periodic boundary. 58

3.8 Set of different particle shapes considered in 3D simulations, where the size of grain d is related to the circumscribing sphere around the grain. 59

3.9 Samples with particle size span $S = 0.2$ (a) and (b) and $S = 0.7$ (c) and (d) for different size-shape correlation on 3D simulation. 59

3.10 3D triaxial test: Screenshot of (a) the sample after construction protocol for $S = 0$ and (b) Schematic representation of triaxial boundary conditions employing rigid lateral walls around the sample. 60

3.11 Schematic representation of two interacting grains, displaying the associated force and branch vectors at contact frame c between particle i and j. 62

3.12 3D-DEM samples composed by spheres: particle size distributions tested for various values of S. 66

3.13 3D-DEM samples composed by spheres: Screenshots of samples with grain size span (a) $S = 0.0$, (b) $S = 0.8$ and testing configuration for the simple shear test with the periodic condition on x and z axis. . . 66

3.14 Evolution of solid fraction ν for the samples with grain size span $S = 0.0$ (a) and $S = 0.8$ (b) as a function of the shear deformation γ_{xy} for all tested values of inter-particle fiction coefficient μ, $P = 10$ [kPa]. . 67

3.15 Evolution of normalized shear strength τ/σ'_n for the samples with grain size span $S = 0.0$ (a) and $S = 0.8$ (b) as a function of the shear deformation γ_{xy} for all tested values of inter-particle fiction coefficient μ, $\sigma'_n = 10$ [kPa]. 68

3.16 Evolution of solid fraction ν (a) and critical friction angle (b) as a function of the inter-particle fiction coefficient μ for all tested grain size span, $P = 10$ [kPa]. 68

3.17 Glass bead: particle size distributions tested on ring shear test. . . . 69

3.18 Ring shear equipment: (1-2) 1 kN shear horizontal load cell, (3) cross-beam (4) touch screen display, (5) 5 kN vertical load cell and (6) 10 mm vertical displacement transducer [44]. 70

3.19 Evolution of τ/σ'_n for samples with $S = 0.8$ and inter-particle frictional coefficient (a) $\mu = 0.4$ and (b) $\mu = 0.8$ for different stress level. 71

3.20 Evolution of volumetric deformation ε_v for samples with $S = 0.8$ and inter-particle frictional coefficient (a) $\mu = 0.4$ and (b) $\mu = 0.8$ for different stress level. 71

4.1 Particle size distributions (psd) as a function of particle size span S. . 76

4.2 (a) Scheme presenting the inner and outer circles of an elongated particle, and (b) examples of particles with elongation equal to 1, 3, and 5. 77

4.3 Screenshots of samples for case A (top) and case B (bottom) for particle size spans $S = 0.0$, $S = 0.3$, $S = 0.6$, and $S = 0.9$. 77

4.4 Scheme of boundary conditions for the shearing tests. The dashed lines represent the periodic boundary along the 'x' axis. 79

4.5 Evolution of solid fraction ν and the shear strength q/p for case A (left, (a) and (c)) and B (right, (b) and (d)) as a function of the shear deformation γ. 80

4.6 Evolution of the solid fraction ν at the steady state as a function of the particle size dispersion S and for cases A and B. Error bars display the standard deviation of the data for the last 20% of deformation. . 81

4.7 Evolution of the shear strength q/p at the steady state as a function of S for cases A and B. Error bars display the standard deviation of the data for the last 20% of deformation. 81

4.8 Screenshots of samples at $\gamma = 400\%$ for case A and particle size dispersions $S = 0.4$(a), $S = 0.8$ (b). Figures (c) and (d) show the same particle size dispersions for case B. 83

4.9 Evolution of the coordination number as a function of the particle size span for cases A and B. 83

4.10 Evolution of the average contact number by particle elongation λ for case A (a) and case B (b). Error bars present the standard deviation of the data. 84

4.11 (a) Evolution of the proportion of floating particles for cases A and B as a function of the particle size span S. Proportion of floating particles by shape class λ for evolving particle size span S and case A (b) and case B (c). Error bars present the standard deviation of the data. . . 85

4.12 (Top) Screenshots highlighting floating particles (gray) and active particles (black), and (Bottom) Force networks for the same set of samples. 86

4.13 Scheme of (a) the reference frame created by contacts between particles, and (b) the reference frame created by branch vectors. 87

4.14 Angular distribution of branch orientations for cases A (a) and B (b) and different values of size dispersion S. 88

4.15 Angular distribution of radial and ortho-radial force intensities for cases A (a,c) and B (b,d) and different grain size span S. 89

4.16 Angular distributions of branch lengths cases A (a) and B (b). 90

4.17 Different anisotropies as a function of the grain size span S for cases A (a) and B (b). 91

4.18 Preferential orientations for the different angular distributions as a function of the grain size span S for cases A (a) and B (b). 92

4.19 Microstructural prediction of the shear strength q/p by means of anisotropies using Eq. (4.13) and Eq. (4.17) along with the macroscopic values measured on Fig. 4.7. 93

4.20 Decomposition of the deviatoric component of stresses by particle shape λ for cases A (a) and B (b) as a function of the grain size span S. . . 94

5.1 Scheme presenting the evolution of corner sharpness, being n_s the number of sides of regular polygons. 111

5.2 Scheme presenting the evolution of grain geometric irregularity as a function of parameter δ, based on [42] 112

5.3 Particle size distribution as a function of particle size span S, where each particle diameter d is normalized by the maximum particle diameter $d_{\max}$. 113

5.4 Screenshots of samples with particle size span S=0.2 (left) and S=0.8 (right) for different size-shape correlation studies. 115

5.5 Scheme of (a) side-vertex and (b) side-side contacts between two grains labeled i and j, where the red circles represent the contact points. . . 116

5.6 Scheme of boundary conditions for the shearing tests. The dashed lines represent the periodic boundary along the x axis, and the gray particles are the ones under this condition 117

5.7 Evolution of shear stress q/p and solid fraction ν (inset) for Cases 1A (a) and 1B (b) as a function of the shear deformation γ. 118

5.8 Evolution of shear stress q/p and solid fraction ν (inset) for Cases 2A (a) and 2B (b) as a function of the shear deformation γ. 118

5.9 Evolution of the average solid fraction ν at critical state as a function of the particle size dispersion S for Case 1 (a) and Case 2 (b). Error bars display the standard deviation of the data. 119

5.10 Evolution of the average critical shear strength q/p as a function of the particle size dispersion S for Case 1 (a) and Case 2 (b). Error bars display the standard deviation of the data. 120

5.11 Evolution of Z at critical state as a function of the particle size dispersion S and for Cases 1A and 1B (a), and evolution of Z_f per particle family for Cases 1A (b) and 1B (c) as a function of d_r and as a function of ϕ_w in the inset figure. 121

5.12 Evolution of Z at critical state as a function of the particle size dispersion S and for Case 2A and 2B (a), and evolution of Z per particle family for Case 2A (b) and Case 2B (c) as a function of d_r and as a function of ϕ_w in the inset figure. 122

5.13 Evolution of the proportion of contact type (k_{sv} and k_{ss}) at critical state as a function of the grain size dispersion S for Cases 1A and 1B (a), and Cases 2A and 2B (b) 123

5.14 Screenshots of samples at critical state for Case 1 (left) and Case 2 (right) for different size span and size-shape correlation. The green and red lines joining the center of mass of touching grains indicate whether it corresponds to a *ss* or *sv* contact, respectively. 124

5.15 Decomposition of the deviatoric component of stresses q/p (at critical state) by contribution of side-vertex q^{sv}/p and side-side q^{ss}/p contacts for Cases 1A (a) and 1B (b) as a function of the grain size span S. . . 125

5.16 Decomposition of the deviatoric component of stresses (at critical state) by shape class for Cases 1A (a) and 1B (b) as a function of the grain size span S. 126

5.17 Decomposition of the deviatoric component of stresses (at critical state) by shape class for Cases 2A (a) and 2A (b) as a function of the grain size span S. 126

6.1 Set of different particle shapes considered in this work. 140

6.2 Particle size distribution (PSD) where each particle diameter d is normalized by the maximum particle diameter $d_{\max}$. The different curves correspond to different ratios $R_D = d_{\max}/d_{\min}$. 141

6.3 Contact types between spheres, polyhedra, and spheres in contact with polyhedra. 143

6.4 Screenshot of a sample after construction protocol for $R_D = 1$ (a); samples with particle size span $R_D = 1.2$ (b) and (c), and $R_D = 5.7$ (d) and (e) for different size-shape correlations. 145

6.5 Schematic representation of triaxial boundary conditions employing rigid lateral walls around the sample. 146

6.6 Evolution volumetric deformation ε_v for Cases A (a) and B (b) as a function of the axial deformation ε_a. 146

6.7 Schematic representation of two interacting grains, displaying the associated force and branch vectors. 147

6.8 Evolution of the normalized shear stress q/p for size-shape correlations A and B, respectively, as a function of the axial deformation ε_a. . . . 148

6.9 Critical state parameters: (a) evolution of mean void ratio $\langle e \rangle$ and (b) normalized mean shear strength in the critical state $\langle q/p \rangle$ as a function of grains size span R_D. Error bars display the standard deviation of the data. 149

6.10 Screenshots of floating particles (black) and bearing-force particles (gray) for Case A (left) and Case B (b) for different grain size dispersion at critical state. 150

6.11 Evolution of (a) ratio of particles engaged in force transmission respect to the total number of particles in the sample and (b) coordination number as a function of grain size span R_D, both measured at critical state. 151

6.12 Screenshots of force network at critical state for Case A (left) and Case B (b) for different grain size rations R_D. The red connections between the centers of touching grains represent the normal forces whose thickness is proportional to magnitude of normal forces. 152

6.13 Probability density functions of normal contact forces at critical state in log-linear scales for Case A (a) and Case B (b). 153
6.14 Microstructural descriptors at critical state: (a) evolution of geometrical and mechanical anisotropies as a function of the grain size ration R_D; (b) comparison between $\langle q/p \rangle$ computed using the granular stress tensor (Eq. (6.1)) and its decomposition in microscopic anisotropies (Eq. (6.7)). 156
7.1 Evolution of ϕ_c as a function of S for grain size-shape correlation based on particle (1) elongation and (2) angularity. Error bars represent the standard deviation of the data. 165
7.2 Evolution of ϕ_c as a function of S for grain size-shape correlation based on pentagon irregularity. Error bars represent the standard deviation of the data. 165
7.3 Evolution of ϕ_c as a function of S for grain size-shape correlation based on angularity in 3D. Error bars represent the standard deviation of the data. 166
7.4 Sand-fine mixtures: (a) particle rounded for each tested material and (b) effects of particle shape and fines content on critical state friction angle for Toyoura sand as host sand [45]. 167
7.5 Particle shapes for (a) Ranjit Sagar dam site and (b) Purulia dam site [37]. 168
7.6 Nilai quarry material: (a) grains passing 2.36 mm and (b) grains passing 20 mm [46]. 168
7.7 Calcareous sand: (a) particle size distribution for tested sand and (b) pictures of different fractions [47]. 169
7.8 Shale rockfill: (a) Characteristic dimensions of the particles, L=largest, I=shortest dimension. (b) particle shape-size correlation [19]. 170
7.9 View of the tested waste rock material of Canadian Malartic [48]. . . 170
7.10 2D DEM dry flow simulation: initial configuration (left) and final deposit (right) of short granular columns for both particle size-elongation uncorrelated and correlated cases. [49] 171
7.11 Printed grains with dispersion in size and shapes. 172

LIST OF SYMBOLS AND ACRONYMS

ASTM	American Society for Testing and Materials International
CD	Contact dynamics
CS	Critical state
CSL	Critical state line
DEM	Discrete element method
DS	Direct shear test
DPI	Design performance index
EGI	Engineer geology index
FS	Factor of safety
MC	Mohr-Coulomb
MD	Molecular dynamics
NAR	Natural angle of repose
LE	Limit equilibrium
REV	Representative elementary volume
SRF	Strength reduction factor
PoF	Probability of failure
psd	Particle size distribution
UCS	Uniaxial compressive strength
WR	Waste rock
WRP	Waste rock pile
WSR	Waste dump and stockpile stability rating
WSRHC	WRPs and stockpile stability rating and hazard classification

c'	Effective cohesion
C_c	Coefficient of curvature
C_u	Coefficient of uniformity
C_0	Proportion of floating particles
$d_{\max}$	Maximum particle diameter
$d_{\min}$	Minimum particle diameter
D	Specimen diameter
e	Void ratio
ε_q	Shear deformation

ε_a	Axial deformation
ε_v	Volumetric deformation
G_s	Specific gravity of solids
I	Inertial number
μ	Inter-particle friction coefficient
ν	Solid fraction
T	Specimen thickness
p'	Mean effective stress
q	Deviatoric shear stress
ϕ	Friction angle
ϕ_c	Critical friction angle
ρ	Density
S	Grain size span
σ'_n	Effective normal stress
τ	Shear stress
v_s	Shearing velocity
W	Specimen width
Z	Coordiantion number

CHAPTER 1 INTRODUCTION

The transition to renewable energy production, such as eolic and solar, or the need to improve energy storage, is crucial for reducing carbon emissions and mitigating climate change. However, it requires a significant production of minerals, which is only expected to grow in the next decades [50]. The mining industry is then critical to ensuring the primary resources for a transition to low-carbon technologies while trying to reach high standards in terms of operation safety and minimum environmental impact. Among those operations, mining sites need to constantly deal with large volumes of rock without economic interest, known as waste rock (WR), that are excavated to reach the ore-rich strata. The amount of WR material generated varies according to the type of mining or whether the site conducts underground mining or open-pit [24]. Due to the large volumes of material generated, waste rock piles (WRPs) are among the largest geotechnical structures worldwide, reaching heights over 700 m [20]. Hence, WRPs represent a technical and environmental challenge regarding chemical, hydrogeological, and mechanical stability [11].

WR materials are commonly composed of large quantities of loose, uncompacted coarse blasted rocks with a broad particle size distribution (psd), from sizeable angular rock clasts of around 1 meter in diameter, along with angular gravel, sand, and silt [13–15, 51]. The heterogeneity of WRPs is also linked to the different lithologies being extracted from the mine, as well as particle segregation produced during the dumping and construction process [11,20]. These inner characteristics of WRPs make their engineering design a complex and challenging task.

The shear strength is one of the main parameters required to design and evaluate the mechanical stability of coarse-grained geotechnical structures (e.g., dams, rockfills, and WRPs). However, standard and even large-scale shearing devices are not necessarily fit to test coarse materials such as WR. To be able to characterize these materials, small-scaling techniques are often needed so a given maximum particle size ($d_{\max}$) respects international engineering standards [52, 53]. Depending on the type of shear test employed, these standards suggest that aspect ratios of around $D/d_{\max} = 5$ to 10 (where D is the characteristic sample size) should be respected [1]. However, contradictory results have been reported on small-scaling samples and further research is needed to better understand the reliability and limitations of scaling techniques [1, 3, 6–8, 13, 17, 19, 31, 35, 37, 48, 54].

Slope stability of loose granular fills, such as WRPs, mainly depends on the critical friction angle (ϕ_c), which has been shown to be independent of the initial configuration of the material [55, 56]. Moreover, several studies have shown that ϕ_c does not seem to depend on the psd, provided that particle shape and roughness remain unchanged along with grain sizes [26, 28–30, 35, 57–60]. Therefore, small-scaling techniques based on altering the psd can be expected to reproduce reliable ϕ_c compared to the field coarse material. However, if the characteristic grain shape and mineralogy change along different grain sizes, altering the psd might also affect the friction angle, which could be the source of the contradictory results mentioned above. Thus, in order to ensure that mechanical parameters obtained on small-scaled samples are representative and reliable, grain shape analyses should be carried out and compared to the original coarse material [19, 35].

Numerical techniques are an alternative to simulate the mechanical behavior of coarse-grained materials that do not fit in laboratory devices. For instance, the Discrete Element Method (DEM) is a particle simulation strategy that allows the simulation of assemblies of granular assemblies under varied boundary conditions [38, 61, 62]. In the frame of the DEM, a broad range of sample sizes, grain shapes, and grain sizes can be simulated and compared to identify the effects of small-scaling the psd on the critical friction angle [29, 35, 42]. These results can then be used to define physical-based scaling laws, needed to analyze experimental results on small-scaled samples [63]. Motivated by the limitations of scaling methods for coarse granular materials, this thesis aims to develop a series of DEM models to study the effects of particle size and shape, which is called grain size-shape correlation in this study, on the critical shear strength of granular materials.

General objective

The main objective of this thesis is to analyze and identify the combined effects of grain size and shape distributions on the critical shear strength of granular media to assess the reliability of small-scaling techniques for coarse granular materials.

Specific objectives

- SO1: Develop numerical DEM shearing tests of granular materials having grain size-shape correlations.
- SO2: Describe the physical sources of the effects of size-shape correlations following a multi-scale approach, linking the mechanisms at the inter-particle contacts with the macromechanical behavior of granular materials.
- SO3: Identify limitations of small-scaling methods for coarse granular materials.

It is expected that the results of this work will allow us to review the reliability of small-scaling techniques employed and to propose recommendations for improving testing methods depending on geometrical material properties. This document is composed of 8 chapters, the contents of which will be described as follows:

- **Chapter 2: Literature review**
  This section focuses on collecting academic and industrial information and works related to mechanical behavior or coarse granular materials, with a particular emphasis on waste rock (WR). We explore the material composition and management of WRPs in a mining environment, followed by the characterization of the physical properties of WR material, centering on its shear strength. Moreover, we reviewed small-scaling techniques, shearing testing devices, and standards (e.g., ASTM) employed for the mechanical characterization of coarse granular materials. Finally, we discuss the advantages and limitations of DEM simulations in studying the effects of grains' geometrical characteristics on the mechanical behavior of granular assemblies.

- **Chapter 3: Methodology**
  This chapter outlines the methodology for DEM simulations to study the behavior of granular materials, focusing on particle shape and size effects. This review combines theoretical and computational approaches to analyze the mechanics of granular materials under varied conditions. Detailed procedures for sample preparation, simulation execution, and data analysis are provided for 2D and 3D simulations. The chapter also addresses the validity and reliability of the numerical simulations, comparing them with experimental results. Limitations of the DEM approach in soil mechanics are discussed to highlight areas for improvement.

- **Chapter 4 ARTICLE 1: Effects of particle size-shape correlations on steady shear strength of granular materials: The case of particle elongation**
  This section investigates how particle size and shape correlations affect the steady shear strength of granular materials, focusing on the effects of particles' elongation. Using 2D DEM simulations, we explore two scenarios: one with large elongated grains and smaller circular grains, and another with large circular grains and smaller elongated grains. The results demonstrate that size-shape correlations significantly impact shear strength and packing properties.

- **Chapter 5 ARTICLE 2: Shear strength of angular granular materials with size and shape polydispersity**

The chapter presents a study that uses 2D DEM simulations to investigate how variations in particle size and shape (including angular grains of regular and irregular geometries) affects the mechanical response of granular materials. The findings indicate that size-shape correlations based on grain sharpness significantly impact the critical shear strength, whereas geometric irregularity has a minimal influence on the material's behavior.

- **Chapter 6 ARTICLE 3: Particle shape distribution effects on the critical strength of granular materials; a 3D study**
  This chapter utilizes 3D DEM simulations to investigate how the correlation between particle size and shape affects the critical shear strength of granular materials. The findings demonstrate that the presence of fine angular particles does not necessarily promote changes in critical shear strength, whereas fine rounded particles have a lubricating effect that decreases the critical shear strength of granular assemblies.

- **Chapter 7: Discussion** This chapter compares our results with existing literature and theoretical frameworks and explores how they can contribute to the characterization of coarse granular materials through small-scaling techniques and the stability analysis of WRPs. Additionally, it evaluates the proposed methodology, pointing out advantages and limitations.

- **Chapter 8: Conclusions** This chapter summarizes the study's key findings, emphasizing the significant impact of size-shape correlations on the mechanical behavior of polydisperse granular materials. Future research directions are also presented.

CHAPTER 2 LITERATURE REVIEW

2.1 Context

Geotechnics focuses on the behavior of earth materials to design, construct, and maintain safe civil structures. The mechanical behavior of soils has been extensively studied and there is an accepted framework for its characterization that strongly relies on laboratory testing [55]. However, due to the size limitations of laboratory devices, the study of coarse granular materials, such as gravelly fluvial soils, rockfill or mine waste rock (WR), is often impossible to perform and their behavior remains not fully understood. Several studies have been carried-out to improve the understanding of the mechanical behavior of coarse granular materials, such as Leussink [64], Marsal [65, 66], Marachi *et al.* [7, 67], Becker *et al.* [36], Ovalle [25], among many others. Nonetheless, they have been limited by the size of available laboratory devices that are unable to contain oversized coarse grains [7, 13, 15]. Therefore, sample small-scaling techniques have been proposed in order to modify the psd, such as the truncated or parallel grading [1, 19]. However, contradictory results have been reported on over- and under-estimations of the shear strength using small-scaling techniques. Presumably, this could be explained by the dispersity or lack of control of material properties, such as particle shape, sample aspect ratio, and initial density [19, 35]. Thus, to evaluate physical-based small-scaling laws for coarse granular materials, it is first necessary to improve the understanding of how these geometric properties contribute to shear strength.

Mine waste management represents a particular case where the characterization of coarse blasted and crushed WR poses many engineering challenges. The mining industry is one of the largest engineering operations globally, and the ore extraction process produces significant amounts of WR. Open-pit mining operations generate a volume of WR of 2 to 3 times the volume of ore extracted, while in underground mining this proportion is relatively lower, about 10% to 20% of extracted ore [24]. Nevertheless, these volumes represent large quantities of coarse, loose, uncompacted materials that are typically stored in waste rock piles (WRPs, Figure 2.1), often reaching several hundred meters in height. Moving large quantities of WR from the pit to the pile can also lead to a lack of available landfill space [14,15,20]. Examples of this situation are mines located in mountainous sites, where the only available spaces are narrow valleys with steep slopes, resulting in very high WRPs [14]. Consequently, WRPs are among the largest geotechnical structures ever built, and the analysis of their physical, hydrogeological, and chemical stability is crucial for safe operation and closure.

The mechanical stability of WRPs is a challenging task since it depends on the material

Figure 2.1 Large waste rock pile constructed with benches at the Canadian Malartic Mine, Québec [11].

properties, pile geometry, foundation conditions, and construction method [11, 68]. In this work, we focus on the mechanical behavior of WR and the characterization of the shear strength of these loose materials. The literature review explores the mechanical behavior characterization of coarse WR material typically used to perform physical stability analyses of WRPs. It reviews various sample small-scaling techniques, focusing on shear strength, geomorphological properties, testing characteristics, and environmental conditions that impact the results.

2.2 Waste rock piles (WRPs)

Mine WRPs are the largest man-made structures in terms of mobilized volume. For instance, Figure 2.2 shows the East WRP of the Antamina copper mine in Peru, which contains approximately 1 billion tons of material, covers an area of 240 hectares, and has a total height of more than 500 meters [12]. WRPs present the following singular geotechnical conditions [20]:

1. Monitoring the mechanical behavior is challenging due to the large WR volumes and high filling rates in dumping processes.
2. The psd is often well-graded, varying from fine material to particles over 1 m in diameter. In addition, due to the dumping deposition process, particle size segregation

between the upper and lower levels of the deposit could be significant.

3. Particle breakage can occur due to the high pressures generated by the height of the deposits. This mechanism increases the finer particle size and material compressibility, while reducing dilatancy.
4. There is significant variability in the void ratio within the bulk of the pile.
5. Coarse particle size makes difficult representative sampling for experimental campaigns.

Figure 2.2 East WRP of the Antamina mine in Peru [12].

2.2.1 Types of waste rock piles

WRPs stand out by their geological composition, structural arrangement, and construction techniques. The WR material may consist of soft rocks sourced from sedimentary formations like coal or salt mines, or hard rocks obtained from metallic mines such as gold, silver, and copper operations [69, 70]. Geometrically, we can classify different types of WRPs based on their overall configuration and topographic limitations, as suggested by Wahler [71].

Method of construction

The construction methods of WRPs are mainly based on the topography and the equipment available for transportation and disposal [72]. The principal construction methods are *End dumping*, *Push dumping*, *Free dumping*, *Dragline*, and *Co-disposal* with tailings. Each method generates different levels of compaction and segregation. The main characteristics of each construction method are the following:

- **End dumping:** WR material is dumped directly from the crest of the WRP face, generating a wide grain size segregation along the slope, where the coarse rock material moves towards the pile toe [70]. This effect generates a significant accumulation of large particles at the bottom, resulting in an open zone for air and water flow [73].

- **Push dumping:** WR material is dumped near the WRP crest and pushed down by dozers over the crest, resulting in lower particle size segregation compared to the end dumping method. Push dumping generates slower velocity in dumping material, causing less segregation within the WRP [74].
- **Free dumping or plug dumping:**, WR material is stored on small piles (or heaps) around 2 m in height. Subsequently, the small piles are spread in layers. This method generates low particle segregation and higher compaction than end dumping and push dumping, but is more expensive [51].
- **Dragline:** WR material is mined and transported with a dragline or bucket excavator. This method is used in large-scale mining (e.g., coal), and generates low segregation because the material is placed directly on the ground surface.
- **Co-disposal:** WR material can also be deposited along with tailings (or other fine-grained material) to help control problems such as acid mine drainage, retention dam stability, and improvement of the containing contaminated material of stored piles [51].

The most common method for constructing WRP is end dumping. This method is favored due to its simplicity and efficiency. However, end dumping can lead to unstable slopes if not managed properly [75].

2.2.2 Factors affecting mechanical stability

WRPs and stockpile stability rating and hazard classification (WSRHC) system highlights 22 key factors or attributes that are considered to affect stability. As shown in Figure 2.3, these factors have been classified into seven groups and separated into two primary groups [12]: the design and performance index (*DPI*) and the engineering geology index (*EGI*). On the one hand, DPI relates to geometrical factors and mass parameters, such as height, slope angle, volume, and dumping rate. On the other hand, factors that influence *EGI* are the geographic location and climate, namely high seismic risk zones and wet environments posing greater challenges [76]. Most failures are linked to the physical characteristics of the foundations, such as topography, overburden type, groundwater conditions, and liquefaction potential [20, 77, 78]. As indicated in Figure 2.3, the mechanical properties of the WR material, including density, particle size distribution, particle shape, intact rock strength, and chemical stability, are taken into account in the *EGI* and play a critical role in maintaining WRP stability [79].

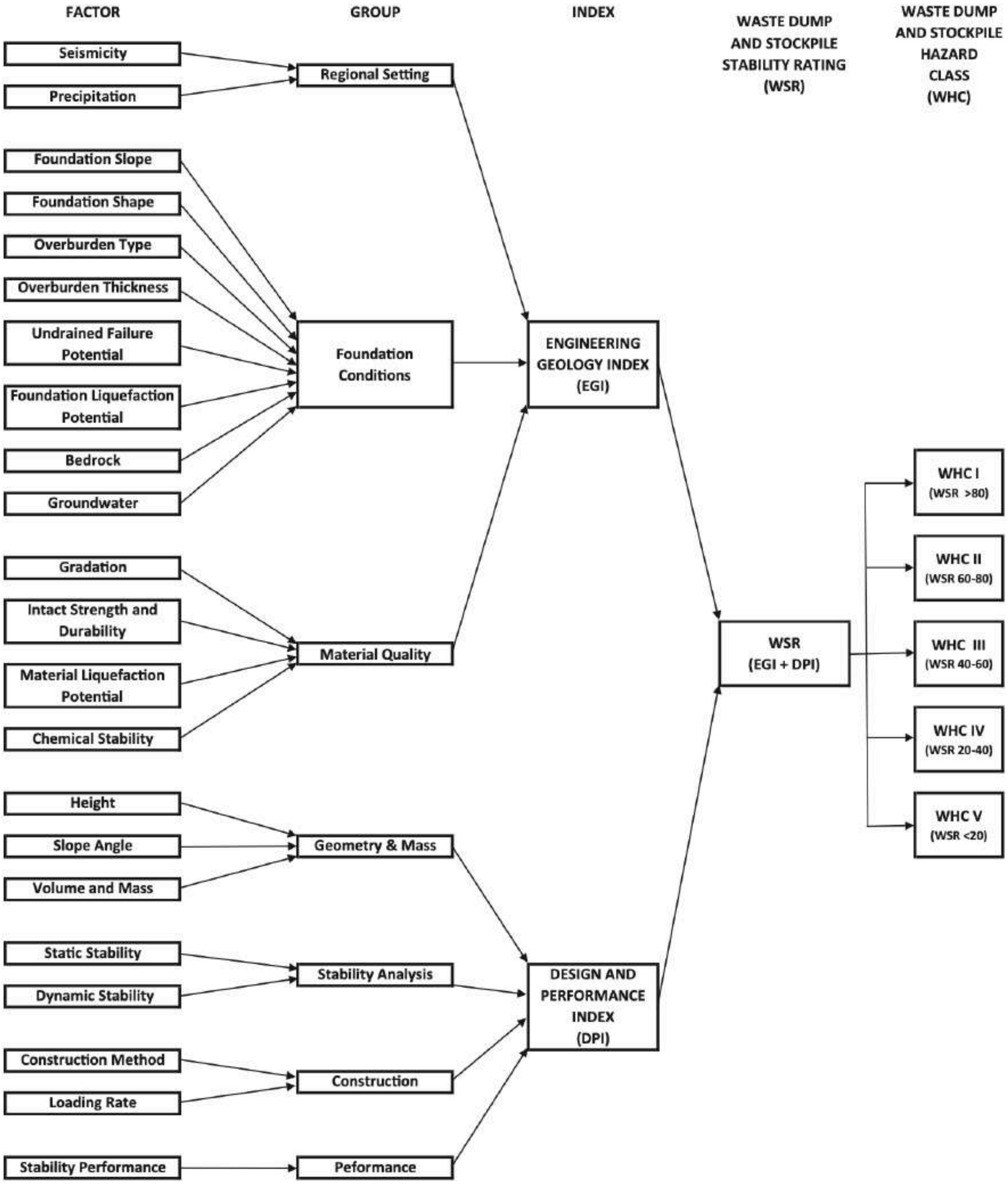

Figure 2.3 Diagram of WRPs and stockpile stability rating and hazard classification system [12].

2.2.3 Waste rock material properties

Particle size distribution (psd)

The psd of soil defines the relative amount of particles according to their size, typically given by mass. The standard ASTM D2488–17 [52] defines the fine fraction as the material that passes through sieve No. 200 (0.075 mm), sands correspond to sieves between No. 200 and No.4 (4.75 mm), gravels between No. 4 and 3” (75 mm) and, finally, the oversized particles correspond to the material coarser than 3”, including cobbles, boulders or rock clasts.

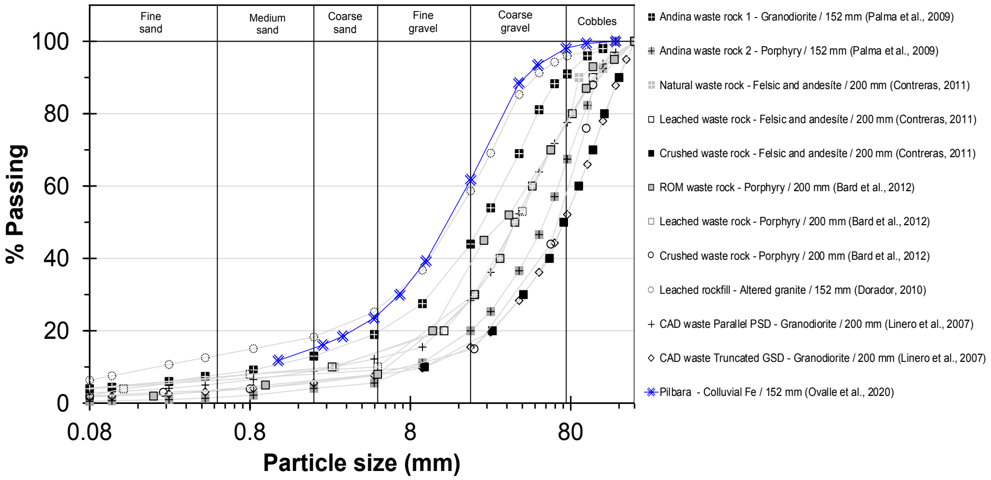

Figure 2.4 Data compilation of psd of WR materials, modified from [13].

The compilation in Figure 2.4 displays the psd of WR materials, where particles coarser than 200 mm were extracted to accommodate samples in large triaxial cells measuring 1 m in diameter [13]. The coefficient of uniformity ($C_u = d_{60}/d_{10}$) ranges between 5 and 30 for various WR materials. In field conditions, WR material generally exhibits C_u values higher than 20 [80, 81], with curvature coefficients ($C_c = d_{30}^2/(d_{60}d_{10})$) typically falling within the range of 1.5 to 6.5, indicating well-graded samples. The psd range for in situ WR material is shown in Figure 2.5 (a), where Granite WR stands out with around 50 % of particles coarser than 1 meter. Figures 2.5 (b) and (c) show typical ranges of WR material with $d_{\max}$ up to 400 mm. Moreover, technological improvement has enabled the characterization of in-situ psd of WRPs with diameters exceeding 1 meter [82].

Particle shape

Rock blasting generates randomly shaped grains of high angularity and sharpness, similar to the category of quarried rock presented in Figure 2.6. Several studies have shown that

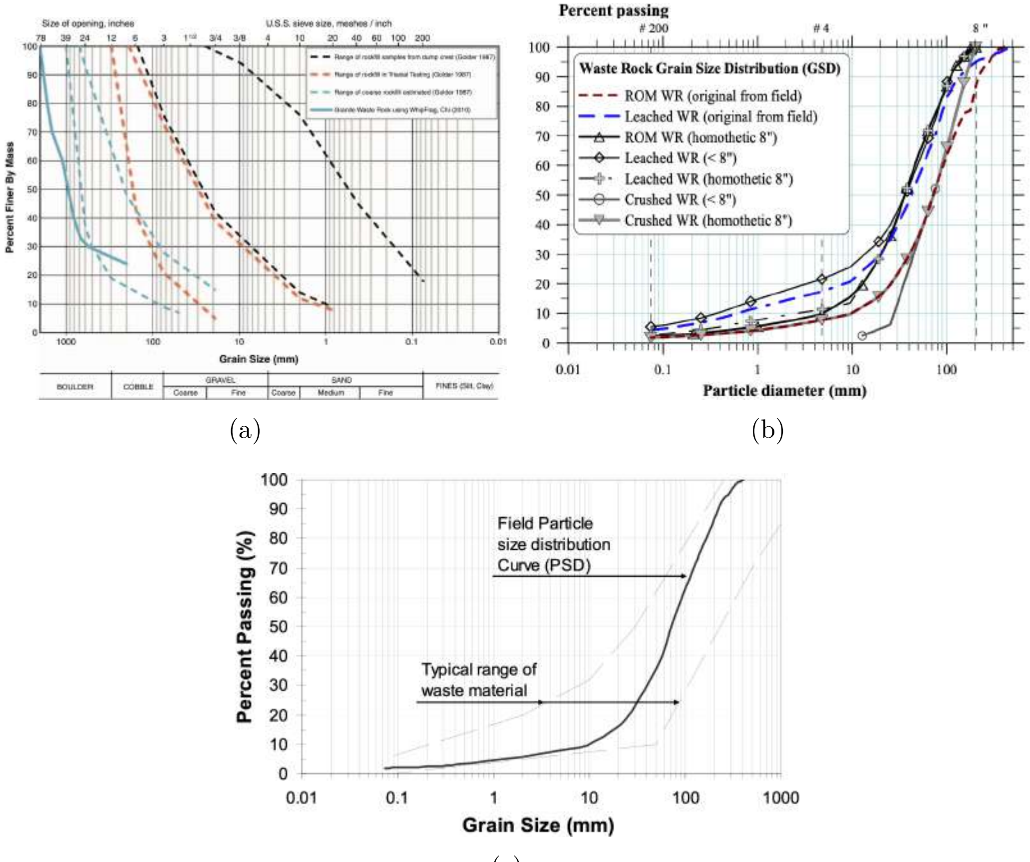

(a)

(b)

(c)

Figure 2.5 Typical psd ranges for WR materials (a) Hawley & Cunning [12], (b) Bard *et al.* [14] and (c) Linero *et al.* [15].

the more angular and elongated the particles are, the higher the critical friction angle [16, 17, 19, 79, 83]. However, quantifying the particle shape characteristics of WR material is a challenging task due to the inherent irregularity and heterogeneity of the grains.

Linero *et al.* [17] studied a WR material from an iron mine in Australia, using shape definitions according to grain by dimensions L=length, I=breath, and S= thickness, as described Figure 2.7(a). They showed that the studied material had grain shape-size correlations, where coarser grains were flatter and less elongated than finer grains. Ovalle & Dano [19] also quantified the particle shape of rockfill materials, measuring the largest (a) and the shortest (c) dimensions of each grain (Figure 2.8 (a)). They showed that their material had a grain shape-size correlation based on the c/a ratio, where fine particles tend to be elongated and coarse particles more rounded. Remarkably, these two-grain shape-size correlations described in these research papers are inverse, namely, in Figure 2.7(b) grain elongation increases with increasing size, while in Figure 2.8(b) it increases with decreasing particle size. These results

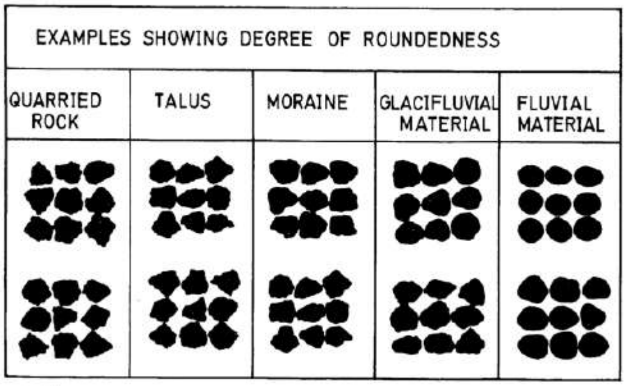

Figure 2.6 Particles' roundness and smoothness from different sources [16].

suggest that when psd is modified for testing on small-scaled samples, grain shape distribution can also be altered, leading to variability in the mechanical behavior between samples at different scales [17, 19]. Thus, the particle shape effect should be an essential factor to consider when altering the psd. The effect of grain shape on the shear strength of granular materials is studied in more detail in Section 2.3.2.

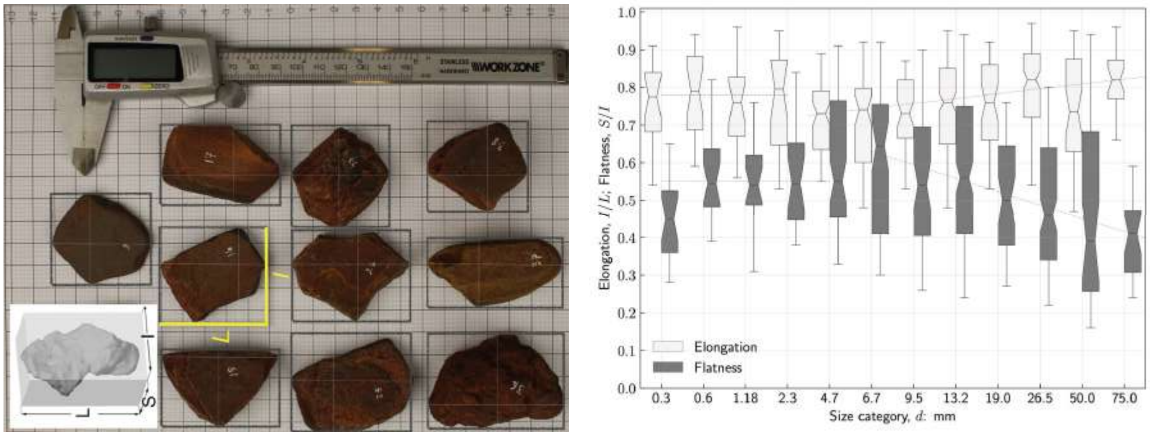

(a)

(b)

Figure 2.7 Iron mine waste rock: (a) Characteristic dimensions of the particles, L=Length, I=Breath, and S= Thickness [17]. (b) Variability of elongation ratio and flatness ratio calculated from the form dimensions L and I for the different size fractions [18].

Intact strength and durability

The intact strength of any individual rock grain impacts the mechanical behavior of WR material, especially in high dumps where inter-particle stresses may exceed the intact strength

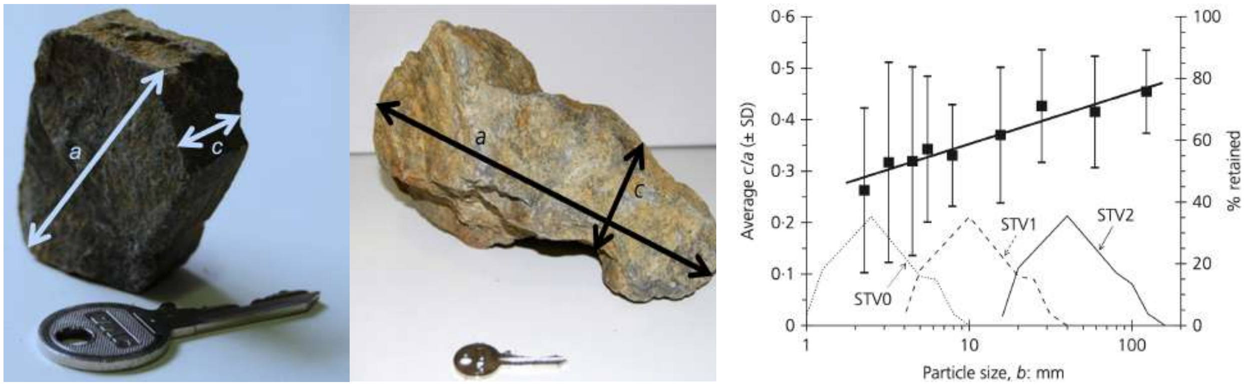

(a) (b)

Figure 2.8 Shale rockfill: (a) Characteristic dimensions of the particles, *a*=largest, *c*=shortest dimension. (b) particle shape-size correlation [19].

of the material and result in particle crushing. Typically, particle strength is defined based on their UCS (uniaxial compressive strength), obtained in an unconfined compression test on standard-size cylindrical specimens. According to Marsal [66], rocks and the corresponding rockfill and WR material can be classified according to their UCS into three wide classes: weak rocks from 3.4 to 17.2 MPa, average strength rocks from 17.2 to 68.9 MPa, and strong rocks from 68.9 MPa or higher.

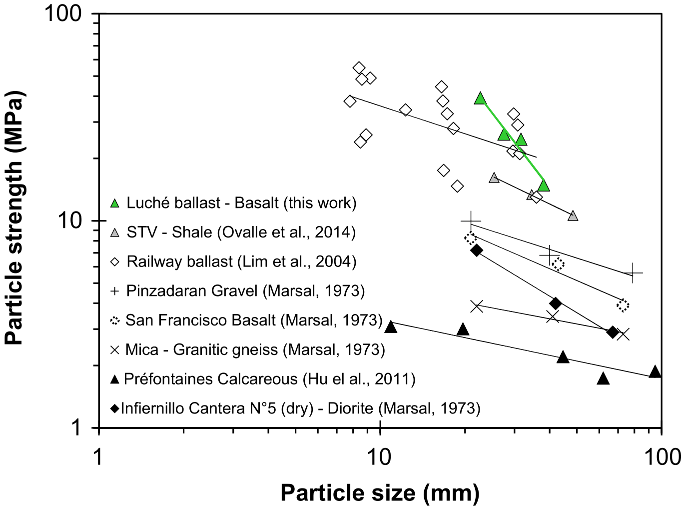

Figure 2.9 Particle crushing strength of different rock aggregates [13].

The size effect on rock particle strength refers to the phenomenon where the strength of rock particles decreases as their size increases, as shown in Figure 2.9. Larger particles are more likely to have micro-cracks and flaws than small grains, leading to lower particle strength [84].

Moreover, particle breakage might alter particles' shape characteristics, modifying their aspect ratio, sphericity, and roundness. As the breakage process progresses from bulk fracture to attrition and abrasion modes, the particles become more rounded [85]. This effect has significant implications in geotechnical engineering and rock mechanics, particularly when evaluating the stability of slopes.

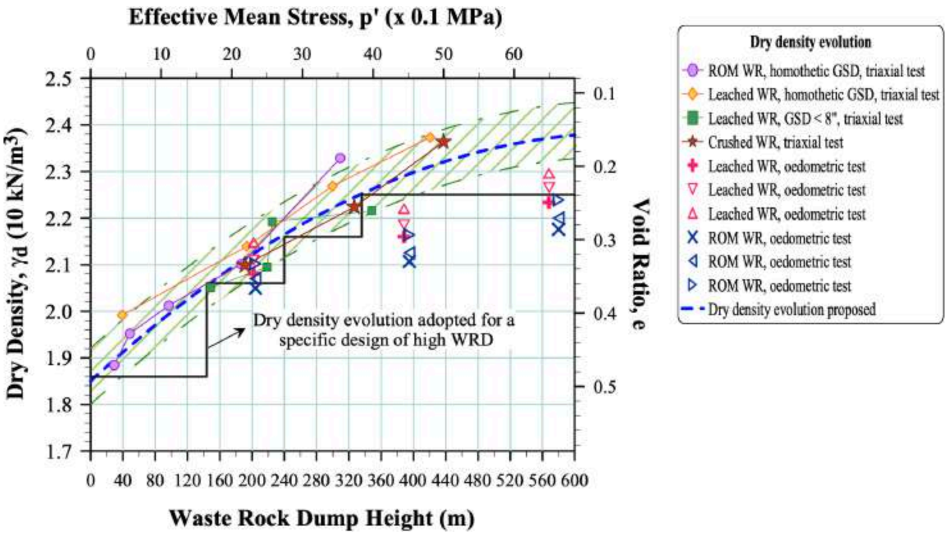

Figure 2.10 Evolution of the dry density with WRP height, estimated from oedometric and compression triaxial tests [14].

Density and void ratio

In situ, the density of a WRP can vary between 1.4 t/m^3 to as high as 2.5 t/m^3 [20, 86–89]. This wide range of values is related to factors such as lithologies, construction methods, and stress history. Another critical factor affecting density in these structures is height. The higher the pile, the greater the stress to which the material at the bottom is subjected. Figure 2.10 shows the evolution of the dry density with WRP height, for a height range from 0 to 600 m in Chilean copper mines [14]. Different lithologies and mineralogical compositions present in WR material also lead to different specific gravity of solids (G_s). For instance, for iron mining G_s can be as high as 4 to 4.8 [90, 91], and in copper mining, its value is typically between 2.7 to 2.8 [14].

Angle of repose

The natural angle of repose (NAR) is the angle of maximum slope inclination at which a loose soil is barely stable [92]. When a pile reaches a predetermined height or base width, the NAR can be estimated by direct measurement and calculated by the inverse tangent of the ratio between height and half of the base width [93]. Some works reported NAR within 35° to 40 ° in WRPs [69, 76](Figure 2.11). The angle of repose is affected by psd, particle shape, density, and mineralogy [11, 68].

Figure 2.11 View of NAR of 50 m high WRP, modified from [12].

2.2.4 Failures and stability acceptance criteria

Currently, limited information exists on the failure of WRPs, and most have been treated as operational accidents without recording the geotechnical characteristics of each event [20]. Failures in WRPs have the potential to harm communities and the environment, impacting a wide area around the mining site. In a study of 50 failures of WRPs in the coal mining industry reported by Dawson *et al.* [77], many cases involved flow slides with significant run-out distances. The causes of each failure are often due to a combination of multiple factors, such as increased loading, earthquakes, liquefaction, floods, and foundation subsidence [77, 78]. WRPs failure modes can be classified into the following types: shallow, deep-seated, foundation, and toe loading/foundation [12]. In the case of coal WRPs, the most devastating failures have been triggered by static liquefaction [15, 20, 78]. However, WRPs constructed under apparently dry conditions over strong, free-draining foundations would not appear to be exposed to liquefaction flow sliding.

It is worth mentioning the well-known case of Aberfan coal tip failure in 1966, UK, which involved the mobilization of 102,060 m^3 of mine waste, tragically resulting in the loss of 144

(a) (b)

Figure 2.12 Failures of WRPs: (a) failure of a 515 m high WRP in a copper mine in Chile [20] and (b) Aberfan coal WR failure, October 21st 1966 [12].

lives (Figure 2.12 (a)) [94]. Other documented cases of coal mine collapse are Eskihisar mine in Turkey [95], Quintette Mine in Canada [77], and Jayant Mine in India [96]. One of the few registers belonging to the copper industry is the Bougainville copper open pit mine in New Guinea in 1982 [70], and the failure of a 515 m high WRP on a copper mine in Chile, in 2004 (Figure 2.12 (b)).

Basic design considerations

The physical stability of WRPs is vital during the whole mining cycle, including the long-term state after mine closure. The foundations of WRPs must be extensively characterized, and short and long-term settlements need to be assessed [11]. The geometrical design of WRPs significantly impacts their mechanical stability [12, 14, 15, 20], and it is recommended to design WRPs with intermediate benches, typically 25 m in height, to decrease the global slope and minimize particle segregation [11, 20].

Figure 2.13 (a) presents a chart for WRPs stability proposed by Hawley & Cunnings [12], which used the waste dump and stockpile stability rating (WSR). WSR is obtained by the relative weighting of the EGI and DPI indexes, presented in Figure 2.3. This methodology facilitates comparing possible alternative configurations or development phases for a given WRP. Figure 2.13 (b) shows five categories linked to WSR, which range from WHC-I (very low hazard) to WHC-V (very high hazard). Despite the previous recommendation, the worst-case scenario occurs when WRPs are built using end dumping or push dumping methods. Although it is not ideal, some companies have to use these methods due to operational constraints, such as open pit backfilling or valley fill dumping [97, 98]. As a result, WRPs constructed in this way are deposited loosely, highlighting the importance of characterization

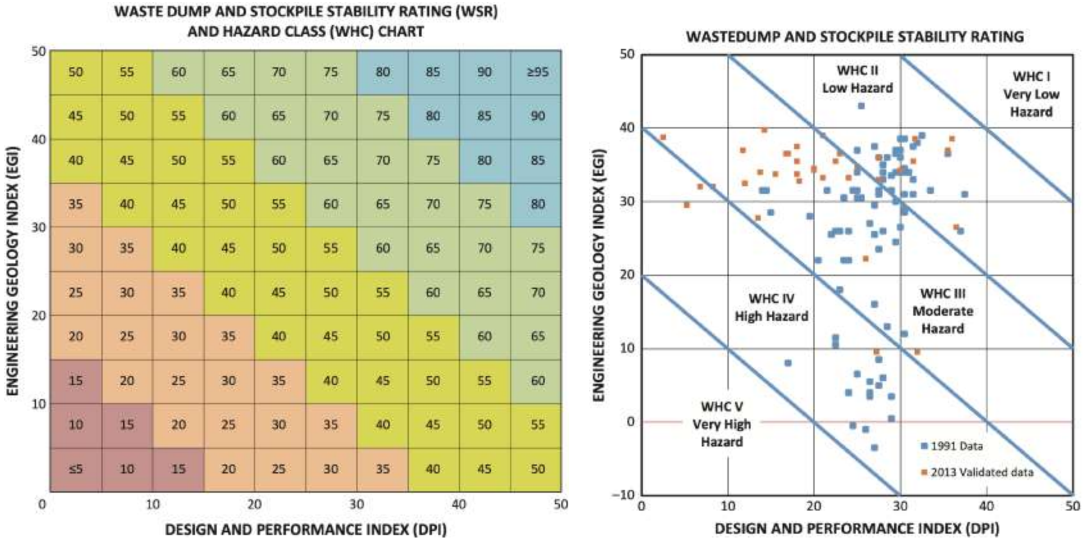

50	55	60	65	70	75	80	85	90	≥95
45	50	55	60	65	70	75	80	85	90
40	45	50	55	60	65	70	75	80	85
35	40	45	50	55	60	65	70	75	80
30	35	40	45	50	55	60	65	70	75
25	30	35	40	45	50	55	60	65	70
20	25	30	35	40	45	50	55	60	65
15	20	25	30	35	40	45	50	55	60
10	15	20	25	30	35	40	45	50	55
≤5	10	15	20	25	30	35	40	45	50

(a) (b)

Figure 2.13 WRP stability rating and hazard: (a) class chart, and (b) chart illustrating the results of the 1991 and 2013 surveys [12].

of critical shear strength as a significant parameter to assess mechanical stability.

2.3 Shear strength of coarse granular materials

The most common way to express the shear strength envelope of granular materials is the Mohr-Coulomb (MC) criteria, which includes a frictional component depending on the effective normal stress (σ'_n), the effective internal friction angle (ϕ'), and a cohesive component given by the effective cohesion (c'). The shear stress on the failure plane is described by the *Mohr-Coulomb Failure Criterion* as:

$$\tau = \sigma'_n \tan\phi' + c'. \tag{2.1}$$

Dry granular materials have null or very low cohesion, being c' negligible. Moreover, when considering the effective principal stresses (σ'_1, σ'_2, σ'_3) under axi-symmetric stress conditions ($\sigma'_2 = \sigma'_3$), we can rewrite Equation 2.1 for the non-cohesive case in terms of mean effective stress $p' = (\sigma'_1 + 2\sigma'_3)/3$ and deviatoric shear stress $q = (\sigma'_1 - \sigma'_3)$ [99] as:

$$q = \frac{6\sin\phi'}{3-\sin\phi'}\, p'. \tag{2.2}$$

Empirical evidence proves, however, that the peak failure envelope of granular soils is nonlinear (Figure 2.14). Non-linearity is mainly due to grain breakage and rearrangement of particles after crushing, which reduces dilatancy [21, 100, 101].

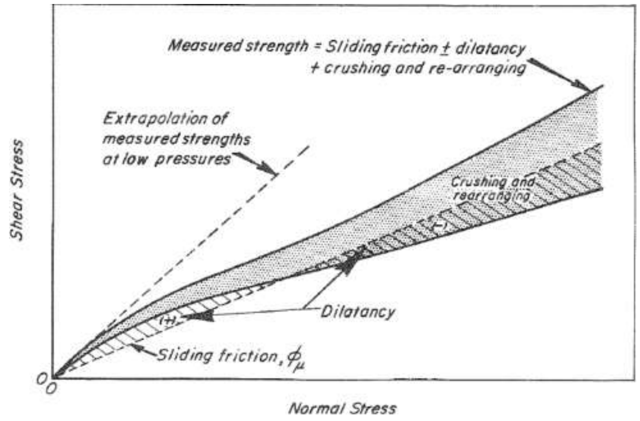

Figure 2.14 Illustrative diagram of the phenomena affecting shear strength in granular materials [21].

The stress-strain behavior of sheared granular materials can be described by the general framework of critical state theory, which occurs when plastic shearing deformation can continue indefinitely without changes in volume or effective stress [55, 102–104]. The critical state, as defined by Roscoe *et al.* [102], is a condition where the soil undergoes continuous shear deformation (ε_q) while maintaining constant p', q and e, which can be described as :

$$\varepsilon_q \to \infty \implies \frac{\partial p'}{\partial \varepsilon_q} = \frac{\partial q}{\partial \varepsilon_q} = \frac{\partial e}{\partial \varepsilon_q} = 0 \ . \tag{2.3}$$

Accordingly, at large shearing deformation and regardless of the initial state, the material reaches its critical void ratio and critical shear strength, also known as steady strength. Therefore, in $e-q-p$ space, the critical state is represented by a single point for a given stress path. These distinct final states are interconnected, forming the critical state line (CSL). Figure 2.15 illustrates the CSL and its projection on the $q-p'$ and $e-p'$ planes. On $q-p'$ space, the CLS is a straight line described as $q = Mp'$. For a dry granular material under axi-symmetric stress conditions $M = 6\sin\phi'/(3-\sin\phi')$ [99], as shown in Equation 2.2. On the other hand, on $e-p'$ space, the CSL shows a non-linear relationship. Particularly for granular soil, this relation can be described mathematically by $e = \Gamma + \lambda(p/p_{ref})^{\xi}$, where Γ, λ and ξ are material constants [105].

Figure 2.16 shows how the stress and void ratio paths reach the critical state. When comparing the behavior of two samples of the same material with different initial densities (dense and loose) and tested under the same effective confining stress and drained condition, the

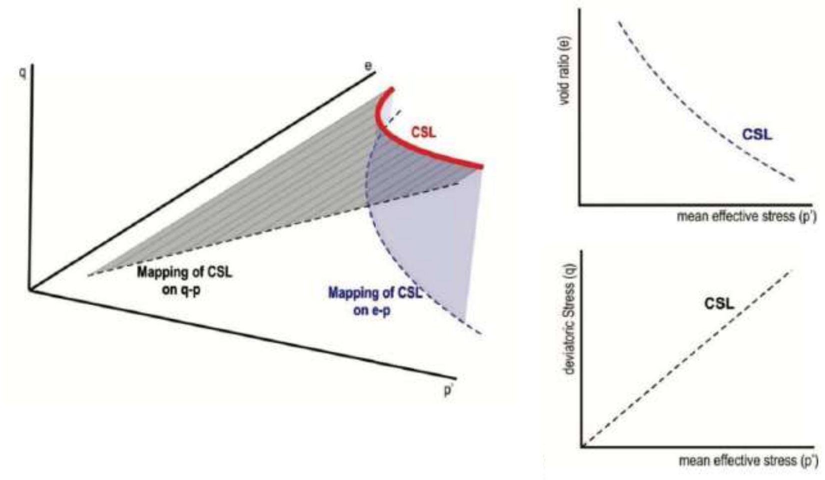

Figure 2.15 Illustrative diagram of the critical state line and its protection on $e-p'$ and $q-p'$ spaces [22].

denser sample will exhibit dilation and a peak shear strength (dashed line in Figure 2.16), while the looser one will contract without a peak strength (continuous line in Figure 2.16). However, both samples will reach the critical state at large shear strain, related to steady shear friction angle or critical friction angle (ϕ_c) and the same critical void ratio. When dealing with dumped WR, note that the loose material will not present dilation or peak shear strength. Therefore, engineering designs of WRPs should be based on ϕ_c.

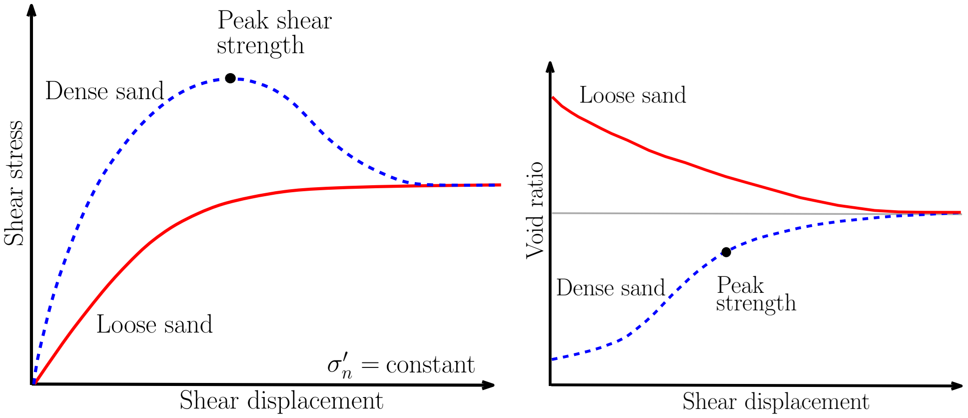

(a) (b)

Figure 2.16 Stress-strain (a) and void ratio (b) paths in the failure surface of a sheared granular material until critical state; dense case in blue and loose case in red; the normal effective stress σ'_n on the surface is the same in both cases.

Ovalle *et al.* [13] compiled 158 drained triaxial compression tests conducted on 33 different materials (sand, ballast, and rockfill materials). Tests on rockfills included only samples performed on ≈1 m in diameter and having $d_{\max}$ between 100 and 200 mm. Figure 2.17 shows the peak friction angle ($\phi_{\max}$) for different granular materials as a function of normal stress (σ'_n), where a clear trend of non-linear stress-dependent friction angles is observed [15,79,106]. This is due to particle crushing and rearrangement being promoted at high stresses [107,108]. Most of these triaxial tests were carried out using oversized materials, which required a modification of psd by applying small-scaling techniques.

2.3.1 Mechanical testing of granular materials

Direct shear, triaxial, and simple shear tests are the most common methods for testing soil shear strength. However, in this section we will discuss only the equipment available for testing coarse granular materials.

Direct shear test

Direct shear (DS) is the most common test used to determine the shear strength at the laboratory. The shear box of a DS device is a rigid metallic container that allows the soil sample to be subjected to an increasing shear displacement on the mid-height horizontal plane, as described in Figure 2.18. The upper box section is subjected to a horizontal force (S), while the bottom section of the box is fixed, and a normal force (N) is applied. This results in forced shearing along the contact surface between two sections. Such a test is usually conducted with a constant rate of horizontal displacement [23]. Standard shear box apparatuses typically carry out tests on soil specimens of 60 mm to 100 mm square section and 20 mm to 25 mm in height, which allows a $d_{\max}$ up to 10 mm (based on ASTM-D3080 [53]). During the test, shear force, lateral displacement, and normal displacement are measured, while the normal force is kept constant [53, 109, 110]. Repeating the DS test for different normal stresses can yield a failure envelope (e.g., Mohr-Coulomb) for a soil sample.

Large-scale testing devices are necessary for evaluating coarse granular materials. For example, Figure 2.19 presents the large DS box developed by Linero *et al.* [18], with a dimension of 720 mm. This type of apparatus allows testing specimens with $d_{\max}$ of approximately 120 mm, based on ASTM D3080. Sample preparation and DS tests are relatively easy and quick to perform compared to other tests. Nevertheless, the DS generates a non-uniform field of stress and deformation in the sample, and failure develops on an imposed plane. Another limitation is that the DS device does not allow controlling drainage conditions, therefore pore pressures cannot be measured.

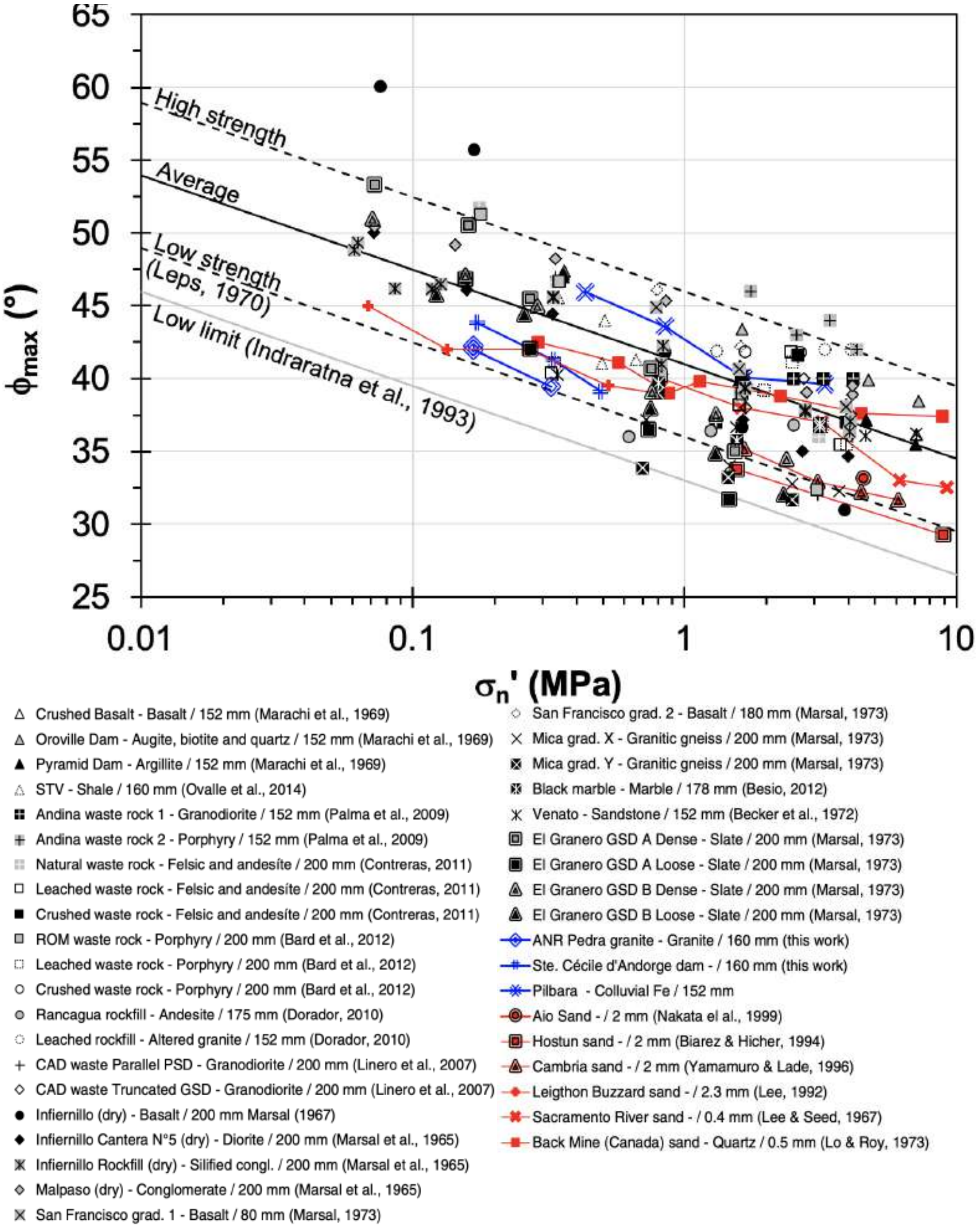

Figure 2.17 Maximum friction angle for compiled sands, ballasts, and rockfill [legend: material name/$d_{\max}$ (mm) (Ref.)] (modified form [13]).

Triaxial shear test

Triaxial devices are widely used to investigate the stress-strain behavior of soils. Figure 2.20 shows a diagram of a typical triaxial apparatus, where a cylindrical soil specimen sample is contained in a pressurized cell to apply isotropic confining stress conditions during the test. The sample sits on the cell between a rigid base and a rigid top cap, which is loaded by a ram

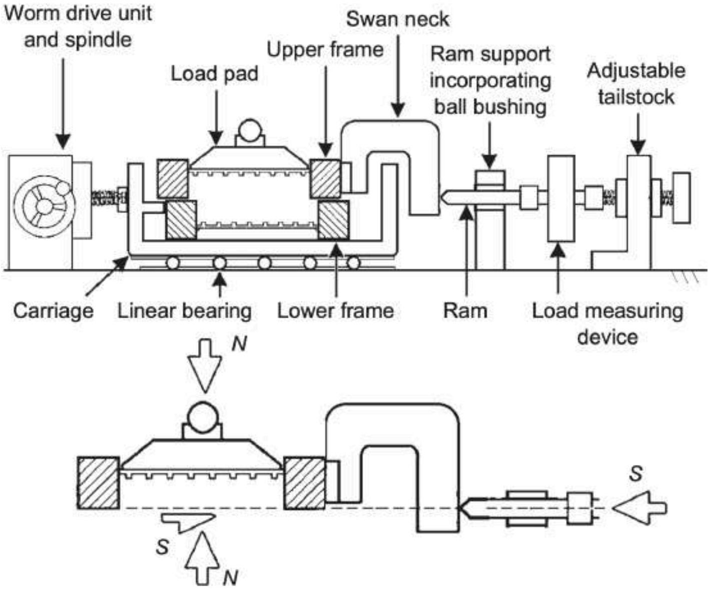

Figure 2.18 General arrangement and free-body diagram of the conventional DS test [23].

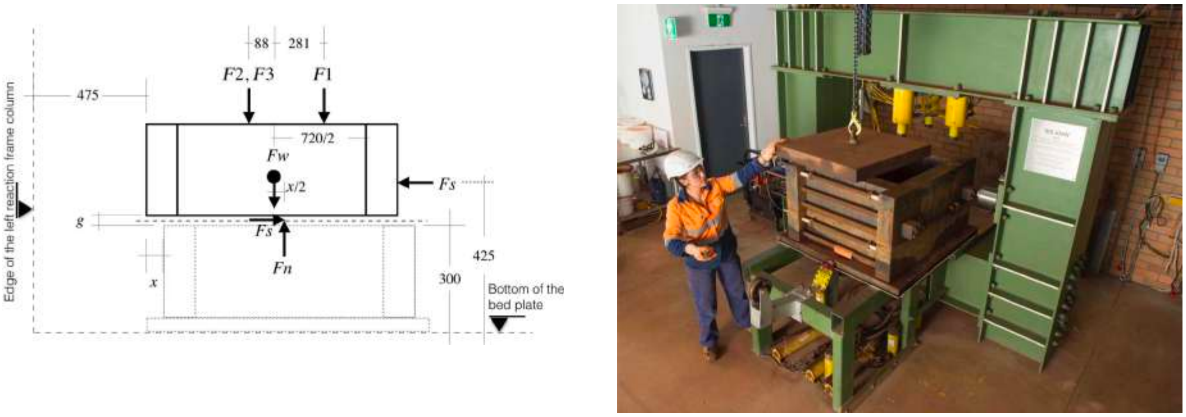

(a)

(b)

Figure 2.19 (a) Loading mode setup, distances in mm; g = gap size; x = shear displacement; and (b) the large direct shear (LDS) equipment [18].

passing through the cell. Loads can be applied to this ram to increase vertical stress until shear failure occurs. The rigid base and the top cap are porous to drain pore fluid from the soil and, if the material is fully saturated, the volumetric strain is directly obtained through the drained water volume. Alternatively, if drainage is prevented, excess pore pressure can be measured [86, 111]. Principal stresses are always controlled and the strain-stress fields are homogeneous within the sample, except if friction is significant on top and bottom surfaces.

These features allow representing in situ conditions through anisotropic (K_0) consolidation and shearing up to failure, while the failure plane location is not predetermined. To express the degree of anisotropic stress, typically a ratio of $K_c = \sigma_1/\sigma_3$ is used [21].

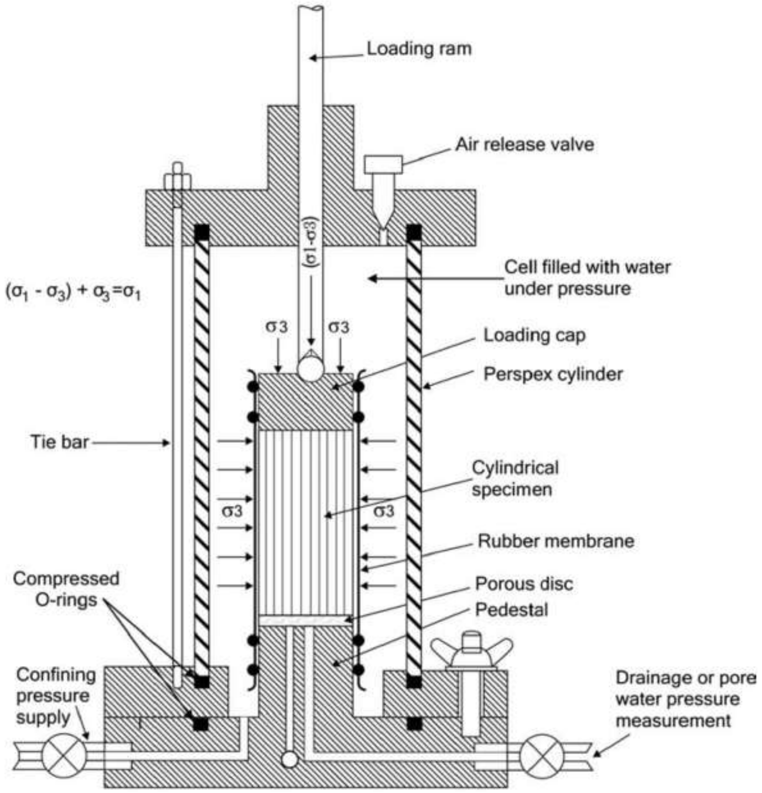

Figure 2.20 Schematic diagram of triaxial apparatus [24].

There are usually three standard triaxial testing conditions: isotopically consolidated drained (CID), consolidated undrained (CIU), and unconsolidated undrained (UU). CID and CIU tests can be performed on non-cohesive (e.g., granular) and cohesive soils, while the UU test is used only for cohesive soils. Each of them is briefly described below:

1. **CID:** the specimen is isotopically consolidated to a specific effective stress state. Subsequently, the axial stress is increased while keeping the effective confining pressure constant. In this test, drainage is allowed and the strain rate must be slow enough to prevent excess pore water pressure building up in the specimen.

2. **CIU:** the specimen is isotopically consolidated to a certain effective stress state. Subsequently, the specimen is sheared to failure by increasing the axial stress under undrained conditions (i.e., constant volume). Pore pressure is measured to monitor the effective stresses.

3. **UU:** this test measures the undrained strength of cohesive soils. Both the consolidation and shearing phases are undrained.

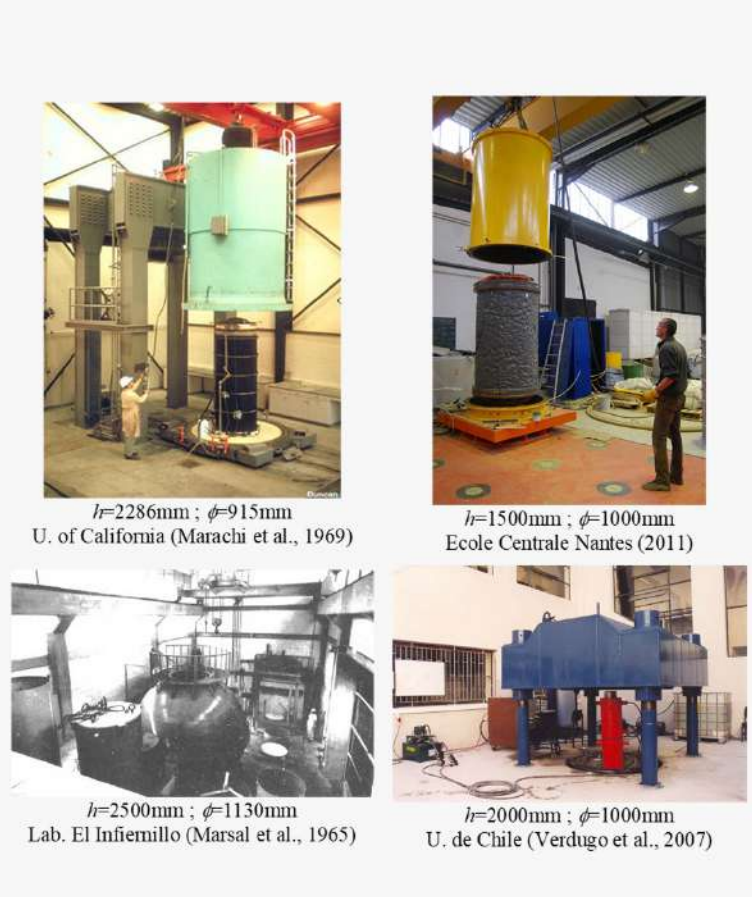

h=2286mm ; ϕ=915mm
U. of California (Marachi et al., 1969)

h=1500mm ; ϕ=1000mm
Ecole Centrale Nantes (2011)

h=2500mm ; ϕ=1130mm
Lab. El Infiernillo (Marsal et al., 1965)

h=2000mm ; ϕ=1000mm
U. de Chile (Verdugo et al., 2007)

Figure 2.21 Large diameter triaxial cells (≈1000mm) (h, ϕ: max. height and diameter of the sample, respectively) [25].

The triaxial test standard dimensions are typically between 35 mm to 150 mm in diameter, limiting tests on coarse granular materials such as WR material. On the other hand, the largest triaxial cells ever built allow testing cylindrical samples of 1000 mm in diameter and 1500 to 2000 mm in height (Figure 2.21) [7, 8, 13–15, 54, 65], with maximum particle size of 160 mm (Figure 2.4 and 2.5), according to the minimum aspect ratio $D/d_{\max} = 6$ [112] specified by the ASTM 7181 [111].

2.3.2 Material and sample geometric properties affecting the shear strength of granular materials

Specimen size effect on shear strength

The representative elementary volume (REV) of a given material gives the minimum size that a sample must have to obtain consistent mechanical behavior. In other words, a REV ensures that the results do not depend on sample size [113–115]. Testing standards (e.g., ASTM) specify minimum required ratios between specimen dimensions and $d_{\max}$, as summarized in Table 2.1. However, standards often disagree on REV these size limitations, and these aspects are not yet undoubtedly validated by experimental results [3, 9, 116, 117].

Table 2.1 Standards of direct shear tests regarding the maximum allowed particle size ($d_{\max}$), specimen width (W), thickness (T), and diameter (D) [1].

Standard	W	T	W/T	Allowed $d_{\max}$
ASTM D3080 [53]	$\geq$ 50 mm	$\geq$ 13 mm	≥ 2	$\min\{T/6, W/10, D/10\}$
AS 1289.6.2.2 [118]	Not specified	$\geq$ 12.5 mm	Not specified	$T/6$
	60 mm	20 mm	3	2 mm
BS 1377–7 [119]	100 mm	25 mm	4	2.5 mm
	305 mm	150 mm	≈ 2	15–20 mm
Eurocode 7 [109]	Not specified	Not specified	—	$T/10$

Cerato & Lutenegger [2] investigated the impact of specimen size on sand internal friction angles with varying $d_{\max}$ values at three compacted states—loose, medium, and dense—by employing three DS boxes of different sizes. All specimens meet the criteria between W, T and $d_{\max}$ required by AS1289.6.2.2 [118], ASTM-D3080 [53], and Eurocode 7 [109] (Table 2.2). Figure 2.22 shows the friction angle versus aspect ratios $W/d_{\max}$ and $T/d_{\max}$ for sands at different densities. Friction angles are almost constant when $W/d_{\max}$ increases for Ottawa sand (Figure 2.22). However, for the FHWA material (Figure 2.22 (b)) and the Morie material (Figure 2.22 (c)), the friction angles decrease when $W/d_{\max}$ increases from 30 to 152, and $T/d_{\max}$ from 13 to 89.

Wang & Gutierrez [117] developed a parametric numerical study of specimen size effect on the direct shear test. They recommended a minimum value of 60 for $L/d_{\max}$, a minimum value of 40 for $H/d_{\max}$, and a range of 1.5 to 2 for L/H. Deiminiat *et al.* [3] investigated sample size effects on DS tests using three different shearing boxes (Table 2.3) for two WR materials (WR1 and WR2), testing seven psd with $d_{\max}$ of 0.85, 1.19, 1.4, 2.36, 3.36, 5.0, and 6.0 mm (Figure 2.23 (a)). For $d_{\max} \leq 1.4$ mm, the friction angle tends to stabilize for $W/d_{\max} \geq 50$.

Table 2.2 Materials and specimen sizes used in direct shear tests by Cerato and Lutenegger [2] (modified from [1]).

Materials	$d_{\max}$ mm	60 mm × 60 mm × 26.4 mm		101.6 mm × 101.6 mm × 40.64 mm		304.8 mm × 304.8 mm × 177.8 mm	
		$T/d_{\max}$	$W/d_{\max}$	$T/d_{\max}$	$W/d_{\max}$	$T/d_{\max}$	$W/d_{\max}$
Ottawa	0.9	29	67	45	113	198	339
FHWA	1.7	16	36	24	60	105	179
Morie	2.0	13	30	20	51	89	152

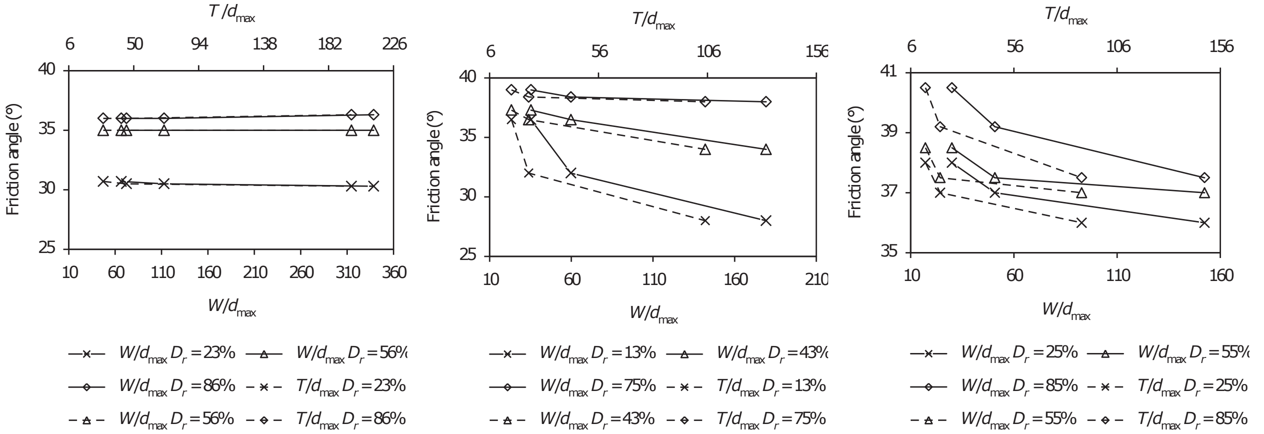

(a) (b) (c)

Figure 2.22 Variation of the friction angle in terms of specimen width and thickness to $d_{\max}$ ratios for specimens with different relative densities (data taken from [2]): (a) Ottawa sand, (b) FHWA (brown mortar), (c) Morie [1].

The results of the literature show that the minimum aspect ratios specified by the standards (Table 2.1) fail to mitigate the specimen size effects on the friction angle of granular material specimens [2,3]. Nevertheless, it is also unclear whether the changes in friction angle are only linked to specimen size effects. The sample preparation process, which involves modifying the d_{max}, results in each sample having a different psd. Furthermore, in the case of rockfills and WR materials, which might exhibit a correlation between particle size and shape, it is uncertain whether the observed change in friction angle is only attributable to the modification of particle size, or if the alteration in particle shape also plays a role. Unfortunately, most works did not systematically measure grain shape along different particle sizes.

Table 2.3 Specimen sizes, $d_{\max}$, and aspect ratios for WR1 and WR2 [3].

$d_{\max}$ mm	38 mm × 38 mm × 45 mm		60 mm × 60 mm × 45 mm		300 mm × 300 mm × 180 mm	
	$T/d_{\max}$	$W/d_{\max}$	$T/d_{\max}$	$W/d_{\max}$	$T/d_{\max}$	$W/d_{\max}$
0.85	45	53	71	53	353	212
1.19	32	38	50	38	252	151
1.4	27	32	43	32	214	129
2.36	16	19	25	19	127	76
3.36	11	13	18	13	89	54
5.0	—	—	12	9	60	36
6.0	—	—	10	8	50	30

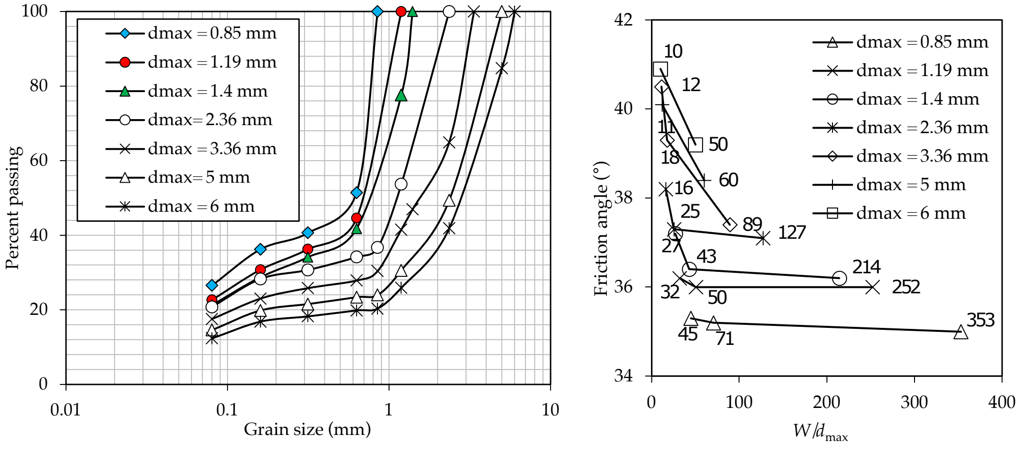

(a) (b)

Figure 2.23 Waste rock material: (a) Psd for cases WR1 and WR2, and (b) friction angle variations as function of $W/d_{\max}$ for WR2 [3].

Effect of psd on the critical friction angle (ϕ_c)

Recent studies have shown that, if the grains have the same shape along different particle sizes within a given granular material, ϕ_c does not depend on the psd. This affirmation is supported by experimental [26, 27, 57] and numerical results [28–30, 35, 58–60]. For instance, Yang & Luo [26] performed undrained triaxial tests with four psds on Fujian sand, varying from very uniform (C_u=1.20) to moderate grading (C_u=3.56). For each psd shown in Figure 2.24(a), a series of tests were carried out under a range of void ratios and confining pressures. Figure 2.24(b) shows that the critical friction angle does not depend on psd. Based on these results, the authors concluded that variations of ϕ_c for different C_u reported in the literature are most likely attributable to a varying particle shape rather than varying psd [26].

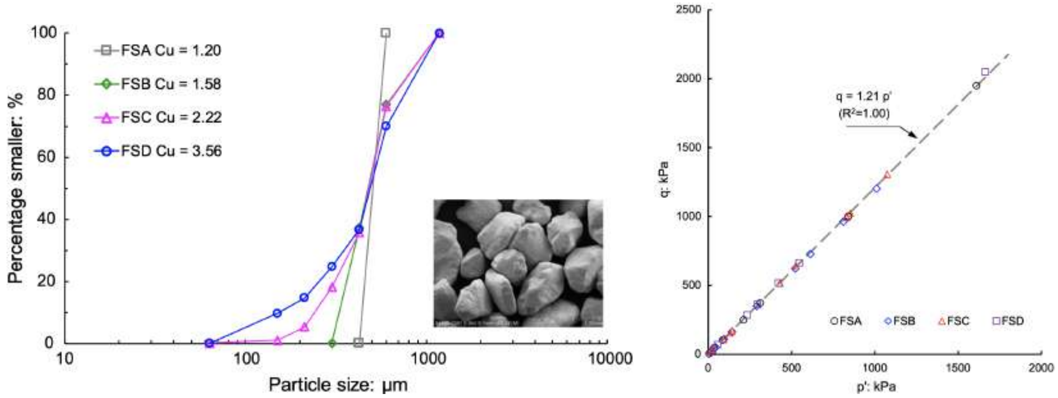

(a) (b)

Figure 2.24 Fujian sand: (a) psd curves of four fractions, (b) critical states in stress space [26].

Polanía *et al.* [27] investigated the impact of psd on the critical shear strength of ceramic bead samples. Figure 2.25(a) shows some sample ranging from monodisperse, bidisperse (mixture) and polydisperse in size, and Figure 2.25(b) presents the evolution of ϕ_c as a function of particle size dispersion $\lambda = d_{\max}/d_{\min}$. The study found that variations in grain size and distribution did not significantly affect ϕ_c.

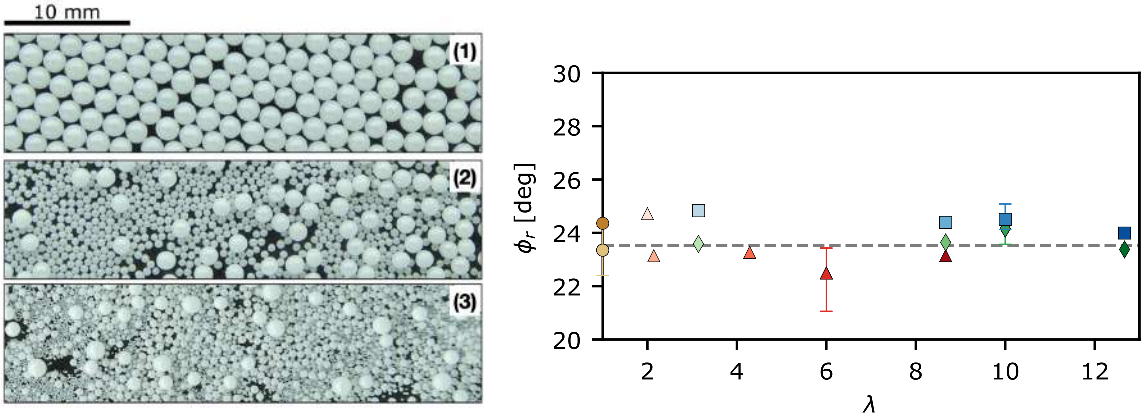

(a) (b)

Figure 2.25 Views of tested granular systems: (a1) monodisperse, (a2) bidisperse and (a3) polydisperse samples; (b) critical friction angle as a function of the size span $\lambda = d_{\max}/d_{\min}$; dashed line shows the mean value for all experiments, and vertical bars indicate the maximum and minimum values between repetitions [27].

Muir-Wood & Maeda [28] developed a numerical model using 2D DEM simulations with circular particles to investigate the influence of psd on the mechanical behavior of granular materials. Figure 2.26 depicts the four psd defined by a Gaussian distribution in weight proportion, characterized by the ratio of maximum to minimum particle size $R_D = D_{\max}/D_{\min}$. The simulations involved isotropic compression followed by shearing of the particle assemblies. Figure 2.27 shows the stress ratio (τ/σ) trends as a function of strain for dense and loose cases. The study found that the normalized shear strength at the critical state is the same for all psd, independent of initial densities.

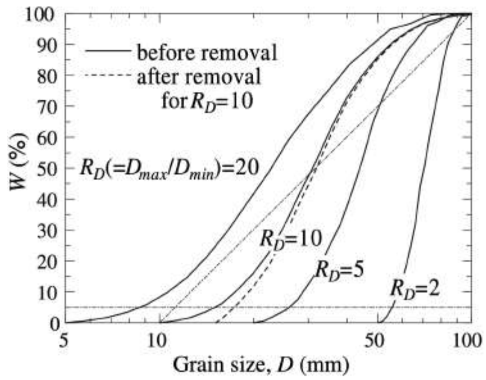

Figure 2.26 Psd for various grading of samples composed of circular discs for DEM analysis [28].

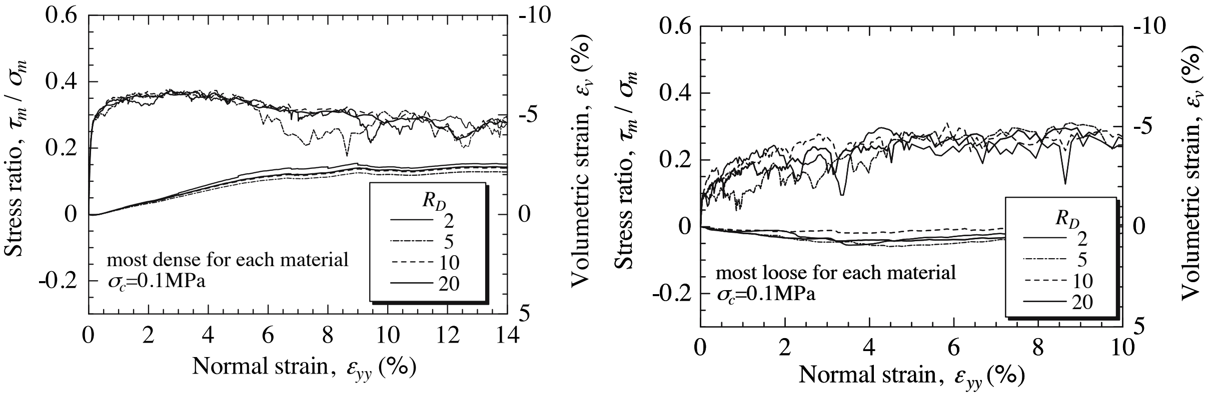

(a) (b)

Figure 2.27 Stress-strain response of 2D DEM simulations of grain assemblies with different psd: (a) dense samples; (b) loose samples [28].

Cantor *et al.* [29, 30] presented a numerical study on the effect of particle shape and psd through 3D DEM simple shear simulations using the software LMGC90 [62, 120]. A set of nine samples was created for each particle shape (spheres and octahedra), where the grain size span varied with the parameter S, defined as:

$$S = \frac{d_{\max} - d_{\min}}{d_{\max} + d_{\min}} \ . \tag{2.4}$$

Figure 2.28 shows that, for both samples formed by spherical and angular grains, the psd does not affect ϕ_c. However, the higher the grain angularity, the higher the critical friction angle. Those findings imply that, provided that particle shape and grain roughness remain unchanged along grain sizes for a given material, a representative ϕ_c can be obtained through shearing tests on samples with different psd (i.e., through scalping or parallel grading).

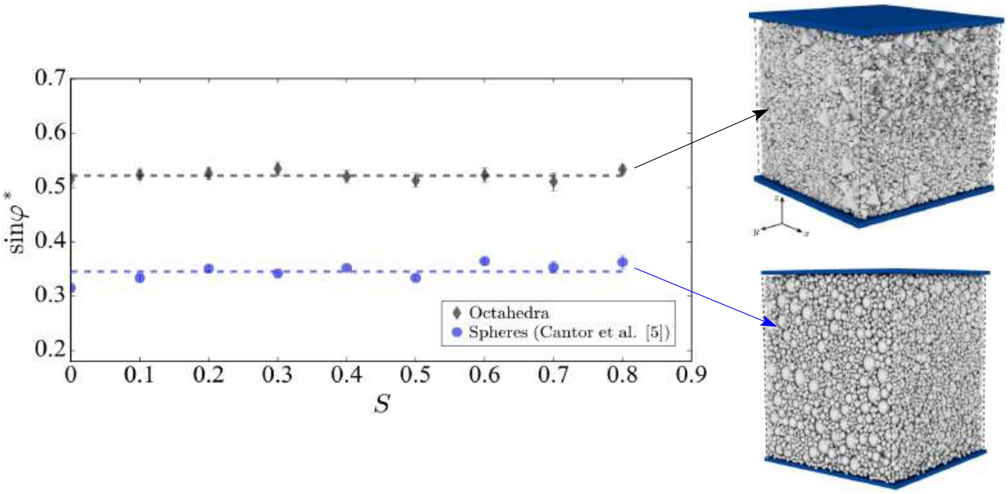

Figure 2.28 Average macroscopic coefficient of friction, error bars represent the standard deviation of the data (mod., from [29, 30]).

Particle shape effect on critical friction angle

Particle shape has a significant influence on the mechanical properties of granular assemblies. Both experimental investigations [19,31,32,45,121–124] and DEM simulations [30,35,42,125–129] have consistently demonstrated the impact of particle shape on ϕ_c.

Shape characterization

Numerous methodologies have been developed to quantify grain shape, ranging from traditional techniques (e.g., sieving or visual classification) to advanced imaging methods, such as scanning electron microscopy and X-ray microtomography. Table 2.4 introduces various shape descriptors, including sphericity, roundness, angularity, and elongation [4, 130]. Sphericity measures how closely a particle shape approaches that of a sphere, while roundness assesses the smoothness of particle edges. Angularity, on the other hand, evaluates the sharpness of particle corners. Recent advancements also include fractal dimension analysis and the application of machine learning algorithms to automate and enhance the precision of shape characterization [131, 132].

Table 2.4 Most used shape descriptors [4].

Shape descriptor	Formula	Range	Parameter/Comments
Form			
Circularity (C) [10]	$\frac{\sqrt{4\pi A}}{P}$	[0,1]	P : Perimeter of surface area
Convexity	$\frac{V}{V_{CH}}$	[0,1]	V_{CH} : Volume of convex hull
Spherecity (S) [10]	$\frac{\sqrt[3]{36\pi V^2}}{A}$	[0,1]	V : Volume A : Surface area
Flatness [133]	$\frac{S}{I}$	[0,1]	S : Thickness I : Breadth
Elongation [133]	$\frac{I}{L}$	[0,1]	L : Length
Roundness			
Roundness (R) [10]	$\frac{\left(\sum_{i=1}^{N} r_i\right)/N}{R_{in}}$	[0,1]	r_i : Radius of corner i N : Numbers of corners
Roundness (R) [134]	$\frac{r}{R_{in}}$	[0,1]	r : Radius of sharpest corner i R_{in} : Inradius
Angularity [4]	$\frac{V \cap V_{el}}{V_{el}}$	[0,1]	V_{el} : Volume of fitted ellipsoid

Experimental tests

Cho *et al.* [31] compiled a database of around 40 sandy soils from published studies to investigate the impact of particle shape on soil properties; Figure 2.29 (a) illustrates some particle shapes analyzed in this study. The tested materials include crushed sands, natural sands, glass beads, granite powder, and Syncrude tailings. Figure 2.29 shows that ϕ_c decreases as particle roundness increases. Moreover, increased grain angularity leads to higher maximum and minimum void ratios, reduced small-strain stiffness, and increased compressibility.

Cavarretta *et al.* [32] conducted experiments using glass ballotini with controlled surface roughness and various particle shapes. Figure 2.30(a) shows the correlation between some shape descriptors of the studied material. The study independently evaluated the effects of particle shape and inter-particle friction. Microscale analyses measured inter-particle friction, contact stiffness, surface roughness, and particle shape, while macroscale behaviors were assessed through triaxial and oedometer tests. The findings indicated that surface roughness and friction had some influence on the material response. However, as shown Figure 2.30(b),

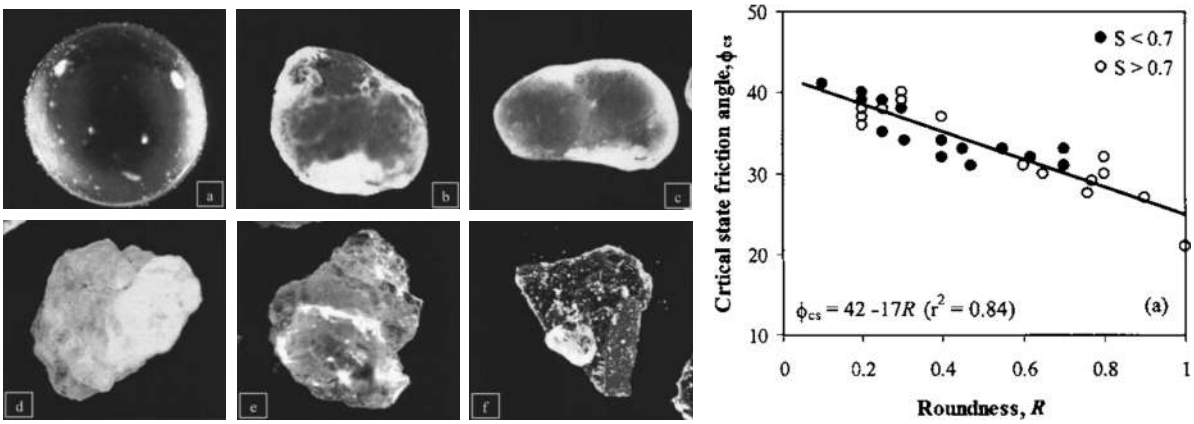

(a) (b)

Figure 2.29 (a) Microphotographs showing various grain shapes encountered in Cho's study, (b) Effect of particle shape on critical state friction angle [31].

particle shape had a greater impact on shear strength. These results show how increasing grain angularity increases the critical state friction angle due to better interlocking and higher shear resistance, enhancing soil strength [31, 32, 45, 121–123].

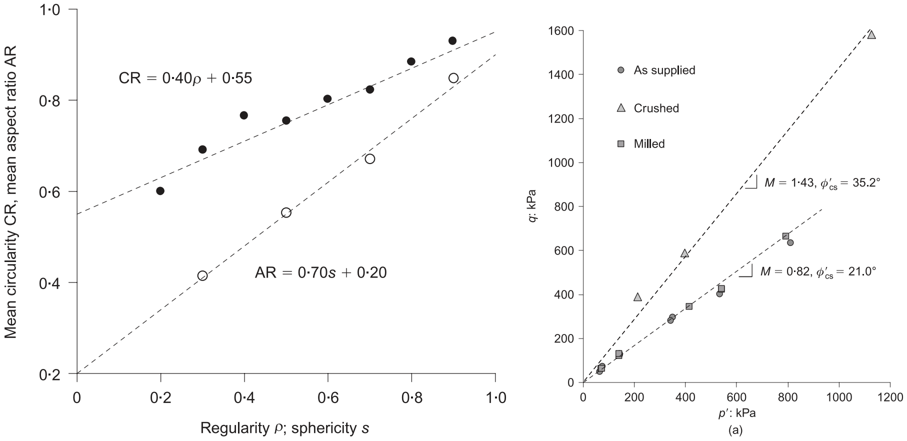

(a) (b)

Figure 2.30 Ballotini Glass Bead: (a) correlation between particle shape descriptors, and (b) $q - p'$ shearing plane [32].

Numerical DEM tests

Azéma & Radjaï [33] simulated 2D elongated particle assemblies under shearing conditions. Figure 2.31(a) shows some samples where η characterizes the particle elongation, varying from $\eta = 0$ (circular particle) to $\eta = 0.7$ (the most elongated particle). The shear strength of the packings increases with particle elongation, as shown in Figure 2.31(b), mainly due to what is described as force anisotropy or heterogeneity in interparticle force transmission. As particles become more elongated, the force distributions broaden and contacts between particles tend to carry larger forces. Besides, grain elongation improved particle interlocking due to particles tending to slide instead of roll on top of each other, resulting in higher strength [124, 125, 127, 135].

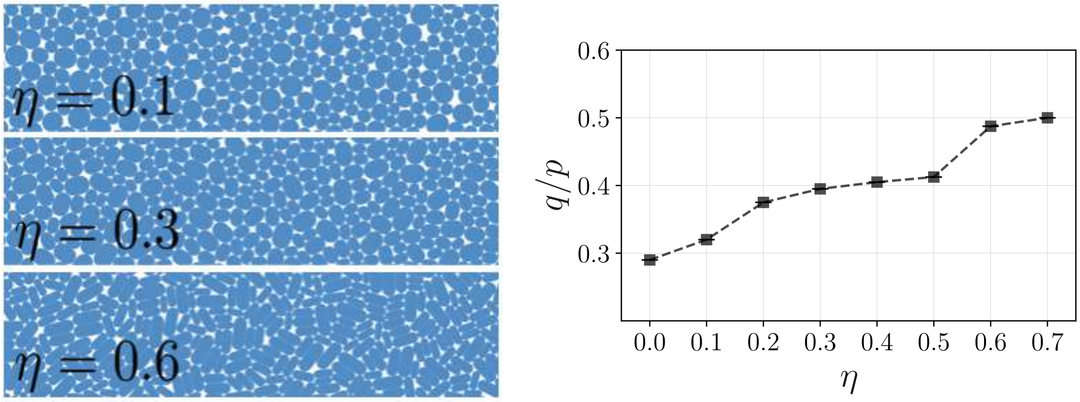

(a)

(b)

Figure 2.31 DEM 2D elongated particles: (a) Initial packing configurations for different particle elongation (η) [33], (b) and normalized shear strength as a function of η.

Azéma *et al.* [128] investigated the mechanical behavior of granular assemblies of irregular polyhedral particles through 3D DEM shearing test. Figure 2.32(a) shows screenshots of different assemblies composed of these polyhedral particles with various degrees of mean angularity $\langle \alpha \rangle$. The particle composition of the assemblies varies from spheres ($\langle \alpha \rangle = 0$) to octahedrons ($\langle \alpha \rangle = 1.2$). As shown in Figure 2.32(b), the findings indicate that the critical shear strength increases with $\langle \alpha \rangle$, up to a certain level beyond which increments in angularity do not lead to additional strength changes.

Grain size-shape mixtures and correlations

Granular mixtures, including rock-sand and sand-silt, are prevalent in many engineering, industrial, and natural processes [136]. Several experimental [34, 45, 57, 123] and numerical [136, 137] studies have investigated the proportion of different materials and their impact on the mechanical properties. For instance, Shin & Santamarina [34] investigated mixtures of round Ottawa sand and angular blasted sand at various mass fractions. These sands had similar D_{50} and low C_u, but differed in particle shape. Blasted sand had a $R = 0.3$ and $S = 0.55$ while Ottawa sand had a $R = 0.9$ and $S = 0.9$. Six mixtures were prepared with angular blasted sand mass fractions of 0%, 20%, 40%, 60%, 80% and 100%. Each test was

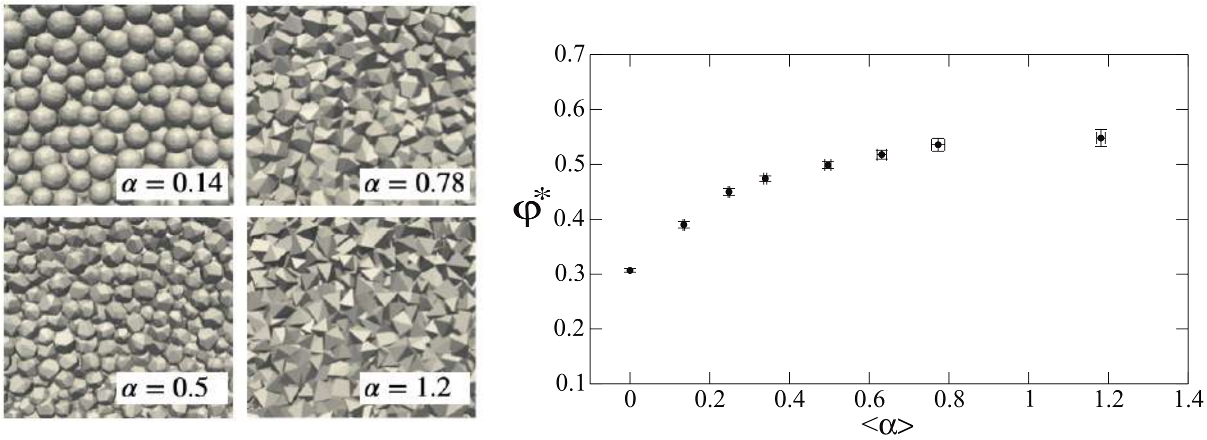

(a) (b)

Figure 2.32 DEM polyhedral particles: (a) Initial packing configurations for different particle angularity (α), and (b) normalized shear strength as a function $\langle\alpha\rangle$ [33].

repeated three to five times to evaluate the variability in the data set. Figure 2.33 shows the evolution of the friction angle as a function of the mass fraction of angular grains. These results prove that including angular particles in a bidisperse material results in higher shear strength.

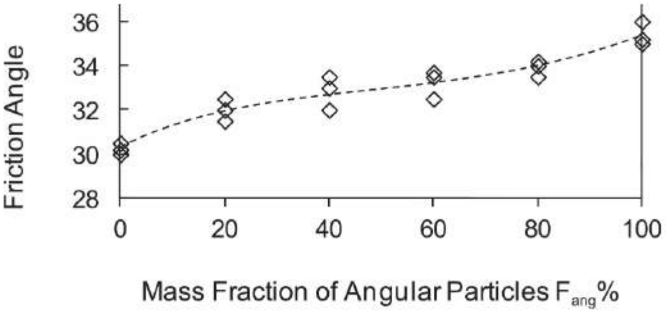

Figure 2.33 Mixture between Ottawa and blasting sand, critical state friction angle based on the angle of repose as a function of the mass fraction of angular particles [34].

In polydisperse systems, particles of varying sizes and shapes are combined, creating complex geometrical arrangements that influence packing density and mechanical properties. Correlations between particle size and shape can be found in granular materials, such as sand [138], rockfill [19], or WR materials [17]. The following studies have investigated cases where the disparity between particle shapes and particle sizes is significant enough to influence the mechanical properties of granular assemblies.

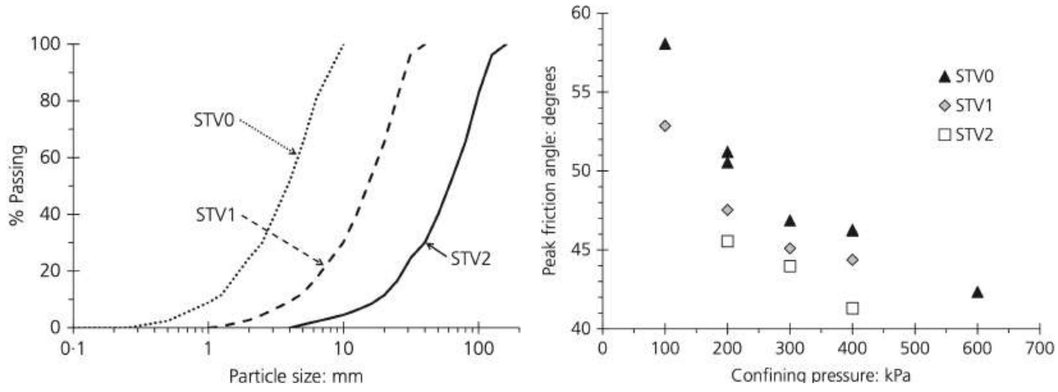

(a) (b)

Figure 2.34 (a) Initial psd of parallel graded STV samples, and (b) peak friction angle as a function of confining pressure for a Shale rockfill [19].

Ovalle & Dano [19] conducted drained triaxial tests on small-scaled samples of a dry shale rockfill material (STV). As shown in Figure 2.8, STV material presents particle shape-size correlation, with finer particles being more elongated than coarse ones. Figure 2.34(a) presents the parallel psds with $d_{\max}$ of 10, 40, and 160 mm, while Cu remains constant in all samples. This suggests that, by applying the parallel grading small-scaling technique, the characteristic particle shape distribution differs for each sample (STV0, STV1, and STV2). Figure 2.34(b) shows the evolution of the peak friction angle as a function of confining pressure for all materials. For each confining pressure, STV0 always presents a higher friction angle than coarser samples STV1 and STV2. The authors highlighted two important points on this behavior: the influence of particle shape distribution on the shear strength and the importance of characterizing the shape of the grains in small-scaling techniques [19, 35].

Linero *et al.* [35] also studied the mechanical response of granular assemblies with size-shape correlation through 2D DEM shearing test simulations. Figure 2.35 presents the study cases, which included mono-shape particles (disks) and shape-size correlated particles (elongated grains). Each study case evaluated 10 psds, which were generated by varying the grain size span S from 0 to 0.9, while maintaining a constant solid volume per particle size class. Figure 2.36 shows the evolution of ϕ_s as a function of the grain size span, where ϕ_c remains constant in samples composed of disks, while it varies significantly in assemblies with shape-size correlation.

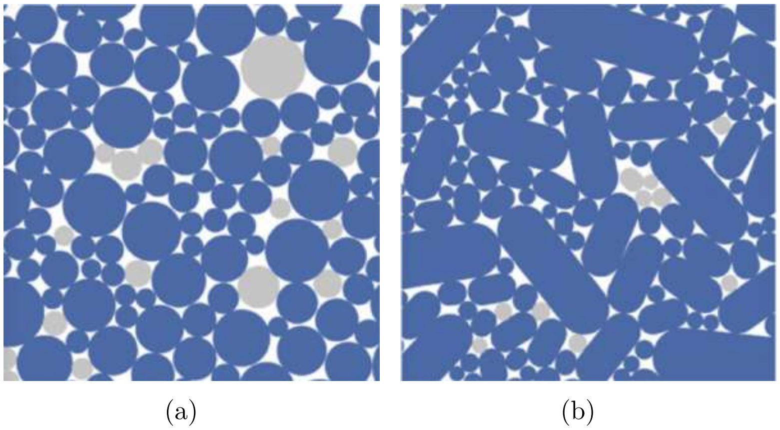

Figure 2.35 Screenshots of 2D DEM samples: (a) assemblies composed of disks and (b) assemblies composed of particles with size-shape correlation based on elongation [35].

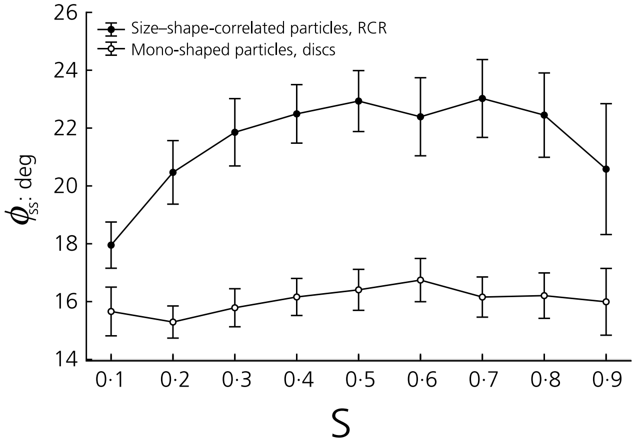

Figure 2.36 Comparison between critical friction angles as a function of S for both study cases [35].

2.3.3 Small-scaling methods for coarse granular materials

Laboratory equipment and test procedures for coarse granular materials are usually limited by particle size, since $d_{\max}$ must be less than a characteristic dimension of the specimen, such as W and T for DS tests, as shown in Table 2.1. Concerning triaxial tests, ASTM D7181 [111] requires $D/d_{\max} \geq 6$. Thus, testing oversized materials requires small sample scaling techniques, such as scalping or truncation, scalping and replacement, matrix modeling, and parallel grading. These techniques alter the psd by defining a $d_{\max}$ that meets standard requirements. These methods assume that small-scale samples with an altered psd could be compared with the results obtained from large-scale shearing tests. However, reported experimental results employing small-scaled samples are apparently contradictory, and the reliability of these techniques is questionable [1, 2, 19].

Scalping or truncated technique

This technique is the simplest and earliest developed scaling-down method commonly used in sample preparation for laboratory tests [5, 139–141]. Proposed by Hennes [139], in this methodology particles coarser than a defined $d_{\max}$ are removed, resulting in an increment of the percentage of all finer particles. Following this method, Zeller & Wullimann [5] conducted a series of drained triaxial tests on rockfill materials. Using field material with $d_{\max} = 600$ mm, they generated four scalped psds with $d_{\max}$ values of 1, 10, 30, and 100 mm, as shown in Figure 2.37(a). The different cylindrical sample dimensions used for each psd and their aspect ratios are presented in Table 2.5. Moreover, the particle shape characterization reported that as $d_{\max}$ decreases in the tested fraction, the characteristic grain shape of the samples becomes more angular and elongated. Figure 2.37(b) shows the behavior of the tested material for different porosities, where friction angle significantly decreases as $d_{\max}$ increases.

Table 2.5 Rockfill materials: $d_{\max}$ of tested material, specimen dimensions, and aspect ratios [5].

d_{max} mm	Height (H) mm	Diameter (D) mm	$D/d_{\max}$
100	900	505	5.05
30	500	252.2	8.4
10	250	160	16
1	150	80	80

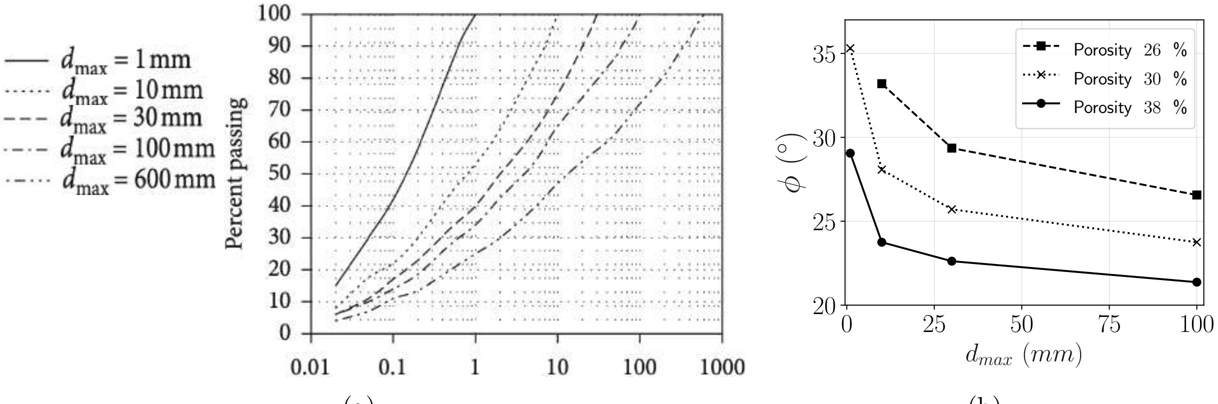

(a)

(b)

Figure 2.37 Rockfill materials: (a) field psd and scalped psds (modified from [1]), and (b) evolution of friction angle as a function of $d_{\max}$ for different porosities (all test at confining pressure of 88 kPa) (modified from [5]).

Al-Hussaini [6] performed triaxial compression tests on crushed ballast material to investigate the influence of particle size, among other factors, on strength and compressibility. The research examined five scalped psds with $d_{\max}$ ranging from 6.4 to 76.2 mm, testing the samples under both dense and medium-dense conditions, as shown in Figure 2.38(a). Three different cylindrical sample dimensions were used, with their aspect ratios presented in Table 2.6. However, the study did not provide information on the characterization of particle shape. Figure 2.38(b) demonstrates that the friction angle increases with increasing $d_{\max}$. The research concluded that particle breakage significantly affects material properties and that the stress level and gradation are critical factors. Furthermore, research by Alias *et al.* [46], Islam *et al.* [142] and Cao *et al.* [47] on scalping has also indicated that the friction angle increases with $d_{\max}$.

Table 2.6 Crushed ballast material: $d_{\max}$ of tested materials, D and aspect ratio, modified from [6].

$d_{\max}$ mm	Diameter (D) mm	$D/d_{\max}$
6.4	71	11
12.7	154	12
25.4	305	12
50.8	305	6
76.2	305	4

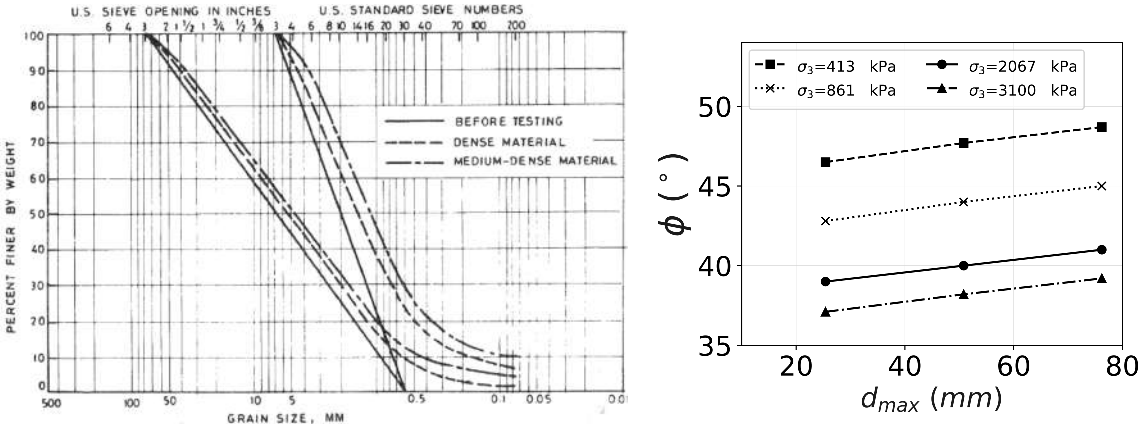

(a) (b)

Figure 2.38 Triaxial tests on crushed ballast material: (a) scalping psd and (b) friction angle as a function of $d_{\max}$ for medium-dense material (modified from [6]).

Parallel grading technique

Similar to the scalping method, this technique excludes particles larger than the targeted $d_{\max}$ by creating a parallel psd compared to the field material. Thus, the shape of the gradation curve is maintained [8, 15, 19, 21, 37, 67, 143–145]. However, a lack of particles finer than the field material's minimum particle size can limit the generation of parallel curves. Conversely, increments in fine fractions could impact the mechanical behavior of scaled samples if silty or clayey materials become over-represented. To avoid this, Verdugo & De La Hoz [145] recommended limiting to no more than 10% of fines content in scaled samples.

Marachi *et al.* [7] investigated the strength and deformation characteristics of four rockfill materials and employed the parallel grading technique to conduct drained triaxial tests. Figure 2.39(a) presents three parallel psds for Pyramid dam material that were tested on three different triaxial specimen sizes while maintaining a relatively constant aspect ratio (Table 2.7). The particle shape of the Pyramid Dam materials included a variety of angular and subangular particles. Figure 2.39 (b) shows the evolution of friction angle as a function of confining pressure for all parallel gradations. The study found that the friction angle decreased by approximately 5 degrees as the maximum particle size of the Pyramid Dam material increased from 12.7 to 152.4 mm. Furthermore, the other three rockfill materials tested also exhibited a reduction in ϕ as the maximum particle size d_{max} increased. This was attributed to the increased particle breakage at larger d_{max} due to size effect on individual particle strength [7, 8].

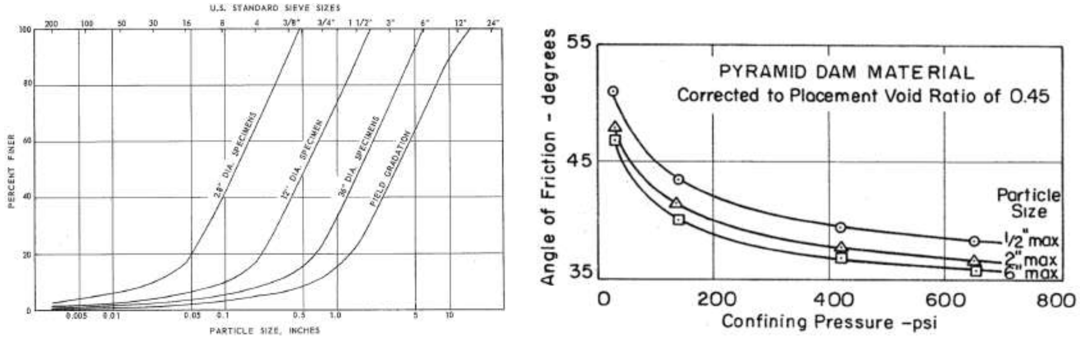

(a) (b)

Figure 2.39 Pyramid rockfill material: (a) parallel gradations and (b) friction angle as a function of confining pressure [36] (data from [7]).

Ovalle *et al.* [8] tested two rockfill materials, a calcareous rock (CP, Figure 2.40 (a)) with subangular grain shape and a quartzite rock (STV, Figure 2.40 (b)) with angular and flattened particles. Drained triaxial tests were performed using two parallel psd with $d_{\max} = 40$ and

Table 2.7 Pyramid rockfill, crushed basalt, Oroville and Venato sandstone materials: $d_{\max}$, D, and aspect ratio [7].

$d_{\max}$ mm	Diameter (D) mm	$D/d_{\max}$
12.7	71.12	5.6
50.8	304.8	6
152.4	914.4	6

160 mm (Table 2.8). The amount of particle breakage increases with $d_{\max}$. Furthermore, for a given confining pressure, the friction angle decreases as $d_{\max}$ increases, as shown in Figure 2.41.

Table 2.8 $d_{\max}$ for materials CP and STV, D and aspect ratios [8].

Material	$d_{\max}$ mm	Diameter (D) mm	$D/d_{\max}$
CP1	40	250	6.25
CP2	160	1000	6.25
STV1	40	250	6.25
STV2	160	1000	6.25

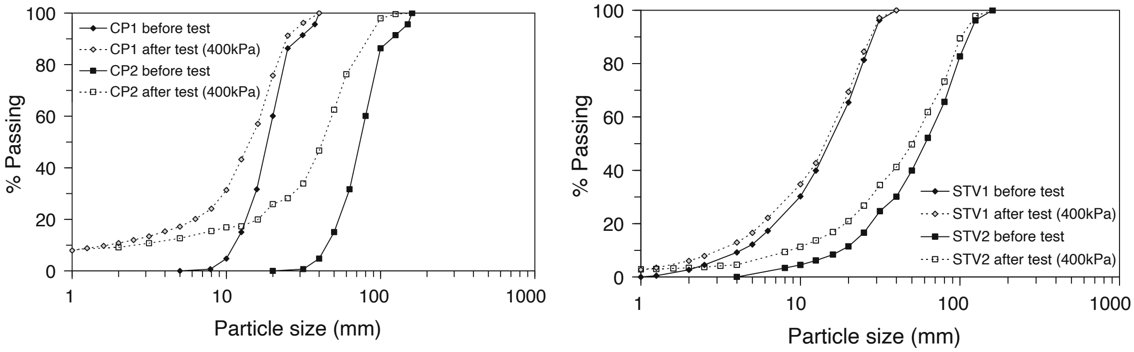

(a) (b)

Figure 2.40 Parallel grading psd for: (a) calcareous rock and (b) quartzite rock material [8].

Deiminiat & Li [9] studied the effect of small-scaling techniques using the scalping and parallel gradation methods on two WR materials. Table 2.9 presents $d_{\max}$ and aspect ratio employed for direct shear testing for both scalped and parallel psds. The two waste rocks ranged from sub-angular to sub-rounded particles, which were used to prepare three testing materials: M1, M2, and M3. Figure 2.42 shows the psd of field material and the small-scaled psds for scalped and parallel methods. The relationship between ϕ and $d_{\max}$ is presented in Figure 2.42(c).

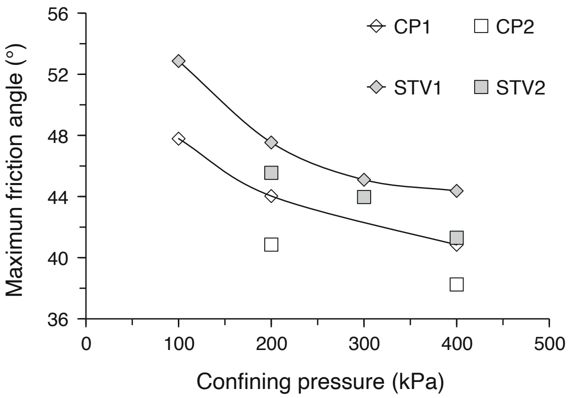

(a)

Figure 2.41 Calcareous rock (CP) and quartzite rock (STV) material: evolution of maximum friction angle as a function of confining pressure [8].

For both methods, the friction angle increases as $d_{\max}$ increases, with the scalped samples exhibiting a higher friction angle than parallel grading.

Table 2.9 Scalping and parallel gradation: $d_{\max}$ and aspect ratio by W and T [9].

$d_{\max}$ mm	$W/d_{\max}$	$T/d_{\max}$
1.19	252	151
1.4	214	129
2.36	127	76
3.36	89	54
5	60	36

The study by Varadarajan *et al.* [37] conducted a series of drained triaxial tests using large-size specimens on rockfill materials. The parallel grading technique was applied to two different rockfill materials: the Ranjit Sagar dam (rounded material- Figure 2.43(a)) and the Purulia dam (angular material - Figure 2.43(b)). Consolidated drained triaxial tests were conducted on small-scaled materials with $d_{\max}$ of 80, 50, and 25 mm through two different specimen sizes with diameters of 381 and 500 mm. Figure 2.44 shows stress-strain behavior for both materials at various confining pressures. Furthermore, Figure 2.44(c) present the evolution of ϕ as a function of $d_{\max}$. For the Ranjit Sagar dam material, the angle of friction increases as $d_{\max}$ increases, while the opposite trend was observed for the Purulia dam material. Additionally, particle breakage increased with particle size and confining pressure for both materials.

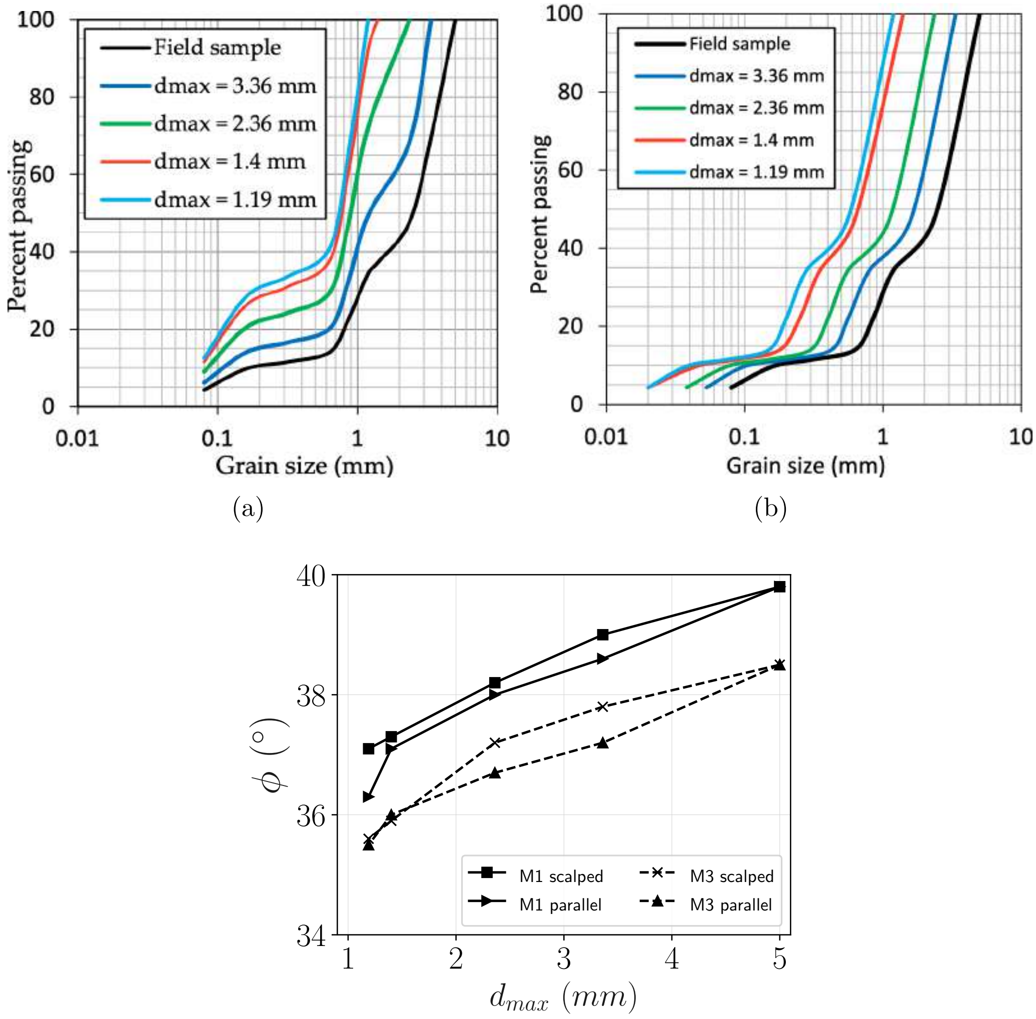

(a)

(b)

(c)

Figure 2.42 Waste rock material: (a) scalped psds, (b) parallel psds, and (c) evolution of friction angle as a function of $d_{\max}$ for both small-scale techniques.

2.3.4 Remarks on small-scaling methods

Modifying the psd can significantly impact the shear response of small-scaled samples compared to field material [19, 35]. This discrepancy can arise because the shear behavior of granular materials is inherently linked to their size and distribution [37]. Moreover, it should be noted that mineralogy, particle strength, particle shape and roughness can be correlated with particle size. Thus, when the small-scaling techniques are employed, these characteristics should be checked to confirm if scaling is still representative and valid [6,9,19,21,31,146]. However, in granular soils where shape and mineralogy are not dependent on particle size, small-scaling techniques can be considered reliable in terms of critical shear strength, since

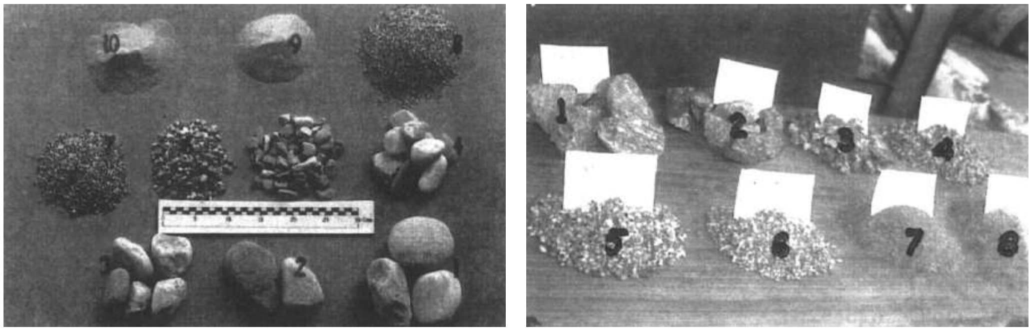

(a) (b)

Figure 2.43 Particle size and shape of rockfill material: (a) Ranjit Sagar dam site and (b) Purulia dam site [37].

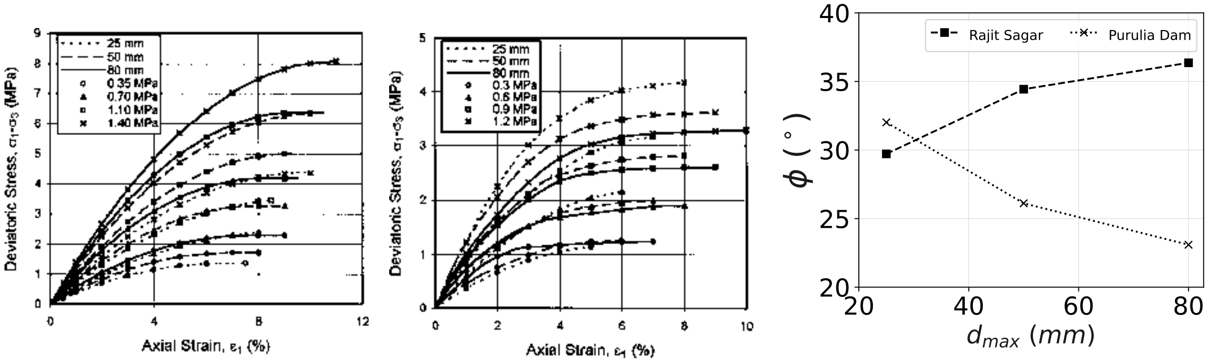

(a) (b) (c)

Figure 2.44 Stress-strain behavior from (a) Ranjit Sagar dam site and (b) Purulia dam site, (c) friction angle as a function of $d_{\max}$ for both materials [37].

this property is not affected by the psd [2, 147–151].

Table 2.10 summarizes different findings on the relationship between grain size and friction angle in various granular materials, test types, and small-scaling techniques. This summary shows that the results are non-consistent; in some cases, strength increases with characteristic particle size, while in others it decreases. The combined effects of materials properties ($d_{\max}$, psd, and particle shape), type of test (direct shear, triaxial, simple shear), and specimen dimension could explain the apparently contradictory results observed on small-scaling granular samples. Particularly, the grain size-shape correlation of granular particles can significantly impact the overall behavior of the granular assembly, including its shear strength and packing characteristics.

Therefore, when scaling down the psd through small-scaling techniques, the complex interplay

Table 2.10 Apparently contradicting result of grain sizes effect on shear strength reported.

Friction angle decreases with grain sizes			
Researcher	Material	Test type	Scaling technique
Zeller & Wullimann [5]	Gravelly	Triaxial	Scalping
Marachi *et al.* [67]	Rockfill	Triaxial	Parallel grading
Varadarajan *et al.* [37]	Rockfill	Triaxial	Parallel grading
Gupta [152]	Rockfill	Triaxial	Parallel grading
Xiao *et al.* [153]	Rockfill	True triaxial	Parallel grading
Ovalle *et al.* [8]	Rockfill	Triaxial	Parallel grading
Friction angle increases with grain sizes			
Researcher	Material	Test type	
Al-Hussaini [6]	Crushed basalt	Triaxial	Scalping
Varadarajan *et al.* [37]	Rockfill	Triaxial	Parallel grading
Alias *et al.* [46]	Gravelly soil	Direct shear	Scalping
Islam *et al.* [142]	Sand	Direct shear	Scalping
Hao & Pabst *et al.* [48]	Waste rock	Triaxial	Parallel grading
Cao *et al.* [47]	Sand	Triaxial	Scalping and replacement
Deiminiat & Li [9]	WR	Direct shear	Scalping and Parallel grading

between size and shape could limit the validity of the results. In this context, DEM modeling becomes a privileged framework, enabling researchers to systematically investigate these intricate relationships between grain size and shape. By explicitly simulating the behavior of individual particles with varying sizes, shapes, and contact laws, DEM models can provide valuable insights into the influence of particle-scale characteristics on the macroscopic response of granular assemblies [40,154]. This allows for a more detailed understanding of how small-scaling techniques might alter these fundamental interactions, guiding the development of more representative and reliable small-scaled testing procedures for granular materials.

2.4 Discrete element method in geomechanics

The discrete element method (DEM) is a numerical simulation approach that explicitly considers individual particles in interaction within a granular material, offering an alternative to the traditional continuum mechanics framework for simulating the mechanical behavior of soil [40]. The pioneering work by Cundall & Strack (1979) was among the first implementations of this numerical method in geomechanics and facilitated access to understanding the forces transmitted through grains (Figure 2.45(a)), adapting Molecular Dynamics (MD) principles to assemblies of grains. Usually, DEM methods derived from Cundall and Strack's approach are also named *smooth* due to the 'smoothness' of particle movements and interactions in time, which refers to the fact that those quantities are differentiable over time.

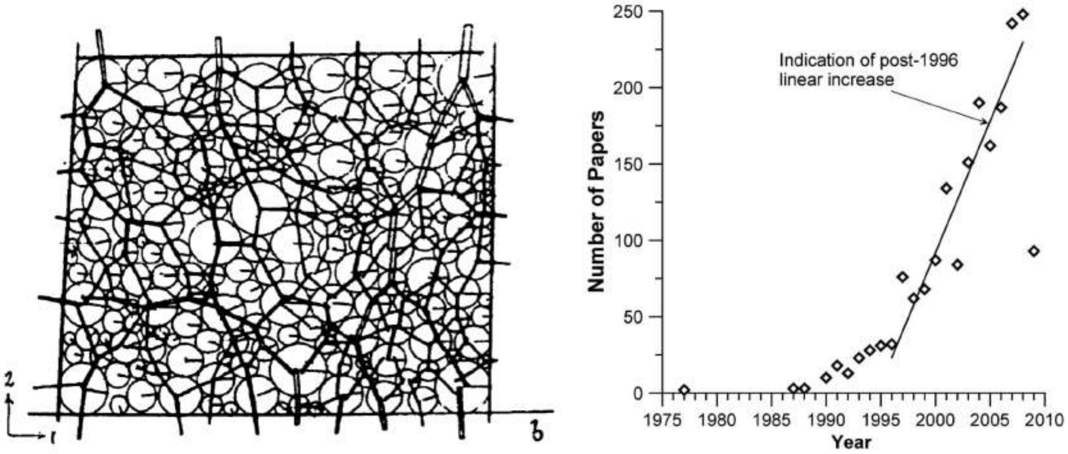

(a) (b)

Figure 2.45 DEM: (a) Simulations of assemblies of discs [38], (b) annual rate of discrete element modeling publications [39]

DEM has gained significant relevance in geomechanics since its original proposal by Cundall and Strack in the late 1970s [155]. Research articles on discrete element modeling have shown exponential growth in recent years (Figure 2.45(b)), driven by improved computational capabilities, advancements in numerical modeling, and a solid theoretical foundation for analyzing granular materials and their response to different load conditions [39]. Other alternatives to the smooth DEM approaches include the contact dynamics method, even-driven methods, and the material point method [156]. It is important to note that most DEM studies utilize spherical particles for the sake of convenience. Spherical shapes are easier to model and require less computational power than nonspherical particle shapes, which, in return, may be more representative of actual soil grains [157].

Smooth-DEM and Contact dynamics (CD) are both particulate simulation methods used to model the behavior of discrete particle systems. Still, they handle particle interactions differently, especially regarding particle shape [156]. Smooth DEM uses continuous (regularized) force laws to determine particle interactions, with forces and potentials computed at every time step. On the other hand, CD is explicitly designed to deal with impenetrable particles that experience unilateral contact and friction. This is achieved by using a time-stepping algorithm that solves interactions between particles using impact laws and Coulomb friction without requiring smooth force laws. This allows the CD method to rely on fewer material parameters at the same time larger time steps can be used.

2.4.1 Smooth-DEM

This method focuses on the interaction forces between particles, which are typically based on potential functions that define the energy landscape of the particle interactions. The forces on each particle are derived from these potentials. This formulation allows one to write the equation of motion as an ordinary differential equation that can be integrated by classical methods since the particles' motions are differentiable. The differential equation to consider is [38]

$$\boldsymbol{M}\frac{d^2\boldsymbol{X}}{dt^2} = \boldsymbol{F}, \tag{2.5}$$

where $\boldsymbol{M}$ is the mass matrix, $\boldsymbol{X}$ corresponds to the positions of the particles, and $\boldsymbol{F}$ are a set of forces (e.g., internal, external, and contact forces). While particles are not considered deformable in this method, contact deflections are simulated by allowing small overlaps at contact points. At these contacts, forces are calculated using virtual springs (Figure 2.46). These springs can be non-linear, and a contact constitutive model defines their force-deformation relationship. The normal and tangential force components (F_n and F_t, respectively) are calculated separately using orthogonal rheological models that combine springs, sliders, and dashpots. Sliders in the normal direction prevent tensile forces, while those in the tangential direction allow relative movement when frictional strength is exceeded, using Coulomb friction [40]. Figure 2.47 illustrates a contact between two disks or spheres. In this case, the contact normal vector aligns with the vector joining the disks' centroids. The contact plane is perpendicular to the contact normal, and its equation can be derived from the contact normal orientation and coordinates [158].

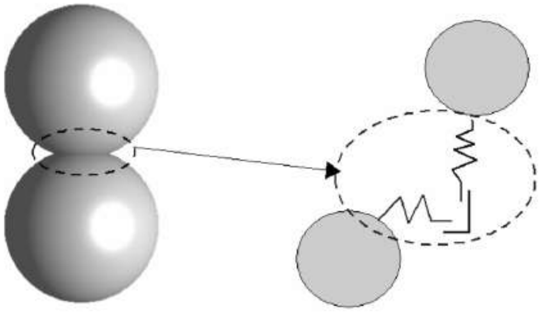

Figure 2.46 Schematic diagram of approach used to model contact interactions in smooth-DEM methods [40].

Where the contact forces are non-zero (Figure 2.48), there will be a contribution to the resultant forces acting on both contacting particles. These contributions will be equal in magnitude and opposite in direction. In compression, the normal inter-particle contact force

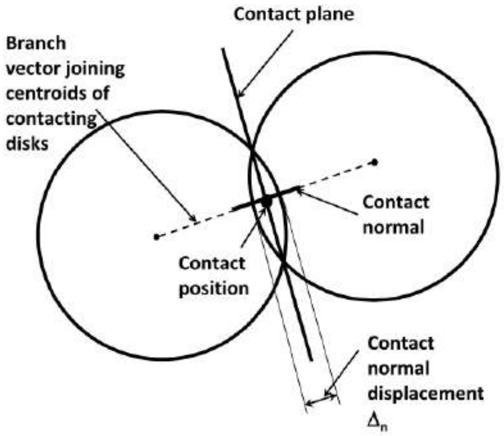

Figure 2.47 Diagram of disk to disk contact geometry [40].

calculated from the particle overlap acts to repulse the two contacting particles from each other. If there is a small separation between the particles, tensile forces will act to draw them toward each other unless the limiting tensile force is exceeded. In geomechanics, the limiting tensile force is often specified as zero, so no inter-particle tension is allowed. This can differ in situations where interparticle bonds (cohesion) want to be simulated. The tangential forces induce both relative rotation and translation. For non-circular or non-spherical particles, the amount of overlap at contact points is determined as the bounded volume between two particles; thus, this approach often necessitates defining the shape of the particle using an equation, largely restricting applications to spheres, ellipsoids, or clusters of spheres.

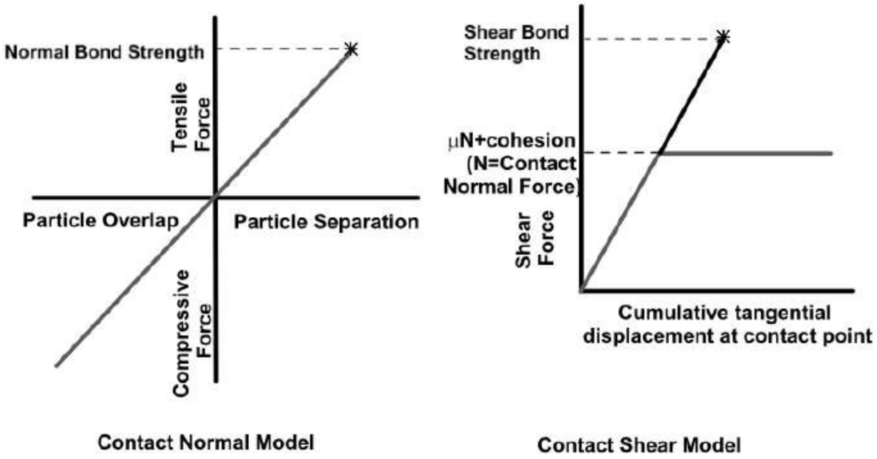

Figure 2.48 Diagram of normal and shear contact force models [40].

It is worth mentioning that the parameters that define the interaction forces between particles in smooth DEM (i.e., stiffness and viscous dissipation) are often challenging to estimate experimentally. In addition, while the virtual overlapping between simple geometric figures (e.g., circles or spheres) is simple to define, it becomes a challenge to describe when using more complex grain shapes.

2.4.2 Contact Dynamics (CD) — Non Smooth-DEM

In this approach, the particles are considered perfectly rigid, and implicit relations between particle velocities and contact force are needed to describe the evolution of mechanical systems over time.The motion of a rigid body can be described by the Newton-Euler equations [154]:

$$\begin{cases} M\,dv = F_{\text{ext}}(t)\,dt + dI \\ J\,d\omega = -\omega \times J\omega + M_{\text{ext}}(t)\,dt + dM \end{cases} \tag{2.6}$$

where, M and J are the mass and inertia matrices, v and ω are the velocity and spin, F_{ext} and M_{ext} are external forces and torques, and dI and dM are impulse measures due to contacts between particles. In non-smooth mechanics, dynamics are governed by differential inclusions and set-valued force laws rather than ordinary differential equations and continuous force laws. This allows for the description of instantaneous changes in velocity and direction that occur during impacts and when frictional sliding begins or stops. For these reasons, the equation of motion is no longer differentiable [159]. The integral equation to consider in this case is

$$\int_t^{t+\Delta t} \boldsymbol{F} dt = \int_t^{t+\Delta t} \boldsymbol{M} \frac{d\boldsymbol{V}}{dt} dt, \tag{2.7}$$

where $\boldsymbol{M}$ is the mass matrix, $\boldsymbol{V}$ corresponds to the velocities of the particles, and $\boldsymbol{F}$ are a set of forces (internal, external, and contact forces). Between the beginning and the end of a time step, the linear and angular velocities of the particles could undergo a jump $\Delta\boldsymbol{V}$.

A fundamental part of CD is the inclusion of conditions, which ensure the impenetrability of particles and the principles of friction are respected. The contact and friction laws can be expressed as follows (Figure 2.49) [41]:

- **Normal contact law**: $0 \leq g \perp \mathcal{R}_n \geq 0$, where g is the gap between particles (which must be non-negative to prevent interpenetration), $\mathcal{R}_n$ is the normal contact force, and $\perp$ indicates that g and $\mathcal{R}_n$ are complementary, i.e., at least one of them must be zero.

- **Friction law**: $\mathcal{R}_t \leq \mu\mathcal{R}_n$ or $\mathcal{R}_t = \mu\mathcal{R}_n$ if $v_t > 0$, where $\mathcal{R}_t$ is the tangential (frictional) force, (μ) is the coefficient of friction and v_t is the relative tangential velocity at the contact point. The magnitude of the tangential force is limited by the product of the normal force and the coefficient of friction, and ($\mathcal{R}_t$) acts against the direction of tangential slip when there is relative motion.

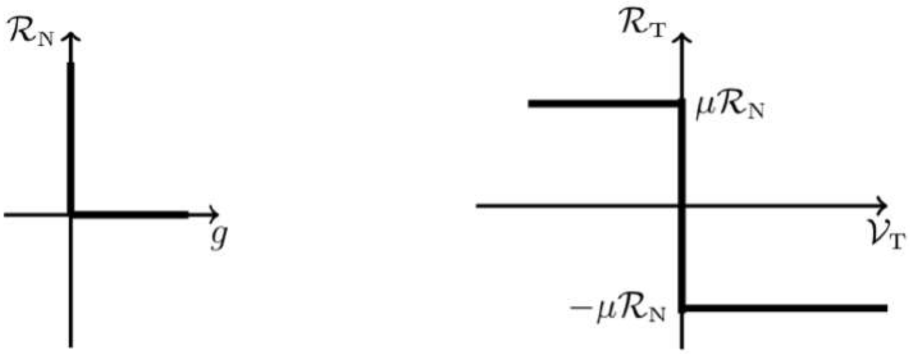

Figure 2.49 Inelastic shock and Coulomb graphs [41]

These conditions are discretized in a time-stepping scheme, which simultaneously resolves the normal and tangential forces at the contacts while enforcing the non-interpenetration condition and the frictional constraints. The resulting computational algorithms can produce outcomes where forces and velocities change discontinuously, hence the term 'non smooth'. Non-smooth DEM does not need a penalization at the contact interaction (i.e., spring and dampers), and no overlapping is allowed between the particles. Therefore, the non-smooth DEM has two advantages over smooth DEM: (1) it does not need to define complex (and often not physically based) contact models, and (2) it allows one to use larger time steps Δt [61].

In summary, while smooth DEM generally handles spherical particle shapes, it is capable of simulating microscopic-scale interactions with continuous forces. The CD method, in contrast, can deal with the mechanics of granular assemblies through more direct handling of particle interactions, making it suitable for simulations where impenetrability and friction are key, such as in geomechanics.

2.4.3 Remarks on the choice of the numerical method

The CD method is a robust and numerically unconditionally stable approach that has been applied to different granular media studies in static or quasi-static regimes [29, 30, 35, 126, 160–167], dynamic flows [162, 168, 169], grain-fluid interactions [170–172], and FEM-discrete element coupling [173].

Although the CD method was originally proposed in the context of rigid body interaction and frictional contact, it has been generalized and applied to cohesive contact cases, capillary bridges, cementing, etc [61,174,175]. It is worth noting that the perfect rigidity of the particles and how the contact laws between particles are implemented cannot be used for studies on the stiffness of grain arrays and wave propagation. However, it is well suited for the study of plastic deformation of granular materials.

While the non-penetration between particles cannot always be fulfilled due to the contact detection phase or numerical tolerances, the contact law formulation is such that the overlaps between particles remain small, and the kinematic constraints are respected during the evolution of a granular system [176]. The numerical studies that will be developed in this work will be carried out using the NSCD method, implemented in the open-source simulation platform LMGC90 [120].

2.5 Concluding remarks

WRPs are among the largest and most complex geotechnical structures due to the volumes and high filling rates that need to be handled during the dumping processes. WR materials are loose, highly heterogeneous, and challenging to characterize given the size limitations to test coarse samples in laboratory devices. The design and mechanical stability analysis of WRPs requires the characterization of the critical friction angle through small-scaled specimens on shearing devices. However, the reliability of the small-scaling techniques and recommended REVs is questionable given the limited and often contradictory results found in the literature.

Recent studies have demonstrated that if particle shape and roughness remain unchanged across grain sizes, the critical friction angle does not depend on the psd [26, 28–30, 35, 57–60]. Nevertheless, particle shape has a significant effect on ϕ_c [19, 30, 31, 35, 42, 45, 121–129]. Since real granular materials can often present grain size-shape correlations, modifications in the psd for small-scaled testing can also alter the grain shape distribution and lead to uncertain changes in the mechanical behavior [17, 19]. An alternative approach to test coarse granular materials that can present grain size-shape correlations is discrete-element modeling and simulation. Multiple particle shapes and sizes can be modeled in the DEM method, reproducing the complexity of WR materials. Several DEM studies have already explored the effects of different grain shapes or sizes, but none has systematically investigated the effects of coupling size-shape correlations, i.e., grain shapes varying across sizes.

DEM simulations are a privileged framework for studying WR materials because they allow identifying the source of the macroscopic critical friction angle through microscopic descriptors. Such information is not straightforward to obtain through experimental shearing devices. Previous works have shown, in particular, that the shear strength of a granular assembly results from geometrical and mechanical properties related to the contact and force networks in the sample. DEM systematic studies that consider the microstructural properties of granular media might allow studying and understanding the limitations of small-scaling techniques.

CHAPTER 3 METHODOLOGY

This section outlines our procedural framework for studying the effects of particle size-shape correlations in granular materials using DEM simulations. It includes material generation, sample preparation, simulation execution, and analysis of results. Additionally, the numerical CD method is validated by comparing DEM simple shear tests on spheres against ring shear tests on glass beads.

3.1 Research approach and design

This study employs a combined methodology that integrates computational and theoretical approaches. DEM simulations are performed to analyze the effects of variations in grain size and shape distributions under different stress and shearing conditions. Microstructural theoretical analyses provide further understanding of the mechanics of granular mechanics, allowing for the investigation of the influence of particles' geometric characteristics on shear strength. This methodology exploits the advantages of both approaches: theoretical analysis provides essential insights and principles, while computational simulations allow for exploration across diverse scenarios and controlled environments. Numerical data on critical shear strength in granular dry materials are collected by systematically adjusting grain size-shape correlation and psd. Qualitative observations and trends can also be examined to understand how combined grain geometrical characteristics affect the mechanical response of the granular material.

3.2 Numerical test series

In our numerical DEM samples, we define the same psds for all grain size-shape correlations, ranging from monodisperse to widely dispersed. The grain size-shape correlation trends are reminiscent of empirical observations, such as variation of grain angularity [5] or elongation [19,35] across particle sizes. Particle shape is characterized by defined geometric shapes, such as circles and polygons in 2D, or spheres and polyhedra in 3D, simplifying the representation of real soil grains. Similarly, two-dimensional simulations are simplified forms of three-dimensional cases. However, these simplifications allow isolating the relevant mechanisms and provide insights and predictive capabilities that are essential for advancing the study of granular materials [30, 33, 42, 128, 177–179]. Due to the lack of systematic studies on grain size-shape correlation in DEM, three 2D case studies were selected based on particle elongation, particle angularity, and particle irregularity. Additionally, 3D simulations focusing on grain size-shape correlations based on angularity were conducted to explore its impact on the mechanical behavior of granular assemblies in a more realistic spatial context. It is worth mentioning that the inter-particle coefficient of friction was set $\mu = 0.4$ for all our simulations.

3.2.1 Modeled material in 2D

Grain elongation

The first grain shape characteristic explored is elongation, motivated by experimental studies of Ovalle & Dano [19] and Linero *et al.* [17]. We explored the following opposite scenarios for the correlation between particle size and shape:

- ***Case 1-A:*** large particles are elongated, and smaller grains tend to be rounded.
- ***Case 1-B:*** large particles are rounded, and smaller ones are elongated.

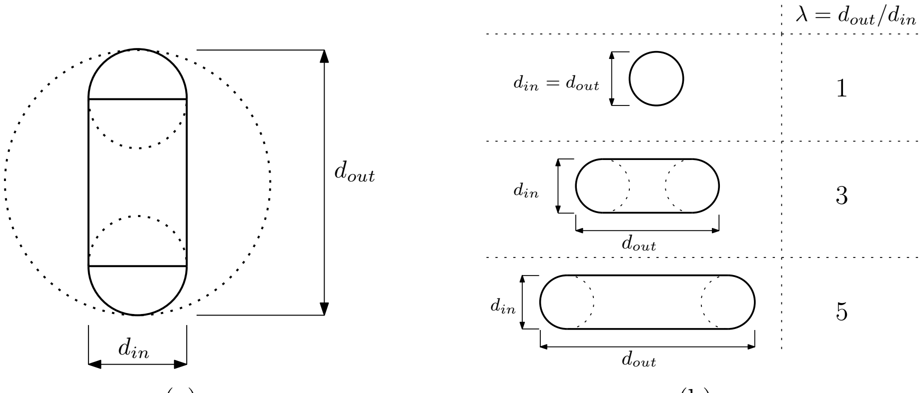

(a) (b)

Figure 3.1 Scheme of 2D elongated particles: (a) Scheme presenting the inner and outer circles of an elongated particle, and (b) examples of particles with elongation equal to 1, 3 and 5.

We modeled elongated particles as rectangles with rounded caps, as shown in Figure 3.1(a). Note that the grain size is defined by the inner diameter $d_{in} = d$ for both circular particles and elongated grains, as commonly done in experimental soil testing. Elongation (λ) is defined by the ratio of the longest dimension to the shortest dimension of the particles, i.e., the ratio between the inner (d_{in}) and outer diameter (d_{out}). Figure 3.1(b) illustrates three levels of particle elongation. Finally, elongation is correlated to grain size by Equation 3.1 and 3.2 for Case 1A and Case 1B, respectively, where λ_{min} and λ_{max} were set between 1 and 5.

$$\lambda(d) = \lambda_{\text{min}} + \frac{d - d_{\text{min}}}{d_{\text{max}} - d_{\text{min}}}(\lambda_{\text{max}} - \lambda_{\text{min}}). \tag{3.1}$$

$$\lambda(d) = \lambda_{\text{min}} + \frac{d_{\text{max}} - d}{d_{\text{max}} - d_{\text{min}}}(\lambda_{\text{max}} - \lambda_{\text{min}}). \tag{3.2}$$

Grain angularity

In this scenario, we use grains with different number of corners, varying in this way the degree of particle sharpness [33, 179]. This is accomplished by using regular polygons and adjusting their number of sides n_s. The sharpest particle is a triangle ($n_s = 3$) and as n_s increases, polygons gradually evolve towards a disk-like shape. Figure 3.2 shows the range of regular polygons used on this set of simulations, where n_s varies from 3 to 64. Combining ten families of particle shapes enables us to investigate two distinct size-shape correlations described as follows:

- ***Case 2-A:*** large particles are rounded, and smaller grains tend to be angular.
- ***Case 2-B:*** large particles are angular, and smaller ones are rounded.

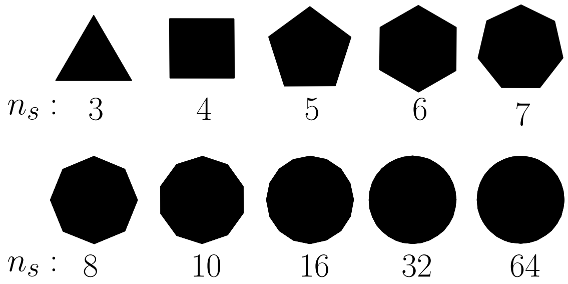

Figure 3.2 Scheme presenting the evolution of corner sharpness, being n_s the number of sides of regular polygons.

Grain irregularity

In the last 2D scenario, we investigate the effects of pentagons ($n_s = 5$) with different degrees of shape irregularity. While regular polygons have evenly spaced vertices, we can simulate geometries where the spacing between vertices varies based on a level of irregularity, as suggested by Nguyen *et al.* [42]. We have selected pentagons due to multiple numerical studies that have characterized them using DEM simulations, using assemblies of mono-sized pentagons [42, 179], thus providing a basis of comparison for our simulations. For a regular pentagon, each vertex angular position can be described as $\theta^k = \theta_0 + 2k\pi/5$, where θ_0 represents the first vertex position relative to the horizontal and k is an integer ranging from 1 to 5. To obtain irregular geometries, the geometry of the regular pentagon by altering the angular positions of vertices denoted by k as follows:

$$\theta^k = \theta_0 + k\frac{2\pi}{5} \pm \frac{\pi}{5} r_{[0,\delta]} \ , \tag{3.3}$$

where $r_{[0,\delta]}$ is a random variable in the range $[0, \delta]$, δ is the degree of irregularity varying from 0 to 1, and the ± sign is randomly chosen for each vertex, as shown in Figure 3.3. This geometrical irregularity of pentagonal grains can be studied in two opposite grain size-shape correlation cases:

- ***Case 3-A:*** large grains are irregular pentagons, while small ones are regular.
- ***Case 3-B:*** large grains are regular pentagons, while small ones are irregular.

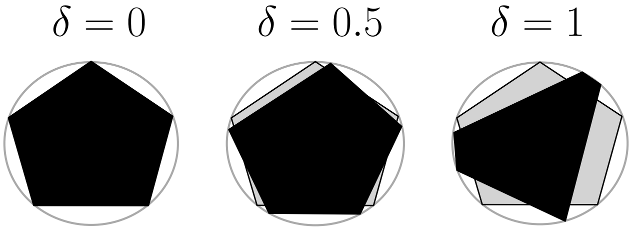

Figure 3.3 Scheme presenting the evolution of grain geometric irregularity as a function of parameter δ, based on [42]

Figure 3.4 shows the three size-shape correlations presented above for the same psd. This series of particle assemblies allows us to characterize the mechanical behavior of granular assemblies with dispersion in sizes and shapes, since each size-shape correlation is studied for a range of psd.

3.2.2 Sample preparation and 2D shear tests

The procedure for generating and testing samples within our DEM framework is meticulously crafted to replicate granular material behavior. This process is separated into several integral steps, each pivotal to the overall simulation fidelity and accuracy. The steps are described as follows:

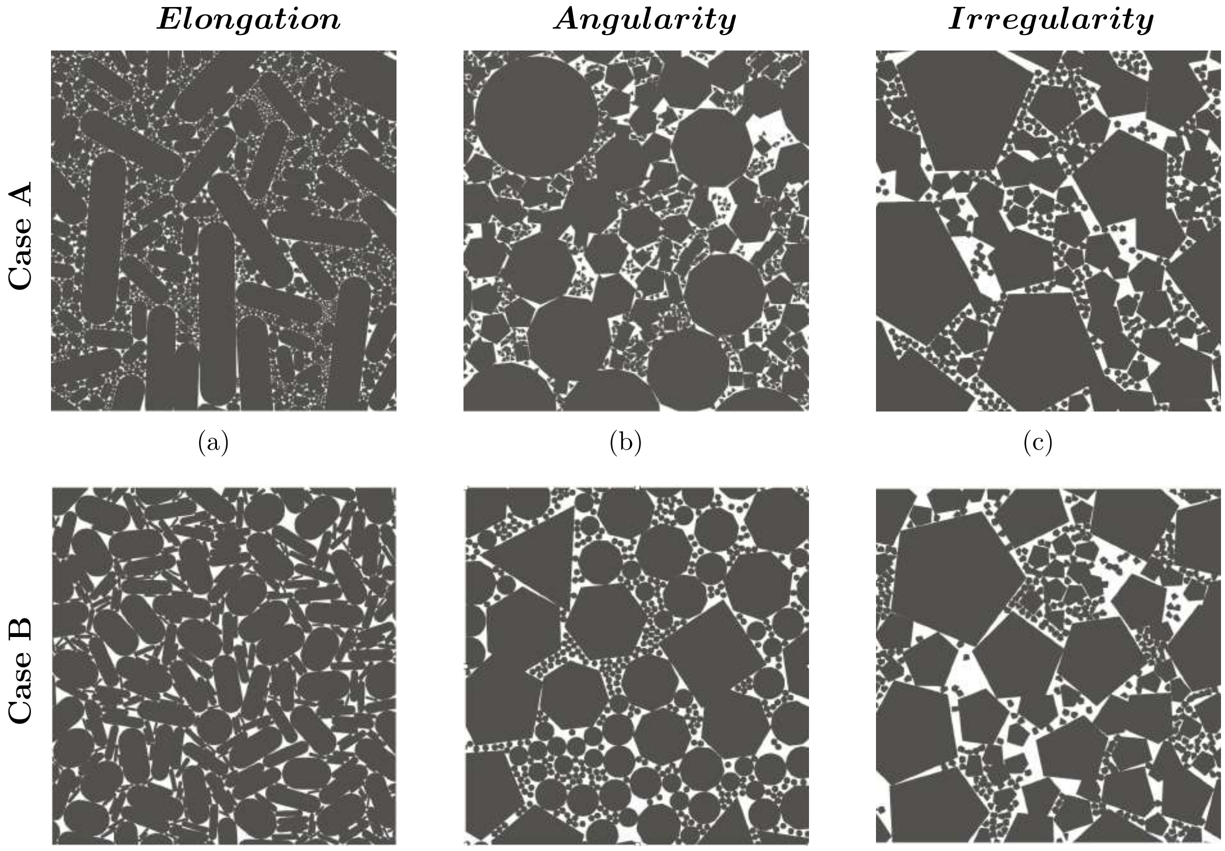

(a) (b) (c)

(d) (e) (f)

Figure 3.4 Screenshots of 2D DEM samples with size-shape correlation based on elongation (left), angularity (center) and irregularity (right). Cases A are in the upper part and Cases B are the lower part.

1. **Material generation:** we define the initial geometrical and physical parameters for our granular material, such as psd, grain shapes, and material properties. Regarding psd, $d_{\max}$ remains constant for all simulations, and $d_{\min}$ changes for each psd as a function of grain size span S, defined as follows:

   $$S = \frac{d_{\max} - d_{\min}}{d_{\max} + d_{\min}} \; . \tag{3.4}$$

   The grain size span ranges from $S = 0.0$ (monodisperse sample) to $S = 0.9$ (highly polydisperse sample) on 0.1 steps. For each shape-size correlation mentioned above, all particles in a sample are generated using a uniform psd for a given S, so the surface fractions are constant across different grain shapes; see Figure 3.5.

2. **Deposition and compression:** The preparation of the samples follows a layer-by-layer deposition, placing particles onto a substrate according to simple geometric

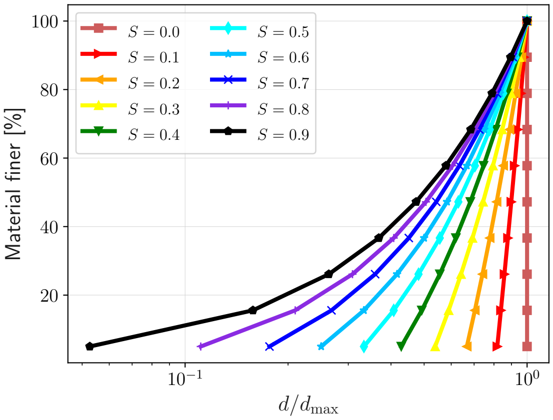

Figure 3.5 Particle size distributions for all modeled materials as a function of particle size span S, where each particle diameter d is normalized by the maximum particle diameter $d_{\max}$.

rules [43, 180, 181]. This process is guided by a potential energy deposition strategy, wherein each particle is positioned at the lowest point on the free surface based on its diameter. The goal of this process is to minimize the potential energy denoted as $\Psi = \sum_{i=1}^{N_p} y(i)$, where $y(i)$ represents the vertical coordinate of particle i, as illustrated in Figure 3.6. After the deposition process, the samples are compressed using an isotropic pressure P that is applied through rigid walls around the sample up to a stable void ratio.

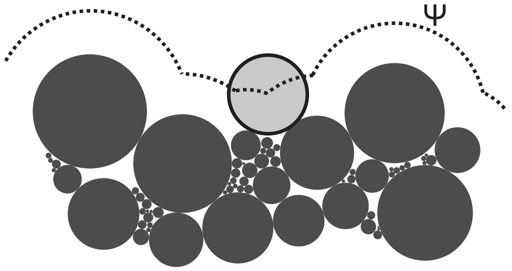

Figure 3.6 Illustration of potential-based deposition method [43].

3. **Shearing test:** the samples are tested in shearing conditions by moving the top and bottom walls horizontally at a constant velocity v, while applying a load P along the vertical axis, as described in Figure 3.7. The shearing velocity v is set using the *inertial number* defined as $I = \dot{\gamma}\langle d\rangle\sqrt{\rho/P}$, being $\langle d\rangle$ the average particle diameter, ρ the particle density and $\dot{\gamma} = v/h_0$, with h_0 the initial sample's height. The inertial number is set to $I = 1 \times 10^{-3}$ for all simulations, which ensures a quasi-static shearing condition [182].

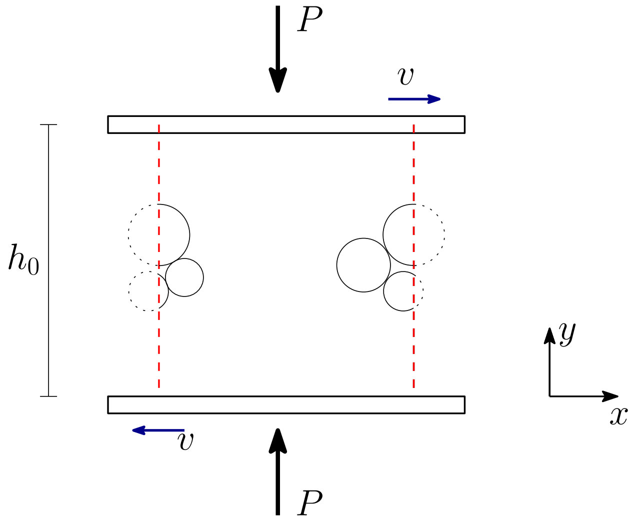

Figure 3.7 Scheme of simple shearing conditions on granular samples; red dashed lines represent the periodic boundary.

Figure 3.7 displays a schematic representation of the shearing test. We also impose periodic boundary conditions along the shearing direction, so any particle and contact crossing the boundary will instantaneously reappear on the corresponding opposite side of the sample. The periodic condition allows us to reach large deformations and avoid finite size effects and local frustrations by lateral walls [61], making it possible to achieve the critical state.

3.2.3 Modeled material in 3D

Transitioning from 2D to 3D simulations marks a significant leap in our methodological approach, providing a more realistic analysis of granular materials. The inherent limitations of 2D models in representing the full spectrum of particle interaction and movement are overcome in the 3D space. The 3D analysis includes particle shapes ranging from regular octahedrons (with $n_f = 8$ faces) to spherical particles at the same time particle size distribution is varied. Figure 3.8 displays the different particle shapes for each particle family (P_i), which include polyhedral particles ranging form $n_f = 8$ ($P1$) to $n_f = 256$ ($P5$), until spheres ($P6$). Two opposite grain size-shape correlations based on particle angularity are examined:

- **Case 4A:** larger grains are rounded while smaller ones are sharper.
- **Case 4B:** larger grains are sharper while smaller ones are rounded.

Figure 3.9 shows samples with $S = 0.2$ and $S = 0.7$ for both grain size-shape correlations.

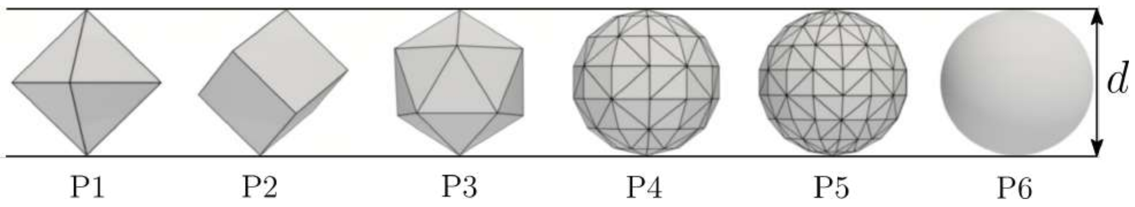

Figure 3.8 Set of different particle shapes considered in 3D simulations, where the size of grain d is related to the circumscribing sphere around the grain.

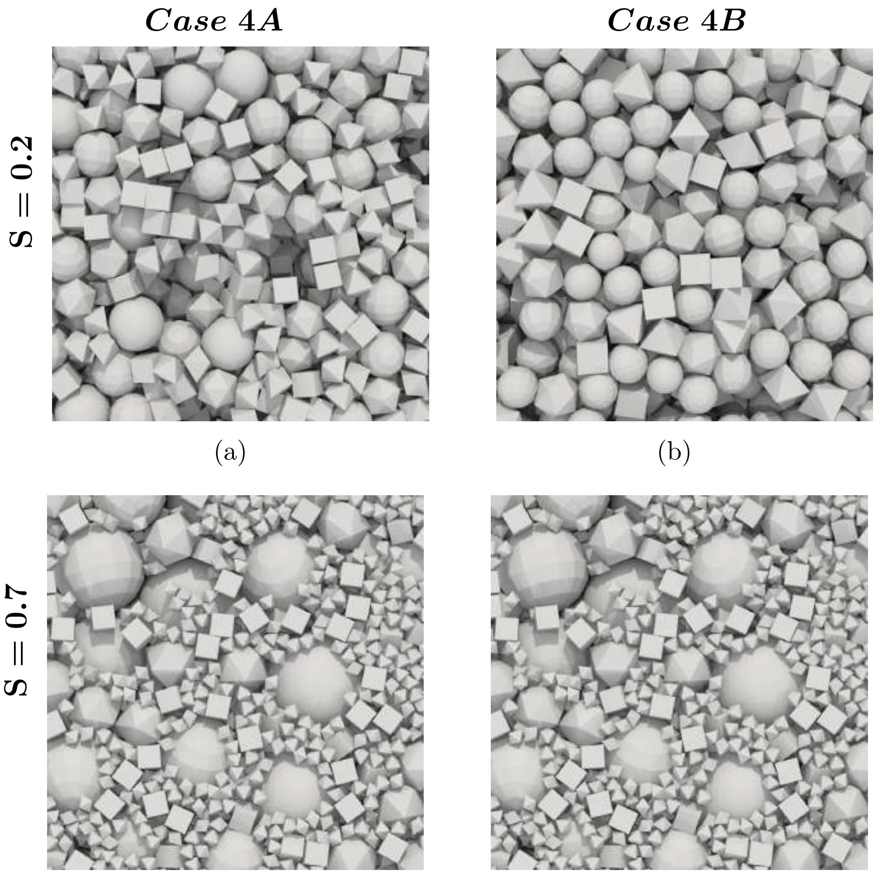

(a) (b)

(c) (d)

Figure 3.9 Samples with particle size span $S = 0.2$ (a) and (b) and $S = 0.7$ (c) and (d) for different size-shape correlation on 3D simulation.

3.2.4 Sample preparation and 3D shear tests

The method for the creation and testing of 3D samples is divided into the same multiple steps used in 2D simulations:

1. **Material generation:** we specify the initial geometric and physical characteristics

of the granular samples, including the distribution of particle sizes, their shapes, and material properties. The psd ranges from $S = 0.0$ to $S = 0.7$ in 0.1 steps and follows a constant volume fraction across different grain shapes, as shown in Figure 3.5.

2. **Deposition and compression:** Particle deposition occurs like the layer-by-layer deposition mentioned previously. The process occurs within a rectangular container of width (W) and height (H), as shown in Figure 3.10(a). Our box dimensions achieve the international testing standard ASTM D7181, ensuring that $H/W = 2$ and $W/d_{\max} \geq 10$. Upon deposition, the granular samples are consolidated under an isotropic pressure P applied using to all faces of the sample box through surrounding rigid walls.

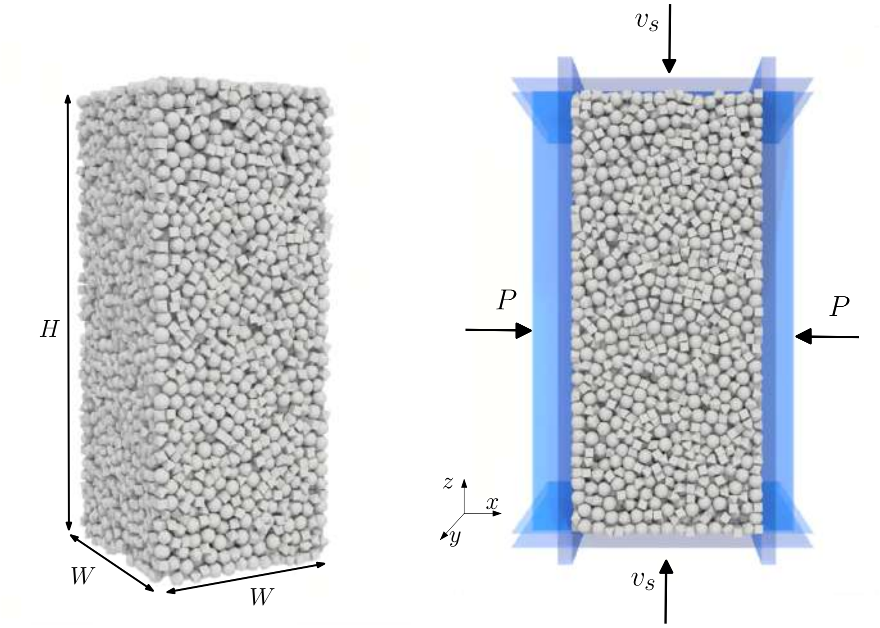

(a) (b)

Figure 3.10 3D triaxial test: Screenshot of (a) the sample after construction protocol for $S = 0$ and (b) Schematic representation of triaxial boundary conditions employing rigid lateral walls around the sample.

3. **Shearing test:** a constant shearing velocity (v_s) is applied to both the upper and lower walls of the samples, while lateral walls maintain constant P, as illustrated in Figure 3.10(b).

3.3 Data analysis

Microscopic descriptors in granular materials refer to characteristics at the scale of individual particles and their contacts. These include contact forces between grains (normal and tangential forces), and the connectivity or coordination number, which is the average number of contacts per particle. The fabric of granular assemblies during shearing can also be described based on the orientation of contacts in space and the network of forces created as grains bear external forces.

Macroscopic descriptors, on the other hand, relate to the bulk properties of a granular assembly. Such descriptors include the stress and strain state under given loading conditions and bulk density. For engineering applications, macroscopic analyses often utilize constitutive models that integrate microscopic insights to predict the behavior of granular materials as a continuum. Combining micro- and macro-scale characteristics creates a unique multi-scale perspective to understand the behavior of granular materials.

3.3.1 Macroscopic descriptors

Packing arrangement

Void ratio (e) and solid fraction (ν) are two definitions able to capture the bulk density. The void ratio is defined as:

$$e = \frac{V_v}{V_s} \ , \tag{3.5}$$

where V_v is the void volume and V_s is the volume of solids. The solid fraction, $\nu = V_s/V$, represents the proportion of the total volume (V) occupied by the solid particles. The solid fraction is directly related to the void ratio, with a higher solid fraction indicating a lower void ratio and, thus, a denser packing.

Shear strength in discrete granular media

The stress state of a granular assembly is characterized by the stress tensor. For a discrete media, an average stress tensor can be expressed as [61, 183–185]:

$$\sigma_{ij} = \frac{1}{V} \sum_{\forall c} f_i^c \ell_j^c \ , \tag{3.6}$$

where f_i^c is the i component of the force vector at contact point c, and ℓ_j^c is the j component of the branch vector (the vector joining the center of mass of touching particles) at contacts c, as shown in Figure 3.11. Note that in this study, we always refer to dry granular materials, thus any effective stress corresponds to the total stress. For the sake of simplicity, all stresses are considered effective hereafter and we are not using the superscript $'$ usually employed to refer to effective measurements.

We describe the stress ratio using the normalized shear stress, defined as the ratio between the deviatoric stress $q = \sigma_1 - \sigma_3$ and the mean stress $p = (\sigma_1 + \sigma_2 + \sigma_3)/3$, where $\sigma_1/\sigma_2/\sigma_3$ are the principal stresses of σ_{ij}. Employing these stress components in the critical state, we can estimate the macroscopic friction angle (ϕ) according to the Mohr-Coulomb failure criterion.

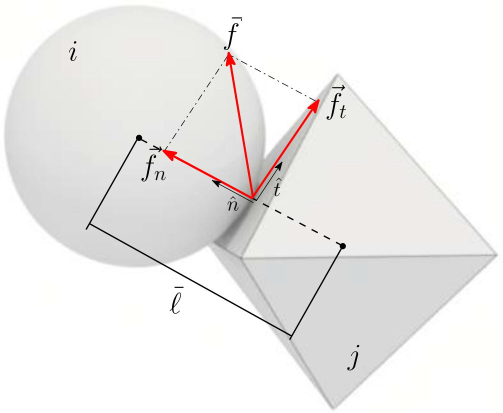

Figure 3.11 Schematic representation of two interacting grains, displaying the associated force and branch vectors at contact frame c between particle i and j.

3.3.2 Microscopic behavior

The arrangement of particles in a granular material plays a crucial role in determining the macroscopic properties. At the contact level, we explore the number of contacts per grain, contact orientations, the orientation and magnitude of contact forces, and relative particle movements during shearing.

Connectivity

Particle connectivity refers to how well connected particles are with their neighbors. Connectivity can be measured in granular materials by examining the number and distribution of contacts between particles. In this vein, one indicator is the number of *load-bearing grains* (N_p^*) within the assembly. Another indicator is the number of no-force-bearing particles, also called *rattlers* or *floating particles*, which are particles with less than two force-bearing contacts. The most commonly used parameter for characterizing connectivity is the average number of contact per grain or *coordination number*, defined as $Z = 2N_c/N_p^*$, where N_c is the total number of force-bearing contacts [186].

Force transmission

The mechanical behavior of granular materials is deeply linked to the force networks that are created by series of grains transmitting forces. In Figure 3.11, a local contact framework consisting of $\hat{n}$ and $\hat{t}$ is illustrated, where $\hat{n}$ denotes the unit vector perpendicular to the contact plane and $\hat{t}$ represents an orthonormal unit vector aligned with the tangential force. The total contact force can be expressed as $\hat{f} = f_n\hat{n} + f_t\hat{t}$, where f_n and f_t represent the magnitudes of the normal and tangential contact forces, respectively. The force distribution within a granular material is often analyzed by examining the probability density function of normal contact forces (PDF) [29,187]. Using such description, it has been shown that contact forces group into two families of forces, creating the so-called *strong* and *weak* force networks. The first is consider the backbone of the granular assembly, carrying relatively large forces, while the second has a secondary role, providing stability to the the strong network [188].

Microstructural anisotropies

The pioneering work of Rothenburg and Bathurst [189] and Oda [190] showed that contact orientations and forces have particular spatial distributions in a granular material. Such observation allowed them to develop an analytical framework in which the stress tensor can be described in terms of angular distributions of contact forces, contact orientations, and particle arrangement (branch vector orientations). Such angular distributions turn out to be easily described by harmonic functions, which ultimately allow us to link the macroscopic stress state with the angular variability (i.e., anisotropy) of microscale fabric descriptors. A series of anisotropy factors are deduced this mathematical approach that quantify the spatial variability of contact distribution and force network: contact anisotropy (a_c), normal branch anisotropy (a_{ℓ_n}), tangential branch anisotropy (a_{ℓ_t}), normal force anisotropy (a_{fn}) and tangential force anisotropy (a_{ft}). The contact anisotropy (a_c) reflects the surplus of contacts aligned in the principal stress direction (θ_σ) and a deficiency of contacts along the perpendicular direction. This anisotropy measure can derived from the Fabric tensor (F_{ij}), which is defined based on the contact orientation vectors $\hat{n}$ [189] as:

$$F_{ij} = \frac{1}{N_c} \sum_{c \forall V} n_i^c n_j^c \ , \tag{3.7}$$

where n_i^c and n_j^c the i and j component of $\hat{n}$, as shown in Figure 3.11. The vector branch lengths can vary in space and present preferred orientations due to different particle shapes and sizes in contact. The branch vector is defined as $\hat{\ell} = \ell_n \hat{n} + \ell_t \hat{t}$, being ℓ_n the branch projection on the normal contact orientation and ℓ_t is the branch projection on the tangential orientation to the contact. Hence, the branch anisotropy is related to two tensors described as follows [177]:

$$L_{ij}^n = \frac{1}{\langle \ell_n \rangle} \sum_{c \forall V} \ell_n^c n_i^c n_j^c \ , \tag{3.8}$$

$$L_{ij}^t = \frac{1}{\langle \ell_n \rangle} \sum_{c \forall V} \ell_t^c n_i^c t_j^c \ , \tag{3.9}$$

being $\langle \ell_n \rangle$ the average branch length projected onto the normal contact orientation.

Finally, the network of forces can also be described using two significant parameters: a_{fn}, accounting for the transmission of normal forces and related with the magnitude of the average normal force at contacts aligned in direction θ_σ; while a_{ft} quantifies the enhanced activation of frictional forces at contacts oriented along $\theta_\sigma \pm \pi/4$ compared to those oriented along θ_σ. These directional differences are deduced from tensors (ξ_{ij}^n) and (ξ_{ij}^t) defined below [189]:

$$\xi_{ij}^n = \frac{1}{N_c} \sum_{c \forall V} f_n^c n_i^c n_j^c \ , \tag{3.10}$$

$$\xi_{ij}^t = \frac{1}{N_c} \sum_{c \forall V} f_t^c n_i^c t_j^c \ . \tag{3.11}$$

The anisotropies are then calculated using the following expressions:

$$a_c = \kappa \ (F_{33} - F_{11}) \ , \tag{3.12}$$

$$a_{\ell_n} = \kappa \ \frac{L_{11}^n - L_{33}^n}{L_{11}^n + L_{22}^n + L_{33}^n} - a_c \ , \tag{3.13}$$

$$a_{\ell_t} = \kappa \ \frac{L_{11} - L_{33}}{L_{11} + L_{22} + L_{33}} - a_c - a_{\ell_n} \ , \tag{3.14}$$

$$a_{fn} = \kappa \ \frac{\xi_{33}^n - \xi_{11}^n}{\xi_{11}^n + \xi_{22}^n + \xi_{33}^n} - a_c \ , \tag{3.15}$$

$$a_{ft} = \kappa \ \frac{\xi_{33} - \xi_{11}}{\xi_{11} + \xi_{22} + \xi_{33}} - a_c - a_{fn} \ , \tag{3.16}$$

where $\xi_{ij} = \xi_{ij}^n + \xi_{ij}^t$ and $L_{ij} = L_{ij}^n + L_{ij}^t$. Numbered subindices in the previous expression denote the corresponding component of each tensor. Coefficient κ may differ based on the test boundary boundary conditions and whether two- or three-dimensional conditions are considered.

One of the major outcomes of this mathematical development is the remarkable link between the macroscopic shear strength and the microscale anisotropies. Neglecting higher order terms in the analytical development behind this analysis, the following equation relates the level of anisotropies of a granular system with the stress ratio [189, 190]:

$$\frac{q}{p} = \kappa \left(a_c + a_\ell + a_{fn} + a_{ft} \right) . \tag{3.17}$$

Through this equation, we can understand what microstructural changes (geometrical or mechanical) are affecting the macroscopic shear strength on a material when sheared.

For more details on the definitions of these tensors, the related anisotropies, and the mathematical calculations that lead to Equation 3.17, please refer to in-depth resources such as those cited in [59, 189, 191].

3.4 Validation of the numerical method

This section aims to validate the CD method by comparing experiments and numerical shear tests on spheres using the platform LMGC90 [120]. Numerical periodic simple shear on spheres is compared with ring shear tests on glass beads.

3.4.1 Numerical simulations

Sample preparation and shearing test

The procedure for generating and testing follows the same steps mentioned in section 3.2, although testing conditions are slightly different.

1. **Material generation:** samples comprise only rigid spherical particles. The grain size spans used are $S = [0, 0.3, 0.6, 0.8]$ and follow constant volume fractions across different grain shapes, as shown in Figure 3.12.

2. **Deposition and compression:** particle deposition occurs inside a rectangular container with a specific length (L) and height (H), as specified in Figure 3.13(c), using the layer-by-layer deposition protocol mentioned previously. Our box dimensions must adhere to the international testing standard ASTM D6467 of ring shear test [192], ensuring $H/d_{\max} \geq 10$. The granular samples are consolidated by applying an effective

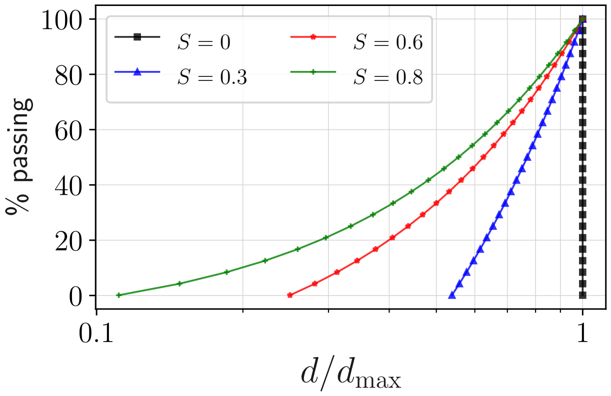

Figure 3.12 3D-DEM samples composed by spheres: particle size distributions tested for various values of S.

normal stress $\sigma_n^{'}$ through rigid walls. Figure 3.13 shows a screenshot for the monodispersed sample ($S = 0$) and the most polydispersed sample ($S = 0.8$).

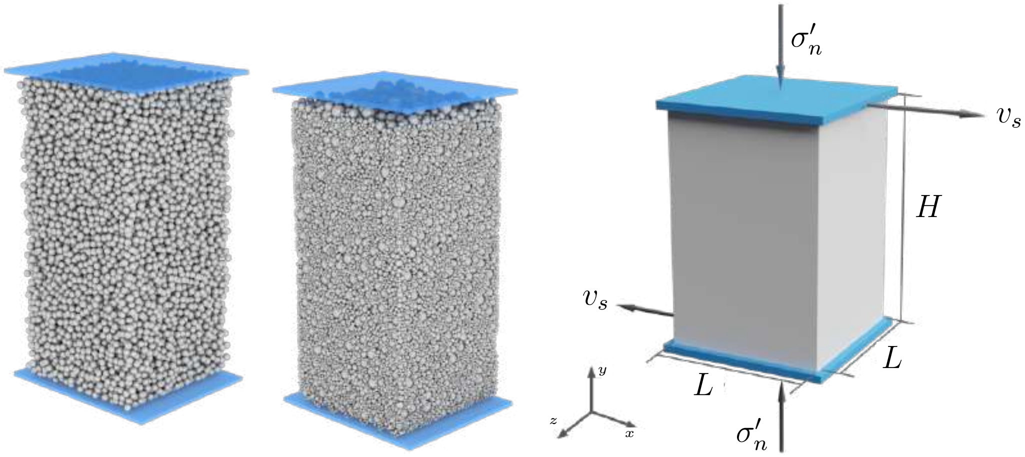

(a) (b) (c)

Figure 3.13 3D-DEM samples composed by spheres: Screenshots of samples with grain size span (a) $S = 0.0$, (b) $S = 0.8$ and testing configuration for the simple shear test with the periodic condition on x and z axis.

3. **Shearing test:** samples are sheared by imposing a shearing velocity v_s in x-axis direction, applied to both the upper and lower walls of the samples, while $\sigma_n^{'}$ is imposed on the y-axis, as shown in Figure 3.13(c). The inertial number is set to $I = 1 \times 10^{-3}$ for all simulations to ensure a quasi-static shearing regime [182]. Moreover, the periodic boundary condition is defined on the x and z axes.

In this validation process, the numerical testing conditions involved varying the inter-particle friction coefficient to $\mu = [0.0, 0.1, 0.2, 0.4, 0.6, 0.8]$, and $\sigma_n^{'}$ to three different values: 10 kPa, 50 kPa, and 100 kPa. These conditions were applied to all the psd examined in the study.

Numerical results

In our numerical simulations, the shear stress is calculated as $\tau = F_x/L^2$ and the effective normal stress is determined as $\sigma'_n = F_y/L^2$, where F_x and F_y represent the forces between grins and walls acting along of x- and y-axes, respectively, based on the scheme depicted in Figure3.13. Figures 3.14 and 3.15 show the evolution of ν and τ/σ'_n for granular assemblies with size dispersion of $S = 0.0$ and $S = 0.8$ as a function of the shear deformation γ_{xy}. For the normalized shear τ/σ'_n, we observe hardening up to $\gamma_{xy} \simeq 0.2$. Then, a transient zone towards the critical state occurs, which varies depending on the sample. However, the critical state is reached around $\gamma_{xy} \simeq 0.4$.

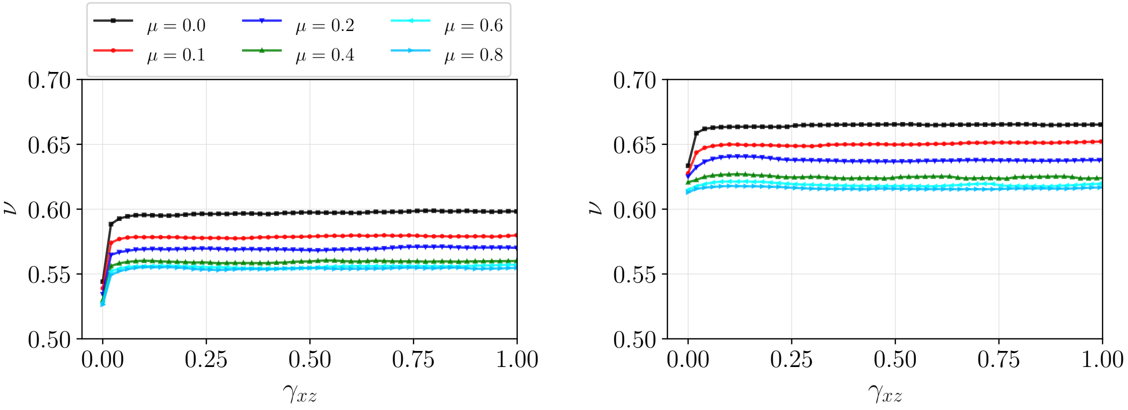

(a) (b)

Figure 3.14 Evolution of solid fraction ν for the samples with grain size span $S = 0.0$ (a) and $S = 0.8$ (b) as a function of the shear deformation γ_{xy} for all tested values of inter-particle fiction coefficient μ, $P = 10$ [kPa].

Figure 3.16(a) shows the evolution of the critical ν as a function of the inter-particle friction coefficient for all the psd tested. We observe that both μ and S have an impact on critical packing density. Higher μ and S values both lead to a decrease in the critical solid fraction.

In terms of shear strength, τ/σ'_n at critical state is related to the critical state friction angle of the material (ϕ_c) as:

$$\sin(\phi_c) = \frac{\tau}{\sigma'_n} \ . \tag{3.18}$$

Figure 3.16(b) shows the evolution of ϕ_c as a function of the μ coefficient for all psd tested.

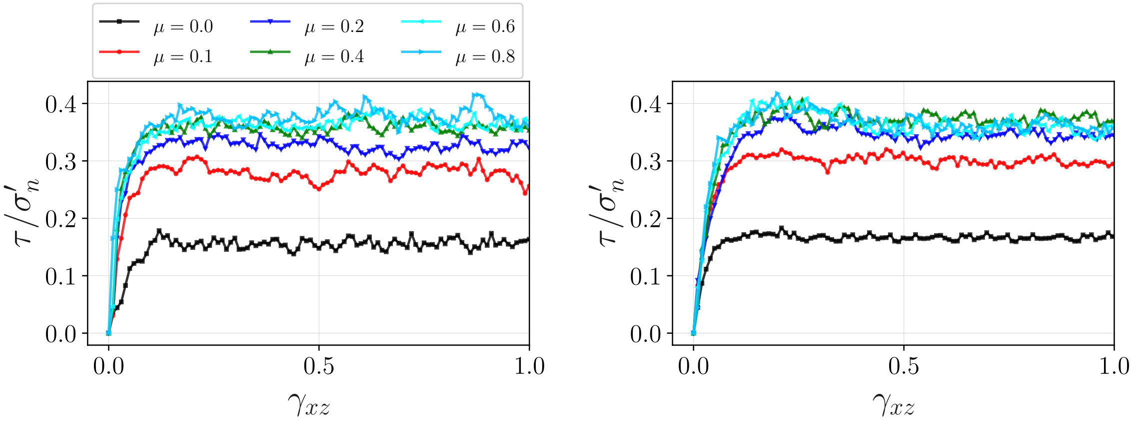

(a) (b)

Figure 3.15 Evolution of normalized shear strength τ/σ'_n for the samples with grain size span $S = 0.0$ (a) and $S = 0.8$ (b) as a function of the shear deformation γ_{xy} for all tested values of inter-particle fiction coefficient μ, $\sigma'_n = 10$ [kPa].

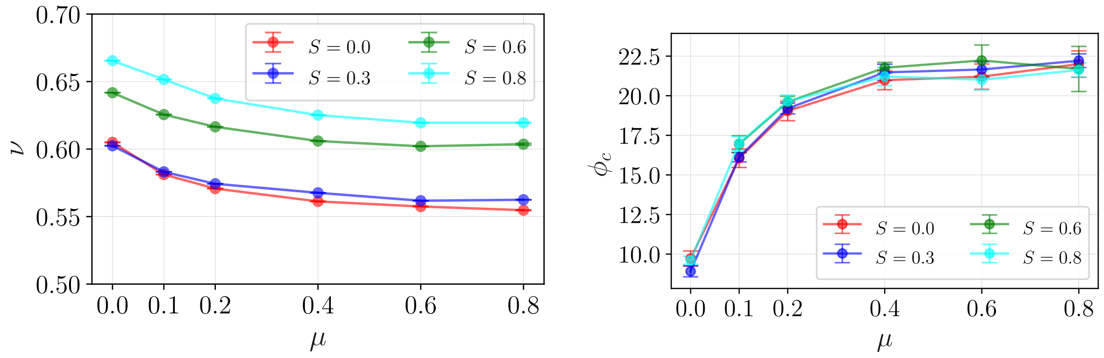

(a) (b)

Figure 3.16 Evolution of solid fraction ν (a) and critical friction angle (b) as a function of the inter-particle fiction coefficient μ for all tested grain size span, $P = 10$ [kPa].

This figure provides us with two important insights: (1) ϕ_c does not depend on psd if all the grains have the same characteristic shape and surface roughness [27–29, 60, 193], (2) the evolution of ϕ_c as a function of μ exhibits an asymptotic behavior, indicating that as μ increases, ϕ_c approaches a limiting value [194–196]. This asymptotic behavior suggests that beyond a certain point, increases in the inter-particle friction coefficient have a minor effect on the critical state friction angle. Similar observations have been reported in previous studies, highlighting that the critical state friction angle becomes nearly constant at high values of μ [197, 198]. This implies that the inter-particle friction coefficient primarily influences the behavior of granular materials up to a certain threshold, beyond which other factors such as particle shape and surface roughness play more significant roles.

3.4.2 Experimental tests

Ring Shear tests on glass beads are conducted to characterize their mechanical behavior and are compared with numerical results. The device model used for the ring shear test is TORSHEAR EmS. Glass beads are carefully selected and cleaned to remove any impurities that could affect the results. The beads are then graded by size using sieves to ensure uniformity and their size dispersion is fixed by the grain size span (S). We tested samples with $S = 0$ and $S = 0.8$, the latter using six different particle diameters, as shown in Figure 3.17.

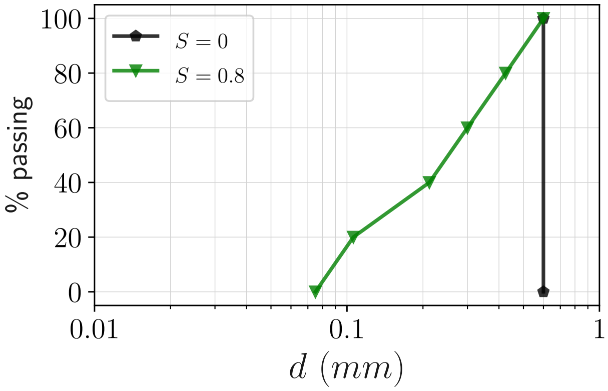

Figure 3.17 Glass bead: particle size distributions tested on ring shear test.

The shear device contains a soil sample 20 mm thick, with inner (R_{in}) and outer (R_{out}) diameters of 70 mm and 100 mm, respectively, confined radially between concentric rigid rings, based on ASTM D6467–17 [192]. During the tests, the vertical displacement (δ_v) is measured by the transducer presented in Figure 3.18 and the volumetric deformation is computed as $\varepsilon_v = \delta_v/h_0$, where h_0 is the sample height after consolidation. The effective normal stress acting on the sample is computed as follows:

$$\sigma'_n = \frac{F_n}{\phi(R_{out}^2 - R_{in}^2)} \, , \tag{3.19}$$

where F_n is the normal vertical force acting on the specimen (see no. 5 in Figure 3.18). The average shear stress supported by the samples is calculated as follows:

$$\tau = \frac{3(F_1 + F_2)L_t}{4\phi(R_{out}^3 - R_{in}^3)} \, , \tag{3.20}$$

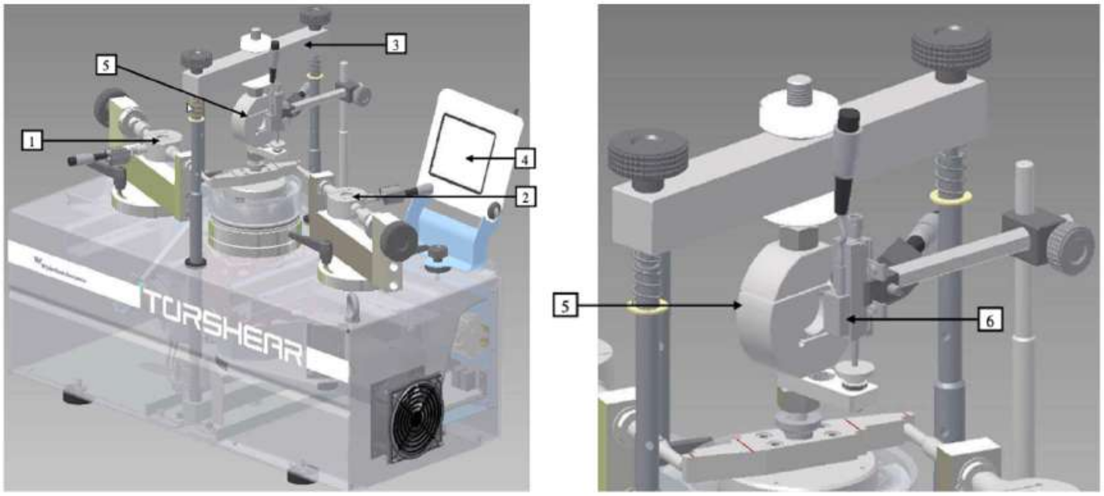

Figure 3.18 Ring shear equipment: (1-2) 1 kN shear horizontal load cell, (3) crossbeam (4) touch screen display, (5) 5 kN vertical load cell and (6) 10 mm vertical displacement transducer [44].

where F_1 and F_2 are the horizontal loads measured (see no. 1 and no. 2 in Figure 3.18) and L_t is the torque arm length. Each test is carried out under a vertical pressure σ_n' equal to 10, 50 and, 100 kPa.

3.4.3 Comparison of numerical and experimental results

Figure 3.19 shows τ/σ_n' as a function γ_{xy} for experimental ring shear tests and DEM simulations under two different σ_n' of 50 and 100 kPa. In both figures, we compare samples composed of spherical grains with $S = 0.8$. The simulation data are presented for friction coefficients $\mu = 0.4$ and 0.8. The trends in the figures show a similar pattern of τ/σ_n' as a function of γ_{xy}. We observe hardening up to $\gamma_{xy} \simeq 0.2$ for both values of σ_n', followed by critical strength. There are slight variations in increasing rates of τ/σ_n' between the experimental and simulation results. However, this difference represents an error of no more than 5%.

Figure 3.20 shows the evolution of ε_v as a function of γ_{xy} for experimental and numerical tests. The results are presented for a size dispersion of $S = 0.8$ and inter-particle friction coefficients of 0.4 and 0.8. Note that, since the DEM model considers perfectly rigid grains, the numerical results are only slightly affected by σ_n'. All samples indicate dilation behavior under shear. However, the magnitude of ε_v varies between the experimental and simulation results. These differences suggest that the DEM simulations underestimate the volumetric deformation compared to the experimental observations under these normal stress values.

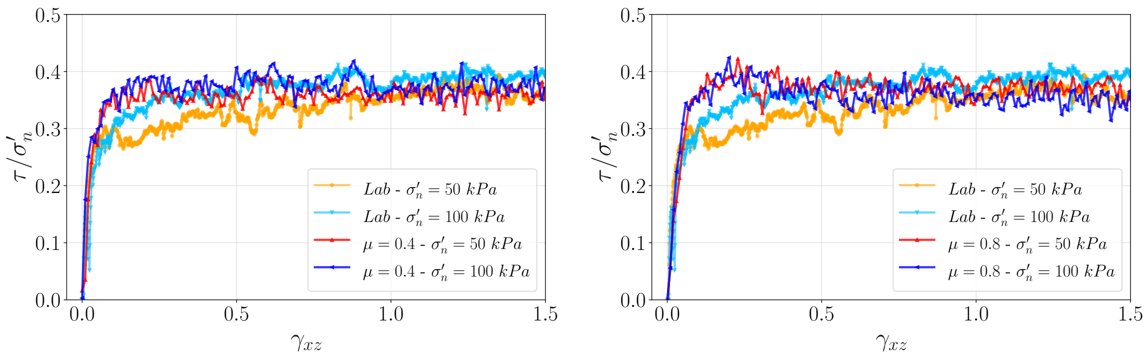

(a) (b)

Figure 3.19 Evolution of τ/σ'_n for samples with $S = 0.8$ and inter-particle frictional coefficient (a) $\mu = 0.4$ and (b) $\mu = 0.8$ for different stress level.

This underestimation of volumetric behavior is more pronounced at lower values of μ. Despite these discrepancies, the overall trends suggest that the DEM model can reasonably replicate the mechanical behavior observed in the laboratory tests, particularly the critical shear strength, which is the most important parameter in this study. Our DEM simulations employ idealized boundary conditions (i.e., periodic boundary), which may lead to effects that differ from the experimental tests, where friction exists between the granular material and the sidewalls [32, 198].

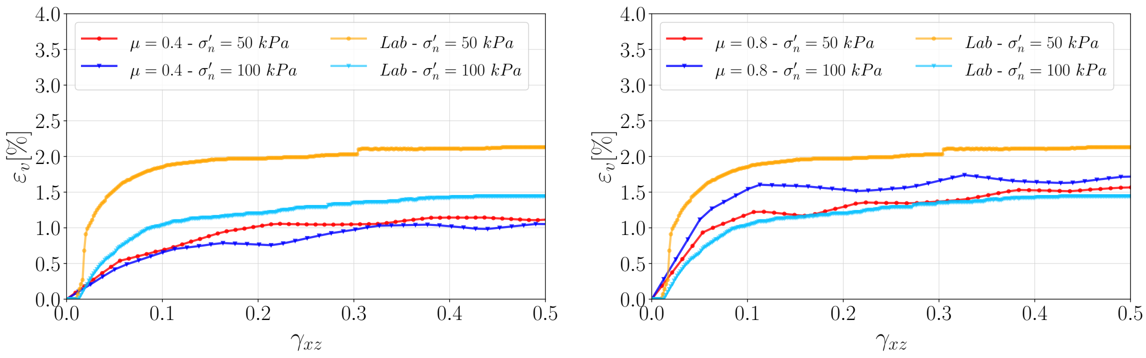

(a) (b)

Figure 3.20 Evolution of volumetric deformation ε_v for samples with $S = 0.8$ and inter-particle frictional coefficient (a) $\mu = 0.4$ and (b) $\mu = 0.8$ for different stress level.

3.4.4 Limitations of using DEM in shearing tests for soil mechanics

While DEM has been widely adopted for simulating the behavior of granular materials in soil mechanics, some limitations need to be acknowledged. DEM often uses idealized grain shapes such as spheres or polyhedra, which may be a strong simplification of the complex geometries and asperities of real soil particles. Consequently, the results obtained from DEM simulations may not fully capture the true contact geometries or force transmission mechanisms in actual soils [28, 29, 40, 60, 199]. Additionally, DEM simulations are computationally expensive, which can limit the sample size, the number of particles, and the duration of the shearing tests. These limitations may affect the accuracy and applicability of the results to real-world scenarios, where soil samples are often much larger in volume and subject to longer periods of loading [193, 198]. Nevertheless, the accuracy of the results can be achieved in assemblies with a limited number of particles as long as the representative elementary volume (REV) complies with the required conditions [148].

Scale effects can arise because the size of the simulated particles and the sample dimensions may not be representative of real soil, resulting in differences in stress distribution and deformation patterns between the simulated model and the actual soil behavior [198–200]. The CD method also assumes rigid, non-breakable particles, whereas real soil particles can undergo breakage and degradation under high-stress conditions. The omission of particle breakage in DEM can lead to an overestimation of soil strength and stiffness, failing to account for the weakening effects observed in actual soil mechanics [8, 201]. Despite these limitations, DEM remains a valuable tool for understanding the fundamental mechanics of granular materials and can provide useful insights when combined with experimental data. However, it is crucial to acknowledge and address these limitations to improve the accuracy and applicability of DEM simulations in soil mechanics research.

CHAPTER 4 ARTICLE 1: Effects of particle size-shape correlations on steady shear strength of granular materials: The case of particle elongation

Journal: International Journal for Numerical and Analytical Methods in Geomechanics.
Published: 17 January 2022.
DOI: https://doi.org/10.1002/nag.3329

Sergio Carrasco[1,2], David Cantor[1,2], Carlos Ovalle*[1,2]

[1] Department of Civil, Geological and Mining Engineering, Polytechnique Montréal, Québec, Canada

[2] Research Institute of Mining and Environment (RIME), UQAT-Polytechnique, Québec, Canada

Corresponding author: carlos.ovalle@polymtl.ca

Abstract: Granular materials often present correlations between particle size and shape due to their geological formation and mechanisms of weathering and fragmentation. It is known that particle shape strongly affects shear strength. However, the effects of shape can be modified by the role the particle plays in a sample given its size. We explore the steady shear strength of samples composed of particles presenting size-shape correlations and we focus on the case of particle elongation in two opposite scenarios: (A) large elongated grains with finer circular grains and (B) large circular grains with elongated finer grains. By means of numerical simulations, we probe the shear strength of samples of varying particle size span from mono to highly polydisperse and particle aspect ratios varying between 1 and 5. We find that the two correlations tested strongly impact the shear strength as particle size span evolves. Microstructural analyses allow us to identify how each correlation affects connectivity and anisotropies linked to the orientation of the particles and load transmission. Decompositions of the stress tensor let us identify the sources of the different mechanical behavior in each correlation and determine the contributions of each particle shape to macroscopic shear strength. This study proves that common small-scaling methods based on truncated or parallel particle size distributions can incur in under/over-estimations of shear strength if particle shapes are not considered in the scaling process.

Keywords: particle size, particle shape, scaling methods, granular materials, discrete-element modeling, elongated particles, shear strength

4.1 Introduction

The mining industry generates large amounts of loose uncompacted granular materials, such as ore stockpiles and mine waste rock dumps that can reach several hundred meter high [1–4]. Physical stability of these large structures must be verified all through engineering designs, because any mass sliding could significantly affect the environment and the mining operation [5,6]. Slope stability of loose granular fills depends on the geometry of the structure, the loading conditions, and the mechanical properties of the granular media [7, 8]. For the latter, mechanical laboratory tests are typically carried out to fit steady-state strength (SSS) parameters for a given failure criterion.

It is well known that normalized SSS (or critical friction angle) of loose granular materials does not depend on packing density, but only on the properties of the grains [9]. Recent works have shown that if the grains have the same shape, SSS does not depend on the particle size distribution (see numerical results in Refs. [10–16], and experimental results in Refs. [17,18]). This finding implies that, since particle shape and grain roughness remain unchanged along with different grain sizes for a given material, representative SSS can be obtained through shearing tests of samples with different particle size distribution (psd). For instance, SSS of very coarse granular materials, such as rockfills or mine waste rock, can be measured through shearing tests of small-scaled samples after removing the coarse (oversized) fraction that cannot be handled in laboratory devices. Among small-scaling methods we can find, for instance, scalping, replacement, or parallel gradation [19–23].

On the other hand, several studies have demonstrated that the SSS strongly depends on particle shape, and materials composed of more angular and/or elongated grains have higher strengths than rounded ones [15, 24–31]. Assemblies of elongated angular particles have high heterogeneity of void size distribution, which enhances grain interlocking and particles tend to slide instead of roll, resulting in higher strength [32, 33].

Particle shape effects could then potentially invalidate small-scaling methods based on altering the psd in granular materials, for instance, composed of rock clasts with strong particle size-shape correlation; i.e., grain shape varies with grain size [34]. For instance, [35] reported a mine waste rock composed of colluvial grains weathered from anisotropic sedimentary rocks, where the coarser the rock aggregate, the more flat the grain shape. This phenomenon was linked to preferential weaknesses in the material due to lamination on large particles. On the contrary, [36] characterized a rockfill material from shale rock where metamorphism induced fine foliation producing more elongated particles as their size was small. In those materials, altering the psd will necessarily change the characteristic shape of the particles, thus affecting the SSS. Therefore, to capture the SSS of prototype coarse materials using small-scaled samples, one should consider not only the size of the grains, but also a representative distribution of particle shapes. However, while particle shape has been largely studied, the effect of shape varying with different particle sizes in a given material remains unclear.

The main objective of this paper is to study the combined effects of particle size and particle shape distributions on the SSS of granular media. In particular, we are interested in the correlation between size and elongation of the grains. By means of two-dimensional discrete-element simulations, we systematically study samples with increasing particle size span linked to the elongation of the grains.

This paper is organized as follows. In Sec. 4.2, we introduce the particle size-shape correlation and the numerical approach to build and shear 2D samples over a large range of grain sizes and grain shape elongations. In Sec. 4.3, we analyze the macromechanical behavior and packing properties in terms of solid fraction and shear strength as a function of shear deformation up to the steady state. In Sec. 4.4, we use microstructural descriptors to characterize the effect of size-shape correlations on particle orientation and connectivity at the SSS. Section 4.5 is focused on the analysis of contributions to strength of micromechanical parameters linked to the geometrical configuration of particles and force transmission mechanisms. We also identify the role of each shape class has on the macroscopic strength. Finally, we conclude and draw perspectives of this work.

4.2 Model material and numerical simulation

Rock masses can produce rounded or elongated particles by weathering or breakage mechanisms based on the genesis, bedding angles, micro fissuring, etc., of the original rock. Then, we need to explore two different scenarios for the correlation between grain size and shape:

- *Case A*: large particles are elongated and smaller grains tend to be rounded.
- *Case B*: large particles are rounded and smaller ones are elongated.

These two cases are modeled in this work by using two-dimensional particles of circular or elongated shapes. The procedure to generate samples for this study is summarized as follows:

1. We define the maximal particle diameter for all our simulations to $d_{max} = 15$ mm,
2. the grain size span S (defined in Eq. (4.1)) allows us to determine a series of samples by fixing the value of S between 0 (monodisperse case) to 0.9 (highly polydisperse case)

in steps of 0.1 (i.e., 10 different samples),

$$S = \frac{d_{max} - d_{min}}{d_{max} + d_{min}}, \tag{4.1}$$

3. using the definition of S, we obtain the minimal particle size diameter d_{min},

4. between d_{min} and d_{max}, we set a particle size distribution, where the probability of having particles with a given surface is constant for all sizes, resulting in the psd shown in Fig. 4.1. For convenience, we discretized the range $[d_{min}, d_{max}]$ in 30 particle sizes,

5. then, we are able to know the number of particles of each size d in the sample. Note that, while for circular grains d is the diameter of the particle, for elongated grains we use the inner diameter as the reference size of the particle, so $d_{in} = d$, as usually done in experimental soil testing (see Fig. 4.2). The inner and outer diameter of an elongated particle define its aspect ratio as follows,

$$\lambda = d_{out}/d_{in}, \tag{4.2}$$

6. using Eq. (3) or (4), depending on the grain size-shape correlation we are studying (case A or B, respectively), we are able to find the corresponding elongation λ for each particle of size d. Note that the limits λ_{min} and λ_{max} were set to 1 (i.e., a circle) to 5, respectively.

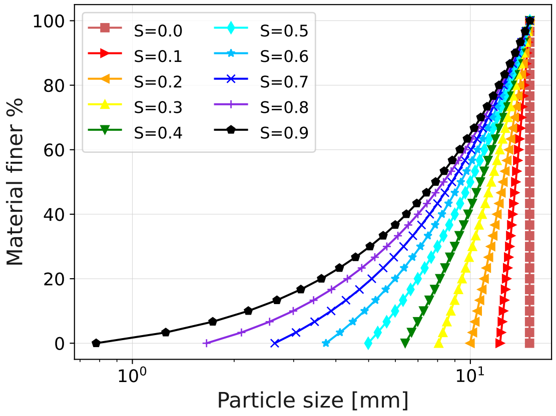

Figure 4.1 Particle size distributions (psd) as a function of particle size span S.

$$\lambda(d) = \lambda_{min} + \frac{d - d_{min}}{d_{max} - d_{min}}(\lambda_{max} - \lambda_{min}). \tag{4.3}$$

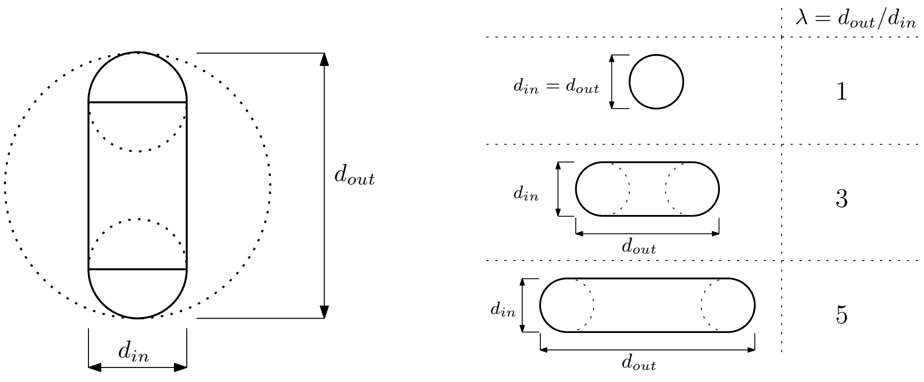

(a) (b)

Figure 4.2 (a) Scheme presenting the inner and outer circles of an elongated particle, and (b) examples of particles with elongation equal to 1, 3, and 5.

$$\lambda(d) = \lambda_{min} + \frac{d_{max} - d}{d_{max} - d_{min}}(\lambda_{max} - \lambda_{min}). \tag{4.4}$$

A distinctive feature of this methodology of particle generation is that it leads to samples in which the grain size span and the particle size distribution can be exactly the same, but the particle shape for each grain varies strongly (see Fig. 4.3).

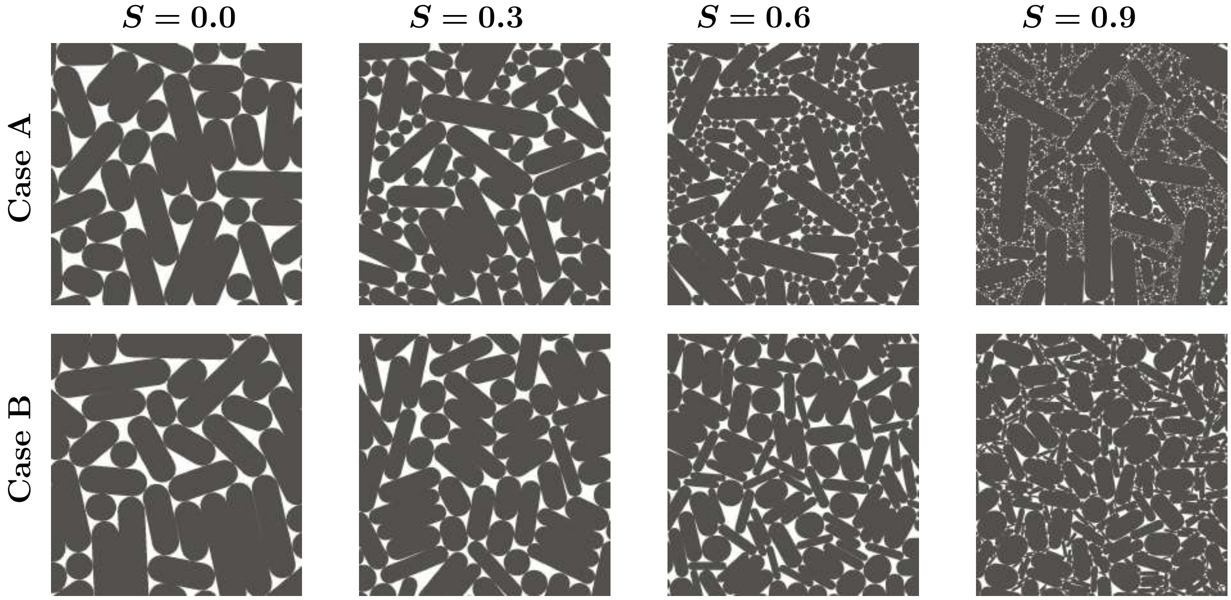

Figure 4.3 Screenshots of samples for case A (top) and case B (bottom) for particle size spans $S = 0.0$, $S = 0.3$, $S = 0.6$, and $S = 0.9$.

Our samples are made up of $N_p \simeq 10\ 000$ particles that are placed in boxes by using an algorithm of deposition based on geometrical rules. We initially compress the samples using an isotropic pressure $P = 10$ kPa via rigid walls around the assemblies up to the point the solid fraction $\nu = A_s/A$, being A_s the area of the grains and A the area of the sample, presents only fluctuations under the 0.1% of the mean value for each sample. Figure 4.3 presents a set of samples for varying S for cases A and B at the end of this compression step. Note that the number of particles used for our tests ensured that the sample height (h_0) respects the ratio $h_0/d_{max} > 20$ for all cases, which is higher than the requirement of geotechnical standards (e.g., $h_0/d_{max} > 6$ ASTM D3080 [37]). Moreover, according to experimental [23, 38] and numerical [39] observations, a ratio of $h_0/d_{max} > 12$ ensures that there is no size effect on the mechanical behavior of sheared granular samples.

We used periodic boundary conditions along the horizontal direction for the shearing tests, implying that any particle or contact crossing the boundary will instantaneously reappear on the corresponding opposite side of the sample (see a scheme of boundary conditions in Fig. 4.4). The periodic boundary allows extending the cell's boundaries to infinity, so the cell works as a coordinate system to locate particle positions. Under this condition, there is no need to apply any external stress or displacements on the lateral boundaries of our models, since the stress/strain field will be simply transmitted through interaction with particles in a neighboring cell [40].

Then, the shearing tests are undertaken by moving both walls along axis 'x' at a constant velocity v while applying load P along the axis 'y'. The shear velocity v is set to follow a quasi-static flow condition, imposed by the inertial number $I = \dot{\gamma}\langle d\rangle\sqrt{\rho/P} \ll 1$, where $\langle d\rangle$ is the average particle diameter, ρ the particle density, and $\dot{\gamma} = v/h_0$, with h_0 being the height of the sample at the beginning of the test. In all our simulations, the inertial number was set to $I = 1 \times 10^{-3}$.

Samples composed of elongated particles often require large deformations to reach a steady state, not only in terms of macroscopic descriptors, but also in terms of particle organization (e.g., particle orientation). For this reason, we sheared our samples up to a cumulated shear strain $\gamma = 400\% = \delta/h_0$, with δ the cumulated displacement of the walls.

Our simulations were performed using the discrete-element approach known as contact dynamics (CD), which considers collections of rigid bodies interacting with unilateral frictional contacts. This strategy employs non-smooth contact laws to iteratively solve contact forces and particle velocities via an implicit time-stepping scheme. For more information on the mathematical framework of the CD method or its implementation, please see Refs. [41–44]. We used the platform LMGC90, which is a free, open-source software for the simulation of discrete mechanical systems in the frame of the CD method [45, 46]. In all the tests, the coef-

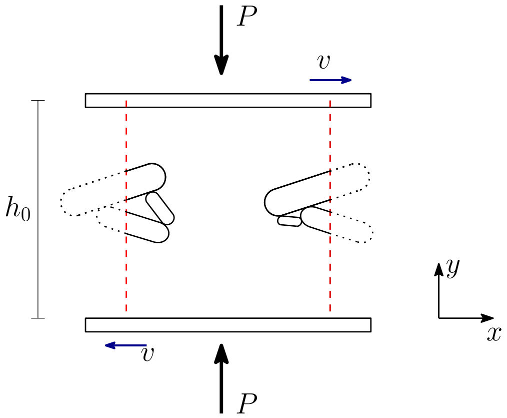

Figure 4.4 Scheme of boundary conditions for the shearing tests. The dashed lines represent the periodic boundary along the 'x' axis.

ficient of friction between particles was set to 0.4 and gravity was neglected. During shearing, particles in contact with the walls were preset to follow the wall displacements by setting the normal and tangential velocities at the contact frame particle-wall to zero. In other words, the interactions wall-particles cannot split apart or slide, but particles are allowed to rotate. This kinematic constraint does not affect the shear response of the sample and effectively transmits the wall's displacements. Videos of the shearing tests can be found in the following link `https://youtu.be/ZX3hl28u4TI`.

4.3 Macroscopic behavior

The macroscopic shearing behavior is characterized using the evolution of the solid fraction ν and the shear strength q/p, being q the deviatoric stress and p the mean pressure of the granular stress tensor σ. This tensor is found using the expression [40, 47–49]

$$\sigma_{ij} = \frac{1}{A} \sum_{\forall c} f_i^c \ell_j^c \tag{4.5}$$

with f the force and ℓ the branch vectors (i.e., the vector joining the center of mass of touching particles at contacts c). We compute $q = (\sigma_1 - \sigma_2)/2$ and $p = (\sigma_1 + \sigma_2)/2$, with σ_1 and σ_2 the principal stresses of σ. Note that $q/p = \sin(\phi)$ at the steady state, with ϕ being the macroscopic friction angle of the material. We characterize the steady state by averaging the different parameters for the last 20% of deformation out of the total 400%. We observed steady values for both ν and q/p as early as $\gamma = 200\%$; however, we applied more deformation to let other structural parameters stabilize, in particular, the orientation of elongated particles (see Fig. 4.5).

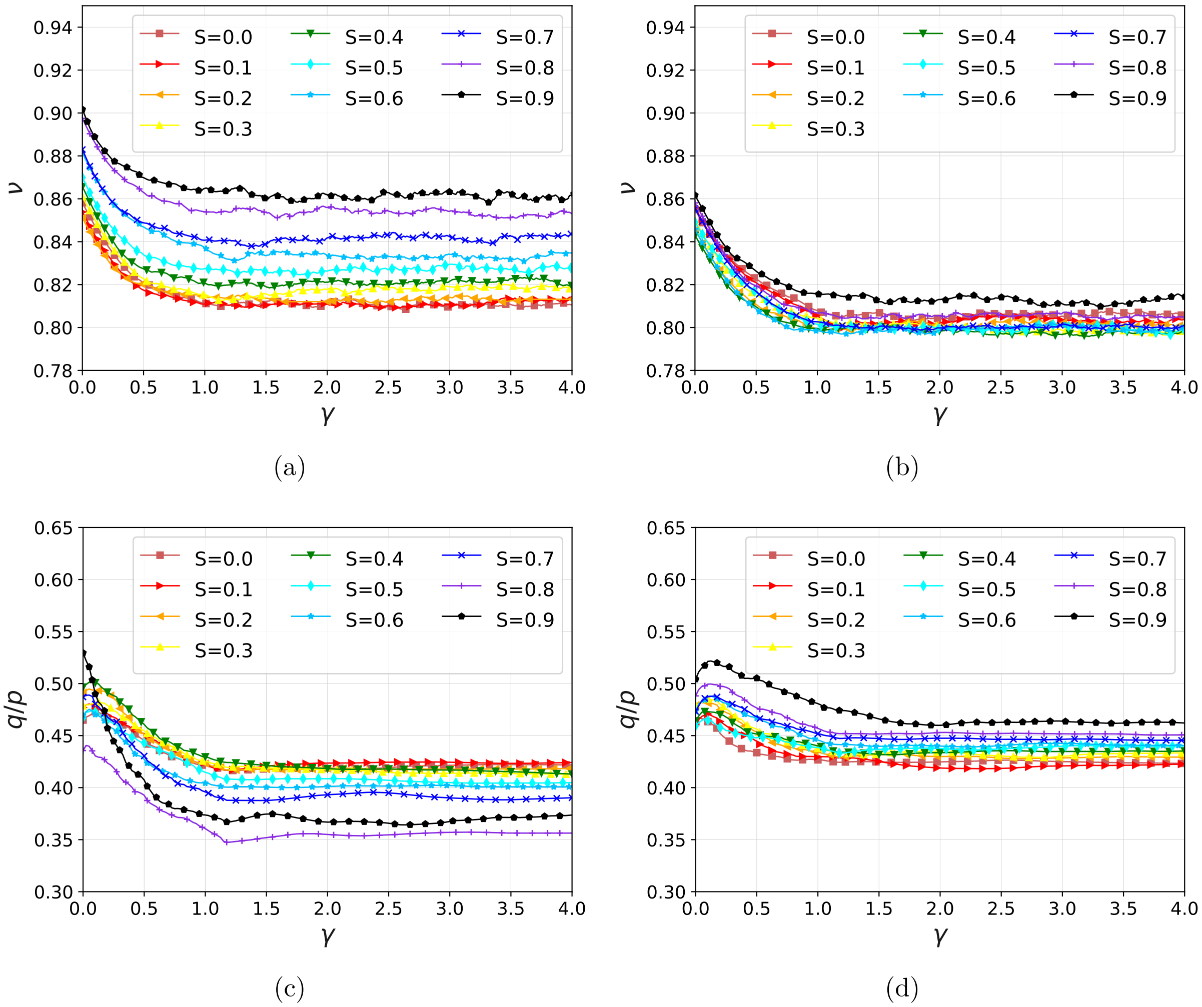

(a) (b)

(c) (d)

Figure 4.5 Evolution of solid fraction ν and the shear strength q/p for case A (left, (a) and (c)) and B (right, (b) and (d)) as a function of the shear deformation γ.

Figure 4.6 shows the evolution of the solid fraction at the steady state as a function of the particle size dispersity S for cases A and B. For case A, we observe that ν gradually increases with S as the smaller rounded grains are capable of filling the pores left by cavities created by larger elongated grains. Surprisingly, case B does not show an analogous behavior. In this case, in which the smaller particles present elongated shapes, the solid fraction seems to be only slightly affected by the grain size distribution and varies with a parabolic trend with a minimal solid fraction of $\nu \simeq 0.8$ for $S = 0.4$ In other words, these samples are unable to develop large enough cavities to allow the smaller elongated particles to fit in. It is only after $S > 0.6$ that the size dispersion can create denser configurations.

In terms of SSS state, Fig. 4.7 presents the evolution of q/p with S for cases A and B. For

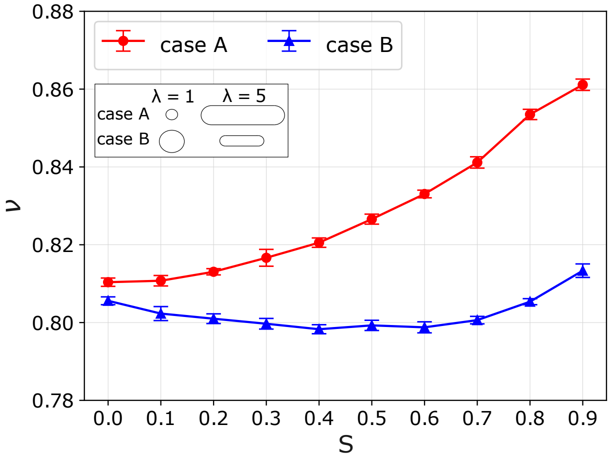

Figure 4.6 Evolution of the solid fraction ν at the steady state as a function of the particle size dispersion S and for cases A and B. Error bars display the standard deviation of the data for the last 20% of deformation.

case A, we observe that the shear strength gradually decreases with S despite the increase in solid fraction we pointed out in the previous figure. For case B, the shear strength barely increases from $q/p \simeq 0.424$ for $S = 0$ to $q/p \simeq 0.46$ for $S = 0.9$. Remarkably, the evolution of density and strength seem uncorrelated for both cases A and B.

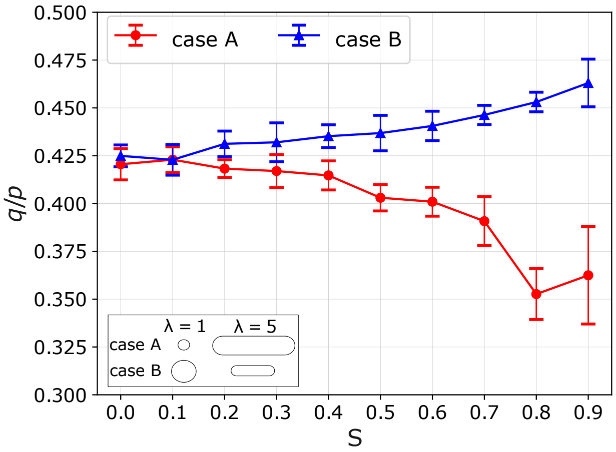

Figure 4.7 Evolution of the shear strength q/p at the steady state as a function of S for cases A and B. Error bars display the standard deviation of the data for the last 20% of deformation.

The evolution of ν and q/p for our set of samples is counterintuitive and diverges from several previous studies showing that particle size distribution does not affect the strength of granular materials. In particular, numerical approaches have shown that elongated particles promote an increase of shear strength [25], and large particles use to bear a larger proportion of the external load than the small particles [27, 50]. That combined size-shape effect does not seem to be reproduced in case A, in which the larger particles are elongated but shear strength turns out to be lower. In turn, for case B, the grain size span effect seems practically negligible when considering the density or the shear strength of the samples.

These results show that particle size-shape correlations deeply modify the SSS and density of granular materials. Foremost, this also suggests that common scaling methods for coarse granular materials should avoid discarding certain granulometric classes only based on particle size, but should also focus on particle shape representativeness on small-scaled samples.

In order to understand the behavior found in our experiments, we need to explore the microstructural characteristics of the samples and the contributions of each size/shape class to the macroscopic strength.

4.4 Microscopic descriptors

We characterize the average configuration of the samples at the steady state by using information related to either the particles or their contacts. Elongated particles under shear deformation tend to rotate, and get aligned along the deformation orientation. Thus, they bear the load along their longest sides. To illustrate this, Fig. 4.8 shows some samples at $\gamma = 400\%$, in which we find most of the elongated particles pointing in the horizontal direction. For circular particles, the rotation is irrelevant. In turn, we observed that the alignment of elongated particles occurs gradually during shear and finds steady values for just slightly larger deformations than those seen for the stabilization of ν and q/p. In particular, we found that the average orientation of elongated grains (i.e., those with $\lambda > 1$) remains between 20° to 30° with respect to the horizontal for all spans S.

On the side of the interactions between particles, we use as an indicator of their connectivity the average number of contacts per particle or *coordination number*, defined as $Z = 2N_c/N_p^*$, being N_c the total number of force-bearing contacts, and N_p^* the effective number of grains transmitting forces. Figure 4.9 shows Z as a function of the particle size span S for cases A and B. While for circular particles Z is expected to remain close to 4, independently of S [51], the inclusion of elongated particles is known to affect the value of Z at the steady state [25, 52]. As the particle size span increases, cases A and B present opposite evolutions with a decrease of Z for assemblies containing big elongated particles (case B) and a drop of connectivity as the samples contain big circular particles (case A). This evolution of Z is not evident in the screenshots presented above. Although for case A, the big elongated particles

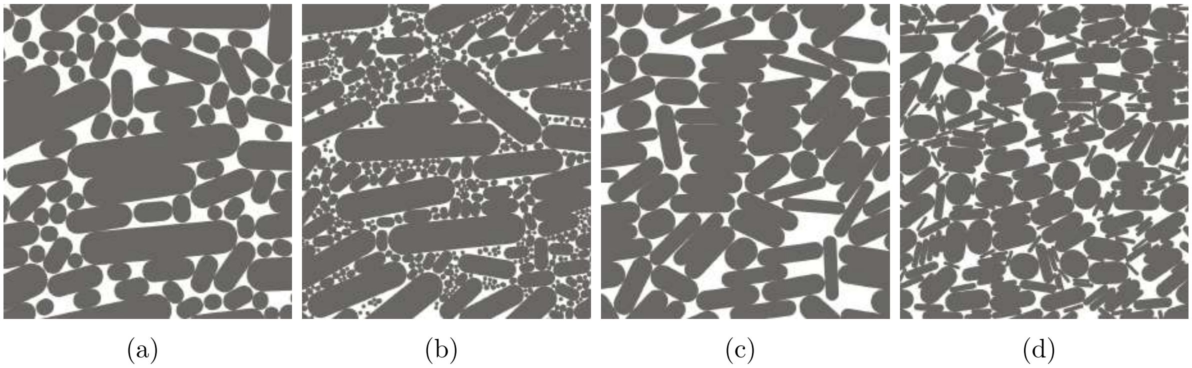
(a) (b) (c) (d)

Figure 4.8 Screenshots of samples at $\gamma = 400\%$ for case A and particle size dispersions $S = 0.4$(a), $S = 0.8$ (b). Figures (c) and (d) show the same particle size dispersions for case B.

seem to gather many small particles around them, those increments of coordination turn out to be only local phenomena are not translated to the macroscale given the fewer large grains in the sample.

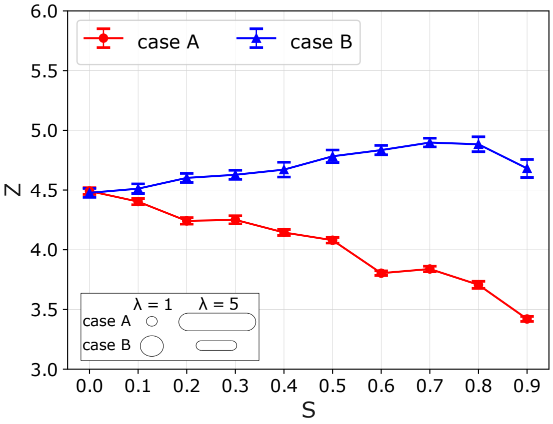

Figure 4.9 Evolution of the coordination number as a function of the particle size span for cases A and B.

To understand these complex compensations of connectivity, we extract the coordination number by particle shape Z_λ (i.e., the average number of contacts per particle of shape λ). Figure 4.10(a) presents the average number of contacts λ in case A. We see that Z_λ increases with λ in agreement with the observation that larger elongated grains are surrounded by many small circular grains with an average of $\simeq$ 13 contacts per particle with elongation $\lambda = 5$. The evolution of Z_λ for case B is more complex (see Fig. 4.10(b)). As λ increases, the increment of connectivity by particle shape changes from a linear trend for $S = 0$, towards a parabolic shape for $S > 0.6$, in which the larger circular grains are not the most connected particles in the assemblies. For those size disperse samples, the most connected shapes seem to have an aspect ratio around $\lambda \simeq 2.5$. For that class of particles, the average number of contacts remains $Z_{\lambda=2.5} \simeq 5$.

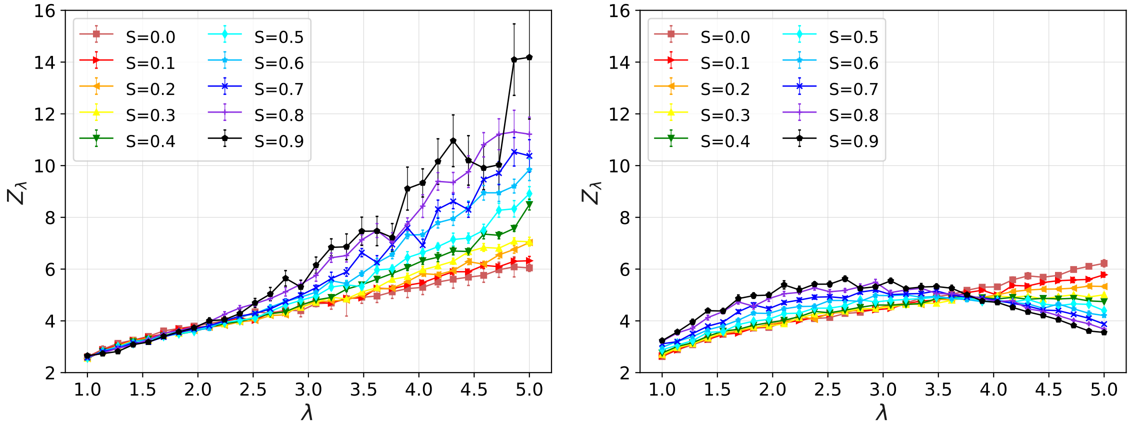

(a)

(b)

Figure 4.10 Evolution of the average contact number by particle elongation λ for case A (a) and case B (b). Error bars present the standard deviation of the data.

Note that these parameters are computed over the particle number of a given shape class. However, the probability of having particles with a given surface is constant for all sizes. In order to identify the contribution of each shape class, it is important to quantify the number of particles excluded from this analysis since bodies having less than two active contacts (i.e., floating particles) are disregarded of the computation pf N_p^*. Figure 4.11(a) shows the evolution of the proportion of floating particles $c_0 = N_p^0/N_p$, with N_p^0 being the number of floating particles, as a function of S for cases A and B. Case A shows c_0 gradually increasing with S as reported in the literature [11, 14, 27]. This phenomenon is supported by a large proportion of smaller particles rattling in the poral space (see Fig. 4.11(b) on the proportion of floating particles by shape class λ). Case B presents an unexpected nonlinear evolution of c_0 with S, first decreasing with S up to $S = 0.6$ and then rapidly increasing again. This is indeed related to the fact that small particles can fill the pores left between larger grains in which they are allowed to rattle. In terms of particle shape class participation, case B shows a compensation mechanism in which, for low values of S, the floating particles mostly belong to the class of smaller grains (see Fig. 4.11(c)). However, as S increases, the small class of particles becomes more active at the load transmission while the bigger particles become less active and rattle.

In order to illustrate the evolution of the floating particle proportions, Figure 4.12 (top)

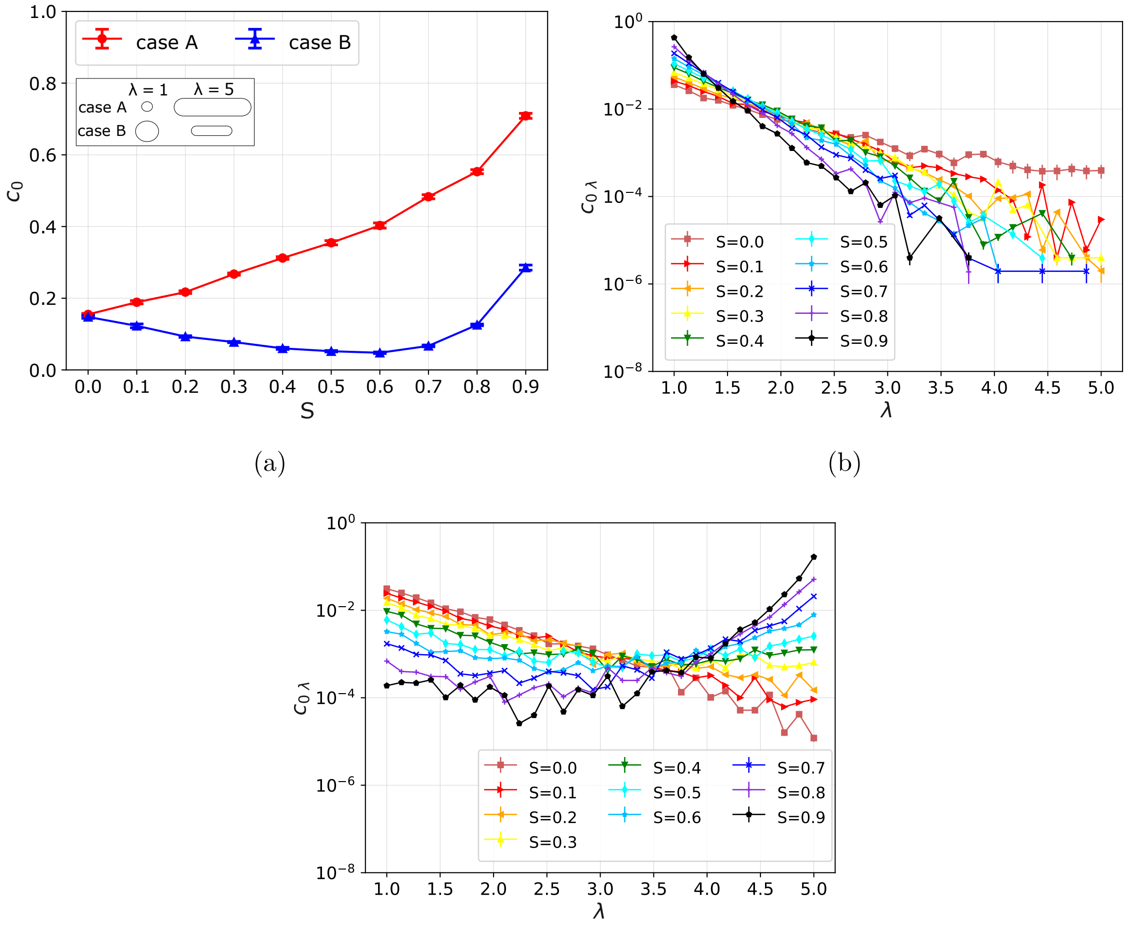

(a)

(b)

(c)

Figure 4.11 (a) Evolution of the proportion of floating particles for cases A and B as a function of the particle size span S. Proportion of floating particles by shape class λ for evolving particle size span S and case A (b) and case B (c). Error bars present the standard deviation of the data.

shows screenshots of the samples in which active particles are shown in black and floating particles in gray for different values of S for cases A and B. At the bottom of the same figure, we present the force transmission within the same samples as bars connecting the center of mass of the particles. The thickness of the bars is proportional to the force intensity at the contacts. We clearly observe the different roles bigger particles have at the force transmission in these samples. While in case A, most of the load is transmitted through the large particles, in case B, more granulometric classes - and in effect, more shape classes - are involved at the force transmission resting importance to the bigger grains.

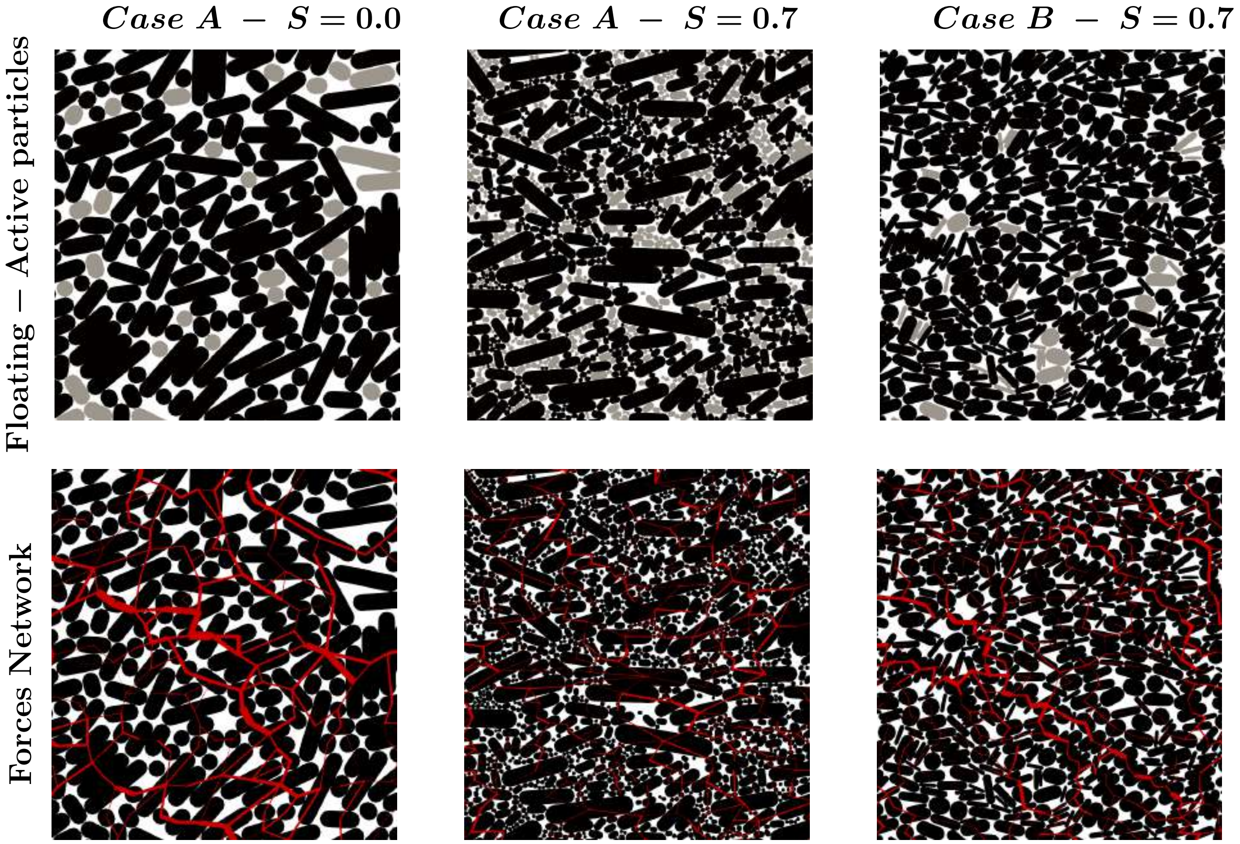

Figure 4.12 (Top) Screenshots highlighting floating particles (gray) and active particles (black), and (Bottom) Force networks for the same set of samples.

4.5 Micromechanical contributions to strength

To understand the drop of strength for case A as a function of S and the apparent independence of strength on S for case B, it is useful to use the decomposition of the granular stress tensor in terms of micromechanical descriptors as proposed by [53].

This approach is based on the fact that contacts, forces, and branch vectors have periodic distributions in space. These distributions can be computed in two different forms. Any interaction between two particles defines a frame having a unitary normal and tangential orientations $\boldsymbol{n}$ and $\boldsymbol{t}$, that allows one to express the contact force as $\boldsymbol{f} = f_n\boldsymbol{n} + f_t\boldsymbol{t}$, with f_n and f_t the normal and tangential contact forces, respectively. On this same frame, the branch vector can be written as $\boldsymbol{\ell} = \ell_n\boldsymbol{n} + \ell_t\boldsymbol{t}$, being ℓ_n and ℓ_t the projections of ℓ on the contact frame. Frame $\{\boldsymbol{n}, \boldsymbol{t}\}$ has been used in many studies to analyze the microstructural properties of regular monosize granular materials. However, for elongated grains, another reference frame has proven to be more adequate [25,54]. The branch vector can alternatively define a frame with $\boldsymbol{n}'$ the unitary vector in the direction of $\boldsymbol{\ell}$, and $\boldsymbol{t}'$ a tangential orientation defined by a 90° counterclockwise rotation of $\boldsymbol{n}'$ (see Fig. 4.13). Using vector $\boldsymbol{n}' = \{n'_x, n'_y\}$, we define the orientation of the branches as $\theta = \mathrm{acos}(n'_x)$.

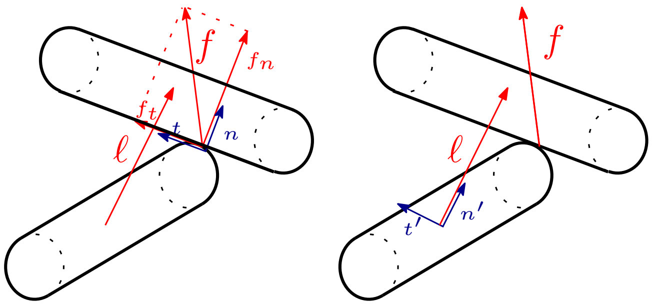

(a) (b)

Figure 4.13 Scheme of (a) the reference frame created by contacts between particles, and (b) the reference frame created by branch vectors.

Standing on the branch frame, we can define the branch orientation probability as

$$P_B(\theta) = N_B(\theta)/N_B, \tag{4.6}$$

where $N_B(\theta)$ is the number of branches pointing at angle θ, and N_B is the total number of active branches in the sample (i.e., branches linked to two grains that carry a non-zero force at the contact). Figure 4.14 presents the distribution P_B for cases A and B and different values of S. These angular distributions can be described using truncated Fourier series as

$$P_B(\theta) = \frac{1}{2\pi}\{1 + a_B \cos 2(\theta - \theta_B)\}, \tag{4.7}$$

with θ_B the preferential orientation of the distribution and a_B the level of anisotropy. Simple fitting of this equation to our data allows us to find these two parameters of the distribution. Note that in case A, the distribution $P_B(\theta)$ is roughly ellipsoidal with an orientation of the major axis varying from $\theta_B \simeq 135°$ for $S = 0$ to $\theta_B \simeq 180°$ for $S = 0.9$. In turn, for case B, the main orientation of the distributions fluctuates but remains close to $\theta_B \simeq 135°$. In the same figures, we plot Eq. (4.7) for each value of S using dashed lines. We remark that the fit is not perfectly matching the discrete distribution of $P_B(\theta)$ for all orientations. In particular, for perpendicular orientations with respect to θ_B, Eq. 4.7 seems to underestimate the value for P_B. When using regular or mono size grains, these first-order Fourier series have proven to capture very well the angular distributions. However, the introduction of elongated grains produces deep perturbations in the microstructure and geometrical organization of the particles.

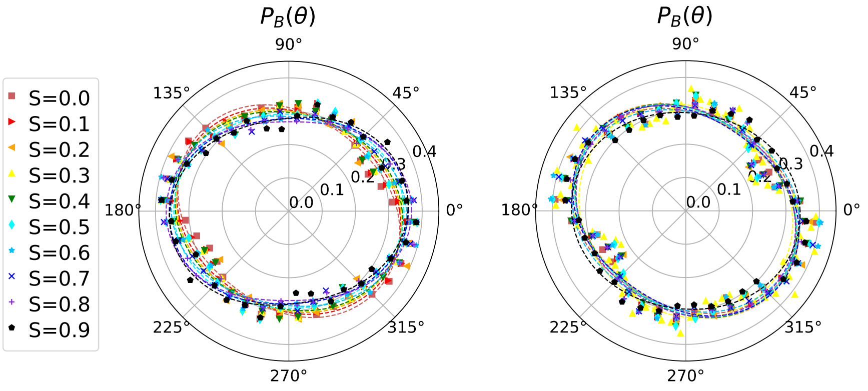

(a) (b)

Figure 4.14 Angular distribution of branch orientations for cases A (a) and B (b) and different values of size dispersion S.

For the analysis of force transmission, note that the total vector force $\boldsymbol{f}$ can be projected on the branch frame letting us find a force acting between the centers of mass of touching grains called *radial force* f'_n, and a shearing equivalent force along with the direction of $\boldsymbol{t}'$, called *ortho-radial force* f'_t. For the radial forces, we can compute their angular distribution as

$$\langle f'_n \rangle(\theta) = \frac{1}{N_B(\theta)} \sum_{B \in \theta} f'_n, \tag{4.8}$$

with $\langle \ldots \rangle$ being the average radial force, and $N_B(\theta)$ the number of branches pointing at angle θ. Similarly, for the ortho-radial forces, the angular distribution can be found as

$$\langle f'_t \rangle(\theta) = \frac{1}{N_B(\theta)} \sum_{B \in \theta} f'_t. \tag{4.9}$$

Figure 4.15 presents these angular distributions for cases A and B and different values of S. These angular force distributions can be described using truncated Fourier series as

$$\langle f'_n \rangle(\theta) = \langle f'_n \rangle \{1 + a_{f_n} \cos 2(\theta - \theta_{f_n})\}, \tag{4.10}$$

and

$$\langle f'_t \rangle(\theta) = -\langle f'_n \rangle \{a_{f_t} \sin 2(\theta - \theta_{f_t})\}, \tag{4.11}$$

with $\langle f'_n \rangle$ the average radial force in the sample, and a_{f_n} and a_{f_t} the radial and ortho-radial force anisotropies, and θ_{f_n} and θ_{f_t} the preferential orientations of each distribution. We observe that for both cases A and B, these radial force distributions are relatively similar, having

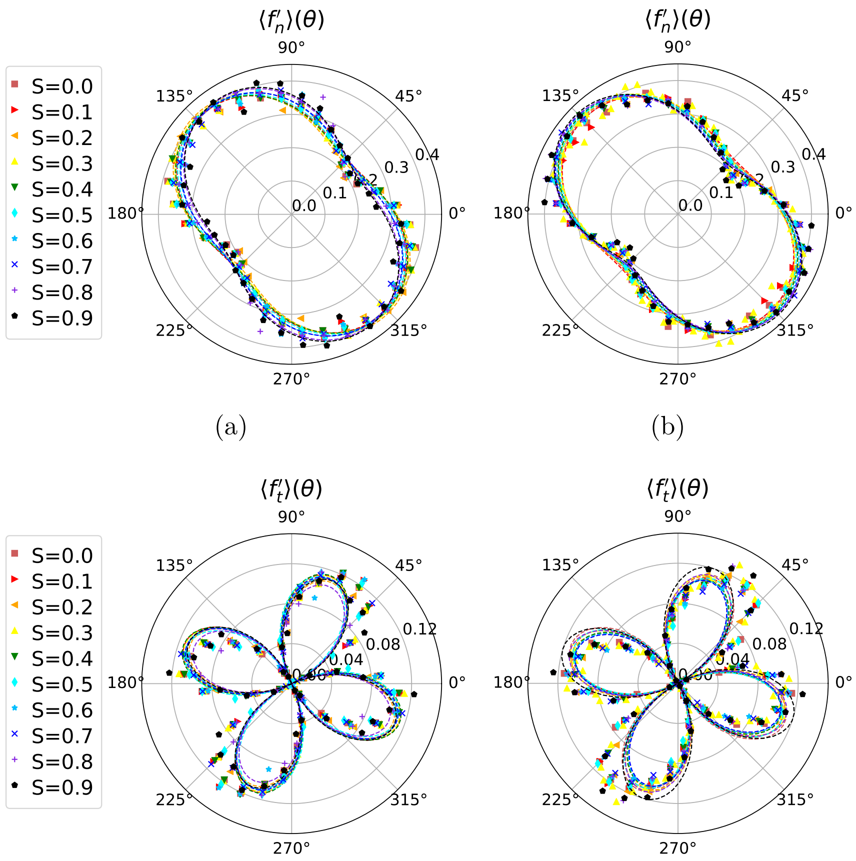

(a) (b)

(c) (d)

Figure 4.15 Angular distribution of radial and ortho-radial force intensities for cases A (a,c) and B (b,d) and different grain size span S.

larger force intensities at orientations $\theta \simeq 135°$. In addition, the distributions seem independent of grain size span S. The ortho-radial force distributions have a four-fold symmetry that is roughly $\pi/2$ periodic. This periodicity is strong among rounded mono-size particles. Nevertheless, as we can observe in Figs. 4.15(c) and (d), elongated particles slightly break this symmetry, so a small mismatch can be observed between the discrete distribution and the Fourier functional forms trying to fit them.

In addition, the analysis of the branch length is more simple since they can be written as $\boldsymbol{\ell} = \ell \boldsymbol{n}'$. Under this definition, the branch vector does not have a tangential component, so only one level of anisotropy is related to this distribution. Figure 4.16 presents the angular distribution of branch lengths for cases A and B and varying particle size span S.

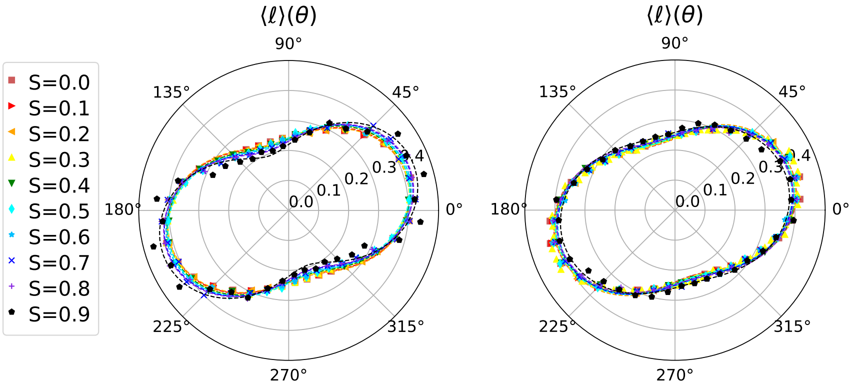

(a) (b)

Figure 4.16 Angular distributions of branch lengths cases A (a) and B (b).

These angular branch distributions can be described as

$$\langle \ell \rangle(\theta) = \langle \ell \rangle\{1 + a_\ell \cos 2(\theta - \theta_\ell)\}, \tag{4.12}$$

with $\langle \ell \rangle$ being the average branch length in the sample, a_ℓ the level of branch length anisotropy, and θ_ℓ the preferential orientation of the distribution. We observe that these distributions change their shape between cases A and B. While for case B, the shape of $\langle \ell \rangle(\theta)$ is evenly ellipsoidal, in case A we observe a larger proportion of branches pointing at $\theta \simeq 20°$, while there is a decrease of branch lengths pointing at the orthogonal orientation $\theta \simeq 110°$.

As mentioned above, simple fitting of the Fourier series to our data allows us to find all the different anisotropies and preferential orientation for the distributions of branch orientations, forces, and branch lengths. Figure 4.17 gathers the values of anisotropies for cases A and B as the particle size span increases. We observe that the anisotropies vary in a large range, spanning from $\simeq 0.1$ for the anisotropy of branch orientations to $\simeq 0.7$ for the ortho-radial force anisotropy.

For case A, the branch orientation anisotropy a_B and the branch length anisotropy a_ℓ seem to increase in similar proportions with S. This behavior is expected since an increase of grain size span also promotes contacts of different shape classes and more variability of branch lengths. On the other hand, the radial and ortho-radial force anisotropies do not seem to be affected by grain size span. For case B, the evolution of anisotropies is quite different. While the branch orientation anisotropy is roughly constant with S, the branch length anisotropy decreases with grain size span. The radial force anisotropy gradually increases with S while the ortho-radial force anisotropy remains almost constant and only increases after $S > 0.7$.

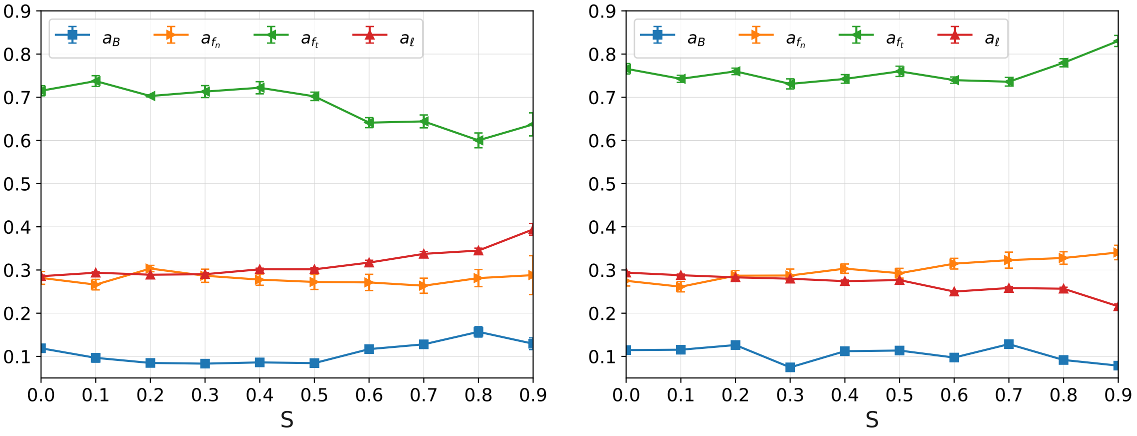

(a) (b)

Figure 4.17 Different anisotropies as a function of the grain size span S for cases A (a) and B (b).

Granular materials in which the particles are regular in size and shape keep particular relations between the main orientations of the different angular distributions, in the form $\theta_{f_n} \simeq \theta_{f_t} \simeq \theta_B$ and $\theta_{\ell'} \simeq \theta_B - \pi/2$. Using these relations, it is possible to deduce a well-known micromechanical expression for the shear strength as [53]

$$q/p \simeq \frac{1}{2}\{a_B + a_{f_n} + a_{f_t} + a_\ell\}. \tag{4.13}$$

However, the alignment of different angular distributions is broken when considering elongated particles and no assumptions can be made on the preferential orientations θ_B, θ_{f_n}, θ_{f_t}, and θ_ℓ. To illustrate this fact, Fig. 4.18 gathers all the preferential orientations as a function of S for cases A and B. Effectively, no evident alignment occurs and the preferential orientations of branches and radial forces. In the meanwhile, the ortho-radial forces and branch main orientations seem independent of S.

Under no assumptions for the preferential orientations of the angular distributions, we can analytically deduce a general expression to describe q/p. Let us write the stress tensor σ_{ij} in integral form as [25]

$$\sigma_{ij} = n_c \int_0^{2\pi} P_B(\theta)\{\langle f'_n\rangle(\theta)n'_i + \langle f'_t\rangle(\theta)t'_i\}\{\langle \ell\rangle(\theta)n'_j\}d\theta, \tag{4.14}$$

where $n_c = N_c/A$ is the surface contact density. This equation is very useful in this form since

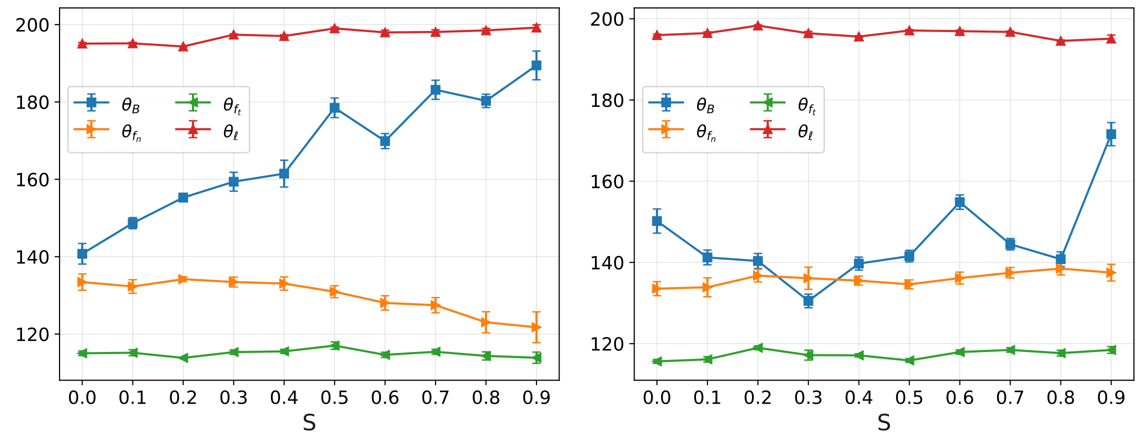

(a) (b)

Figure 4.18 Preferential orientations for the different angular distributions as a function of the grain size span S for cases A (a) and B (b).

it involves the set of angular distributions of branches and forces we previously characterized. Considering that the stresses p and q can also be written as

$$p = \frac{\sigma_{11} + \sigma_{22}}{2}, \tag{4.15}$$

and

$$q = \sqrt{\left\{\frac{1}{2}(\sigma_{11} - \sigma_{22})\right\}^2 + \sigma_{12}^2}, \tag{4.16}$$

we find the different components of σ_{ij} integrating Eq. (4.14), neglecting higher-order terms and crossed products of different anisotropies. We then deduce that the shear strength in the absence of any supposition upon the preferential orientations of the angular distributions as (see Appendix A for a complete derivation of the following expression)

$$q/p \simeq \frac{1}{2}\sqrt{a_B^2 + a_{f_n}^2 + a_{f_t}^2 + a_\ell^2}. \tag{4.17}$$

Despite the apparent similarity of this equation to Eq. (4.13), we should underline the fact that they are fundamentally different, deduced upon different suppositions, and should not be used arbitrarily. They do depend on the microstructure.

In Fig. 4.19, we plot the macroscopic shear strength observed in Fig. 4.7 and its prediction using both Eqs. (4.13) and (4.17) for cases A and B as a function of grain size span S. We see that Eq. (4.13) mismatches the measured shear strength. In turn, Eq. (4.17) fits very well the values of q/p.

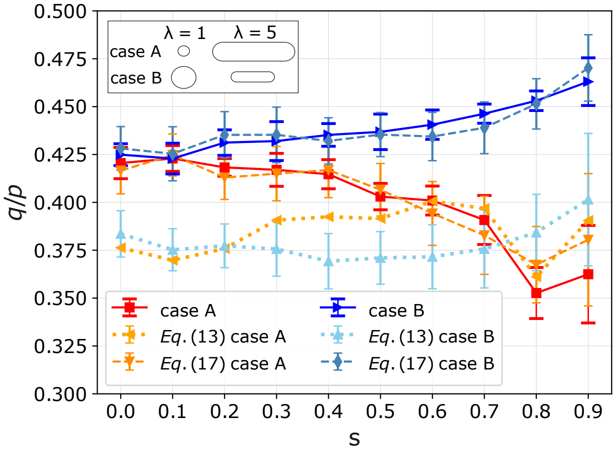

Figure 4.19 Microstructural prediction of the shear strength q/p by means of anisotropies using Eq. (4.13) and Eq. (4.17) along with the macroscopic values measured on Fig. 4.7.

Then, we can understand that the drop of shear strength in case A is mainly supported by the drop of ortho-radial force anisotropy, despite increments of branch length and branch orientation anisotropies. This means that these samples are subjected to larger variations of local shear forces between grains. As shown by [14, 25], the friction mobilization scales with a_{f_t}. So, samples in case A are potentially mobilizing more friction due to kinematic restrictions that prevent the sample from deforming through the rotation of the bodies. In case B, despite a drop of branch length anisotropy, the increments of radial force anisotropy and the slight increment of ortho-radial force anisotropy are compensating mechanisms behind the almost independence of q/p with S, which is in the same vein of many other numerical experiments investigating the shear behavior of regular size and shape grains. This opposite behavior between size-shape correlations A and B suggests that particle shape is a parameter that should be carefully analyzed before proposing a specific particle size scaling method. Moreover, identifying preferential shapes for each particle size can be fundamental for each scaling approach.

Since the role of each particle shape in a given psd can largely vary for a given granular material. We can decompose the total shear strength q/p in order to assess the contributions of each shape class on the shear strength, as [55]

$$q/p = \frac{1}{p}\sum_{i=1}^{N_{sc}} q_i, \tag{4.18}$$

where q_i is the deviatoric component of each size class (sc). The corresponding value q_i is found using the granular stress tensor (Eq. (4.5)), but taking into account only the grains belonging to a particular sc.

Figure 4.20 presents the deviatoric contributions of shape classes to q/p for correlations A and B as a function of the increasing particle size span S. Note that we group the shape classes in intervals of λ of 1. For instance, the subscripts in λ_{1-2} mean that such a value gathers q for the interval of particle elongations $\lambda \in [1, 2)$.

For case A, in which bigger particles are elongated, we expected that circular grains (i.e., λ_{1-2}) contribute relatively less to the shear strength as S increases. This is indeed observed as the value q_i for λ_{1-2} decreases with S. The contributions of shape classes λ_{2-3} and λ_{3-4} also tend to decrease with S. On the other hand, the contributions of elongated big grains λ_{4-5}, remain almost independent of S and, for large grains size spans S, they are indeed the particles contributing the most to the shear strength. These curves help to understand that the drop of q/p in case A is due to a decrease of shear strength provided by the less elongated grains.

For case B, while q_i for λ_{2-3}, λ_{3-4}, and λ_{4-5} are practically independent with S, the contribution of the more circular grains (i.e., λ_{1-2}) gradually increases with S and remains as the main support to the shear strength among all the shape classes.

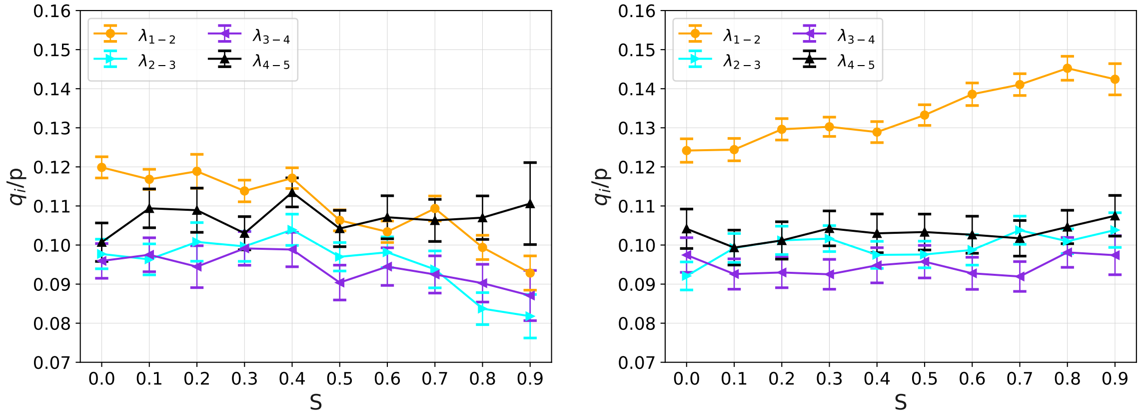

(a)

(b)

Figure 4.20 Decomposition of the deviatoric component of stresses by particle shape λ for cases A (a) and B (b) as a function of the grain size span S.

4.6 Conclusions

In this paper, we studied granular assemblies in which correlations size-shape were considered in two scenarios: particle size distributions having A) large elongated and finer circular grains and B) large circular grains and finer elongated grains. Both correlations can be linked to distinctive geological formations and rock genesis. Our granular assemblies varied in grain size span from monosize to polydisperse systems in which the ratio $d_{max}/d_{min} = 19$, and the elongation of particles reached an aspect ratio of 5. Using a discrete-element approach, we tested these granular assemblies under periodic quasi-static shear conditions up to a cumulated shear deformation $\gamma = 400\%$.

We characterized the steady shear strength and packing fraction as a function of the grain size span. We observed that, contrary to results in literature in which the shear strength turns out to be independent of the grain size span, including size-shape correlations deeply modify the mechanical response of the assemblies. In particular, systems in which larger grains are elongated and small grains are circular show a drop of shear strength as the grain size span increases. The opposite correlation, in which larger grains are circular and small grains are elongated, showed that shear strength barely increases with grain size span. These observations point out the importance of considering the shape of the grains when dealing with scaling methods in geotechnical engineering.

To understand the different behavior in cases A and B, we undertook a microstructural and micromechanical analysis starting with particle orientation and connectivity. We showed that the average number of contacts per grain or coordination number Z evolves similarly to the shear strength. While Z decreases with grain size span for case A, its value slowly increases for case B. This result is counterintuitive given that case A has big elongated grains that are supposed to accommodate many neighboring smaller grains around them. Despite this, since the probability of having particles with a given surface is constant for all sizes, those elongated big grains turn out to be just a few in number and, although locally they have greater connectivity, this is not translated to the averaged value of Z at the macroscale. As shown in the literature, the proportion of floating particles c_0 was found to increase in case A with particle size span. Nonetheless, case B showed a more complex behavior in which the value of c_0 decreases with grain size span and finds a minimum value for $S \simeq 0.6$. In this case, c_0 is able to increase only when the size dispersion is $S > 0.6$. This seems to be related to the capacity of the bigger grains to create large enough voids for the smaller grains to rattle inside. Thus, wider particle size distributions are necessary when materials have a correlation type B in order to increase both their density and proportion of floating particles at the steady state.

Then, employing a decomposition of the granular stress tensor in terms of microstructural anisotropies, we found out that the anisotropy of tangential forces is the main element supporting the variations of q/p at the macroscopic scale. This analysis had to include an extended and detailed characterization of contacts, force intensities, and branch lengths since elongated particles break many of the standard relations and simplifications that can be done when making this microstructural analysis with rounded or mono-sized grains.

Nonetheless, the approach of decomposing q/p - into geometrical and force anisotropies - is still robust enough to link the micro and macro scales. Finally, we also decomposed the deviatoric component of the shear strength q/p by contributions of different shape classes. This analysis showed that larger particles tend to contribute more to the shear strength as the grain size span increases. This is less evident, though, when the larger particles are elongated. Rounded particles seem to have an important role in shear strength independently of their granulometric class. This fact suggests that scaling methods based on truncated psd can add important errors to the estimation of shear strength and parallel scaling methods should certainly not avoid the size-shape correlations when it is such that the large grains are rounded and the small are elongated.

Future studies in this vein should focus on additional elements of realistic correlations in the shape and size properties of geomaterials including angularity, the fracture strength of the grains, or extending this work to three-dimensional grains. It would be also worth analyzing the small strain and peak strength behavior of elongated grains since their orientation may strongly affect the mechanical response. The validation of these numerical observations by means of experimental tests is also needed but seldom seen in the literature. The challenges of experimental testing to reproduce broad grain size distribution while taking into account the shape is still an open issue that calls for large-scale testing or alternative physical approaches.

Acknowledgements

This research benefited from the financial support of the Natural Sciences and Engineering Research Council of Canada (NSERC) [Ref. RGPIN-2019-06118], the Fonds de recherche du Québec - Nature et technologies (FRQNT) through the « Programme de recherche en partenariat sur le développement durable du secteur minier-II » [Ref. 2020-MN-281267] and the industrial partners of the Research Institute on Mines and the Environment (RIME) UQAT-Polytechnique (irme.ca/en). The authors acknowledge Dr. Sandra Linero and Pr. Emilien Azéma for fruitful and supportive discussions. Numerical simulations were made possible through support from Compute Canada under the Resources for Research Groups 2021 program (Project ID 3604). This support is gratefully acknowledged.

Data Availability Statement

The data that support the findings of this study are available from the corresponding author upon reasonable request.

Appendix A: Derivation of the decomposition of shear strength in terms of anisotropies

The granular stress tensor is defined as

$$\sigma_{ij} = \frac{1}{A}\sum_{\forall c} f_i \ell_j, \tag{4.19}$$

with f the contact forces, ℓ the branch vectors, and A the area contained within the walls of the sample. We can alternatively write the stress tensor as contributions of forces and branches (i.e., moments) by angular sectors as

$$\sigma_{ij} = \frac{1}{A}\sum_{\forall \theta_k, k=1}^{N} \sum_{\forall c \in \theta_i} f_i(\theta)\ell_j(\theta), \tag{4.20}$$

where θ_k is a small interval of angle θ, and N is the number of intervals considered between 0 and 2π. The innermost summation can be approximate by considering the number of contacts N_c in the interval θ_i as

$$\sigma_{ij} = \frac{1}{A}\sum_{\forall \theta_k, k=1}^{N} N_c(\theta)\langle f_i\rangle(\theta)\langle \ell_j\rangle(\theta), \tag{4.21}$$

where the distributions of f and ℓ are replaced by their averaged measures $\langle \dots \rangle$ in the interval, and $N_c(\theta)$ is the number of contacts pointing in the same interval k. This last step supposes that no correlation exists between force intensities and branch lengths which is verified in our simulations. Since the contact orientation probability is $P_c(\theta) = N_c(\theta)/N_c$, we can rewrite the stress tensor as

$$\sigma_{ij} = n_c \sum_{\forall \theta_k, k=1}^{N} P_c(\theta)\langle f_i\rangle(\theta)\langle \ell_j\rangle(\theta), \tag{4.22}$$

where the volumetric density of contacts is $n_c = N_c/A$.

For large enough granular assemblies, the discrete sums can be replaced by integrals as follows:

$$\sigma_{ij} = n_c \int_0^{2\pi} P_c(\theta)\langle f_i\rangle(\theta)\langle \ell_j\rangle(\theta)d\theta. \tag{4.23}$$

Note that the distribution of forces and branches can be split in their normal and tangential components since

$$\langle f_i\rangle(\theta) = \langle f_n\rangle(\theta)n_i + \langle f_t\rangle(\theta)t_i, \text{ and} \tag{4.24}$$

$$\langle \ell_j\rangle(\theta) = \langle \ell_n\rangle(\theta)n_j + \langle \ell_t\rangle(\theta)t_j, \tag{4.25}$$

where, n and t are the unitary vectors defining the contact frame between two bodies. Then, the stress tensor can be written as

$$\sigma_{ij} = n_c \int_0^{2\pi} P_c(\theta)\{\langle f_n\rangle(\theta)n_i + \langle f_t\rangle(\theta)t_i\}\{\langle \ell_n\rangle(\theta)n_j + \langle \ell_t\rangle(\theta)t_j\}d\theta. \tag{4.26}$$

On the other hand, the distributions of $P_c(\theta)$, $\langle f_n\rangle(\theta)$, $\langle f_t\rangle(\theta)$, $\langle \ell_n\rangle(\theta)$, and $\langle \ell_t\rangle(\theta)$, can be described using first order Fourier series as

$$P_c(\theta) = \frac{1}{2\pi}\{1 + a_c\cos 2(\theta - \theta_c)\}, \tag{4.27}$$

$$\langle f_n\rangle(\theta) = \langle f_n\rangle\{1 + a_{f_n}\cos 2(\theta - \theta_{f_n})\}, \tag{4.28}$$

$$\langle f_t\rangle(\theta) = -\langle f_n\rangle\{a_{f_t}\sin 2(\theta - \theta_{f_t})\}. \tag{4.29}$$

$$\langle \ell_n\rangle(\theta) = \langle \ell_n\rangle\{1 + a_{\ell_n}\cos 2(\theta - \theta_{\ell_n})\}, \text{ and} \tag{4.30}$$

$$\langle \ell_t\rangle(\theta) = -\langle \ell_n\rangle\{a_{\ell_t}\sin 2(\theta - \theta_{\ell_t})\}, \tag{4.31}$$

where a_c, a_{f_n}, a_{f_t}, a_{ℓ_n}, and a_{ℓ_t} correspond to the level of anisotropy of each distribution and θ_c, θ_{f_n}, θ_{f_t}, θ_{ℓ_n}, and θ_{ℓ_t} are the preferential orientations for each distribution.

Replacing these angular distributions in Eq. (4.26) and arranging terms, we obtain

$$\begin{aligned}\sigma_{ij} = \frac{n_c\langle f_n\rangle\langle \ell_n\rangle}{2\pi}\int_0^{2\pi} & \{1 + a_c\cos 2(\theta - \theta_c)\} \\ & [\{1 + a_{f_n}\cos 2(\theta - \theta_{f_n})\}n_i - \{a_{f_t}\sin 2(\theta - \theta_{f_t})\}t_i] \\ & [\{1 + a_{\ell_n}\cos 2(\theta - \theta_{\ell_n})\}n_j - \{a_{\ell_t}\sin 2(\theta - \theta_{\ell_t})\}t_j]d\theta.\end{aligned} \tag{4.32}$$

In a 2D configuration, the mean pressure p on a granular assembly is defined as

$$p = \frac{\sigma_{11} + \sigma_{22}}{2}, \tag{4.33}$$

and the deviatoric stress q is defined as

$$q = \frac{\sigma_1 - \sigma_2}{2} = \sqrt{\left\{\frac{1}{2}(\sigma_{11} - \sigma_{22})\right\}^2 + \sigma_{12}^2}. \tag{4.34}$$

To find p and q, we need then to find expressions for σ_{11}, σ_{22}, and σ_{12} using Eq. (4.32). The equation to integrate for σ_{11} is:

$$\begin{aligned}\sigma_{11} = \frac{n_c\langle f_n\rangle\langle \ell_n\rangle}{2\pi}\int_0^{2\pi} & [\{1 + a_c\}\{1 + a_{f_n}\}\{1 + a_{\ell_n}\}\cos^2(\theta) \\ & + \{1 + a_c\}\{a_{f_t}\}\{a_{\ell_t}\}\sin^2(\theta) \\ & + \{1 + a_c\}\{1 + a_{f_n}\}\{a_{\ell_t}\}\cos(\theta)\sin(\theta) \\ & + \{1 + a_c\}\{a_{f_t}\}\{1 + a_{\ell_n}\}\sin(\theta)\cos(\theta)]d\theta.\end{aligned} \tag{4.35}$$

For σ_{22}, it is:

$$\begin{aligned}\sigma_{22} = \frac{n_c\langle f_n\rangle\langle \ell_n\rangle}{2\pi}\int_0^{2\pi} & [\{1 + a_c\}\{1 + a_{f_n}\}\{1 + a_{\ell_n}\}\sin^2(\theta) \\ & + \{1 + a_c\}\{a_{f_t}\}\{a_{\ell_t}\}\cos^2(\theta) \\ & - \{1 + a_c\}\{1 + a_{f_n}\}\{a_{\ell_t}\}\sin(\theta)\cos(\theta) \\ & - \{1 + a_c\}\{a_{f_t}\}\{1 + a_{\ell_n}\}\cos(\theta)\sin(\theta)]d\theta.\end{aligned} \tag{4.36}$$

And, for σ_{12}, it is:

$$\begin{aligned}\sigma_{12} = \frac{n_c\langle f_n\rangle\langle \ell_n\rangle}{2\pi}\int_0^{2\pi} & [\{1+a_c\}\{1+a_{f_n}\}\{1+a_{\ell_n}\}\cos(\theta)\sin(\theta) \\ & -\{1+a_c\}\{a_{f_t}\}\{a_{\ell_t}\}\sin(\theta)\cos(\theta) \\ & -\{1+a_c\}\{1+a_{f_n}\}\{a_{\ell_t}\}\cos^2(\theta) \\ & +\{1+a_c\}\{a_{f_t}\}\{1+a_{\ell_n}\}\sin^2(\theta)]d\theta.\end{aligned} \tag{4.37}$$

These integrals yield to the following expressions (for the sake of simplicity, we omit terms of triple products of anisotropies):

$$\begin{aligned}\sigma_{11} = \frac{n_c\langle f_n\rangle\langle \ell_n\rangle}{2} & [1+\frac{a_c}{2}\cos 2(\theta_c)+\frac{a_{f_n}}{2}\cos 2(\theta_{f_n})+\frac{a_{f_t}}{2}\cos 2(\theta_{f_t}) \\ & +\frac{a_{\ell_n}}{2}\cos 2(\theta_{\ell_n})+\frac{a_{\ell_t}}{2}\cos 2(\theta_{\ell_t}) \\ & +\frac{a_c a_{\ell_n}}{2}\cos 2(\theta_c-\theta_{\ell_n})+\frac{a_c a_{f_n}}{2}\cos 2(\theta_c-\theta_{f_n}) \\ & +\frac{a_{\ell_n} a_{f_n}}{2}\cos 2(\theta_{\ell_n}-\theta_{f_n})+\frac{a_{\ell_t} a_{f_t}}{2}\cos 2(\theta_{\ell_t}-\theta_{f_t})\ ]\end{aligned} \tag{4.38}$$

$$\begin{aligned}\sigma_{22} = \frac{n_c\langle f_n\rangle\langle \ell_n\rangle}{2} & [1-\frac{a_c}{2}\cos 2(\theta_c)-\frac{a_{f_n}}{2}\cos 2(\theta_{f_n})-\frac{a_{f_t}}{2}\cos 2(\theta_{f_t}) \\ & -\frac{a_{\ell_n}}{2}\cos 2(\theta_{\ell_n})-\frac{a_{\ell_t}}{2}\cos 2(\theta_{\ell_t}) \\ & +\frac{a_c a_{\ell_n}}{2}\cos 2(\theta_c-\theta_{\ell_n})+\frac{a_c a_{f_n}}{2}\cos 2(\theta_c-\theta_{f_n}) \\ & +\frac{a_{\ell_n} a_{f_n}}{2}\cos 2(\theta_{\ell_n}-\theta_{f_n})+\frac{a_{\ell_t} a_{f_t}}{2}\cos 2(\theta_{\ell_t}-\theta_{f_t})\ ]\end{aligned} \tag{4.39}$$

$$\sigma_{12} = \frac{n_c\langle f_n\rangle\langle \ell_n\rangle}{2}[\frac{1}{2}a_c\sin 2(\theta_c)+\frac{1}{2}a_{f_n}\sin 2(\theta_{f_n})+\frac{1}{2}a_{f_t}\sin 2(\theta_{f_t}) \tag{4.40}$$

$$\begin{aligned} & +\frac{1}{2}a_{c\ell_n}\sin 2(\theta_{\ell_n})+\frac{1}{2}a_{\ell_t}\sin 2(\theta_{\ell_t}) \\ & -\frac{1}{2}a_c a_{f_t}\sin 2(\theta_c-\theta_{f_t})-\frac{1}{2}a_{f_t}a_{\ell_n}\sin 2(\theta_{f_t}-\theta_{\ell_n}) \\ & -\frac{1}{2}a_c a_{\ell_t}\sin 2(\theta_{\ell_t}-\theta_c)-\frac{1}{2}a_{f_n}a_{\ell_t}\sin 2(\theta_{\ell_t}-\theta_{f_n})\ ]\end{aligned} \tag{4.41}$$

Then, an expression for the mean pressure reads as

$$\begin{aligned} p = \frac{\sigma_{11}+\sigma_{22}}{2} = \frac{n_c \langle f_n\rangle \langle \ell_n\rangle}{2} [1 &+ \frac{1}{2} a_c a_{\ell_n} \cos 2(\theta_c - \theta_{\ell_n}) \\ &+ \frac{1}{2} a_c a_{f_n} \cos 2(\theta_c - \theta_{f_n}) \\ &+ \frac{1}{2} a_{\ell_n} a_{f_n} \cos 2(\theta_{\ell_n} - \theta_{f_n}) \\ &+ \frac{1}{2} a_{\ell_t} a_{f_t} \cos 2(\theta_{\ell_t} - \theta_{f_t}) \ ] \end{aligned} \tag{4.42}$$

The expression for the deviatoric stresses is:

$$\begin{aligned} q = \sqrt{\left\{\frac{1}{2}(\sigma_{11}-\sigma_{22})\right\}^2 + \sigma_{12}^2} = \frac{n_c \langle f_n\rangle \langle \ell_n\rangle}{2} \frac{1}{2} [& a_c^2 + a_{f_n}^2 + a_{f_t}^2 + a_{\ell_n}^2 + a_{\ell_t}^2 \\ &+ 2a_c a_{\ell_n} \cos 2(\theta_c - \theta_{\ell_n}) \\ &+ 2a_c a_{\ell_t} \cos 2(\theta_c - \theta_{\ell_t}) \\ &+ 2a_c a_{f_n} \cos 2(\theta_c - \theta_{f_n}) \\ &+ 2a_c a_{f_t} \cos 2(\theta_c - \theta_{f_t}) \\ &+ 2a_{\ell_n} a_{\ell_t} \cos 2(\theta_{\ell_n} - \theta_{\ell_t}) \\ &+ 2a_{\ell_n} a_{f_n} \cos 2(\theta_{\ell_n} - \theta_{f_n}) \\ &+ 2a_{\ell_n} a_{f_t} \cos 2(\theta_{\ell_n} - \theta_{f_t}) \\ &+ 2a_{\ell_t} a_{f_n} \cos 2(\theta_{\ell_t} - \theta_{f_n}) \\ &+ 2a_{\ell_t} a_{f_t} \cos 2(\theta_{\ell_t} - \theta_{f_t}) \\ &+ 2a_{f_n} a_{f_t} \cos 2(\theta_{f_n} - \theta_{f_t}) \ ]^{1/2} \end{aligned} \tag{4.43}$$

It is important to highlight that, so far, these deductions have not made any assumption on the orientation of the angular distributions or correlations between their preferential orientations. Even more, the size of the particles has not intervened in all the Equations above.

If we suppose that the contributions of crossed products of anisotropies is negligible, the expression for the shear strength q/p is simply:

$$\frac{q}{p} = \frac{1}{2}\sqrt{a_c^2 + a_{f_n}^2 + a_{f_t}^2 + a_{\ell_n}^2 + a_{\ell_t}^2}. \tag{4.44}$$

Alternatively, when the angular distributions keep a certain correlations (which is observed in the case of regular and not elongated grains), Eq. (4.32) can be simplified for a given test conditions since $\theta_c \simeq \theta_{f_n} \simeq \theta_{f_t}$ and $\theta_{\ell_n} \simeq \theta_{\ell_t}$, so the shear strength q/p yields to the simpler and more commonly seen expression

$$\frac{q}{p} = \frac{1}{2}(a_c + a_{f_n} + a_{f_t} + a_{\ell_n} + a_{\ell_t}) \tag{4.45}$$

Bibliography

[1] S. Linero, C. Palma, and R. Apablaza, "Geotechnical characterisation of waste material in very high dumps with large scale triaxial testing," in *Proceedings of the 2007 International Symposium on Rock Slope Stability in Open Pit Mining and Civil Engineering.* Australian Centre for Geomechanics, 2007, pp. 59–75.

[2] L. Valenzuela, E. Bard, J. Campaña, and M. E. Anabalón, "High waste rock dumps–challenges and developments," in *Proceedings of 1st International seminar on the management of rock dumps, stockpiles and heap leach pads*, 2008, pp. 65–78.

[3] E. Bard, M. E. Anabalón, and J. Campaña, "Waste rock behavior at high pressures: dimensioning high waste rock dumps," *Elementary mechanics of soil behaviour*, pp. 83–112, 2012.

[4] M. Aubertin, "Waste rock disposal to improve the geotechnical and geochemical stability of piles," in *Proceedings of the 23rd World Mining Congress (WMC 2013), Montreal, Canada*, 2013.

[5] J. C. Santamarina, L. A. Torres-Cruz, and R. C. Bachus, "Why coal ash and tailings dam disasters occur," *Science*, vol. 364, no. 6440, pp. 526–528, 2019.

[6] M. Aubertin, M. Maknoon, and C. Ovalle, "Waste rock pile design considerations to promote geotechnical and geochemical stability," *Canadian Geotechnique – The CGS Magazine: Fall*, vol. 2, no. 3, pp. 44–47, 2021.

[7] J. M. Duncan, S. G. Wright, and T. L. Brandon, *Soil strength and slope stability.* John Wiley & Sons, 2014.

[8] Y. Yang, G. Sun, H. Zheng, and C. Yan, "An improved numerical manifold method with multiple layers of mathematical cover systems for the stability analysis of soil-rock-mixture slopes," *Engineering Geology*, vol. 264, p. 105373, 2020.

[9] J. Biarez, P.-Y. Hicher *et al.*, *Elementary mechanics of soil behaviour: saturated remoulded soils.* Balkema, Rotterdam, 1994.

[10] C. Voivret, F. Radjai, J. Y. Delenne, and M. S. El Youssoufi, "Space-filling properties of polydisperse granular media," *Phys Rev. E*, vol. 76, p. 021301, 8 2007.

[11] C. Voivret, F. Radjai, J. Y. Delenne, and M. S. El-Youssoufi, "Multiscale force networks in highly polydisperse granular media," *Phys. Rev. Lett.*, vol. 102, p. 178001, 2009.

[12] D. M. Wood and K. Maeda, "Changing grading of soil: Effect on critical states," *Acta Geotechnica*, vol. 3, pp. 3–14, 2008.

[13] E. Azéma, S. Linero, N. Estrada, and A. Lizcano, "Shear strength and microstructure of polydisperse packings: The effect of size span and shape of particle size distribution," *Phys. Rev. E*, vol. 96, 8 2017.

[14] D. Cantor, E. Azéma, P. Sornay, and F. Radjai, "Rheology and structure of polydisperse three-dimensional packings of spheres," *Phys. Rev. E*, vol. 98, no. 5, p. 052910, 2018.

[15] S. Linero, E. Azéma, N. Estrada, S. Fityus, J. Simmons, and A. Lizcano, "Impact of grading on steady-state strength," *Géotechnique Letters*, vol. 9, no. 4, pp. 328–333, 2019.

[16] M. Wu, J. Wang, A. Russell, and Z. Cheng, "Dem modelling of mini-triaxial test based on one-to-one mapping of sand particles," *Géotechnique*, vol. 71, no. 8, pp. 714–727, 2021.

[17] G. Li, C. Ovalle, C. Dano, and P.-Y. Hicher, "Influence of grain size distribution on critical state of granular materials," in *Constitutive modeling of geomaterials.* Springer, 2013, pp. 207–210.

[18] J. Yang and X. D. Luo, "The critical state friction angle of granular materials: does it depend on grading?" *Acta Geotechnica*, vol. 13, pp. 535–547, 6 2018.

[19] N. D. Marachi, C. K. Chan, H. B. Seed, and J. M. Duncan, *Strength and Deformation Characteristics of Rockfill Materials*, ser. Report No. TE-69-5. Berkeley, CA: Department of Civil Engineering, University of California, Berkeley, 1969.

[20] R. Verdugo and K. de la Hoz, "Strength and stiffness of coarse granular soils," in *Soil stress-strain behavior: Measurement, modeling and analysis.* Springer, 2007, pp. 243–252.

[21] C. Ovalle, E. Frossard, C. Dano, W. Hu, S. Maiolino, and P. Y. Hicher, "The effect of size on the strength of coarse rock aggregates and large rockfill samples through experimental data," *Acta Mechanica*, vol. 225, pp. 2199–2216, 2014.

[22] C. Ovalle, S. Linero, C. Dano, E. Bard, P.-Y. Hicher, and R. Osses, "Data compilation from large drained compression triaxial tests on coarse crushable rockfill materials," *J. Geotech. Geoenviron.*, vol. 146, p. 06020013, 9 2020.

[23] A. Deiminiat, L. Li, F. Zeng, T. Pabst, P. Chiasson, and R. Chapuis, “Determination of the shear strength of rockfill from small-scale laboratory shear tests: A critical review,” *Adv. Civ. Eng.*, vol. 2020, pp. 1–18, 11 2020.

[24] G.-C. Cho, J. Dodds, and J. C. Santamarina, “Particle shape effects on packing density, stiffness, and strength: Natural and crushed sands,” *J. Geotech. Geoenviron.*, vol. 132, no. 5, pp. 591–602, 2006.

[25] E. Azéma and F. Radjai, “Stress-strain behavior and geometrical properties of packings of elongated particles,” *Phys. Rev. E*, vol. 81, no. 5, p. 051304, 2010.

[26] T. Matsushima and C. S. Chang, “Quantitative evaluation of the effect of irregularly shaped particles in sheared granular assemblies,” *Granular matter*, vol. 13, no. 3, pp. 269–276, 2011.

[27] D. H. Nguyen, E. Azéma, p. Sornay, and F. Radjai, “Effects of shape and size polydispersity on strength properties of granular materials,” *Phys. Rev. E*, vol. 91, p. 032203, 3 2015.

[28] F. N. Altuhafi, M. R. Coop, and V. N. Georgiannou, “Effect of Particle Shape on the Mechanical Behavior of Natural Sands,” *J. Geotech. Geoenviron.*, vol. 142, no. 12, p. 04016071, 2016.

[29] Y. Xiao, L. Long, T. Matthew Evans, H. Zhou, H. Liu, and A. W. Stuedlein, “Effect of particle shape on stress-dilatancy responses of medium-dense sands,” *J. Geotech. Geoenviron.*, vol. 145, p. 04018105, 2019.

[30] D. Sarkar, M. Goudarzy, and D. König, “An interpretation of the influence of particle shape on the mechanical behavior of granular material,” *Granular Matter*, vol. 21, 8 2019.

[31] M. Q. Xu, N. Guo, and Z. X. Yang, “Particle shape effects on the shear behaviors of granular assemblies: irregularity and elongation,” *Granular Matter*, vol. 23, 5 2021.

[32] J. Yang and L. M. Wei, “Collapse of loose sand with the addition of fines: The role of particle shape,” *Géotechnique*, vol. 62, pp. 1111–1125, 12 2012.

[33] A. A. Peña, R. García-Rojo, and H. J. Herrmann, “Influence of particle shape on sheared dense granular media,” *Granular Matter*, vol. 9, pp. 279–291, 6 2007.

[34] Y. Deng, Y. Yilmaz, A. Gokce, and C. S. Chang, “Influence of particle size on the drained shear behavior of a dense fluvial sand,” *Acta Geotechnica*, pp. 1–18, 2021.

[35] S. Linero, S. Fityus, J. Simmons, A. Lizcano, and J. Cassidy, “Trends in the evolution of particle morphology with size in colluvial deposits overlying channel iron deposits,” in *EPJ Web of Conferences*, vol. 140. EPJ Web of Conferences, 2017, p. 14005.

[36] C. Ovalle and C. Dano, “Effects of particle size–strength and size–shape correlations on parallel grading scaling,” *Géotechnique Letters*, vol. 10, no. 2, pp. 191–197, 2020.

[37] ASTM, “D3080–04: Standard test method for direct shear test of soils under consolidated drained conditions,” American Society for Testing and Materials, West Conshohocken, PA, Standard, 2004.

[38] A. B. Cerato and A. J. Lutenegger, “Specimen size and scale effects of direct shear box tests of sands,” *Geotech. Test. J.*, vol. 29, no. 6, pp. 507–516, 2006.

[39] P. Schuhmacher, “Rhéologie des écoulements granulaires : variables internes et effets d’échelle,” Thèse de doctorat, Université Montpellier, 2016.

[40] F. Radjai and F. Dubois, *Discrete-element modeling of granular materials.* Wiley-Iste, 2011.

[41] J. J. Moreau, “Unilateral contact and dry friction in finite freedom dynamics,” in *Nonsmooth mechanics and Applications.* Springer, 1988, pp. 1–82.

[42] M. Jean and J. J. Moreau, “Unilaterality and dry friction in the dynamics of rigid body collections,” in *1st Contact Mechanics International Symposium.* 1st Contact Mechanics International Symposium, 1992, pp. 31–48.

[43] F. Radjai and V. Richefeu, “Contact dynamics as a nonsmooth discrete element method,” *Mechanics of Materials*, vol. 41, no. 6, pp. 715–728, 2009, advances in the Dynamics of Granular Materials.

[44] F. Dubois, V. Acary, and M. Jean, “The contact dynamics method: A nonsmooth story,” *Comptes Rendus Mécanique*, vol. 346, no. 3, pp. 247–262, 2018.

[45] F. Dubois, M. Jean, and et al, “LMGC90 wiki page,” https://git-xen.lmgc.univ-montp2.fr/lmgc90/lmgc90_user/wikis/home, 2021, [Online; accessed 18-Oct-2021].

[46] F. Dubois, M. Jean, M. Renouf, R. Mozul, A. Martin, and M. Bagnéris, “LMGC90,” in *10e colloque national en calcul des structures.* 10e colloque national en calcul des structures, 2011, p. 8 p.

[47] R. J. Bathurst and L. Rothenburg, “Micromechanical aspects of isotropic granular assemblies with linear contact interactions,” *J. Appl. Mech.*, vol. 55, pp. 17–23, 1988.

[48] B. Andreotti, Y. Forterre, and O. Pouliquen, *Granular media: between fluid and solid.* Cambridge University Press, 2013.

[49] F. Nicot, N. Hadda, M. Guessasma, J. Fortin, and O. Millet, “On the definition of the stress tensor in granular media,” *International Journal of Solids and Structures*, vol. 50, no. 14-15, pp. 2508–2517, 2013.

[50] C. Ovalle, C. Voivret, C. Dano, and P.-Y. Hicher, “Population balance in confined comminution using a physically based probabilistic approach for polydisperse granular materials,” *Int. J. Numer. Anal. Methods Geomech.*, vol. 40, no. 17, pp. 2383–2397, 2016.

[51] J.-N. Roux, “Geometric origin of mechanical properties of granular materials,” *Phys. Rev. E*, vol. 61, pp. 6802–6836, Jun 2000.

[52] M. Boton, E. Azéma, N. Estrada, F. Radjai, and A. Lizcano, “Quasistatic rheology and microstructural description of sheared granular materials composed of platy particles,” *Phys. Rev. E*, vol. 87, p. 032206, Mar 2013.

[53] L. Rothenburg and R. J. Bathurst, “Analytical study of induced anisotropy in idealized granular materials,” *Géotechnique*, vol. 39, no. 4, pp. 601–614, 1989.

[54] D. Cantor, C. Ovalle, and E. Azéma, “Microstructural origins of crushing strength for inherently anisotropic brittle materials,” *Int. J. Solids Struct.*, vol. 238, p. 111399, 2022.

[55] D. Cantor, E. Azéma, and I. Preechawuttipong, “Microstructural analysis of sheared polydisperse polyhedral grains,” *Phys. Rev. E*, vol. 101, p. 062901, Jun 2020.

CHAPTER 5 ARTICLE 2: Shear strength of angular granular materials with size and shape polydispersity

Journal: OpenGeomechancis.
Published: 05 September 2023.
DOI: https://doi.org/10.5802/ogeo.15

Sergio Carrasco[1,2], David Cantor[1,2], Carlos Ovalle*[1,2], Paula Quiroz-Rojo[1,2,3]

[1] Department of Civil, Geological and Mining Engineering, Polytechnique Montréal, Québec, Canada

[2] Research Institute of Mining and Environment (RIME), UQAT-Polytechnique, Québec, Canada

[3] LMGC, Université de Montpellier, CNRS, Montpellier, France

Corresponding author: carlos.ovalle@polymtl.ca

Abstract: Shear strength characterization of coarse granular materials often requires modifying the original material in order to fit samples in standard testing devices. This is done, however, at the expense of changing the particle size distribution (psd), employing scaling-down techniques such as parallel grading or scalping methods. Such procedures hide, nevertheless, another challenge. As a given particle size can present a characteristic grain shape, altering the grain size distribution can strongly modify the distribution of grain shapes. While the effects of grain shape on shear strength have been vastly covered in the literature, the effect of having different shapes along grain sizes has yet to be systematically assessed and understood. This article explores the critical shear strength of samples composed of particles with size-shape correlations using 2D discrete element simulations. Two cases of particle shape variability across grain sizes are studied: (1) the sharpness of grains' corners - modeled via the number of sides of regular polygons - and (2) the geometric irregularity of grains - where the corners of a polygon are not necessarily evenly spaced. The effects of these geometrical properties on the shear strength are assessed through a series of numerical simple shearing tests up to large levels of deformation. We find that granular materials presenting different number of sides across grain sizes can strongly modify their mechanical response depending on the grain-size correlation. On the contrary, grain shape irregularity turns out not to have a major effect on the critical shear strength. Microstructural analyses allow us to identify how each correlation affects load transmission mechanisms between grains, and the contribution of each grain shape class to the macroscopic shear strength. This work shows that particle sizes are not the only sample descriptor to consider when applying scaling-down techniques. It is equally key to characterize particle shapes across grain sizes to capture the material's mechanical response adequately.

Keywords: shear strength, particle shape, polydispersity, discrete-element modeling, grain size distribution

5.1 Introduction

Stability analyses of earth fills composed of coarse granular materials, such as rockfill dams, mine waste rock dumps, railway ballast, or gravel dikes, require to characterize the shear strength properties of oversized particles that often do not fit in laboratory devices [1–7]. In such cases, small-scaled samples using scalping or parallel grading techniques are usually prepared to carry out shearing tests [2,8–10]. Although numerous research has been reported about the effect of these techniques on the shear strength of granular materials, the results widely vary up to the point of being contradictory. While some studies have indicated that shear strength decreases with grain size [2, 11–14], others have shown the opposite behavior [15–18]. The sources of this apparent contradiction are presumably found in several sample and testing characteristics, and inherent material properties.

Firstly, concerning sample and testing characteristics, comparing different materials is challenging since neither clear standards have been formulated to assess the relative density of oversized materials nor have authors systematically reported whether their samples are prepared in dense or loose conditions. Therefore, some studies might have used dense samples and reported the peak strength, while others might have tested loose materials and obtained the critical strength. Moreover, using the relative density as a basis for shear strength comparison is not the most appropriate because different particle size distribution (psd) have different density limits [19, 20]. In addition, materials can undergo grain crushing at certain stress levels depending on their particle strength, which implies lower dilatancy and, thus, a reduced peak strength [21–23]. Finally, the aspect ratio between the maximum particle size and the characteristic sample size, which is known to have a significant impact on the strength [24–26].

Secondly, concerning inherent material properties, altering the psd when preparing small-scaled samples might affect the packing density and, consequently, the peak strength. On the other hand, several works have shown that if all the grains have the same characteristic shape and surface roughness, the critical strength does not depend on the psd [27–35].

However, small scaling techniques could also alter the characteristic grain shape of the material, which would strongly affect the critical strength [34, 36–41]. This phenomenon has been confirmed by recent studies showing that particle shape could be correlated with grain size due to sedimentary lamination or fine foliation induced by metamorphism in some rockfill materials [42–45]. Shearing tests over those materials have shown significant differences in critical shear strength after applying small-scaling techniques. Therefore, representative small-scaling sample preparation based only on reducing characteristic grain size needs to be revised if the particle shape distribution changes.

The main objective of this paper is to study the effects of grain size-shape correlations and psd on the critical strength of granular materials. This research extends the work of [46], which presented the effect of particle elongation correlated with grain sizes by introducing a comprehensive analysis of the effects of grain angularity and grain geometric irregularity. We use discrete element modeling (DEM) of 2D granular samples over a large range of psd and analyze the results regarding the macromechanical behavior under critical state conditions. We also isolate the contribution of each family of grain shape and size to the total shear strength, allowing us to describe and understand the effect of particle characteristics on the critical strength.

Is there any particular granulometric class that mainly backs up the macroscopic shear strength? Are grains with sharper corners allowing samples to develop more shear strength independently of their size? What are the main grain geometrical characteristics controlling shear strength that scaling methods should rely on? This research aims to shed light on this set of questions.

5.2 Model material and numerical simulation

We create 2D numerical samples in which grain sizes vary widely from mono-size to highly polydisperse configurations. As grain sizes vary, we also consider two cases of grain shape-size correlations detailed in the following.

5.2.1 Grain shape size correlations

Case 1

In this case, we consider grains whose corners can be more or less sharp, being able to develop, respectively, more or less shear strength as shown in the literature [47, 48]. This is achieved by varying the number of sides n_s of regular polygons. This parameter is lower bound to 3, which corresponds to a regular triangle, and as n_s increases, polygons gradually approach the shape of a disk. We choose to vary n_s in the range $[3, 64]$ as shown in Figure 5.1, giving us the possibility to explore two different size-shape correlations:

- ***Case 1A:*** large grains have large n_s while small have sharper corners.
- ***Case 1B:*** large grains have sharper corners while small ones have large n_s.

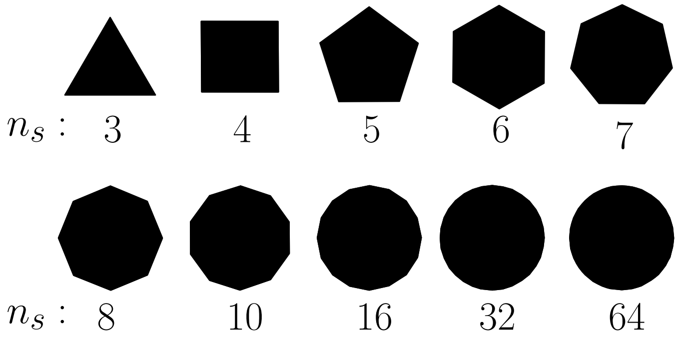

Figure 5.1 Scheme presenting the evolution of corner sharpness, being n_s the number of sides of regular polygons.

Case 2

In the second case, we explore another component of grain geometries: shape irregularity of a polygon ($n_s = 5$). While the vertices are evenly separated for a regular polygon, we can model geometries in which the vertices' separation varies as a function of a level of irregularity, as proposed by [38]. We choose to use pentagons for this part of the study since numerous numerical studies have reported their characterization using DEM simulations for mono-size pentagon assemblies [38, 48], providing a reference point for our simulations. For a regular pentagon, the angular position of each vertex can be defined by $\theta^k = \theta_0 + 2k\pi/5$, where θ_0 is the position of the first vertex from the horizontal, and k is an integer varying from 1 to 5. We can alternatively modify the geometry of the regular pentagon by changing the angular position of vertices k as:

$$\theta^k = \theta_0 + k\frac{2\pi}{5} \pm \frac{\pi}{5} r_{[0,\delta]} \ , \tag{5.1}$$

being $r_{[0,\delta]}$ a random variable in the range $[0, \delta]$, δ is the degree of irregularity that can vary from 0 to 1, and the ± sign is randomly chosen for each vertex; see Figure 5.2.

Similarly to case 1, the geometrical irregularity of pentagonal grains can be studied in two opposite situations:

- ***Case 2A:*** large grains are irregular pentagons while small ones are regular.
- ***Case 2B:*** large grains are regular pentagons while small ones are irregular.

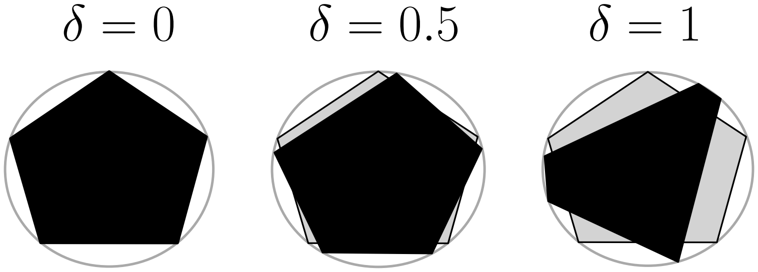

Figure 5.2 Scheme presenting the evolution of grain geometric irregularity as a function of parameter δ, based on [38]

5.2.2 Granular sample generation

The construction of numerical samples follow the following procedure:

1. the maximum circumscribing particle diameter $d_{\mathrm{max}} = 15$ mm is defined for all the simulations (note that a polygonal grain size is defined by the diameter of the circle that circumscribes the polygon),
2. the number of samples is fixed using the grain size span S (defined in Eq. 5.2) varying from 0 (monodisperse sample) to 0.9 (highly polydisperse sample) in steps of 0.1 (i.e., ten different samples per case),

$$S = \frac{d_{\mathrm{max}} - d_{\mathrm{min}}}{d_{\mathrm{max}} + d_{\mathrm{min}}} \ , \tag{5.2}$$

3. minimal particle size d_{min} is calculated by means of S for each sample,
4. the range d_{min} to d_{max} is discretized in $N_f = 10$ particle sizes and a uniform psd is set. This means that the surface of a given particle size class is constant for all sizes, resulting in the psd shown in Figure 5.3,
5. depending on the size-shape correlation (i.e., Case 1 or 2), we are able to find the corresponding shape for each particle of size d.

The last step of the procedure is performed using the following set of rules:

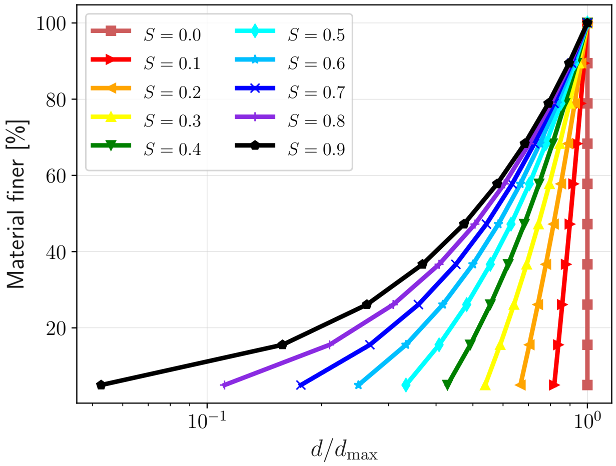

Figure 5.3 Particle size distribution as a function of particle size span S, where each particle diameter d is normalized by the maximum particle diameter $d_{\max}$.

- For Case 1, one of the shapes in the set $n_s \in [3, 4, 5, 6, 7, 8, 10, 16, 32, 64]$ is assigned to each grain size.
- For Case 2, the following equations characterize the level of irregularity as a function of the relative grain diameter in the assembly d_r, defined as:

$$d_r = \frac{d - d_{\min}}{d_{\max} - d_{\min}} \ . \tag{5.3}$$

  Note that this reduced diameter varies between 0 and 1, as the grain belongs to either the smaller or larger classes of particles in the assembly. When the large grains are the most irregular ones the irregularity is equal to $\delta(d) = d_r$ (Case 2A), and when the large grains are the most regular ones, $\delta(d) = 1 - d_r$ (Case 2B).

Finally, Figure 5.4 shows the significant advantage of this generation routine which allows creating assemblies with the same psd, yet the particle shape for each grain size varies significantly. In terms of Wadell's circularity, defined as $\phi_w = c/C$, being c the perimeter of a circle of the same area as the plane figure, and C is the actual perimeter of the plane figure [49], Case 1 shows ϕ_w evolving from 0.77 for triangles to 0.99 for polygons with 64 sides. In Case 2, ϕ_w varies from 0.93 for regular pentagons to ~ 0.905 for the most irregular pentagon. To complement the description of psd, we compared the grain size span parameter S, with the D_{50}, the uniformity coefficient ($C_u = D_{60}/D_{10}$), and the ratio between the maximum to minimum particle sizes ($R_D = d_{\max}/d_{\min}$). These parameters are presented in Table 6.1 below.

Table 5.1 Parameters $d_{\max}$, $d_{\min}$, R_D, D_{50} and C_u for different values of S.

S	$d_{\max}$ $[mm]$	$d_{\min}$ $[mm]$	R_D	D_{50} $[mm]$	C_u
0	15.0	15.0	1.0	15.0	1.0
0.1	15.0	12.3	1.2	13.7	1.1
0.2	15.0	10.0	1.5	12.5	1.2
0.3	15.0	8.1	1.9	11.5	1.4
0.4	15.0	6.4	2.3	10.7	1.6
0.5	15.0	5.0	3.0	10.0	1.8
0.6	15.0	3.8	4.0	9.4	2.2
0.7	15.0	2.7	5.7	8.8	2.6
0.8	15.0	1.7	9.0	8.3	3.2
0.9	15.0	0.8	19.0	7.9	4.2

5.2.3 DEM simulation

The numerical samples are tested in order to characterize their shear strength properties using a discrete element method known as contact dynamics (CD). The CD method is an approach capable of simulating collections of rigid bodies interacting with frictional contacts. This strategy uses a non-smooth definition of contact laws, which is ideal for dealing with bodies of varied shapes without the need to define stiffness or damping parameters at the variety of contacts that can occur between bodies. In Figure 5.5, we can notice that in the case of polygons in contact, two different types of interactions can occur: (1) side-vertex (sv) and (2) side-side (ss). A sv contact is a single corner of a polygon contacting a side of a neighboring particle. A ss contact between two rigid polygons can be defined by two point contacts on the common side representing the tangential line [50]. Despite this numerical treatment of a ss contact, the choice of their loci is inconsequential and only the sum of the two contact forces has a mechanical sense. For more information about the mathematical framework and numerical implementation of the CD method, see references [51–54].

Each numerical sample is built with $N_p \simeq 10\ 000$ particles, which are placed layer-by-layer in boxes by mean of a potential energy deposition protocol as described in Ref. [55–57]. This approach is an efficient strategy to achieve relatively dense random packing configurations without the need of time consuming dynamic simulations. The samples are initially compressed using an isotropic pressure $P = 10$ kPa using rigid walls around the grain assembly up to a stable solid fraction $\nu = A_s/A$, where A_s is the total surface area of grains and A the containing box area. Moreover, all our tests ensured that the sample height (h_0) respects the ratio $h_0/d_{\max} > 10$ to avoid size effects on the mechanical behavior [26, 58, 59].

As shown in Figure 5.6, simple shearing tests are performed by moving the upper and lower

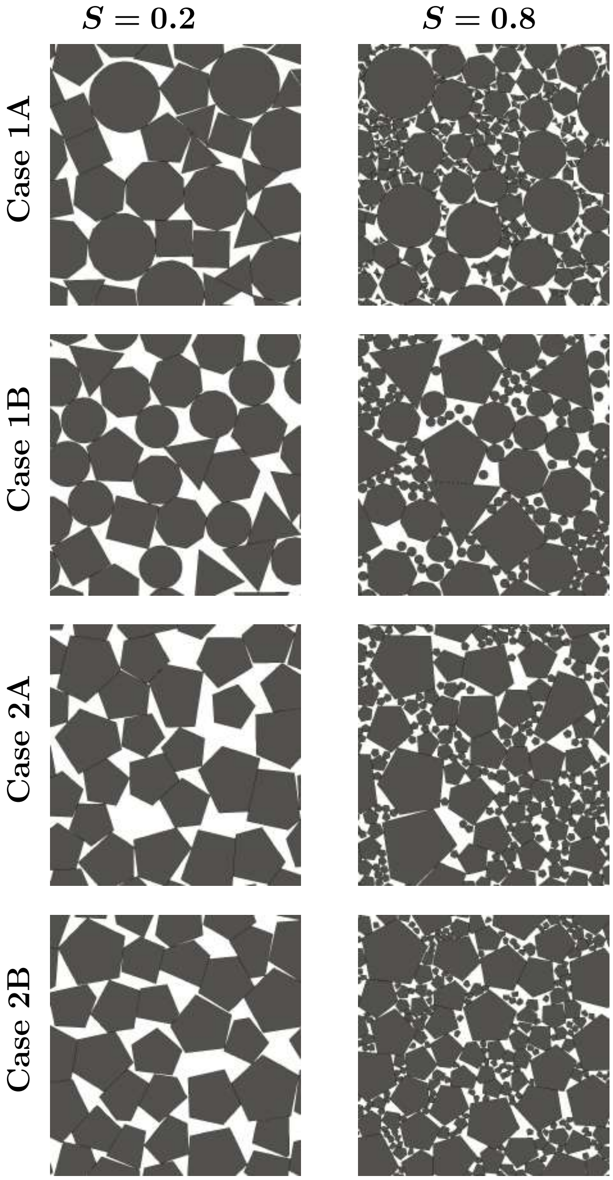

Figure 5.4 Screenshots of samples with particle size span S=0.2 (left) and S=0.8 (right) for different size-shape correlation studies.

wall along axis 'x' at constant velocity v, while applying vertical pressure P along axis 'y'. We set up the shear velocity v to apply a quasi-static shearing by imposing an inertial number $I = \dot{\gamma}\langle d\rangle\sqrt{\rho/P} \ll 1$ [60], where $\dot{\gamma} = v/h$, h the height of the sample, $\langle d\rangle$ is the average particle circumdiameter, and ρ the grains' density. The value of the inertial number was set to $I = 1 \times 10^{-3}$ for all the tests.

In order to reach critical state in terms of macroscopic and microscopic descriptors, we sheared our samples up to a cumulated shear strain $\gamma = \delta_x/h = 400\%$, being δ_x the cumulated hori-

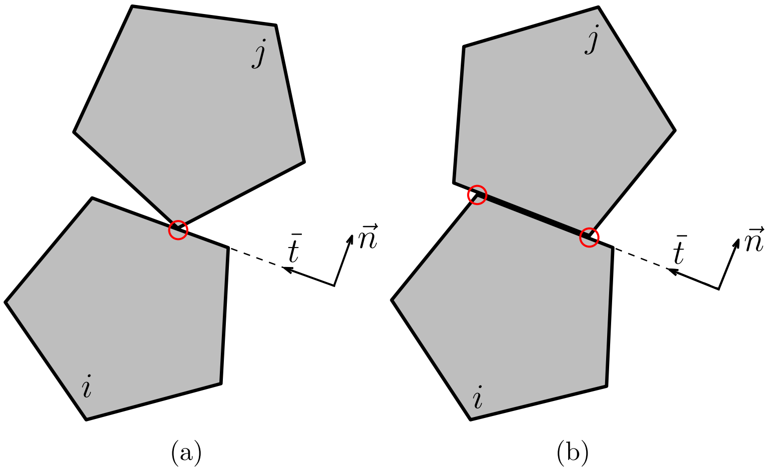

Figure 5.5 Scheme of (a) side-vertex and (b) side-side contacts between two grains labeled i and j, where the red circles represent the contact points.

zontal displacement of the walls. This large deformation was reached by employing periodic boundary conditions along the shearing direction, which allows any particle or contact crossing the periodic boundary to reappear on the sample's opposite side (see Figure 5.6). To effectively apply the shearing deformation, we set all particles in contact with the upper and lower walls to follow the wall displacements as if they were 'glued' to the boundary, avoiding sliding between grains and walls. For the interactions between grains, the coefficient of friction was set to $\mu = 0.4$, and gravity was set to zero to avoid pressure gradients. All shearing tests were performed using the free open-source software LMGC90, capable of simulating discrete mechanical systems in the frame of the CD method [61, 62].

5.3 Macroscopic behavior

The macroscopic behavior in our tests can be characterized by the solid fraction ν and the normalized shear stress q/p, being q the deviatoric stress and p the mean pressure of the granular stress tensor σ. This tensor is computed using the following expression [63–65]:

$$\sigma_{ij} = \frac{1}{A} \sum_{\forall c} f_i^c \ell_j^c \ , \tag{5.4}$$

where f_i^c is the i component of the force at contact c, and ℓ_j^c is the j component of the branch vector (i.e., the vector joining the center of mass of touching particles at contacts c). We use the principal stresses of σ (i.e., σ_1 and σ_2) to calculate $q = (\sigma_1 - \sigma_2)/2$ and $p = (\sigma_1 + \sigma_2)/2$. The coefficient of internal fiction is given by $\mu^* = q/p = \sin(\phi)$ at the critical state, being ϕ

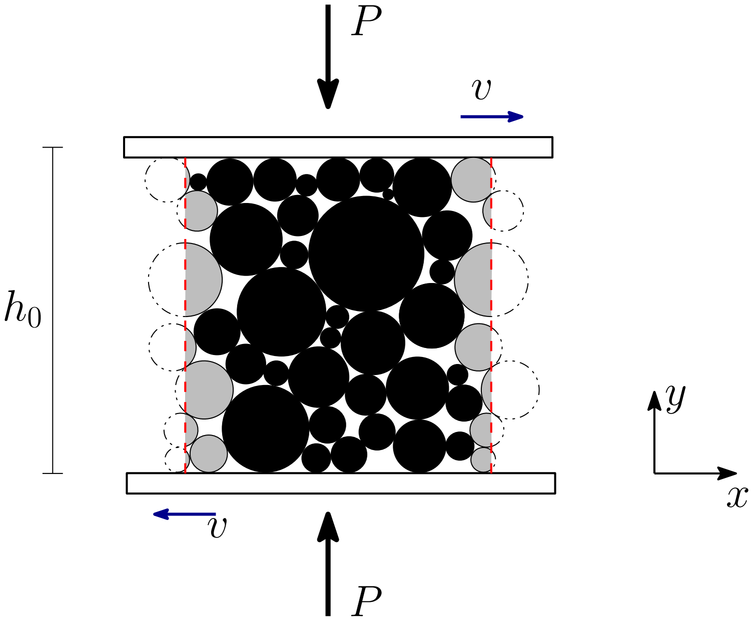

Figure 5.6 Scheme of boundary conditions for the shearing tests. The dashed lines represent the periodic boundary along the x axis, and the gray particles are the ones under this condition

the macroscopic friction angle of the material.

Figures 5.7 and 5.8 show the evolution of ν and q/p for all cases as a function of the shear deformation γ. For the shear stress q/p, we observe a gradual gain of resistance in all the cases up to $\gamma \sim 0.2$. Then, a transient zone towards the steady state takes place that varies depending on the material. While in Case 1A the steady state is reach around $\gamma \sim 0.4$, in case 1B the stabilization occurs more rapidly, as soon as $\gamma \sim 0.3$. For the Cases 2A and 2B, the shear strength stabilization occurs practically at the same levels of deformation (i.e., $\gamma \sim 0.3$). In terms of volume of the sample, we observe that in all cases the solid fraction finds steady values earlier than the shear strength, around $\gamma \sim 0.25$. Although the critical state is reached before $\gamma \sim 0.5$, we decided to shear the samples up to 400% shear deformation to ensure that both macroscopic and microscopic parameters find stable values despite relatively small fluctuations. To characterize the critical state, we average the values for the last 100% of deformation out of the total 400% accumulated.

Figure 5.9 shows the evolution of the average solid fraction for both cases and all the grain size spans in the critical state. For Cases 1A and 1B (Figure 5.9(a)), we can observe that solid fraction increases from $\nu \simeq 0.8$ for $S = 0$ to $\nu \simeq 0.85$ for $S = 0.9$. Nevertheless, while for Case 1A ν gradually increases with S as small angular grains can fill voids between larger particles, in Case 1B, the solid fraction presents a parabolic trend with a minimal

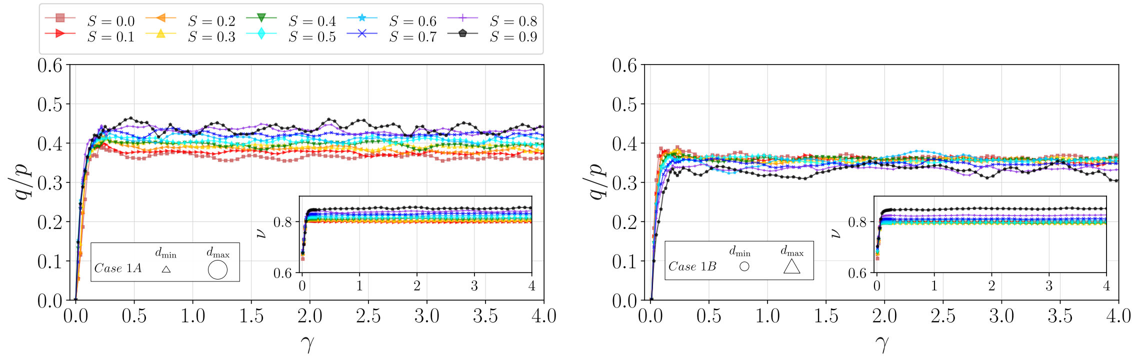

(a) (b)

Figure 5.7 Evolution of shear stress q/p and solid fraction ν (inset) for Cases 1A (a) and 1B (b) as a function of the shear deformation γ.

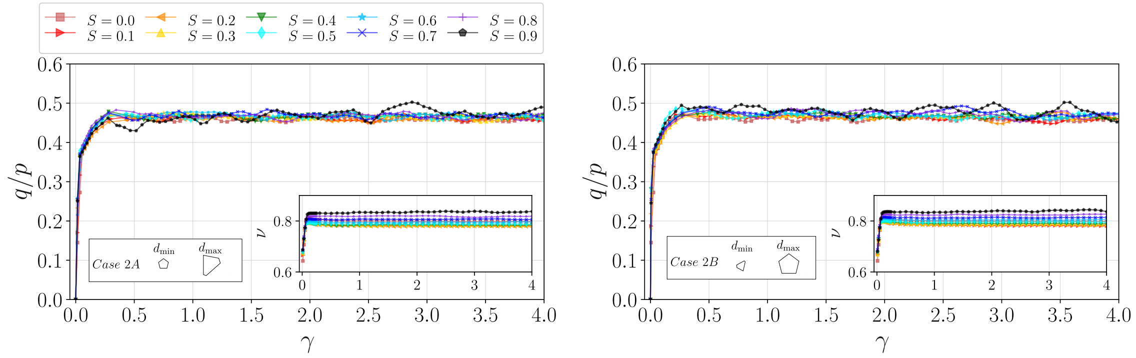

(a) (b)

Figure 5.8 Evolution of shear stress q/p and solid fraction ν (inset) for Cases 2A (a) and 2B (b) as a function of the shear deformation γ.

$\nu \simeq 0.79$ for $S = 0.4$. This evolution in Case 1B might be related to the development of large cavities between large sharper particles only after $S > 0.5$. Despite the difference in size-shape correlation, we obtain a similar value of ν for both cases for $S = 0.9$.

On the other hand, Figure 5.9(b) shows that Cases 2A and 2B have similar evolutions of ν as grain size span increases, being Case 2B slightly denser than Case 2A. This suggests that small irregular pentagons can more efficiently fill the voids left by larger regular pentagons.

In terms of critical state shear strength, Figure 5.10 shows the evolution of the average q/p for the different size-shape correlations. For assemblies composed of same-shape regular polygons, previous studies have shown that the shear strength varies exponentially as a function of particle sharpness, from $q/p \simeq 0.27$ for disks [27] to $q/p \simeq 0.47$ for triangles [48]. Effectively, the mean values of q/p at critical state that we found in Figure 5.10(a) lay between

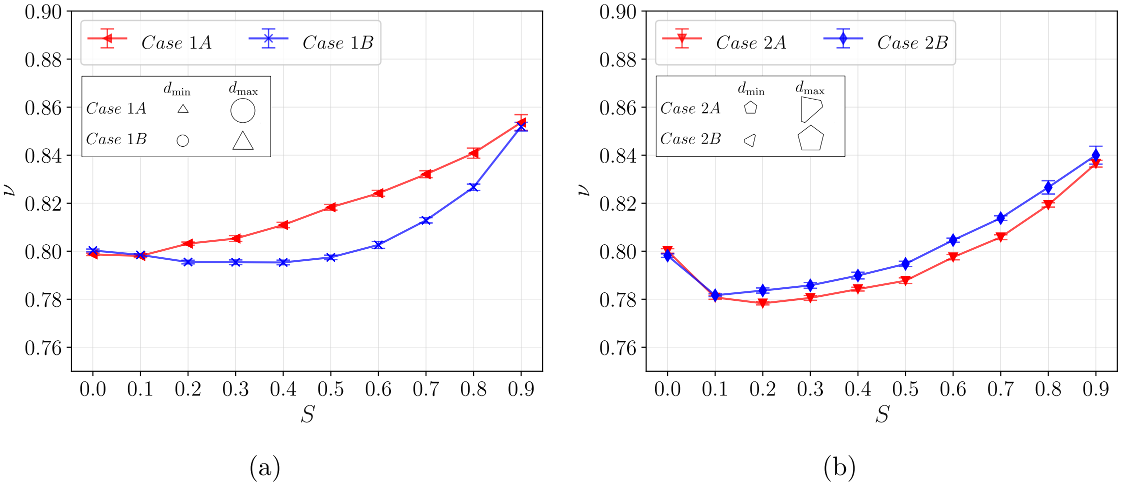

Figure 5.9 Evolution of the average solid fraction ν at critical state as a function of the particle size dispersion S for Case 1 (a) and Case 2 (b). Error bars display the standard deviation of the data.

those extreme cases. For Case 1A, the shear strength increases linearly as S increases from $q/p \simeq 0.36$ for $S = 0$ to $q/p \simeq 0.43$ for $S = 0.9$, while for Case 1B, the shear strength slightly decreases to $q/p \simeq 0.32$ for $S = 0.9$.

Figure 5.10(b) shows the evolution of the shear strength in the critical state as a function of S for Cases 2A and 2B. Unexpectedly, both cases show similar trends for q/p, being slightly higher as the grain size span increases. However, this variation is so small that we can suggest that the shear strength is practically independent of the size-shape correlation. Figure 5.10(b) also shows values of q/p for granular assemblies composed of only regular ($\delta = 0$) and irregular pentagons ($\delta = 1$) assemblies, being $q/p = 0.49$ and $q/p = 0.46$, respectively [38, 48]. It is observed that the different results of q/p in our simulations are within such a range, although slightly closer to the case of irregular particles.

This set of results put in evidence the fact that (1) grain sharpness plays a major role on the macroscopic shearing response and (2) equal particle size distributions may present dramatically different macroscopic behavior (in terms of strength and density) depending on their grain size-shape correlation.

In order to understand the macroscopic effects of each grain shape given its relative size in a sample, it is key to explore micromechanical aspects related to the grain organization and force transmission mechanisms for each of the cases tested.

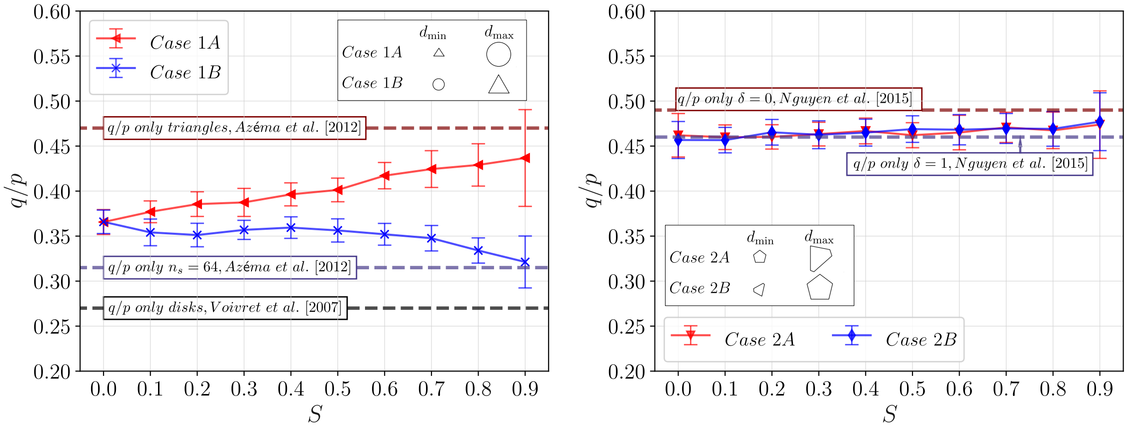

(a)

(b)

Figure 5.10 Evolution of the average critical shear strength q/p as a function of the particle size dispersion S for Case 1 (a) and Case 2 (b). Error bars display the standard deviation of the data.

5.4 Microscopic behavior

5.4.1 Connectivity

We can characterize the particle organization using an indicator of their connectivity through the *coordination number* or average number of contacts per load-bearing grain. This parameter is defined as $Z = 2N_c/N_p^*$, where N_c is the total number of force-bearing contacts, and N_p^* the number of grains transmitting forces. The coordination number excludes all particles having less than two active contacts (i.e., floating particles) to compute N_p^*. In this vein, it is also possible to estimate the proportion of grains not participating in the transmission of forces as $c_0 = N_p^0/N_p$, being N_p^0 the number of floating particles and N_p the total number of particles in the assembly.

Figure 5.11(a) shows the evolution of Z and c_0 as a function of S for Cases 1A and 1B. For mono-shape polygonal assemblies, the coordination number is bounded between $Z \in [3.1, 3.5]$ [47]. The inclusion of grains with different sharpness affects the connectivity at critical state, allowing the assemblies to have a broader range for Z. As grain size span increases, Cases 1A and 1B present opposite trends with an increase of Z for assemblies containing large particles with low sharpness (high n_s) (varying from $Z = 3.6$ to 3.9 in Case 1A) and a drop of connectivity as the assembly contains large sharp grains (low n_s) (from $Z = 3.6$ to 3.3 for Case 1B). The inset in the same figure shows the evolution of c_0 as a function of S for Cases 1A and 1B. In both cases, c_0 gradually increases with S due to a large proportion of small particles

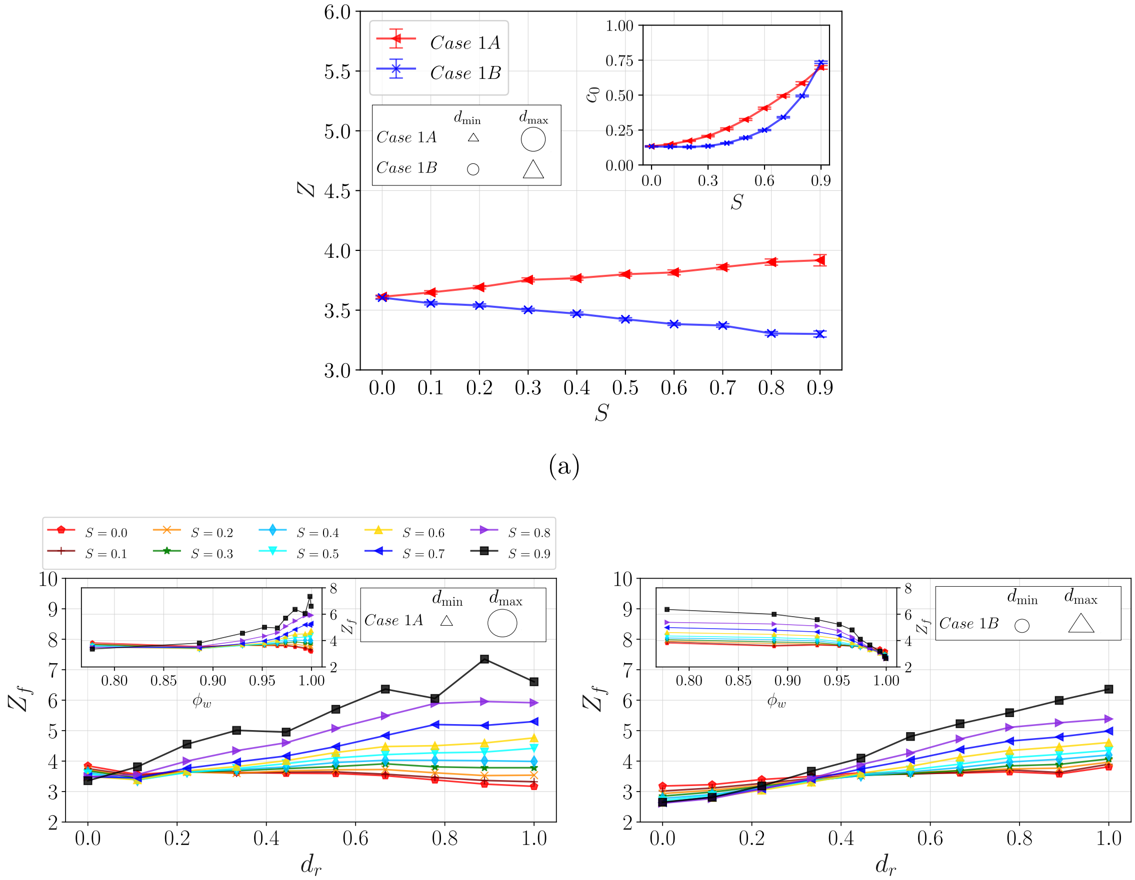

(a)

(b)

(c)

Figure 5.11 Evolution of Z at critical state as a function of the particle size dispersion S and for Cases 1A and 1B (a), and evolution of Z_f per particle family for Cases 1A (b) and 1B (c) as a function of d_r and as a function of ϕ_w in the inset figure.

rattling between larger particles; namely, c_0 increases from ~ 0.16 for $S = 0$ to ~ 0.70 for $S = 0.9$ for Cases 1A and 1B, respectively. To analyze this behavior in detail, we consider the coordination number by particle family Z_f (i.e., the average number of contacts per particle of shape n_s or δ) as a function of d_r. Figures 5.11(b) and 5.11(c) present the average number of contacts Z_f in Cases 1A and 1B as a function of d_r. Interestingly, we observe an almost linear dependence between Z_f and d_r, with an increasing slope as S increases. Similar behavior is observed in simulations of spheres and irregular pentagons [33, 38]. These figures confirm that larger particles are always more connected than small ones independently of the grain shape distribution. If we compare Z_f in inset figures of Cases 1A and 1B, larger particles with high n_s are always better connected than larger sharper particles, as opposed to the smaller particles where less circular grains tend to be more connected. This behavior is presumably due to the capacity of small sharper particles to reach neighboring particles

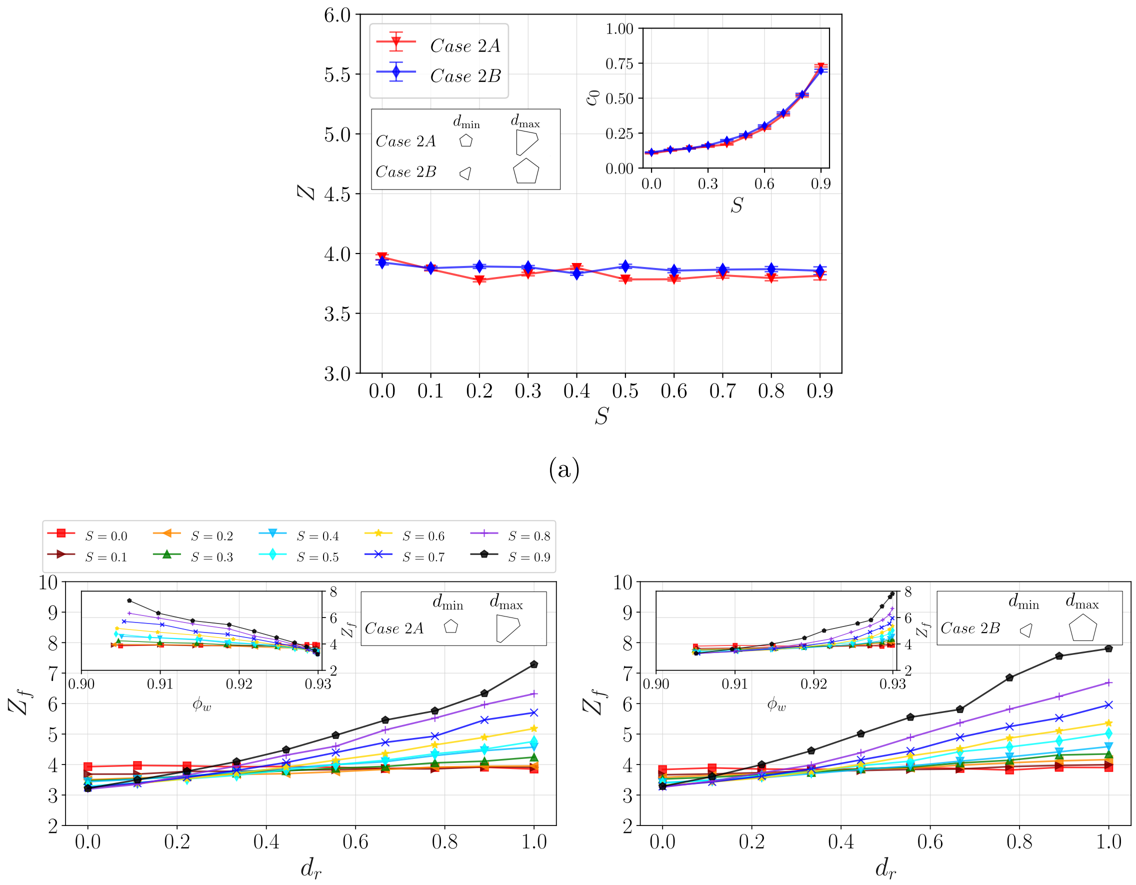

(a)

(b)

(c)

Figure 5.12 Evolution of Z at critical state as a function of the particle size dispersion S and for Case 2A and 2B (a), and evolution of Z per particle family for Case 2A (b) and Case 2B (c) as a function of d_r and as a function of ϕ_w in the inset figure.

with their corners that are normally unreachable for less angular grains [47].

In Figure 5.12(a), we can observe Z and c_0 as a function of S for Cases 2A and 2B. We observe that the connectivity among grains is almost constant with a value of $Z = 3.8$, regardless of S. Both size-shape correlations of irregular to regular pentagons (i.e., Cases 2A and 2B) allow having a better-connected assembly than for only regular pentagons, where $Z = 3.2$ [47]. Figures 5.11(b) and 5.11(c) present the average number of contacts Z_f in Cases 2A and 2B as a function d_r. We can observe - as in Cases 1A and 1B - a linear dependence between Z_f and d_r that is almost identical in both cases. Comparing both size-shape correlations based on irregularity, we can hardly detect a difference in the microstructural evolution of connectivity. Therefore, the sharpness of the grains in Cases 2A and 2B (i.e., pentagons), instead of their degree of irregularity, seems to be a more meaningful geometric parameter controlling the behavior of these assemblies.

5.4.2 Influence of the type of contact between grains

Previous numerical works have shown that contact types between angular grains can play a crucial role in the development of macroscopic strength [66–70]. For instance, it has been observed that the proportion of side-side contacts in packings of polygons under shearing has an essential role in stress transmission and mobilization of strength for most angular particles. Nevertheless, those results were found in samples containing only grains of the same shape, and it is not clear whether that observation holds up for size-shape correlated grain assemblies.

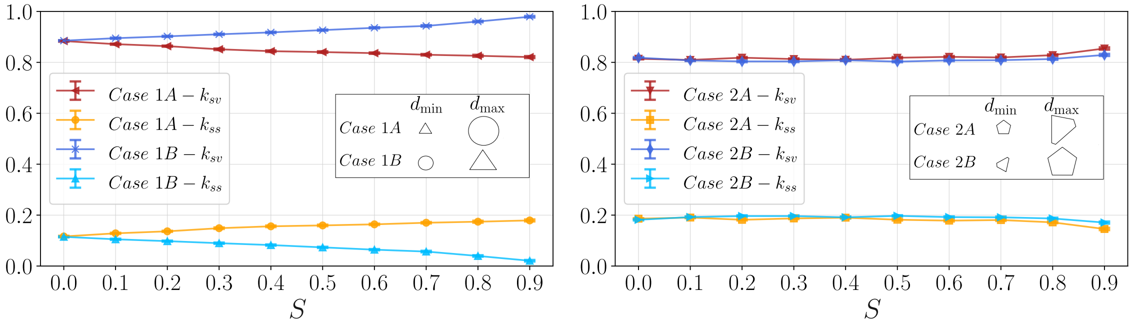

(a)

(b)

Figure 5.13 Evolution of the proportion of contact type (k_{sv} and k_{ss}) at critical state as a function of the grain size dispersion S for Cases 1A and 1B (a), and Cases 2A and 2B (b)

We study the influence of the side-vertex and side-side contacts in our samples. As shown in Figure 5.13, we quantify the proportion k of each type of contact (i.e., k_{ss} and k_{sv}, respectively), as a function of S. We can observe that the proportion of contacts type evolves in opposite trends for Cases 1A and 1B. As a matter of fact, the number of ss contacts increases for Case 1A and decreases for Case 1B as the grain size span increases, which agrees with the macroscopic shear strength trends.

Using mono-shape assemblies, [47] have shown that k_{ss} varies exponentially as a function of particle sharpness, from $k_{ss} \simeq 0$ for circles to $k_{ss} \simeq 0.25$ for triangles. Despite the fact that larger grains are always better connected than smaller ones, our results suggest that the capability of granular samples with size-shape correlations to generate ss contacts is mainly determined by the shape of the classes of small grains. This can be understood considering the fact that there are many more small grains in the sample compared to larger grains, so they can promote a greater numerical proportion of their preferred contact type. To put this

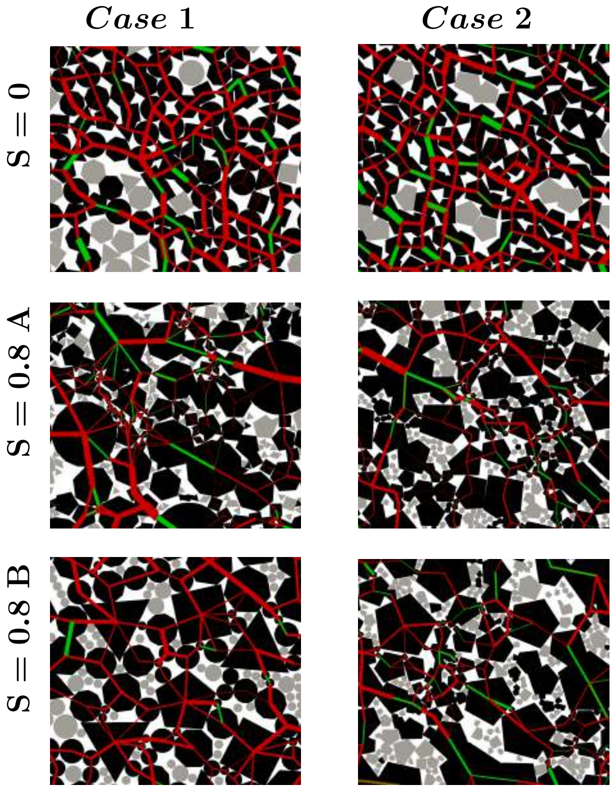

Figure 5.14 Screenshots of samples at critical state for Case 1 (left) and Case 2 (right) for different size span and size-shape correlation. The green and red lines joining the center of mass of touching grains indicate whether it corresponds to a *ss* or *sv* contact, respectively.

in evidence, Figure 5.14 shows screenshots of the samples at a given instant under critical state for Cases 1A and 1B with $S = 0.0$ and $S = 0.8$; floating particles are shown in light gray, while grains transmitting forces are shown in black. The lines connecting the centers of touching grains correspond to the contact network and the line thickness is proportional to the magnitude of the normal force. The color of the lines also indicates whether it is *ss* (green) or *sv* (red) contact.

For Cases 2A and 2B, Figure 5.13(b) shows the proportion of k_{sv} and k_{ss} as a function of S. Both contact proportions remain very similar for all grain size spans and all size-shape correlations, which is consistent with the strength found in such Cases.

While the proportion of number of contacts is of great interest, the effective contribution of each contact type to the macroscopic strength might be slightly different due to the magnitude of forces that each contact carries depending on the size of grains in interaction. To explore the micromechanical contributions of the contact type to the macroscopic shear strength, we can define the stress tensor as a sum of two partial tensors representing the contribution of

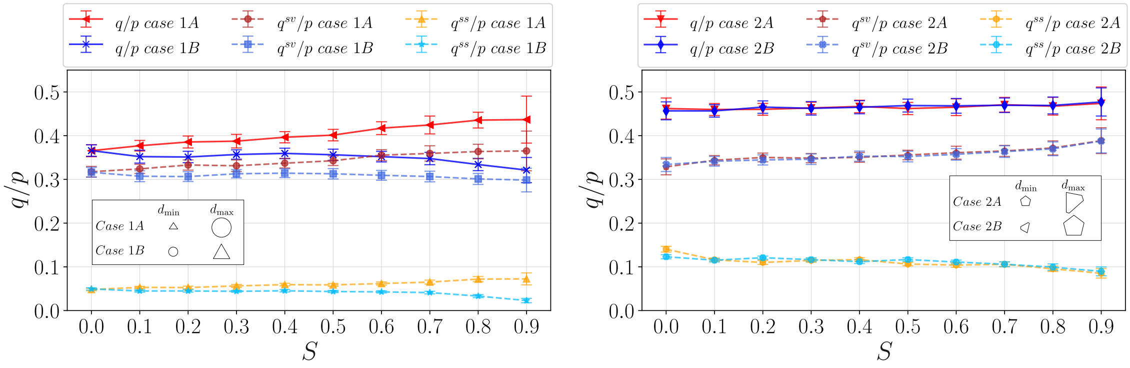

(a) (b)

Figure 5.15 Decomposition of the deviatoric component of stresses q/p (at critical state) by contribution of side-vertex q^{sv}/p and side-side q^{ss}/p contacts for Cases 1A (a) and 1B (b) as a function of the grain size span S.

sv and ss contacts. Employing the expression (6.1) and limiting the sum per contact type as:

$$\sigma_{ij} = \sigma_{ij}^{sv} + \sigma_{ij}^{vv} \ , \tag{5.5}$$

where

$$\sigma_{ij}^{sv} = \frac{1}{A} \sum_{\forall c^{sv}} f_i^c \ell_j^c \ , \tag{5.6}$$

and

$$\sigma_{ij}^{ss} = \frac{1}{A} \sum_{\forall c^{ss}} f_i^c \ell_j^c \ , \tag{5.7}$$

being c^{sv} and c^{ss} the corresponding contacts types. Using these partial tensors, we can compute the contribution of each one to the macroscopic strength since $q = q^{ss} + q^{sv}$, being q^{ss} and q^{sv}, the deviatoric components of each partial tensor. Figure 5.15 shows the evolution of q/p, q^{sv}/p, and q^{ss}/p as a function of grain size span S. For Case 1B, where larger particles are sharper and smaller ones have high n_s, the contributions of sv contacts remain constant as S increases, even though the number of contacts k_{sv} increases with the size dispersion.

On the other hand, for Case 1A, both contact types increase their contributions to q/p as S increases, although it is only k_{ss} the one that increases as the S increases.

For Cases 2A and 2B, the evolution of q^{sv}/p and q^{ss}/p is practically the same for both cases as S increases. There are no major differences in the contributions to shear strength, whether the fraction of smaller grains is composed of regular or irregular pentagons. Nonetheless, the contribution to shear strength of sv contacts increases while that of ss decreases in similar proportions. This compensation of contributions helps to explain why the macroscopic response q/p remains practically constant with S.

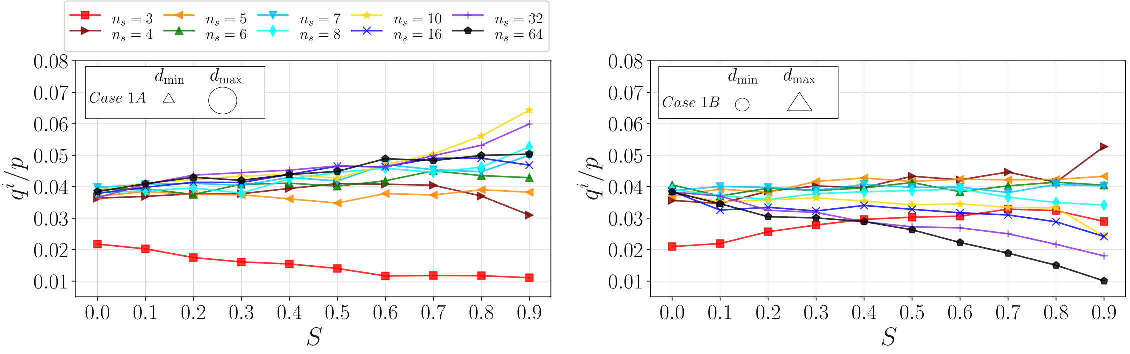

(a)

(b)

Figure 5.16 Decomposition of the deviatoric component of stresses (at critical state) by shape class for Cases 1A (a) and 1B (b) as a function of the grain size span S.

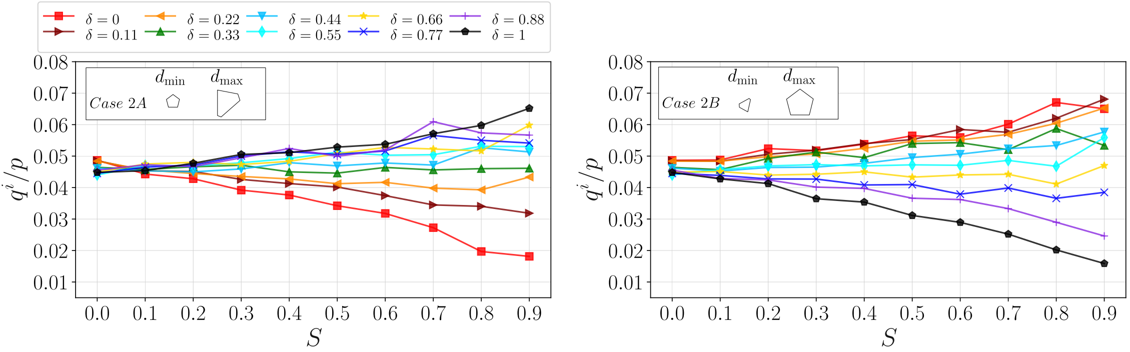

(a)

(b)

Figure 5.17 Decomposition of the deviatoric component of stresses (at critical state) by shape class for Cases 2A (a) and 2A (b) as a function of the grain size span S.

5.4.3 Contributions to shear strength by shape class

We employ an alternative decomposition of q/p to access the contributions of each shape class on the critical shear strength [71]

$$\frac{q}{p} = \frac{1}{p}\sum_{i=1}^{N_{sc}} q^i \ , \tag{5.8}$$

being q^i the deviatoric component of the granular stress tensor σ^i for each particle *shape class* (sc) in the assembly. This tensor is computed using the following expression:

$$\sigma^i_{mn} = \frac{1}{A} \sum_{\forall N^{*i}_p} f^c_m r^c_n \ , \tag{5.9}$$

where N^{*i}_p is any load-bearing grain with a given shape 'i', f^c_m is the m component of the force at contact c, and r^c_n is the n component of the vector joining the center of mass of particle and the contact point. We use the principal stresses of σ^i (i.e., σ^i_1 and σ^i_2) to calculate $q^i = (\sigma^i_1 - \sigma^i_2)/2$ and $p^i = (\sigma^i_1 + \sigma^i_2)/2$ for each family shape. Figure 5.16 presents the deviatoric contributions by shape classes to q/p at critical state for size-shape correlations 1A and 1B as a function of S. Note that the shape classes are separated into ten groups for Cases 1A and 1B as they are categorized by the number of sides of the grains. For mono-size samples $S = 0$, we observe that, at critical state, all polygons contribute q^i/p around 0.35 to 0.40, except for the triangles where q^i/p is slightly lower. In general, the coarse fractions of the sample increase their contributions to total critical q/p. This behavior is even more marked as size span S increases.

For Case 1A, the coarser and less sharp fractions increase their contributions by around $30 - 70\%$ when passing from monodisperse to highly polydisperse samples. For Case 1B, where the coarse fraction is composed of sharper grains, we observe that only the most sharp classes (i.e., triangles and squares) increase their contribution to the global shear strength.

On the other hand, by studying the evolution of q^i/p at critical state for the finer fraction of particles, we can observe for Case 1A that square and triangular particles decrease their contribution as S increases. In particular, the sharpest particles reduce to almost half their contribution to the global shear strength as S increases. For Case 1B, we observe a significant drop in the contributions to strength of small less sharp grains as S increases. For instance, 10-side polygons decrease their contribution by almost half, and for 64-side polygons, the drop of about 1/4 when comparing the mono-size and the polydisperse cases.

These curves help to understand that the drop of critical q/p in Case 1B is mainly due to a significant decrease in shear strength provided by the less sharp grains. In contrast, Case 1A has a generalized increment of critical q/p because small sharp grains contribute significantly to the shear strength, while larger less sharp grains present slight increments of strength.

Figure 5.17 shows the evolution of q^i/p to critical shear strength for Cases 2A and 2B, where the shape class is related to the irregularity of pentagonal grains. We observe an identical evolution of contributions by shape class for both cases. The drop in strength of the finer fraction is fully compensated by the increase in the contribution of the coarse fraction, regardless of the characteristic grain shape of the finer fraction.

5.5 Conclusion

This paper studied the effects of granular assemblies presenting correlations between the size and the shape of the grains. Two cases covering different shape descriptors were considered and modeled. In the first case, we use regular polygons with two different size-shape correlations: Case 1A, where large grains are less sharp than small ones, and Case 1B, where large grains are sharper than small ones. In the second case, we use pentagons with two different size-shape correlations: Case 2A, where large grains are regular pentagons and small ones are irregular, and Case 2B, where large grains are irregular pentagons and small ones are regular. Our granular assemblies varied from mono-size to polydisperse arrangements of grains where $d_{\max}/d_{\min} \simeq 20$. Employing the discrete element method known as contact dynamics, we simulated 2D granular assemblies under simple shearing employing periodic quasi-static conditions up to a cumulated shear deformation of $\gamma = 400\%$.

We observed that size-shape correlations based on sharpness profoundly modify the mechanical response of the granular assemblies, while grain irregularity in pentagons did not show any significant impact on the mechanical behavior as grain size span is varied.

In systems with size-shape correlation based on grain sharpness, assemblies in Case 1A show that shear strength significantly increases with grain size span. The opposite size-shape correlation, Case 1B, shows a drop in shear strength as the grain size span increases.

To understand the differences between Cases 1A and 1B, we undertook a series of microstructural analyses and showed that each correlation strongly affects the grain connectivity, being the assembly in Case 1A able to develop more contacts per particle on average. Furthermore, we decomposed the connectivity by grain size and observed that the connectivity of larger grains always increases independently of the grain size-shape correlation. Our results also related higher values of Z with the presence of more side-side contacts, which allows a more stable contact network to be formed.

Finally, we also decomposed the deviatoric component of the shear strength critical q/p by contributions of different shape classes. This analysis showed that larger grains contribute more to the shear strength as the grain size span increases. This phenomenon is more intense when large grains are less sharp. In turn, the same analysis showed that smaller grains have fewer contributions to the shear strength as the grain size span increases. Specifically, the contribution of smaller particles drops around two times more when their shapes have a large number of sides than when the particles are sharp.

For Cases 2A and 2B, we also decomposed q/p at critical state by contributions of different shape classes q^i/p, showing a practically identical evolution of contributions by shape class for both cases, being the largest grains those always contributing more than the small grains. The increase in the contribution of the coarse fraction is then fully compensated by the drop in resistance of the finer fraction. Consequently, there is no difference in whether the finer fraction is regular or irregular.

Together with a previous research on the effects of particle size-elongation correlations [46], this work proves that different grain size-shape correlations can have major effects on the critical shear strength and solid fraction of granular assemblies. These facts suggest that scaling methods based on scalping or parallel psd can imply significant errors when estimating the shear strength of a material in a small-scaled sample if grain shapes are not taken into account in the procedure.

Future studies on this topic should focus on exploring more realistic size-shape correlations seen in geomaterials, as well as include the possibility of grains to break. Another important challenge in this topic concerns the extension and validation of the two-dimensional size-shape correlations to three-dimensional modeling and simulation. The validation of these numerical observations concerning grain shape and size effects through laboratory tests is highly desired but rarely seen in the literature. The challenges of experimental testing to reproduce broad grain size distribution while carefully controlling the grain shape is still an open issue that calls for large-scale testing or alternative physical approaches.

Conflicts of Interest

The authors do not have any conflicts of interest.

Acknowledgements

This research work benefited from the financial support of the Natural Sciences and Engineering Research Council of Canada (NSERC) [Ref. RGPIN-2019-06118], the Fonds de recherche du Québec — Nature et technologies (FRQNT) through the « Programme de recherche en partenariat sur le développement durable du secteur minier-II » [Ref. 2020-MN-281267], the industrial partners of the Research Institute on Mines and the Environment (RIME) UQAT-Polytechnique (irme.ca/en). This research also was enabled in part by support provided by Calcul Quebec (calculquebec.ca) and Compute Canada (computecanada.ca).

Bibliography

[1] R. Marsal, "Large scale testing of rockfill materials," *J. Soil Mech. Found. Div.*, vol. 93, no. 2, pp. 27–43, 1967.

[2] N. Marachi, C. Chan, and H. Seed, "Evaluation of properties of rockfill materials," *J. Soil Mech. Found. Div.*, vol. 98, no. 1, pp. 95–114, 1972.

[3] N. Barton and B. Kjærnsli, "Shear strength of rockfill," *J. Geotech. Eng.*, vol. 107, no. 7, pp. 873–891, 1981.

[4] B. Indraratna, D. Ionescu, and H. Christie, "Shear behavior of railway ballast based on large-scale triaxial tests," *J. geotechn. geoenviron.*, vol. 124, no. 5, pp. 439–449, 1998.

[5] H. Matsuoka, S. Liu, D. Sun, and U. Nishikata, "Development of a new in-situ direct shear test," *Geotech. Test. J*, vol. 24, no. 1, pp. 92–102, 2001.

[6] E. Bard, M. E. Anabalón, and J. Campaña, "Waste rock behavior at high pressures: dimensioning high waste rock dumps." Wiley Online Library, 2011, pp. 83–112.

[7] C. Ovalle, S. Linero, C. Dano, E. Bard, P.-Y. Hicher, and R. Osses, "Data compilation from large drained compression triaxial tests on coarse crushable rockfill materials," *J. Geotech. Geoenviron.*, vol. 146, p. 06020013, 9 2020.

[8] R. Verdugo and K. de La Hoz, "Strength and stiffness of coarse granular soils," in *Soil stress-strain behavior: Measurement, modeling and analysis.* Springer, 2007, pp. 243–252.

[9] W. Hu, C. Dano, P.-Y. Hicher, J.-Y. Le Touzo, F. Derkx, and E. Merliot, "Effect of sample size on the behavior of granular materials," *Geotech. Test. J.*, vol. 34, no. 3, pp. 186–197, 2011.

[10] E. Frossard, C. Ovalle, C. Dano, P.-Y. Hicher, S. Maiolino, and W. Hu, "Size effects due to grain crushing in rockfills shear strength," in *18th International Conference for Soil Mechanics and Geotechnical Engineering*, 2013.

[11] J. Zeller and R. Wullimann, "The shear strength of the shell materials for the goschenenalp dam, switzerland," in *4th International Conference on Soil Mechanics and Foundation Engineering*, vol. 2, 1957, pp. 399–415.

[12] A. Varadarajan, K. Sharma, K. Venkatachalam, and A. Gupta, “Testing and modeling two rockfill materials,” *J. Geotech. Geoenviron.*, vol. 129, no. 3, pp. 206–218, 2003.

[13] Y. Xiao, H. Liu, Y. Chen, and W. Zhang, “Particle size effects in granular soils under true triaxial conditions,” *Géotechnique*, vol. 64, no. 8, pp. 667–672, 2014.

[14] C. Ovalle, E. Frossard, C. Dano, W. Hu, S. Maiolino, and P. Y. Hicher, “The effect of size on the strength of coarse rock aggregates and large rockfill samples through experimental data,” *Acta Mech.*, vol. 225, pp. 2199–2216, 2014.

[15] M. Al-Hussaini, “Effect of particle size and strain conditions on the strength of crushed basalt,” *Can. Geotech. J.*, vol. 20, no. 4, pp. 706–717, 1983.

[16] S. Linero, C. Palma, and R. Apablaza, “Geotechnical characterisation of waste material in very high dumps with large scale triaxial testing,” in *Proceedings of the 2007 International Symposium on Rock Slope Stability in Open Pit Mining and Civil Engineering.* Australian Centre for Geomechanics, 2007, pp. 59–75.

[17] P. Cao, M. Jiang, and Z. Ding, “Effects of particle size on mechanical behaviors of calcareous sand under triaxial conditions,” *Jpn. Geotech. Soc. spec. publ.*, vol. 8, no. 5, pp. 182–187, 2020.

[18] A. Deiminiat and L. Li, “Experimental study on the reliability of scaling down techniques used in direct shear tests to determine the shear strength of rockfill and waste rocks,” *CivilEng*, vol. 3, no. 1, pp. 35–50, 2022.

[19] T. L. Youd, D. Nichols, E. Helley, and K. LaJoie, “Liquefaction potential of unconsolidated sediments in the southern san francisco bay region, california,” US Geological Survey, Tech. Rep., 1973.

[20] J. Zheng and R. D. Hryciw, “Index void ratios of sands from their intrinsic properties,” *J. Geotech. Geoenviron.*, vol. 142, no. 12, p. 06016019, 2016.

[21] B. O. Hardin, “Crushing of soil particles,” *J. Geotech. Eng.*, vol. 111, no. 10, pp. 1177–1192, 1985.

[22] P. V. Lade, J. A. Yamamuro, and P. A. Bopp, “Significance of particle crushing in granular materials,” *J. Geotech. Eng.*, vol. 122, no. 4, pp. 309–316, 1996.

[23] C. Ovalle, C. Dano, P.-Y. Hicher, and M. Cisternas, “Experimental framework for evaluating the mechanical behavior of dry and wet crushable granular materials based on the particle breakage ratio,” *Can. Geotech. J.*, vol. 52, no. 5, pp. 587–598, 2015.

[24] S. Amirpour Harehdasht, M. N. Hussien, M. Karray, V. Roubtsova, and M. Chekired, “Influence of particle size and gradation on shear strength–dilation relation of granular materials,” *Can. Geotech. J.*, vol. 56, no. 2, pp. 208–227, 2019.

[25] A. Deiminiat, L. Li, F. Zeng, T. Pabst, P. Chiasson, and R. Chapuis, “Determination of the shear strength of rockfill from small-scale laboratory shear tests: A critical review,” *Adv. Civ. Eng.*, vol. 2020, pp. 1–18, 11 2020.

[26] A. B. Cerato and A. J. Lutenegger, “Specimen size and scale effects of direct shear box tests of sands,” *Geotech. Test. J.*, vol. 29, no. 6, pp. 507–516, 2006.

[27] C. Voivret, F. Radjai, J. Y. Delenne, and M. S. El Youssoufi, “Space-filling properties of polydisperse granular media,” *Phys Rev. E*, vol. 76, p. 021301, 8 2007.

[28] D. Muir Wood and K. Maeda, “Changing grading of soil: Effect on critical states,” *Acta Geotech.*, vol. 3, pp. 3–14, 2008.

[29] G. Li, C. Ovalle, C. Dano, and P.-Y. Hicher, “Influence of grain size distribution on critical state of granular materials,” in *Constitutive modeling of geomaterials.* Springer, 2013, pp. 207–210.

[30] E. Azéma, S. Linero, N. Estrada, and A. Lizcano, “Shear strength and microstructure of polydisperse packings: The effect of size span and shape of particle size distribution,” *Phys. Rev. E*, vol. 96, 8 2017.

[31] H. S. Amirpour, M. Karray, M. Hussien, and M. Chekired, “Influence of particle size and gradation on the stress-dilatancy behavior of granular materials during drained triaxial compression,” *Int. J. Geomech.*, vol. 17, no. 9, p. 04017077, 2017.

[32] J. Yang and X. D. Luo, “The critical state friction angle of granular materials: does it depend on grading?” *Acta Geotech.*, vol. 13, pp. 535–547, 6 2018.

[33] D. Cantor, E. Azéma, P. Sornay, and F. Radjai, “Rheology and structure of polydisperse three-dimensional packings of spheres,” *Phys. Rev. E*, vol. 98, no. 5, p. 052910, 2018.

[34] S. Linero, E. Azéma, N. Estrada, S. Fityus, J. Simmons, and A. Lizcano, “Impact of grading on steady-state strength,” *Géotech. Lett.*, vol. 9, no. 4, pp. 328–333, 2019.

[35] Y. Deng, Y. Yilmaz, A. Gokce, and C. Chang, “Influence of particle size on the drained shear behavior of a dense fluvial sand,” *Acta Geotech.*, vol. 16, no. 7, pp. 2071–2088, 2021.

[36] G.-C. Cho, J. Dodds, and J. C. Santamarina, “Particle shape effects on packing density, stiffness, and strength: Natural and crushed sands,” *J. Geotech. Geoenviron.*, vol. 132, no. 5, pp. 591–602, 2006.

[37] E. Azéma and F. Radjai, “Stress-strain behavior and geometrical properties of packings of elongated particles,” *Phys. Rev. E*, vol. 81, no. 5, p. 051304, 2010.

[38] D. H. Nguyen, E. Azéma, p. Sornay, and F. Radjai, “Effects of shape and size polydispersity on strength properties of granular materials,” *Phys. Rev. E*, vol. 91, p. 032203, 3 2015.

[39] F. N. Altuhafi, M. R. Coop, and V. N. Georgiannou, “Effect of Particle Shape on the Mechanical Behavior of Natural Sands,” *J. Geotech. Geoenviron.*, vol. 142, no. 12, p. 04016071, 2016.

[40] Y. Xiao, L. Long, T. Matthew Evans, H. Zhou, H. Liu, and A. W. Stuedlein, “Effect of particle shape on stress-dilatancy responses of medium-dense sands,” *J. Geotech. Geoenviron.*, vol. 145, p. 04018105, 2019.

[41] C. Nouguier-Lehon, “Effect of the grain elongation on the behaviour of granular materials in biaxial compression,” *C. R. Mécanique*, vol. 338, no. 10, pp. 587–595, 2010, micromechanics of granular materials.

[42] C. Ovalle and C. Dano, “Effects of particle size–strength and size–shape correlations on parallel grading scaling,” *Géotech. Lett.*, vol. 10, no. 2, pp. 191–197, 2020.

[43] S. Linero, S. Fityus, J. Simmons, A. Lizcano, and J. Cassidy, “Trends in the evolution of particle morphology with size in colluvial deposits overlying channel iron deposits,” in *EPJ Web of Conferences*, vol. 140. EPJ Web of Conferences, 2017, p. 14005.

[44] Y. Liu, F. Guillard, B. Marks, P. Rognon, and I. Einav, “The perpetual shearing of granular soils under low stresses using the stadium shear device,” *Open Geomechanics*, vol. 3, pp. 1–19, 2022.

[45] R. Kawamoto, E. Andò, G. Viggiani, and J. E. Andrade, “All you need is shape: Predicting shear banding in sand with ls-dem,” *J. Mech. Phys. Solids*, vol. 111, pp. 375–392, 2018.

[46] S. Carrasco, D. Cantor, and C. Ovalle, “Effects of particle size-shape correlations on steady shear strength of granular materials: The case of particle elongation,” *Int. J. Numer. Anal. Methods. Geomech.*, vol. 46, no. 5, pp. 979–1000, 2022.

[47] E. Azéma, N. Estrada, and F. Radjai, “Nonlinear effects of particle shape angularity in sheared granular media,” *Phys. Rev. E*, vol. 86, no. 4, p. 041301, 2012.

[48] N. Estrada, E. Azéma, F. Radjai, and A. Taboada, “Identification of rolling resistance as a shape parameter in sheared granular media,” *Phys. Rev. E*, vol. 84, no. 1, p. 011306, 2011.

[49] H. Wadell, “Sphericity and roundness of rock particles,” *The Journal of Geology*, vol. 41, no. 3, pp. 310–331, 1933.

[50] G. Saussine, C. Cholet, P. Gautier, F. Dubois, C. Bohatier, and J. Moreau, “Modelling ballast behaviour under dynamic loading. part 1: A 2d polygonal discrete element method approach,” *Comput. Methods Appl. Mech. Eng.*, vol. 195, no. 19, pp. 2841–2859, 2006.

[51] J. J. Moreau, “Unilateral contact and dry friction in finite freedom dynamics,” in *Nonsmooth mechanics and Applications.* Springer, 1988, pp. 1–82.

[52] M. Jean and J. J. Moreau, “Unilaterality and dry friction in the dynamics of rigid body collections,” in *1st Contact Mechanics International Symposium.* 1st Contact Mechanics International Symposium, 1992, pp. 31–48.

[53] F. Radjai and V. Richefeu, “Contact dynamics as a nonsmooth discrete element method,” *Mech. Mater.*, vol. 41, no. 6, pp. 715–728, 2009, advances in the Dynamics of Granular Materials.

[54] F. Dubois, V. Acary, and M. Jean, “The contact dynamics method: A nonsmooth story,” *C. R. Mécanique*, vol. 346, no. 3, pp. 247–262, 2018.

[55] C. Voivret, F. Radjai, J.-Y. Delenne, and M. S. El Youssoufi, “Space-filling properties of polydisperse granular media,” *Phys. Rev. E*, vol. 76, no. 2, p. 021301, 2007.

[56] R. Jullien, A. Pavlovitch, and P. Meakin, “Random packings of spheres built with sequential models,” *J. Phys. A Math. Theor.*, vol. 25, no. 15, p. 4103, 1992.

[57] W. M. Visscher and M. Bolsterli, “Random packing of equal and unequal spheres in two and three dimensions,” *Nature*, vol. 239, pp. 504–507, 1972.

[58] P. Schuhmacher, “Rhéologie des écoulements granulaires : variables internes et effets d’échelle,” Thèse de doctorat, Université Montpellier, 2016.

[59] ASTM, “D6528–17: Standard test method for consolidated undrained direct simple shear testing of fine grain soils,” American Society for Testing and Materials, West Conshohocken, PA, Standard, 2017.

[60] GDR-MiDi, “On dense granular flows,” *Eur. Phys. J. E*, vol. 14, pp. 341–365, 2004.

[61] F. Dubois, M. Jean, and et al, “LMGC90 wiki page,” https://git-xen.lmgc.univ-montp2.fr/lmgc90/lmgc90_user/wikis/home, 2023, [Online; accessed 15-Mar-2023].

[62] F. Dubois, M. Jean, M. Renouf, R. Mozul, A. Martin, and M. Bagnéris, “LMGC90,” in *10e colloque national en calcul des structures.* 10e colloque national en calcul des structures, 2011, p. 8 p.

[63] L. Rothenburg and R. J. Bathurst, “Analytical study of induced anisotropy in idealized granular materials,” *Géotechnique*, vol. 39, no. 4, pp. 601–614, 1989.

[64] B. Andreotti, Y. Forterre, and O. Pouliquen, *Granular media: between fluid and solid.* CUP, 2013.

[65] F. Nicot, N. Hadda, M. Guessasma, J. Fortin, and O. Millet, “On the definition of the stress tensor in granular media,” *Int. J. Solids Struct.*, vol. 50, no. 14-15, pp. 2508–2517, 2013.

[66] M. Boton, E. Azéma, N. Estrada, F. Radjai, and A. Lizcano, “Quasistatic rheology and microstructural description of sheared granular materials composed of platy particles,” *Phys. Rev. E*, vol. 87, p. 032206, Mar 2013.

[67] T. Matsushima and C. S. Chang, “Quantitative evaluation of the effect of irregularly shaped particles in sheared granular assemblies,” *Granul. Matter*, vol. 13, no. 3, pp. 269–276, 2011.

[68] R. C. Hidalgo, I. Zuriguel, D. Maza, and I. Pagonabarraga, “Role of particle shape on the stress propagation in granular packings,” *Phys. Rev. Lett.*, vol. 103, no. 11, p. 118001, 2009.

[69] M. Acevedo, R. C. Hidalgo, I. Zuriguel, D. Maza, and I. Pagonabarraga, “Influence of the feeding mechanism on deposits of square particles,” *Phys. Rev. E*, vol. 87, p. 012202, Jan 2013.

[70] T. Kanzaki, M. Acevedo, I. Zuriguel, I. Pagonabarraga, D. Maza, and R. Hidalgo, “Stress distribution of faceted particles in a silo after its partial discharge,” *Eur. Phys. J. E*, vol. 34, no. 12, pp. 1–8, 2011.

[71] D. Cantor, E. Azéma, and I. Preechawuttipong, “Microstructural analysis of sheared polydisperse polyhedral grains,” *Phys. Rev. E*, vol. 101, p. 062901, Jun 2020.

CHAPTER 6 ARTICLE 3: Particle shape distribution effects on the critical strength of granular materials

Journal: Computers and Geotechnics.
Submitted: 1st August 2024.

Sergio Carrasco[1,2], David Cantor[1,2], Frédéric Dubois[3] Carlos Ovalle*[1,2]

[1] Department of Civil, Geological and Mining Engineering, Polytechnique Montréal, Québec, Canada

[2] Research Institute of Mining and Environment (RIME), UQAT-Polytechnique, Québec, Canada

[3] LMGC, Université de Montpellier, CNRS, Montpellier, France

Corresponding author: carlos.ovalle@polymtl.ca

Abstract: This study investigates the influence of correlations between particle morphology and gradation on the critical shear strength of three-dimensional granular assemblies via numerical simulations. While grain shape is acknowledged to play a central role in the mechanical behavior of granular media, only a few works have explored the combined effects of grain shapes varying with grain size. Employing three-dimensional discrete-element simulations, we explore the shear behavior of samples with diverse particle size distributions, where grain shapes (ranging from spheres to very angular polyhedra) are assigned based on the relative size of each particle. Using drained triaxial shear tests, we analyze the macroscopic behavior up to large deformation levels. Micro-mechanical analyses are also conducted to understand the underlying mechanisms governing the observed macroscopic behavior, highlighting the role of grain connectivity and force transmission. Surprisingly, well graded samples composed of coarse angular grains and fine rounded ones are not capable of developing higher shear strengths than uniform samples with the same diversity on grain shapes. Conversely, samples where coarser grains are rounded and fines are angular, show constant shear strength as the PSD becomes broader. These findings underscore the importance of simultaneously considering grain size and shape distributions for the assessment of realistic granular soil behavior.

Keywords: discrete-element modeling, granular materials, shear strength, particle size distribution, particle shape distribution

6.1 Introduction

Geotechnical and mining engineering often deal with materials whose mechanical properties are challenging to characterize. This is particularly evident for coarse granular materials, such as crushed rock obtained after blasting and grinding. These materials, composed of grains of varied geological origin and displaying a wide range of sizes, shapes and strengths, are the building blocks for structures such as rockfill dams and mine waste rock piles [1–4]. The challenges for the mechanical characterization of coarse grain assemblies lie in the fact that, while laboratory tests can be performed on materials composed of fine gravels, sands or any finer grains, coarse granular materials may contain large cobbles and clasts that are impossible to fit in standard testing devices [5]. Historical attempts to overcome this limitation have consisted of building large laboratory shearing devices [6–10], large oedometric cells [11, 12] and *in situ* direct shear boxes [2, 13, 14].

The condition to test a representative mass of material relates the minimal sample dimension with its maximum particle size [15–18]. Even when very large testing methods are used, it is often necessary to reduce the characteristic grain size of rockfill materials by removing the coarsest size fraction to meet standard geotechnical testing requirements [19]. This is usually achieved using downscaling methods, such as parallel grading or scalping, which inevitably alter the particle size distribution (PSD) of the original material. In doing so, other material properties may also change, such as particle shape distribution, if the material presents grain size-shape correlations [20, 21]. A number of studies have proven that changes in PSD do not affect the critical shear strength as long as the particle shape remains constant [22–24, 27]. However, if the characteristic grain shape is altered by removing coarse particles, the mechanical behavior of the small-scaled sample might not be representative of the original material [25, 26]. Scaling methods are then not appropriate in materials having grain size-shape correlations. This topic, however, remains poorly understood and the coupled effects of varying grain shape as a function of grain size has only been covered by a few works, such as the experimental studies by [27] and [28], or more recently, using two-dimensional discrete-element simulations [29–31].

The discrete-element method (DEM) [32, 33] provides a privileged framework to explore the mechanics of granular media, as it allows for the explicit description of the particle geometry while exploring the multi-scale response of the material. These discrete multi-scale approaches have become key to understanding the complex behavior of disordered granular systems composed of spheres, regular polyhedra, and ellipsoids [34–37]. More realistic grain shapes have also been considered through the use of irregular polyhedra and clusters of spheres [38–40], although the number of particles and length of simulations are quickly limited by computational costs. These studies have certainly provided a comprehensive understanding of macro- and micro-mechanical behavior of granular materials, but have neglected the fact that soil often presents grain shape variations across grain sizes.

In this paper, we introduce a systematic DEM study of the effects of the particle shape distribution on the mechanical behavior of granular materials. While previous works have used mono-size mixtures of different grain shapes (bi-shape or mixtures) [41,42], this work explores a wide range of gradings in samples presenting grain size-shape correlations. Despite the fact that our study motivation focuses on the critical shear strength of coarse granular materials, our outcomes and observations are also valuable to other granular mechanics problems such as determining the runout distance of dry granular flows [43] or the analysis of mechanisms behind grain segregation and layering [44].

This manuscript is organized as follows. In section 6.2, we introduce the material model and size-shape correlation that allowed us to build a set of 3D numerical samples, from mono-size to highly variable in particle sizes, and containing grain shapes from spheres to very angular polyhedra. In section 6.3, we analyze the macro-mechanical behavior of the numerical samples when subjected to triaxial shearing up to relatively large deformations. In Section 6.4, we use a series of micro-structural descriptors to characterize the effect of size-shape correlations on grain connectivity and force transmission mechanisms. We also identify the contribution each shape class makes to macroscopic shear strength. Finally, we conclude and draw perspectives of this work.

6.2 Numerical Model

6.2.1 Dispersity of grain size and shape

The dispersity of grain geometry and properties, also referred as to *polydispersity*, is common in natural and industrial granular materials [28, 45]. First, in terms of size variability of grains, the PSD is usually the preferred tool to quantify the size classes present in a material, based on the mass of sample coarser or finer than a certain size. However, the PSD alone does not provide any insight into particle shape properties. The grain shapes can be described by countless factors, being the most common the angularity, elongation, sphericity and roughness [20, 46].

In this work, we consider three-dimensional numerical assemblies with PSD varying from mono-size, uniform samples up to well-graded grain assemblies. The spectrum of particle shapes is varied from regular octahedral to perfect spheres. Figure 6.1 displays the six different shapes ($P1$ to $P6$) considered in this study. Note that the typical size of grain d is related to the circumscribing sphere around the grain.

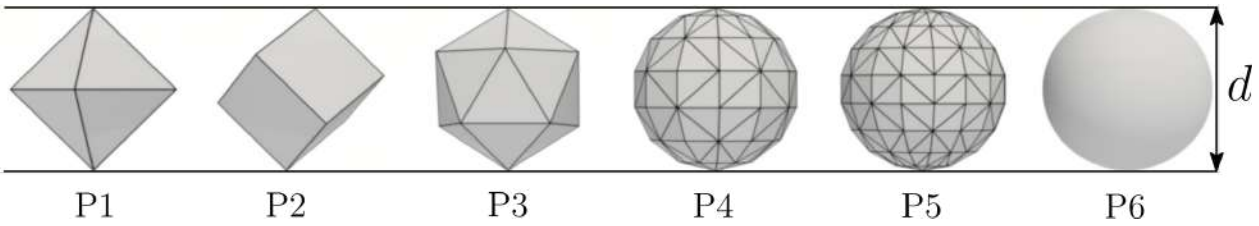

Figure 6.1 Set of different particle shapes considered in this work.

Table 6.1 Geometrical characteristics of grains $P1$ to $P6$. n_v is the number of vertices, n_f is the number of faces, V_P/V_s is the ratio between the volume of particle and the corresponding circumscribing sphere, A_P/A_s is the ratio between the particle surface area and that of the circumscribing sphere, and $\mathcal{S}$ is the sphericity, which denotes the ratio of the surface area of a sphere with equivalent volume to that of the given particle [47].

Particle	n_v	n_f	V_P/V_s	A_P/A_s	$\mathcal{S}$
P1	6	8	0.32	0.55	0.84
P2	8	12	0.37	0.64	0.80
P3	12	20	0.61	0.76	0.93
P4	74	144	0.91	0.95	0.98
P5	130	256	0.95	0.97	0.99
P6	Spheres	—	1	1	1

Table 6.1 displays a summary of some relevant geometrical properties of each particle, relative to a spherical shape. Note that the shapes selected for this work have different degrees of axial symmetry. For instance, particles $P1$ (octahedra), $P2$ (cube) and $P3$ (icosahedron) are platonic solids and all their faces have the same shape, while polyhedra $P4$ and $P5$ are symmetric at least along one of their axis. While we could have chosen other irregular or non-convex polyhedral shapes, there are a few factors motivating the current selection: (1) a gradual increment of vertices or sides of polyhedra is a simple strategy to modify the angularity of the grains, and more complex shapes might have required a set of multiple parameters for their geometrical description; (2) contact detection between polyhedra is not a trivial problem, and venturing into non-convex grain shapes implies using less optimized strategies to contact detection that would increase computational cost.

In terms of the relations between grain size and shape, two correlations were explored:

- **Case A:** larger grains are rounded while smaller ones are angular.

- **Case B:** larger grains are angular while smaller ones are rounded.

The choice of these correlations is not arbitrary. Experimental works focused on assessing grain size-shape correlations have observed that both correlations may exist in natural geological materials [20, 28], due to the configuration of mineral in the rock from which the grains derived. The process of creating correlated size-shape grains can be broken down into the following steps:

- **(i)** The PSD breadth is defined by selecting a maximum and minium particle diameter, $d_{\max}$ and $d_{\min}$, respectively, and the ratio $R_D = d_{\max}/d_{\min}$ varied from $R_D = 1$ (mono-size) to $R_D = 5.7$.
- **(ii)** The range $d_{\min}$ to $d_{\max}$ is divided into six and the particles shapes $P1$ to $P6$ are assigned to each sub-size. This produces a certain number of grains per size that ensures that a uniform particle distribution by mass is achieved. In other words, there are more particles in number of the finer class of grains than in the coarser class; see PSDs in Figure 6.2.
- **(iii)** Depending on whether Case A or B is being generated, an appropriate shape is assigned to each specific particle size d.

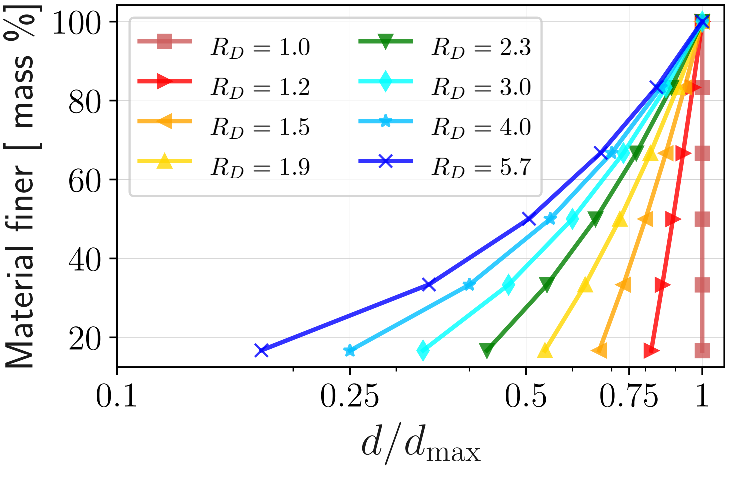

Figure 6.2 Particle size distribution (PSD) where each particle diameter d is normalized by the maximum particle diameter $d_{\max}$. The different curves correspond to different ratios $R_D = d_{\max}/d_{\min}$.

6.2.2 Particle simulation

This numerical study is developed on a discrete-element approach named non-smooth contact dynamics (NSCD). Different to ‘smooth’ DEM, such as that proposed by Cundall and Strack [32], the NSCD is a discrete method that considers particles as perfectly rigid bodies interacting through mutual exclusion and dry friction [33, 48, 49]. This approach removes the necessity for a regularized relationship between particle overlapping and contact force often characterized by contact stiffness and damping coefficients. Instead, the NSCD operates by considering interactions between grains being ruled by Newton’s coefficient of restitution and Coulomb’s friction law. In effect, the time-stepping strategy in NSCD relies on tracking changes in relative velocities between particles and momentum transfer, which can be integrated to find contact forces and body displacements. Although a complete rigidity of grains cannot be numerically assured, initializing each step with preceding force calculations reduces fluctuations below acceptable levels, generally falling beneath the numerical solution. For more details about the mathematical framework and numerical implementation of the NSCD method, please see Refs [50, 51].

The NSCD time-stepping is composed of three main ingredients: (i) contact detection, (ii) resolution of contact force and particle relative velocities, and (iii) update of body positions and forces. The contact detection is based on the distance between the particles, and this distance can be computed differently depending on the interaction type. In numerical assemblies composed of bodies of different angularity, from spheres to very angular particles, a variety of interactions can be produced as sphere-sphere, polyhedron-polyhedron, or sphere-polyhedron touch. Note that - still today - DEM simulations very often are developed using spherical grains or clumps of spheres that mimic more complex grain shapes. Real polyhedral grains are less common due to the complexity of interactions, limitations in computational power and management of the data structure whose size can be significant. In this work, we use full polyhedral bodies as well as an implementation that allows us to combine, for the first time in the frame of NSCD, polyhedra with spherical grains. Such a large variety of grain shapes and interactions is rarely seen in DEM simulations.

The simplest set of interactions that can occur in our simulations refers to touching sphere, where the distance between two spheres is calculated using the center-to-center distance and respective radii. More challenging is the contact detection between polyhedra, where the distance between a pair of bodies is determined by calculating a separation plane using Cundall’s “common plane” technique [52]. Such a method iteratively defines the plane that minimizes the distances from the vertices of each polyhedra to the separating plane [52]. Finally, the distance between a sphere and a polyhedron is calculated by projecting the sphere

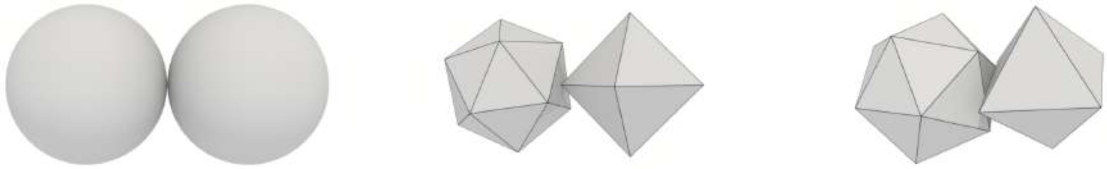

(a) point contact sphere-sphere (b) vertex to face (c) edge to face

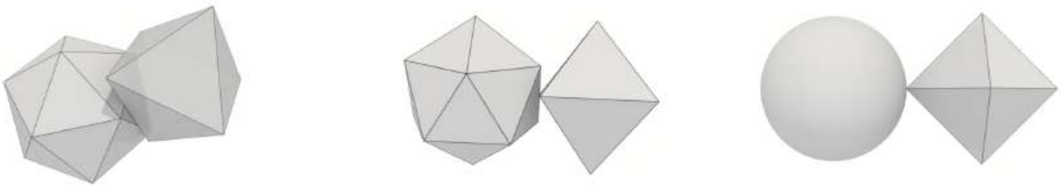

(d) face to face (e) edge to edge (f) vertex to sphere

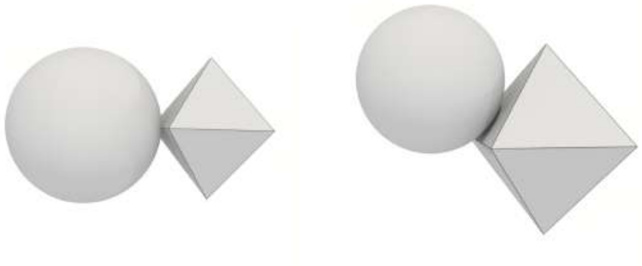

(g) edge to sphere (h) face to sphere

Figure 6.3 Contact types between spheres, polyhedra, and spheres in contact with polyhedra.

center onto the polyhedra surface, and determining the distance between the projected point and the polyhedron's center.

Eight different contact situations between particles can arise when including polyhedra and spheres in an assembly. Among sphere-sphere contacts we can find (a) point contacts; while between polyhedra we can find (b) vertex-to-face, (c) edge-to-face, (d) face-to-face and (e) edge-to-edge.; finally, between spheres and polyhedra we can find (f) point-to-vertex, (g) point-to-edge and (h) point-to-face. See Figure 6.3 for a schematic representation of each contact type. Note that single contact points represent all sphere-particle, vertex-face and edge-edge contacts, while in the numerical code two and three contact points are needed to describe edge-face and face-face contacts [53].

The contact force resolution in NSCD is an iterative process that stabilizes contact force and particle relative velocities fluctuations within a certain tolerance. The implicit nature of the time integrator makes it unconditionally stable. Only the time step (Δt) needs to be adapted for each simulation or set of boundary conditions, so it is a fraction of the collision time between particles τ_c. In practice, this is achieved by prescribing the relationship $\Delta t \ll \tau_c \approx d/v_{max}$, where d is the typical particle size and v_{max} is the maximum velocity a particle can reach at any given time.

6.2.3 Sample generation

Numerical samples for this study were created with a number of particles (N_p) that varied depending on the particle size distribution. N_p ranged between 10 000 for $R_D = 1$ to 25 000 for $R_D = 5.7$. Assemblies of grains were built by sequentially placing grains in a box of square base W and height D, using geometrical protocols [54, 55]. The box dimensions and scale followed the laboratory testing standard ASTM D7181, thus, keeping a consistent sample ratio $H/W = 2$ and a sample size that ensured a ratio $W/d_{\max} \geq 10$. Figure 6.4(a) shows a screenshot of a sample created following such a protocol.

In order to prepare the samples for triaxial shearing, they were previously compressed by applying controlled forces to rigid walls on all faces of the sample box up to an isotropic pressure $P = 10$ kPa. This compression is continued until the void ratio $e = V_v/V_s$ (V_v denotes the volume of voids and V_s the volume of solid grains) is stabilized. Figures 6.4(b) to (e) display screenshots of the samples after isotropic compression for the different size-shape correlations and R_D. During isotropic compression, gravity and friction between particles and walls were set to zero, so no internal pressure gradients are created and the applied stresses on the box correspond to principal stresses.

Drained triaxial shear tests were conducted by applying a constant vertical velocity (v_s) to the upper and lower walls, while lateral walls maintain constant confinement pressure P; see schematic representation of boundary conditions in Figure 6.5. Upon shearing, the interaction between grains was modeled using a Coulomb's dry frictional coefficient $\mu = 0.4$. The shearing rate was determined based on the inertial number $I = d\dot{\gamma}\sqrt{\rho/P}$, where $\rho = 2600$ kg/m^3 is the particle's density, $\dot{\gamma} = v_s/h_0$ is the shear rate and h_0 is the height of the sample after isotropic compression. In order to ensure a quasi-static shearing regime, the inertial number was set to 1×10^{-3} [56]. The axial strain $\varepsilon_a = \Delta h/h_0$, where Δh is the change in sample

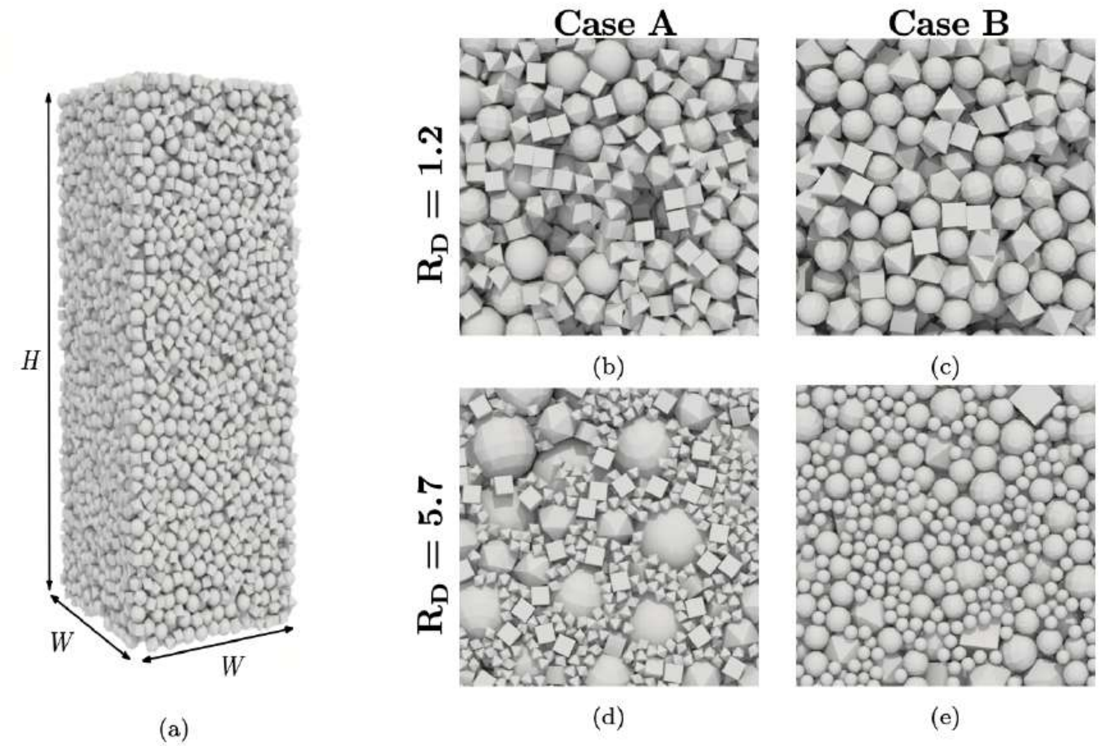

Figure 6.4 Screenshot of a sample after construction protocol for $R_D = 1$ (a); samples with particle size span $R_D = 1.2$ (b) and (c), and $R_D = 5.7$ (d) and (e) for different size-shape correlations.

height along the direction of shearing, reached 0.4 in all the simulations.

All the simulations were performed on the modeling platform LMGC90 [57,58], a free, open-source software capable of simulating discrete mechanical systems using the NSCD method.

6.3 Macroscopic mechanical behavior

The mechanical behavior was studied through measurements for stress, strain and deformation quantities during shearing. First, the volumetric strain was computed using its relationship with the sample's void ratio as $\varepsilon_v = (e - e_0)/(1 + e_0)$, where e_0 is void ratio after isotropic consolidation. Figure 6.6 illustrates the evolution of volumetric strain as a function of the applied vertical strain ε_a. At lower levels of axial deformation, samples with low R_D display an initial phase of contraction from $\varepsilon_a = 0$ to 0.15, followed by a period of dilatation. All specimens eventually reach a steady volumetric strain beyond $\varepsilon_a \approx 0.3$.

Secondly, the macroscopic mechanical response was characterized through the normalized shear stress q/p, where q is the deviatoric stress and p is the average pressure within an

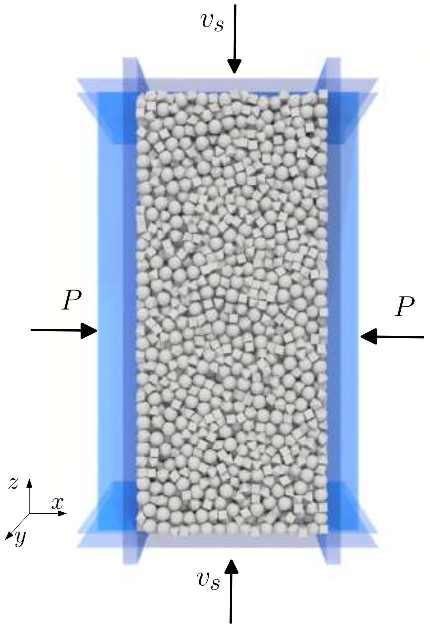

Figure 6.5 Schematic representation of triaxial boundary conditions employing rigid lateral walls around the sample.

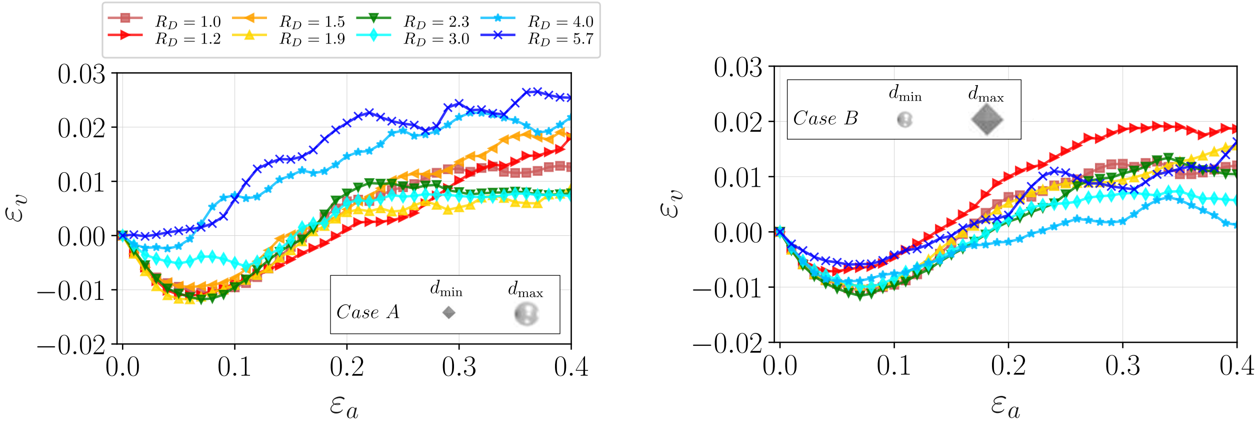

(a) Case A

(b) Case B

Figure 6.6 Evolution volumetric deformation ε_v for Cases A (a) and B (b) as a function of the axial deformation ε_a.

assembly. These quantities are measured using the granular stress tensor σ, defined as [59,60]:

$$\sigma_{ij} = \frac{1}{V} \sum_{\forall c} f_i^c \ell_j^c \ , \tag{6.1}$$

where f_i^c is the i component of the force at contact c, and ℓ_j^c is the j component of the branch vector, the vector joining the center of mass of touching particles at contacts c; these definitions are illustrated in Figure 6.7. We use the principal stresses of σ (i.e., σ_1, σ_2, σ_3) to calculate $q = (\sigma_1 - \sigma_3)$ and $p = (\sigma_1 + \sigma_2 + \sigma_3)/3$. The evolution of q/p as a function of the axial strain is presented Figure 6.8. We can observe a gradual increase in shear resistance in all cases up to $\varepsilon_a \approx 0.1$. Beyond this point, and despite some fluctuations, q/p reaches a steady value. The stress-strain behavior let us suggest that the set of granular samples consistently reach critical state after an axial strain $\varepsilon_a \approx 0.3$, as plastic shear deformations continue indefinitely under constant volume and stress state [61].

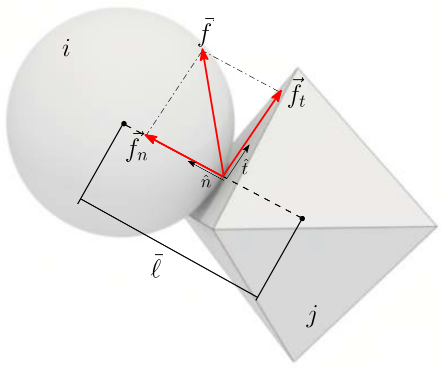

Figure 6.7 Schematic representation of two interacting grains, displaying the associated force and branch vectors.

To compare the size-shape correlation effects on the mechanical behavior, we plot in Figure 6.9(a) the evolution of the mean values for $\langle e \rangle$ and $\langle q/p \rangle$ at critical state, as a function of R_D. Note that $\langle e \rangle$ and $\langle q/p \rangle$ are computed using the last 10% of axial deformation ε_a. For $\langle e \rangle$, Case A exhibits a gradual decrease as function of R_D, while Case B displays a parabolic evolution, first increasing up to $R_D \approx 1.5$ and then gradually decreasing for larger grain size spans. This behavior is consistent with the results of previous studies, which showed that the void ratio of granular materials decreases as the R_D increases [55, 62]. This effect is clearly more pronounced in Case A since the smaller particles have angular shapes, allowing them to fit more closely together.

In terms of the normalized shear stress in the critical state $\langle q/p \rangle$, Figure 6.9(b) shows that shear strength is practically independent of R_D for Case A (around $\langle q/p \rangle \approx 1.2$), while Case B, it exhibits a drop in $\langle q/p \rangle$ as R_D increases. For the grain dispersion studied, Case A shows a similar behavior to that observed in mono-shape grain assemblies where critical shear strength remains unchanged for differences PSDs [22, 53]. Nevertheless, Case B shows

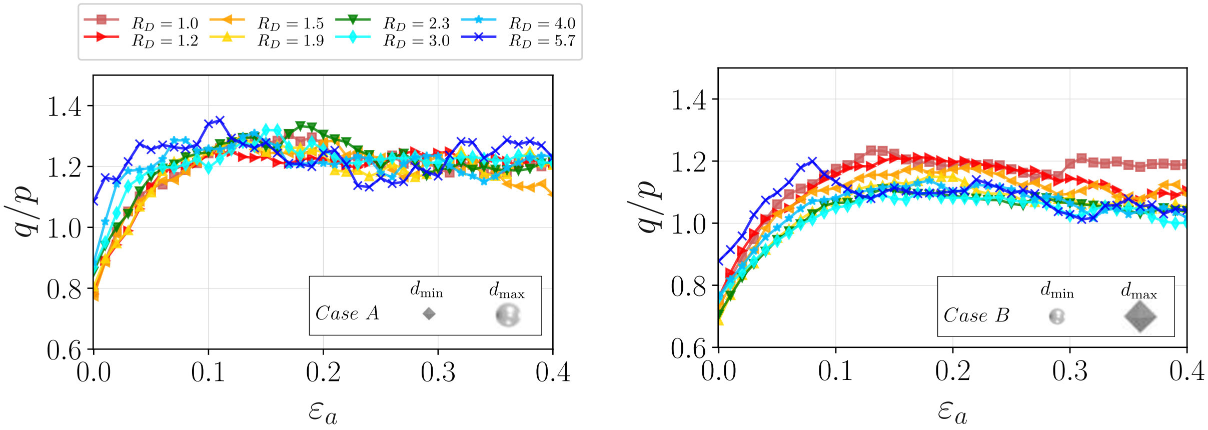

Figure 6.8 Evolution of the normalized shear stress q/p for size-shape correlations A and B, respectively, as a function of the axial deformation ε_a.

a counterintuitive behavior, where samples with larger angular grains and fine rounded ones are incapable of developing any larger strength when the grain size dispersion increases. While the behavior of correlations B were first observed numerically on 2D simulations [31], it is remarkable that these 3D simulations strongly differ from the 2D studies regarding correlations A.

In order to better understand the mechanisms at the origin of these macroscopic observations, the following sections explore the microstructural and micromechanical characteristics of the different samples during shear steady flow.

6.4 Characterization at the microscale

6.4.1 Connectivity

Particle connectivity refers to the degree to which solid grains are in contact with each other. The first indicator of connectivity we analyze is the number of load-bearing grains (N_p^*). Figure 6.10 illustrates screenshots of the specimens in the critical state for Cases A and B, with R_D values of 1.5 and 5.7. Load-bearing grains are visualized in gray, while no-force-bearing (floating) particles are displayed in black.

For both correlations A and B, we remark that fewer particles belong to the force-bearing structure as PSD becomes broader as small particles are able to fit in the void spaces between larger ones. Figure 6.11(a) shows the evolution of the ratio of force-bearing grains at critical state, with respect to the total number of grains in the sample (N_p^*/N_p) as a function of R_D. As expected, the ratio N_p^*/N_p decreases as R_D increases. There is only a slight increment

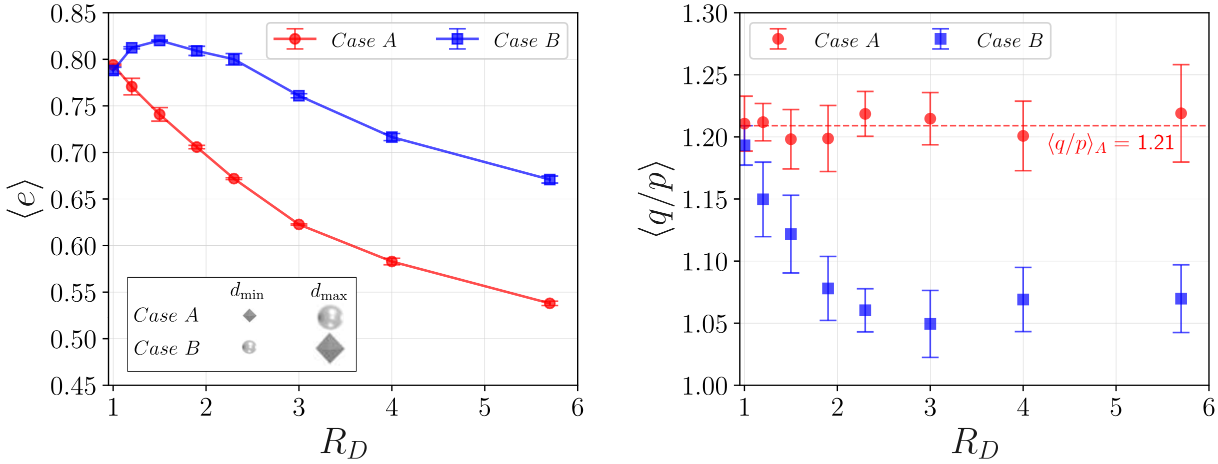

Figure 6.9 Critical state parameters: (a) evolution of mean void ratio $\langle e \rangle$ and (b) normalized mean shear strength in the critical state $\langle q/p \rangle$ as a function of grains size span R_D. Error bars display the standard deviation of the data.

of the proportion of grains engaged in force-bearing for Case B up to $R_D \approx 1.5$, presumably due to the capacity of large angular grains to reach more distant particles with their sharp edges. Such gain in connectivity is then lost as soon as the smaller grains start to rattle in the poral space and no longer contribute to force transmission.

Regarding mean number of contact per load-bearing grain or *coordination number* ($Z = 2N_c/N_p^*$, where N_c is the number of force-carrying contacts), Figure 6.11(b) presents the evolution of this parameter at critical state as R_D increases. For correlation A, Z seems to be not affected by the grain size distribution, presenting a value of $Z \simeq 3.5$. In contrast, in Case B Z shows an asymptotic trend, increasing from $Z = 3.5$ for $R_D = 1$ to $Z = 4.5$ for $R_D = 2$. It is again surprising that Case B presents a larger average number of contacts per grain at critical state, while the shear strength of such samples decreases with R_D. This behavior reveals that other microstructural elements, instead of the relatively simple scalar measure Z, must be acting together to explain the drop of macroscopic shear strength.

6.4.2 Force network

At the contact scale, a local framework $(\hat{n}, \hat{t})$ is formed by $\hat{n}$, the unit vector perpendicular to the contact plane between grains, and $\hat{t}$, an orthonormal unit vector oriented along the tangential force direction, as displayed in Figure 6.7. In such frame, interparticle forces can be defined as $\hat{f} = f_n\hat{n} + f_t\hat{t}$, where f_n and f_t are the normal and tangential contact forces,

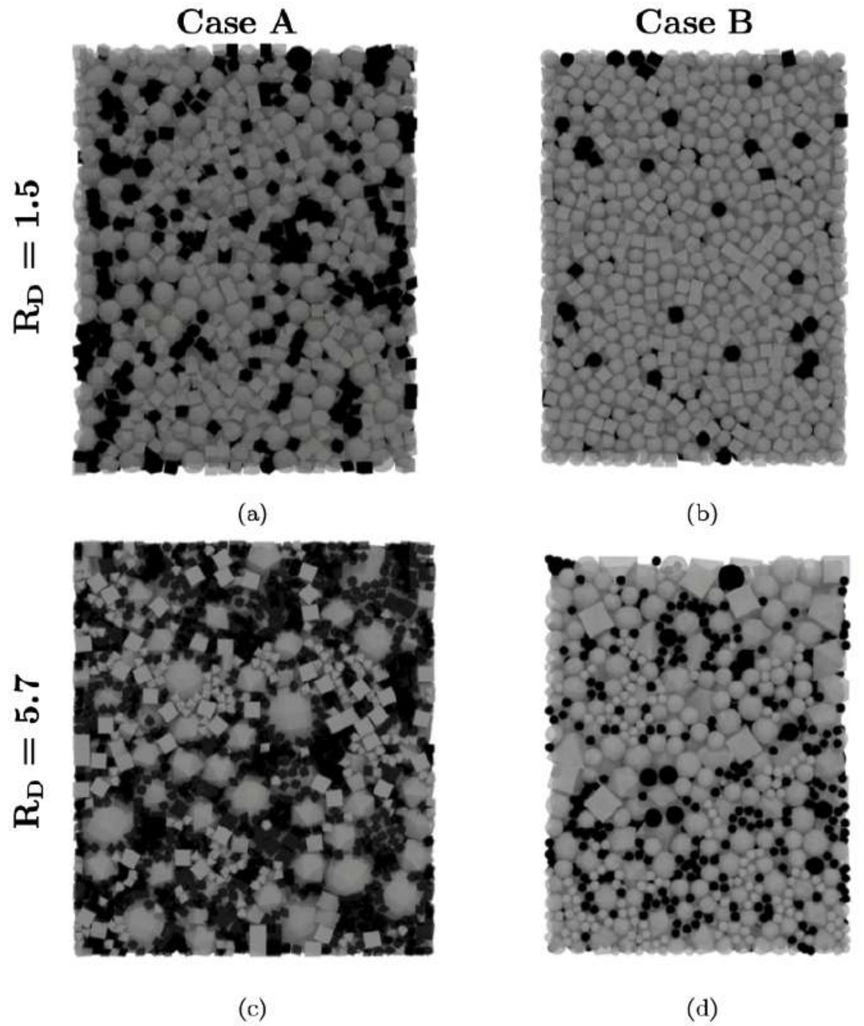

Figure 6.10 Screenshots of floating particles (black) and bearing-force particles (gray) for Case A (left) and Case B (b) for different grain size dispersion at critical state.

respectively.

Figure 6.12 illustrates a map of the normal forces at critical state, displayed as columns between the mass centers of touching grains. The thickness of the columns are related to the magnitude of the corresponding normal contact force. Visual inspection reveals the anisotropic and heterogeneous nature of these force networks. In Case A, where smaller particles are angular and larger ones are rounded, the heterogeneity of contact forces appears to be amplified at higher values of R_D. However, in Case B there are no major differences in force network architecture as R_D changes (see Figures 6.12b and 6.12d). This finding, together with the connectivity analysis in the previous section, indicates that a class of fine rounded particles improves connectivity at critical state and contributes to a more uniform

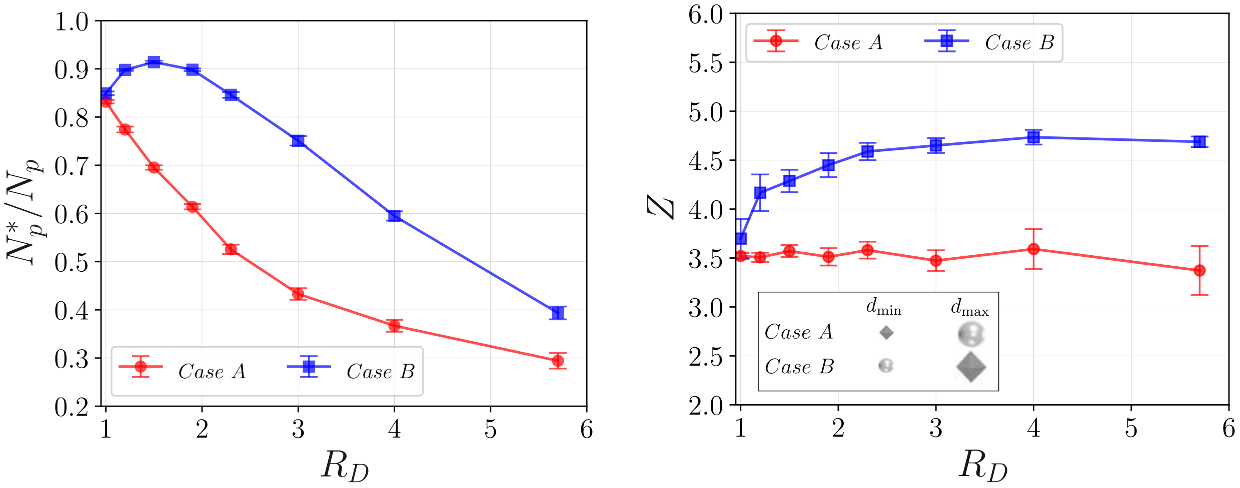

Figure 6.11 Evolution of (a) ratio of particles engaged in force transmission respect to the total number of particles in the sample and (b) coordination number as a function of grain size span R_D, both measured at critical state.

force distribution in our granular samples.

Force distribution within a granular assembly is commonly studied through the probability density function (PDF) of contact force magnitudes, generally exhibiting two features: (i) the PDF generally follows a decreasing exponential pattern of forces exceeding the average; (ii) for forces below the mean, the probability of having small-magnitude forces does not decline to zero [63, 64].

Figure 6.13 shows the probability density functions of normal forces $P(f_n)$ in log-linear scales for cases A and B at critical state, normalized by the mean normal force $\langle f_n \rangle$. For Case A, we note an important increase in the capability of the grain assembly to transmit larger forces as R_D increases. Samples with a broad particle size distribution can present forces up to three times the maximum forces observed in a mono-size sample. On the other hand, Case B presents only a slight increase in force magnitude as R_D increases. These figures are in agreement with the previous observations in grain connectivity and force network at critical state.

6.4.3 Fabric and contact and force anisotropies

To understand the drop of critical strength for Case B as a function of S and the apparent independence of strength on S for case A, it is useful to use the decomposition of the granular stress tensor in terms of micromechanical descriptors, following the works of Oda [65] and

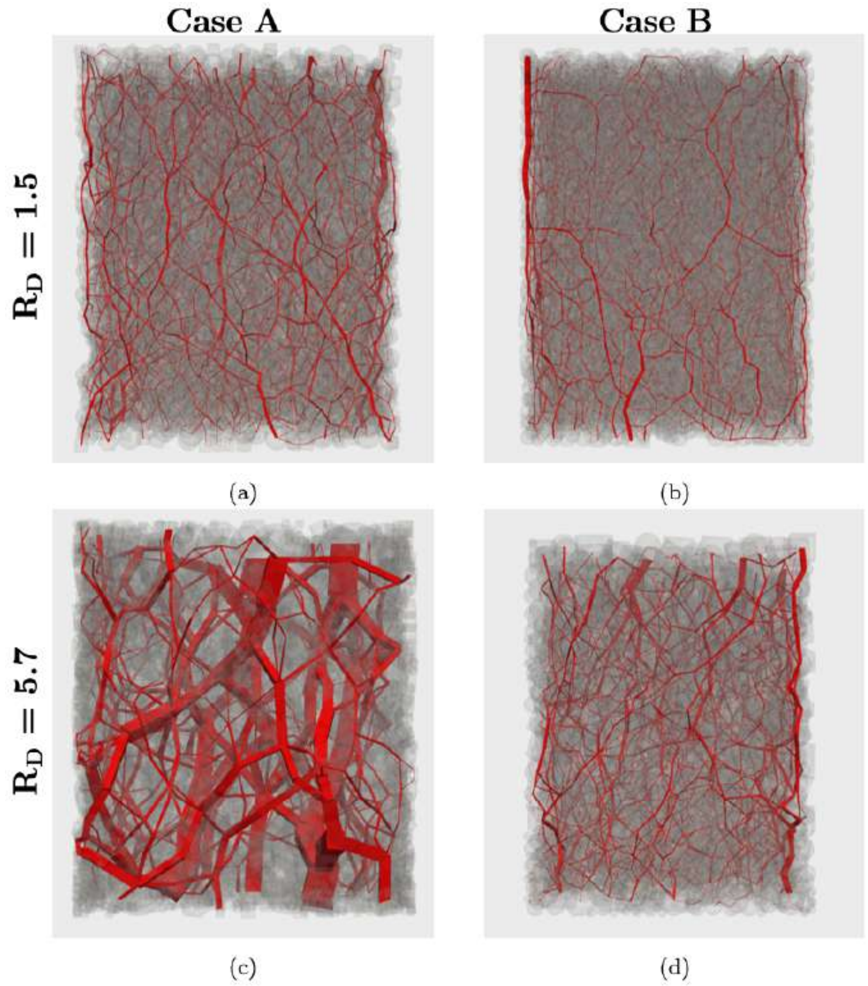

(a) (b) (c) (d)

Figure 6.12 Screenshots of force network at critical state for Case A (left) and Case B (b) for different grain size rations R_D. The red connections between the centers of touching grains represent the normal forces whose thickness is proportional to magnitude of normal forces.

Rothenburg & Bathurst [66]. This approach is based on the fact that contacts, forces and branch vectors have distributions in space that can be described using harmonic functions.

First, the contact anisotropy (a_c) represents the excess of contacts oriented in a certain direction and the lack of contacts along the perpendicular direction. This anisotropy is linked to the Fabric tensor (F_{ij}), which is defined based on the contact normal vectors $\hat{n}$ as:

$$F_{ij} = \frac{1}{N_c} \sum_{c \in V} n_i^c n_j^c \ , \tag{6.2}$$

so $a_c = 5/6(F_{33} - F_{11})$, where F_{33} is the component of the fabric tensor in the vertical direction (i.e., along axis z) and F_{11} is the horizontal component (along axis x).

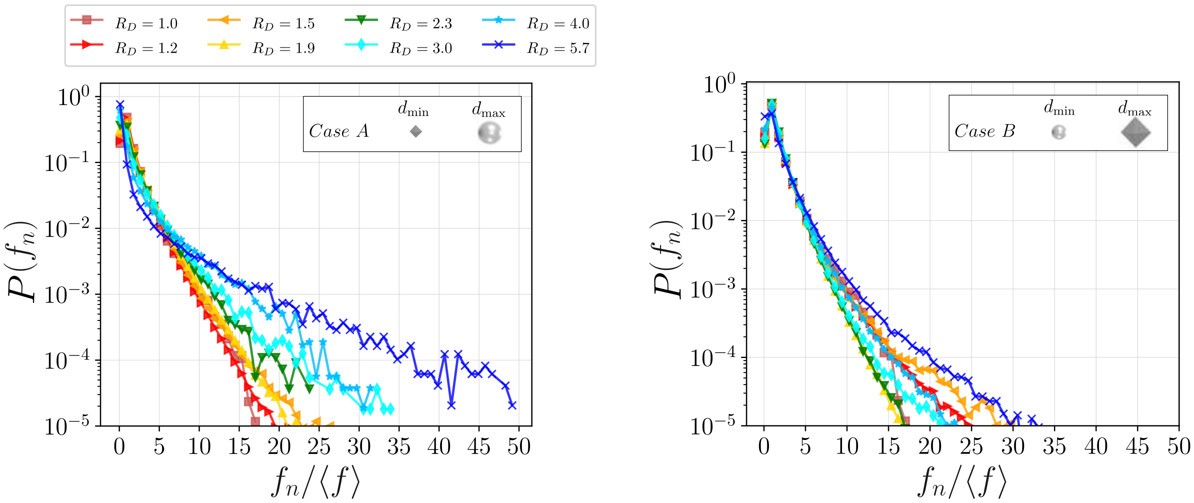

Figure 6.13 Probability density functions of normal contact forces at critical state in log-linear scales for Case A (a) and Case B (b).

Secondly, the geometric arrangement of grains of different shapes and sizes leads to vector branch lengths that can vary in space and present preferred orientations. Consider the branch vector (i.e., the vector connecting the centers of two touching particles) represented in the contact framework as $\hat{\ell} = \ell_n \hat{n} + \ell_t \hat{t}$, where ℓ_n is the branch projection on the normal contact orientation, and ℓ_t is the branch projection on the tangential orientation to the contact. In this case, the anisotropy of branch orientations needs to be considered for its normal and tangential components. In other words, this anisotropy is associated to two different tensors defined as:

$$L^n_{ij} = \frac{1}{\langle \ell_n \rangle} \sum_{c \in V} \ell^c_n n^c_i n^c_j \ , \tag{6.3}$$

and

$$L^t_{ij} = \frac{1}{\langle \ell_n \rangle} \sum_{c \in V} \ell^c_t n^c_i t^c_j \ , \tag{6.4}$$

where $\langle \ell_n \rangle$ is the average branch length projected onto the normal contact orientation. Using these definitions, the associated anisotropy in branch length orientations is simply defined as $a_{\ell_n} = \frac{5}{6} \frac{L^n_{11} - L^n_{33}}{L^n_{11} + L^n_{22} + L^n_{33}} - a_c$ and $a_{\ell_t} = \frac{5}{6} \frac{L_{11} - L_{33}}{L_{11} + L_{22} + L_{33}} - a_c - a_{\ell_n}$, where L^n_{ij} corresponds to the ij component of the tensor L^n, and L_{ij} corresponds to the ij component of the tensor $L_{ij} = L^n_{ij} + L^t_{ij}$.

Finally, anisotropies in the orientation of contact forces can also be represented using similar tensors, defined as

$$\xi^n_{ij} = \frac{1}{\langle f_n \rangle} \sum_{c \in V} f^c_n n^c_i n^c_j \tag{6.5}$$

and

$$\xi^t_{ij} = \frac{1}{\langle f_n \rangle} \sum_{c \in V} f^c_t n^c_i t^c_j \ . \tag{6.6}$$

The corresponding anisotropies of normal and tangential force magnitudes can be found as $a_{f_n} = \frac{5}{6}\frac{\xi^n_{11}-\xi^n_{33}}{\xi^n_{11}+\xi^n_{22}+\xi^n_{33}} - a_c$ and $a_{f_t} = \frac{5}{6}\frac{\xi_{11}-\xi_{33}}{\xi_{11}+\xi_{22}+\xi_{33}} - a_c - a_{ft}$, where ξ^n_{ij} corresponds to the ij component of the tensor ξ^n and ξ_{ij} corresponds to the ij component of the tensor $\xi_{ij} = \xi^n_{ij} + \xi^t_{ij}$.

The variables a_c, a_{ℓ_n}, a_{ℓ_t}, a_{f_n} and a_{f_t} not only provide indicators for the degree of anisotropy in spacial orientations for each of their corresponding parameters. They also have a deeper connection with the stress state. As shown analytically and validated in the literature [30, 66–69], their relationship with q/p reads as follows:

$$\frac{q}{p} = \frac{6}{5}(a_c + a_{\ell_n} + a_{\ell_t} + a_{f_n} + a_{f_t}) \ . \tag{6.7}$$

This remarkable property allows us to understand the underlying geometrical and mechanical mechanisms at the origin of macroscopic critical shear strength variations discussed before.

Figure 6.14(a) shows the evolution of a_c, a_{ℓ_n},a_{ℓ_t}, a_{fn} and a_{ft} as a function of R_D for both Cases A and B at critical state. In terms of geometrical anisotropies, we observe that a_c decreases as the grain size dispersion increases, which suggests that adding small particles to the assemblies contributes to creating contacts more homogeneously in all orientations. This phenomenon occurs despite the fact that many of the small particles may rattle the poral space during shearing. In any case, the drop in contact orientation anisotropy is relatively similar in both correlations A and B. For branch length anisotropies, similar trends are observed for both cases A and B, with a slightly increment in their values as the grain size ratio R_D increases. This behavior is simply due to the fact that branch lengths have all the same length for mono-size grains, but, as the grain size dispersion broadens, different branch lengths can be created as particles of different classes interact.

In terms of mechanical anisotropies, the tangential force anisotropy a_{f_t} surprisingly remains constant for both cases, with a value of $a_{f_t} \simeq 0.15$. This suggests that the mobilization of friction forces is not significantly affected by the size span and varied grain shapes. In contrast, the anisotropy related to the normal contact force a_{f_n} shows rather different trends for both cases of size-shape correlations. For Case A, a_{f_n} gradually increases as R_D increases, while the variations of this parameter in Case B are substantially smaller. This behavior is linked to the force distributions displayed in Figure 6.13, where the force network shows a more heterogenous spacial distribution in Case A, while the architecture of the networks remains quite similar across different PSDs in Case B.

In Figure 6.14(b), the macroscopic critical shear strength is presented using the granular stress tensor (Eq. (6.1)) and its approximation based on the addition of anisotropies (Eq. (6.7)). As observed in the figure, the microscopic description of anisotropies exhibit a very good match with the critical shear strength measures via $\langle q/p \rangle$. Only small differences are observed as the grain size distribution becomes broader, still the values lie within the error bars for the data in the steady flow state.

We can now conclude that, for Case A, the increments in a_{f_n} are offset by the drop in a_c, which explains why the macroscopic shear strength remains constant with R_D. A similar behavior has been observed in mono-shape samples, where $\langle q/p \rangle$ does not depend on PSD because the increase in a_{f_n} is matched by the decrease in a_c [53, 64]. For Case B, such a compensation between geometric and mechanic anisotropies only partially occurs for certain grain size ratios R_D. Before $R_D \approx 3$, we observe that both the contact orientation and normal force anisotropies gradually decrease as grain size dispersion increases. Only once $R_D \geq 3$, a_{f_n} is able to increase and can compensate further reductions in a_c. This behavior highlights the underrated role that rounded fine grains were thought to play in polydisperse granular assemblies up to date.

6.5 Conclusions

This research investigated the mechanical behavior of granular assemblies presenting correlations between the size and shape of grains. Two distinct correlations, labeled Case A and Case B, were examined. In Case A, fine grains are more angular than coarse ones, whereas in Case B, fine grains are rounder. The study also considers granular assemblies ranging from mono-sized to polydisperse with a maximum size ratio $d_{\max}/d_{\min} \simeq 6$. Utilizing the discrete-element method known as non-smooth contact dynamics, three-dimensional granular assemblies were built and tested under triaxial shearing conditions, reaching an accumulated axial deformation of $\varepsilon_a = 0.4$.

The investigation of the shear behavior in steady flow state revealed that size-shape correlations significantly - and counterintuitively - influence the mechanical response of granular materials. In Case A, shear strength remains practically unchanged as grain size dispersion increases, whereas Case B exhibits a decline in shear strength with increasing grain size span.

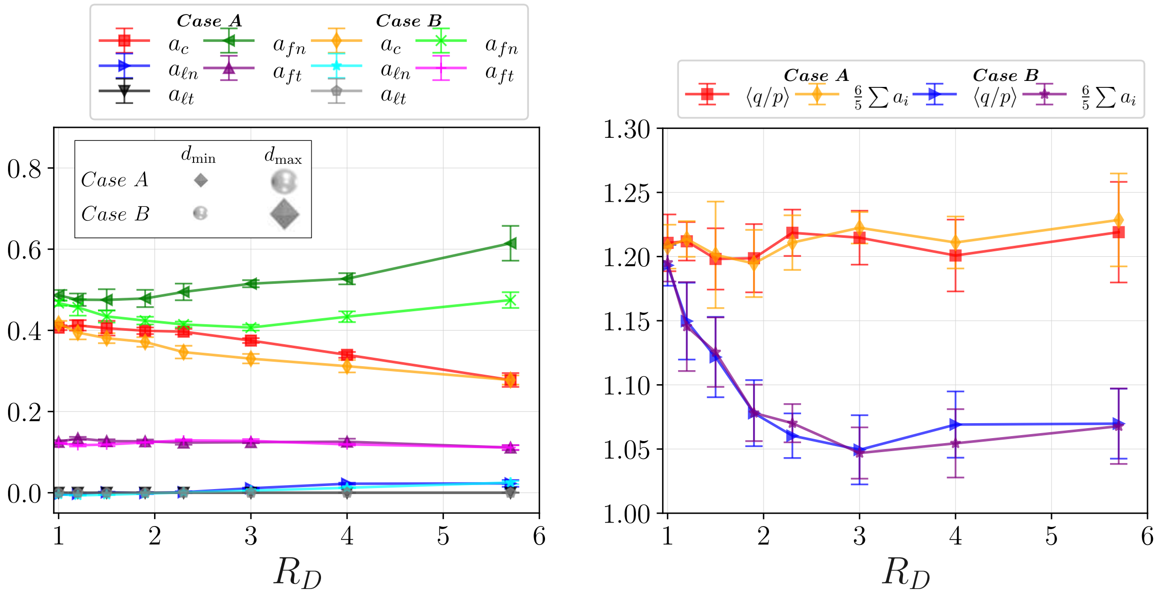

Figure 6.14 Microstructural descriptors at critical state: (a) evolution of geometrical and mechanical anisotropies as a function of the grain size ration R_D; (b) comparison between $\langle q/p \rangle$ computed using the granular stress tensor (Eq. (6.1)) and its decomposition in microscopic anisotropies (Eq. (6.7)).

This behavior is accompanied by complex microstructural mechanisms linked to contact organization and force transmission mechanisms. For instance, the loss of macroscopic shear strength in Case B occurs together with particles having more contacts on average. Conversely, Case A showed a rather constant coordination number as grain size dispersion increased.

Further analysis involved decomposing the granular stress tensor in terms of microstructural anisotropies that take into account the heterogenous distribution in space of contacts and forces between grains. This approach has been systematically employed in the literature and was successfully validated in this work. In particular, it was found that the anisotropy linked to contact orientations and normal force magnitudes primarily drive variations in macroscopic shear strength. This detailed microscopical analysis helped us reveal that smaller grains may have a larger role in mechanical strength than previously considered. While for mono-shape granular assemblies the smaller grains are mainly considered to belong to the class of grains that likely to rattle in the poral space, this simplified vision seems no longer sufficient when dealing with assemblies of grains with varied particle shapes. In particular, it seems that small rounded grains have a lubricating effect that restrain assemblies with coarse angular grains (Case B) from developing larger shear strengths. In turn, assemblies of large rounded grains with a class of angular fine grains (Case A) are also limited from developing larger shear strengths, although they do not show any relevant change in macroscopic shear strength as the grain size dispersion is broadened.

Future studies in the vein of this work should explore more realistic mechanisms that may modify the mechanical behavior of granular matter. In particular, grains with different sizes and shapes are prone to wear and break as the material is sheared. For this, different fragmentation models can be implemented along the grain size-shape correlations. Experimental validation is certainly also critical and highly wanted in order to highlight the relevance of a discrete-element approach. Finally, the poral space is another element to explore in these assemblies where the geometry and size of pores can be strongly affected by variable grain size and shape composition. The analysis of this void space may be relevant for problems related to hydraulic conductivity or internal erosion.

Conflicts of Interest

The authors declare no conflicts of interest.

Data availability statement

The data supporting this study's findings are available from the corresponding author upon reasonable request.

Acknowledgements

This research work benefited from the financial support of the Natural Sciences and Engineering Research Council of Canada (NSERC) [Ref. RGPIN-2019-06118], the Fonds de recherche du Québec — Nature et technologies (FRQNT) through the 'Programme de recherche en partenariat sur le développement durable du secteur minier-II' [Ref. 2020-MN-281267], the industrial partners of the Research Institute on Mines and the Environment (RIME) UQAT-Polytechnique (irme.ca/en). This research was also partially enabled by Calcul Quebec (calculquebec.ca) and Compute Canada (computecanada.ca) support.

Bibliography

[1] R. Marsal, "Large scale testing of rockfill materials," *J. Soil Mech. Found. Div.*, vol. 93, no. 2, pp. 27–43, 1967.

[2] N. Barton and B. Kjærnsli, "Shear strength of rockfill," *J. Geotech. Eng.*, vol. 107, no. 7, pp. 873–891, 1981.

[3] M. Aubertin, B. Bussière, and L. Bernier, *Environnement et gestion des rejets miniers.* Presses Internationales Polytechnique, 2002.

[4] C. Ovalle, E. Frossard, C. Dano, W. Hu, S. Maiolino, and P. Y. Hicher, "The effect of size on the strength of coarse rock aggregates and large rockfill samples through experimental data," *Acta Mech.*, vol. 225, pp. 2199–2216, 2014.

[5] C. Ovalle, S. Linero, C. Dano, E. Bard, P.-Y. Hicher, and R. Osses, "Data compilation from large drained compression triaxial tests on coarse crushable rockfill materials," *J. Geotech. Geoenviron.*, vol. 146, p. 06020013, 9 2020.

[6] N. Marachi, C. Chan, and H. Seed, "Evaluation of properties of rockfill materials," *J. Soil Mech. Found. Div.*, vol. 98, no. 1, pp. 95–114, 1972.

[7] G. E. Bauer and Y. Zhao, "Shear strength tests for coarse granular backfill and reinforced soils," *Geotech. Test. J.*, vol. 16, no. 1, pp. 115–121, 1993.

[8] R. Verdugo and K. de La Hoz, "Strength and stiffness of coarse granular soils," in *Soil stress-strain behavior: Measurement, modeling and analysis.* Springer, 2007, pp. 243–252.

[9] W. Hu, C. Dano, P.-Y. Hicher, J.-Y. Le Touzo, F. Derkx, and E. Merliot, "Effect of sample size on the behavior of granular materials," *Geotech. Test. J.*, vol. 34, no. 3, pp. 186–197, 2011.

[10] S. Linero-Molina, L. Bradfield, S. G. Fityus, J. V. Simmons, and A. Lizcano, "Design of a 720-mm square direct shear box and investigation of the impact of boundary conditions on large-scale measured strength," *Geotech. Test. J*, vol. 43, p. 1463, 2020.

[11] L. A. Oldecop and E. E. Alonso, "Testing rockfill under relative humidity control," *Geotech. Test. J.*, vol. 27, no. 3, pp. 269–278, 2004.

[12] R. Osses, J. Pineda, C. Ovalle, S. Linero, and E. Sáez, “Scale and suction effects on compressibility and time-dependent deformation of mine waste rock material,” *Engineering Geology*, 2024, in press.

[13] H. Matsuoka, S. Liu, D. Sun, and U. Nishikata, “Development of a new in-situ direct shear test,” *Geotech. Test. J*, vol. 24, no. 1, pp. 92–102, 2001.

[14] C. Ovalle, G. Girumugisha, D. Cantor, and S. Ouellet, “Size effects assessment of mine waste-rock shear strength combining numerical, laboratory and in situ approaches,” in *SSIM 2023: Third International Slope Stability in Mining Conference.* Australian Centre for Geomechanics, 2023, pp. 291–300.

[15] A. B. Cerato and A. J. Lutenegger, “Specimen size and scale effects of direct shear box tests of sands,” *Geotech. Test. J.*, vol. 29, no. 6, pp. 507–516, 2006.

[16] S. Amirpour Harehdasht, M. N. Hussien, M. Karray, V. Roubtsova, and M. Chekired, “Influence of particle size and gradation on shear strength–dilation relation of granular materials,” *Can. Geotech. J.*, vol. 56, no. 2, pp. 208–227, 2019.

[17] D. Cantor and C. Ovalle, “Sample size effects on the critical state shear strength of granular materials with varied gradation and the role of column-like local structures,” *Géotechnique*, pp. 1–12, 2023, published Online: December 04, 2023. [Online]. Available: https://doi.org/10.1680/jgeot.23.00032

[18] G. Girumugisha, C. Ovalle, and S. Ouellet, “Sample size effect on shear strength of mine waste rock using the scalping method,” in *Geo-Congress 2024*, 2024, pp. 313–320.

[19] ASTM, *D7181-20: Standard Test Method for Consolidated Drained Triaxial Compression Test for Soils.* ASTM International Standar, 2020.

[20] S. Linero, S. Fityus, J. Simmons, A. Lizcano, and J. Cassidy, “Trends in the evolution of particle morphology with size in colluvial deposits overlying channel iron deposits,” in *EPJ Web of Conferences*, vol. 140. EPJ Web of Conferences, 2017, p. 14005.

[21] M. Meng, X. Duan, J. Shi, X. Jiang, L. Cheng, and H. Fan, “Influence of particle gradation and morphology on the deformation and crushing properties of coarse-grained soils under impact loading,” *Acta Geotech.*, vol. 18, no. 11, pp. 5701–5719, 2023.

[22] D. Muir Wood and K. Maeda, “Changing grading of soil: Effect on critical states,” *Acta Geotech.*, vol. 3, pp. 3–14, 2008.

[23] G. Li, C. Ovalle, C. Dano, and P.-Y. Hicher, “Influence of grain size distribution on critical state of granular materials,” in *Constitutive modeling of geomaterials.* Springer, 2013, pp. 207–210.

[24] J. Yang and X. D. Luo, “The critical state friction angle of granular materials: does it depend on grading?” *Acta Geotech.*, vol. 13, pp. 535–547, 6 2018.

[25] G.-C. Cho, J. Dodds, and J. C. Santamarina, “Particle shape effects on packing density, stiffness, and strength: Natural and crushed sands,” *J. Geotech. Geoenviron.*, vol. 132, no. 5, pp. 591–602, 2006.

[26] I. Cavarretta, M. Coop, and C. O’sullivan, “The influence of particle characteristics on the behaviour of coarse grained soils,” *Géotechnique*, vol. 60, no. 6, pp. 413–423, 2010.

[27] J. Yang and L. Wei, “Collapse of loose sand with the addition of fines: the role of particle shape,” *Géotechnique*, vol. 62, no. 12, pp. 1111–1125, 2012.

[28] C. Ovalle and C. Dano, “Effects of particle size–strength and size–shape correlations on parallel grading scaling,” *Géotech. Lett.*, vol. 10, no. 2, pp. 191–197, 2020.

[29] S. Linero, E. Azéma, N. Estrada, S. Fityus, J. Simmons, and A. Lizcano, “Impact of grading on steady-state strength,” *Géotech. Lett.*, vol. 9, no. 4, pp. 328–333, 2019.

[30] S. Carrasco, D. Cantor, and C. Ovalle, “Effects of particle size-shape correlations on steady shear strength of granular materials: The case of particle elongation,” *Int. J. Numer. Anal. Methods. Geomech.*, vol. 46, no. 5, pp. 979–1000, 2022.

[31] S. Carrasco, D. Cantor, C. Ovalle, and P. Quiroz-Rojo, “Shear strength of angular granular materials with size and shape polydispersity,” *Open Geomechanics*, vol. 4, pp. 1–14, 2023.

[32] P. Cundall and O. Strack, “A discrete numerical model for granular assemblies,” *Géotechnique*, vol. 29, no. 1, pp. 47–65, 1979.

[33] J. J. Moreau, “Unilateral contact and dry friction in finite freedom dynamics,” in *Non-smooth mechanics and Applications.* Springer, 1988, pp. 1–82.

[34] F. Nicot, F. Darve, and R. Group, “A multi-scale approach to granular materials,” *Mech. Mater.*, vol. 37, no. 9, pp. 980–1006, 2005.

[35] E. Azéma, F. Radjai, and F. Dubois, “Packings of irregular polyhedral particles: Strength, structure, and effects of angularity,” *Phys. Rev. E*, vol. 87, no. 6, p. 062203, 2013.

[36] K. Wu, W. Sun, S. Liu, and G. Cai, "Influence of particle shape on the shear behavior of superellipsoids by discrete element method in 3d," *Adv. Powder Technol.*, vol. 32, no. 11, pp. 4017–4029, 2021.

[37] P. Adesina, C. O'Sullivan, and T. Wang, "Dem study on the effect of particle shape on the shear behaviour of granular materials," *Comput. Part. Mech.*, pp. 1–20, 2023.

[38] Z. Nie, Y. Zhu, X. Wang, and J. Gong, "Investigating the effects of fourier-based particle shape on the shear behaviors of rockfill material via dem," *Granul. Matter*, vol. 21, pp. 1–15, 2019.

[39] M. Q. Xu, N. Guo, and Z. X. Yang, "Particle shape effects on the shear behaviors of granular assemblies: irregularity and elongation," *Granul. Matter*, vol. 23, no. 2, p. 25, 2021.

[40] M. Fan, D. Su, and X. Chen, "Framework for incorporating multi-level morphology of particles in dem simulations: independent control of polydisperse distributions of roundness and roughness while preserving form distributions in granular materials," *Acta Geotech.*, pp. 1–24, 2024.

[41] J. Gong, X. Pang, Y. Tang, Z. Yang, J. Jiang, and X. Ou, "Effects of angularity and content of coarse particles on the mechanical behaviour of granular mixtures: a dem study," *Granul. Matter*, vol. 26, no. 1, p. 17, 2024.

[42] E. Illana, K. Qyteti, M. Scharnowski, M. Brömmer, S. Wirtz, and V. Scherer, "Shape-changing particles for locally resolved particle geometry in dem simulations," *Particuology*, vol. 89, pp. 185–190, 2024.

[43] J.-Y. Nie, Y. Cui, Z. Wu, L. Zhang, and J. Fang, "Dem study on role of fines in mobility of dry granular flows considering particle size-shape correlation," *Comput. Geotech.*, vol. 166, p. 105980, 2024.

[44] H. A. Makse, S. Havlin, P. R. King, and H. E. Stanley, "Spontaneous stratification in granular mixtures," *Nature*, vol. 386, no. 6623, pp. 379–382, 1997.

[45] J. Zhao, S. Zhao, and S. Luding, "The role of particle shape in computational modelling of granular matter," *Nature Reviews Physics*, vol. 5, no. 9, pp. 505–525, 2023.

[46] V. Angelidakis, S. Nadimi, and S. Utili, "Shape analyser for particle engineering (shape): Seamless characterisation and simplification of particle morphology from imaging data," *Comput. Phys. Commun.*, vol. 265, p. 107983, 2021.

[47] H. Wadell, "Sphericity and roundness of rock particles," *J. Geol.*, vol. 41, no. 3, pp. 310–331, 1933.

[48] M. Jean and J. J. Moreau, "Unilaterality and dry friction in the dynamics of rigid body collections," in *1st Contact Mechanics International Symposium.* 1st Contact Mechanics International Symposium, 1992, pp. 31–48.

[49] F. Dubois, V. Acary, and M. Jean, "The contact dynamics method: A nonsmooth story," *C. R. Mécanique*, vol. 346, no. 3, pp. 247–262, 2018.

[50] M. Renouf, F. Dubois, and P. Alart, "A parallel version of the non smooth contact dynamics algorithm applied to the simulation of granular media," *J. Comput. Appl. Math.*, vol. 168, no. 1-2, pp. 375–382, 2004.

[51] F. Radjai and V. Richefeu, "Contact dynamics as a nonsmooth discrete element method," *Mech. Mater.*, vol. 41, no. 6, pp. 715–728, 2009, advances in the Dynamics of Granular Materials.

[52] F. Dubois, "Numerical modeling of granular media made of polyhedral particles," 2011.

[53] D. Cantor, E. Azéma, and I. Preechawuttipong, "Microstructural analysis of sheared polydisperse polyhedral grains," *Phys. Rev. E*, vol. 101, p. 062901, Jun 2020.

[54] R. Jullien, A. Pavlovitch, and P. Meakin, "Random packings of spheres built with sequential models," *J. Phys. A Math. Theor.*, vol. 25, no. 15, p. 4103, 1992.

[55] C. Voivret, F. Radjai, J.-Y. Delenne, and M. S. El Youssoufi, "Space-filling properties of polydisperse granular media," *Phys. Rev. E*, vol. 76, no. 2, p. 021301, 2007.

[56] GDR-MiDi, "On dense granular flows," *Eur. Phys. J. E*, vol. 14, pp. 341–365, 2004.

[57] F. Dubois, M. Jean, M. Renouf, R. Mozul, A. Martin, and M. Bagnéris, "LMGC90," in *10e colloque national en calcul des structures.* 10e colloque national en calcul des structures, 2011, p. 8 p.

[58] F. Dubois, M. Jean, and et al, "LMGC90 wiki page," `https://git-xen.lmgc.univ-montp2.fr/lmgc90/lmgc90_user/wikis/home`, 2023, [Online; accessed 2-Jul-2024].

[59] B. Andreotti, Y. Forterre, and O. Pouliquen, *Granular media: between fluid and solid.* CUP, 2013.

[60] F. Nicot, N. Hadda, M. Guessasma, J. Fortin, and O. Millet, “On the definition of the stress tensor in granular media,” *Int. J. Solids Struct.*, vol. 50, no. 14-15, pp. 2508–2517, 2013.

[61] A. N. Schofield and P. Wroth, *Critical state soil mechanics.* McGraw-hill London, 1968, vol. 310.

[62] E. Azéma, S. Linero, N. Estrada, and A. Lizcano, “Shear strength and microstructure of polydisperse packings: The effect of size span and shape of particle size distribution,” *Phys. Rev. E*, vol. 96, 8 2017.

[63] V. Richefeu, M. S. El Youssoufi, E. Azéma, and F. Radjai, “Force transmission in dry and wet granular media,” *Powder Technol.*, vol. 190, no. 1-2, pp. 258–263, 2009.

[64] D. Cantor, E. Azéma, P. Sornay, and F. Radjai, “Rheology and structure of polydisperse three-dimensional packings of spheres,” *Phys. Rev. E*, vol. 98, no. 5, p. 052910, 2018.

[65] M. Oda, “Fabric tensor for discontinuous geological materials,” *Soils Found.*, vol. 22, no. 4, pp. 96–108, 1982.

[66] L. Rothenburg and R. J. Bathurst, “Analytical study of induced anisotropy in idealized granular materials,” *Géotechnique*, vol. 39, no. 4, pp. 601–614, 1989.

[67] F. Radjai and V. Richefeu, “Bond anisotropy and cohesion of wet granular materials,” *Philosophical Transactions of the Royal Society A: Mathematical, Physical and Engineering Sciences*, vol. 367, no. 1909, pp. 5123–5138, 2009.

[68] C. Voivret, F. Radjai, J. Y. Delenne, and M. S. El Youssoufi, “Multiscale force networks in highly polydisperse granular media,” *Phys. Rev. Lett.*, vol. 102, p. 178001, 2009.

[69] N. Guo and J. Zhao, “The signature of shear-induced anisotropy in granular media,” *Comput. Geotech.*, vol. 47, pp. 1–15, 2013.

CHAPTER 7 DISCUSSION

The behavior of granular materials is a complex topic that has been the subject of extensive research in various fields, including civil engineering, powder technology, and geophysics. A crucial aspect of granular systems is the influence of particle size and shape on their macroscopic and microscopic properties [196]. DEM simulations have emerged as a powerful tool for investigating these intricate relationships, allowing researchers to explore the micromechanics of granular assemblies in a level of detail that is often challenging to achieve through physical experiments [39].

7.1 Rethinking the main findings

DEM simulations using the CD method consider rigid particles interacting through a dry-fictional contact law (e.g., the Mohr-Coulomb model), with inter-particle friction of $\mu = 0.4$ in our case. This simple yet robust model allowed us to isolate the effects of particle size and shape, defining basic grain geometries. It is worth noting that we were not trying to simulate real rock clasts, but merely identifying the trends in strength while grain sizes and shapes vary within a granular media.

To fill the gap of systematic studies on the combined effects of shape and size using DEM, two 2D case studies showed concluding results: (i) particle elongation and (ii) particle angularity.

(i) Correlating size and grain elongation: when coarser particles were elongated and finer grains were circular, ϕ_c decreased from 25° to 20° as S increased from 0 to 0.9 (Figure 7.1(a)). The analyses indicated that elongated particles tend to create significant void spaces and reduce the overall packing density of the granular assembly. Despite their potential to fill these voids, the fine circular grains did not provide sufficient interlocking to enhance strength. On the other hand, when coarser particles were circular and finer grains were elongated, ϕ_c increases from 25° to 29° as S increases from 0 to 0.9. In this case, coarse circular particles formed a stable contact network due to their ability to roll and adjust into a dense packing arrangement, while finer elongated grains fitted into the voids between circular particles, enhancing interlocking and frictional resistance.

(ii) Correlating size and grain angularity: if the granular assembly had coarse rounded particles and fine angular grains, ϕ_c increased from 21° to 28° as S increased from 0 to 0.9 (Figure 7.1(b)). This behavior can be attributed to enhanced interlocking provided by the angular fine grains, which efficiently fit within the voids created by the larger rounded parti-

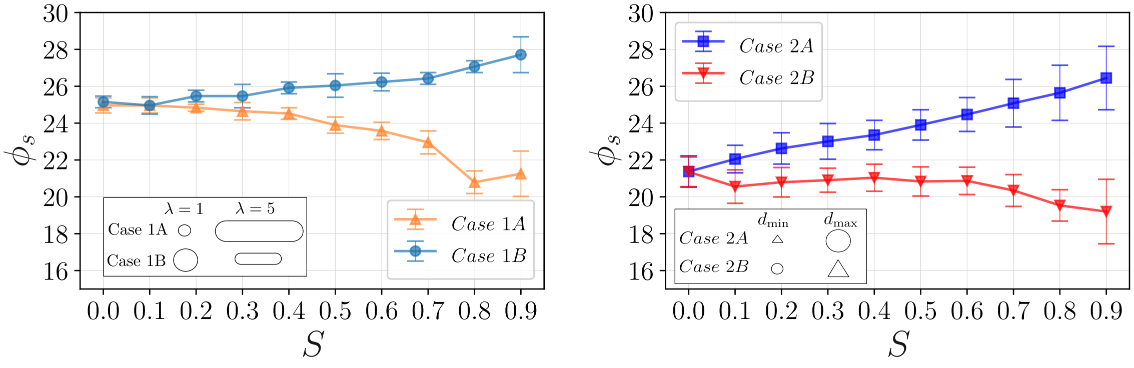

(a)

(b)

Figure 7.1 Evolution of ϕ_c as a function of S for grain size-shape correlation based on particle (1) elongation and (2) angularity. Error bars represent the standard deviation of the data.

cles. The rounded particles formed a stable structure that provided a supportive framework, while the angular grains contributed to increased mechanical interlocking. Conversely, when the assembly comprised coarse angular particles and fine rounded grains, ϕ_c decreased from 21° to 18° as S increased from 0 to 0.9. Here, coarse angular particles created a strong framework, but the fine rounded grains did not interlock efficiently, leading to decreased shear strength as the size span increased.

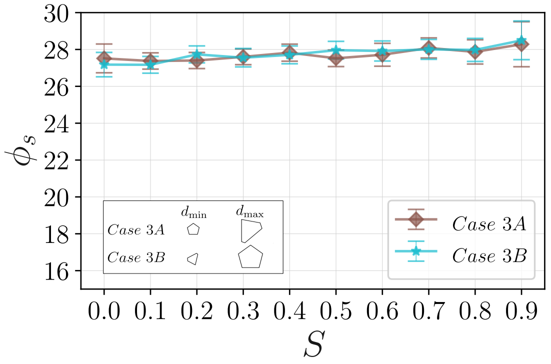

Figure 7.2 Evolution of ϕ_c as a function of S for grain size-shape correlation based on pentagon irregularity. Error bars represent the standard deviation of the data.

As shown in Figure 7.2, the lack of substantial modification of ϕ_c due to size-shape correlation based on irregularity suggests that irregular pentagonal shapes may not introduce enough grain shape variation to significantly alter the critical friction angle.

A last case explored the effects of size-shape correlations in 3D granular assemblies, focusing on coarse rounded particles and fine angular grains, analogous to our 2D analyses. The me-

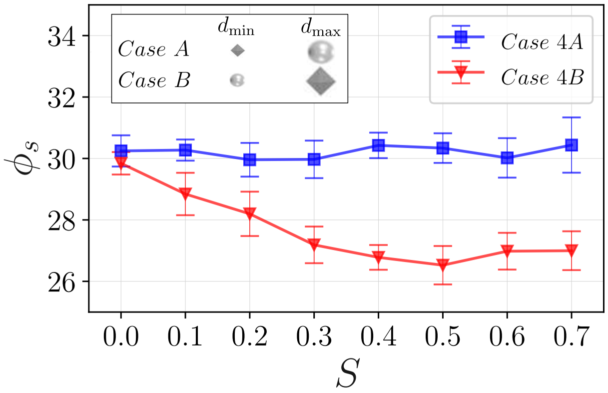

Figure 7.3 Evolution of ϕ_c as a function of S for grain size-shape correlation based on angularity in 3D. Error bars represent the standard deviation of the data.

chanical response in 3D assemblies exhibited trends similar to those observed in 2D systems (Figure 7.3). When fine grains were angular, ϕ_c remained consistent as S increased, maintaining a friction angle of 30° across the range, which is similar to most angular sands [34, 213]. This consistency is attributed to the angular fine particle fraction facilitating higher force transmission between particles, thereby maintaining constant connectivity despite increasing size dispersion. Conversely, ϕ_c declined with increasing S when fine grains were rounded, decreasing from 30° at $S = 0$ to 27° at $S = 0.7$. Microstructural analyses highlighted that this is due to the increased number of contacts per particle, leading to a less anisotropic force network and thus reduced overall strength.

In general, all the cases showed that samples with an angular fine fraction lead to increased strength compared to materials with a rounded fine fraction, thanks to enhanced interlocking in voids between coarse grains.

7.2 Comparison with previous studies

Yang & Wei [45] explored the role of particle shape in the shear behavior of sand-fines mixtures. Two types of fines, angular crushed silica fines, and rounded glass beads were mixed with two uniform quartz grains of sand (Toyoura sand and Fujian sand) to create four binary mixtures. The particle roundness of each material was measured, and the results are presented in Figure 7.4(a). The critical state friction angle slightly increased when angular fines were used in the mixture, while it decreased with rounded fines, as shown for Toyoura sand in Figure 7.4(b). This is consistent with our results, where angular fines promote interlocking and thus enhanced strength [205].

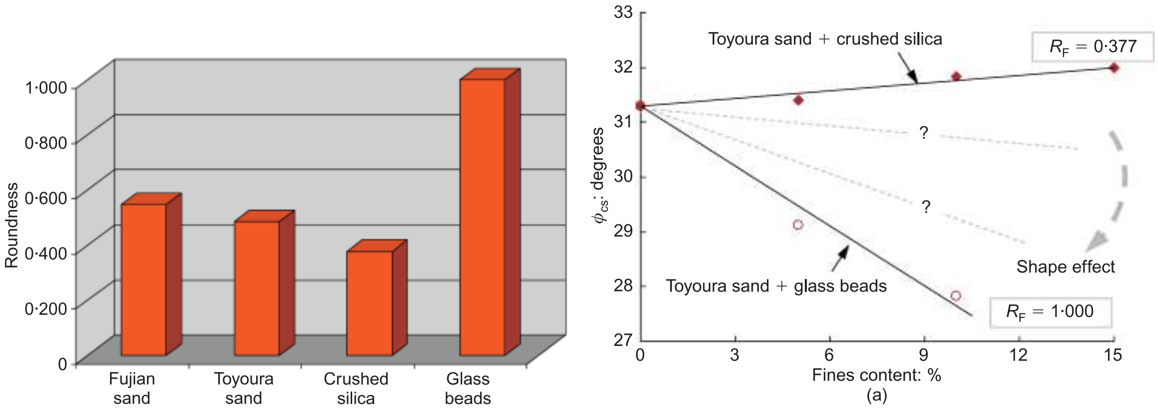

(a) (b)

Figure 7.4 Sand-fine mixtures: (a) particle rounded for each tested material and (b) effects of particle shape and fines content on critical state friction angle for Toyoura sand as host sand [45].

Numerous studies have investigated the influence of small-scale techniques on the shear strength of granular materials. However, findings from these studies have been apparently contradictory. Some cases reported decreasing shear strength with increasing grain size [5, 7, 8, 37, 153], while others have observed the opposite trend [6, 9, 47, 48]. A potential factor contributing to these apparent contradictions could be the correlation between particle size and shape (Table 2.10). For instance, the pioneering study on small-scaling techniques conducted by Zeller & Wullimann [5] reported a rockfill material with grain size-shape correlation. As $d_{\max}$ decreased, the average particle shape became more angular and elongated. They performed a series of drained triaxial tests with α varying from 5 to 80. As shown in Figure 2.37(b), they obtained that the shear strength increased in finer samples, presumably due to size-shape correlations.

The study by Varadarajan *et al.* [37] investigated the behavior of two scaled materials using parallel gradation and triaxial tests: (1) Ranjit Sagar dam material with rounded characteristic particle shape (Figure 7.5 (a)) and (2) Purulia dam material with angular characteristic particle shape (Figure 7.5 (b)). The first case showed increasing shear strength with particle size, while the second material exhibited the opposite trend. The lack of comprehensive shape characterization across grain sizes may contribute to the apparent contradictions in those results. This is particularly the case in Ranjit material, whose grains seem rounded in the coarse fraction and angular in the fine fraction, as shown in Figure 7.5 (a). Moreover, testing samples with low aspect ratios ($\alpha = [5, 8, 15]$) could also be a possible source of dispersion in strength. Indeed, recent research on the minimum representative volume to test coarse granular material recommends that the minimum values proposed by standards (e.g., ASTM) are insufficient to avoid the specimen size effect [147,149]. Recent experimental [147] and numerical [148, 150] studies have shown that the minimum aspect ratio $\alpha = D/d_{max}$ for triaxial test should be larger than $\alpha \geq 12$.

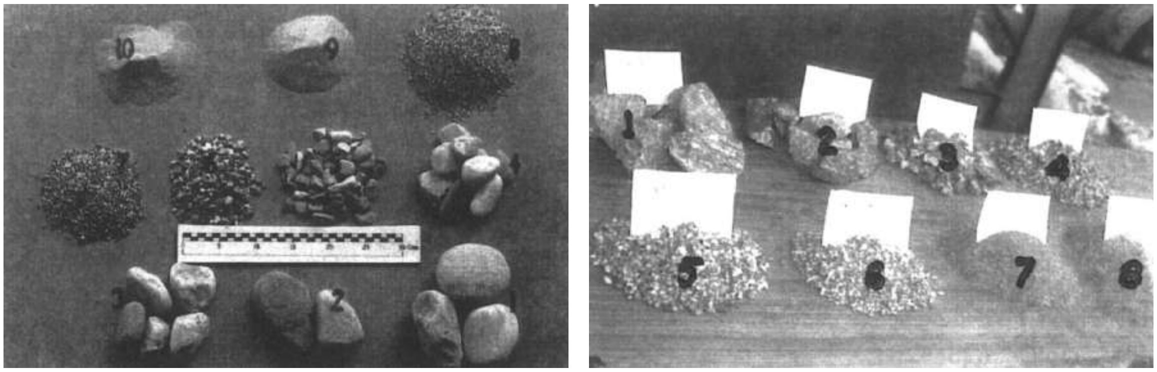
(a) (b)

Figure 7.5 Particle shapes for (a) Ranjit Sagar dam site and (b) Purulia dam site [37].

Another example where size-shape correlation might have a role is in the study of Alias *et al.* [46]. They tested material from Nilai quarry and examined the impact of particle size on the shear strength using two $d_{\max}$ and two direct shear boxes under the same stress conditions; the aspect ratio was the same for both cases $T/d_{\max} = 10$. As exhibited in Figure 7.6(a), visual inspection of the Nilai material suggests a size-shape correlation, with fine particles being more rounded and coarse particles having more angular shape (Figure 7.6(b)). The study reported that the critical friction angle increases as d_{max} increases, which might be simply because angularity increases with grain size.


(a) (b)

Figure 7.6 Nilai quarry material: (a) grains passing 2.36 mm and (b) grains passing 20 mm [46].

Similarly, Cao *et al.* [47] investigated calcareous sand focusing on particle size effects using triaxial tests on samples with $d_{\max}$ of 2 mm (G1) and 20 mm (G2), these psds are shown in Figure 7.7(a); both samples had $\alpha \geq 10$ and same shearing conditions. Visual inspection of this sand suggested a size-shape correlation, as shown in Figure 7.7(b), with fine particles being more rounded and coarse particles having a more elongated shape. The results showed that the shear strength increased with particle size, which could be explained by elongated shapes of coarse grains contributing to enhanced interlocking, thereby improving the overall shear strength of the material.

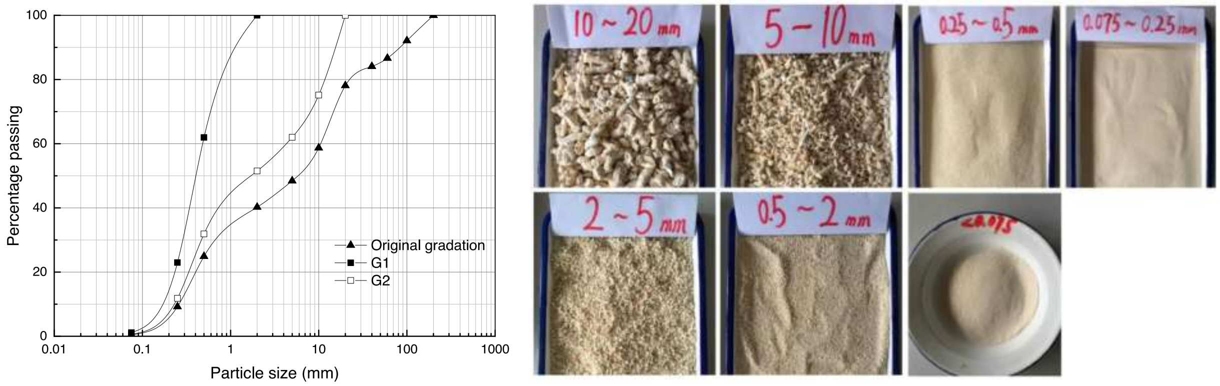

(a) (b)

Figure 7.7 Calcareous sand: (a) particle size distribution for tested sand and (b) pictures of different fractions [47].

Ovalle and Dano [19] studied the mechanical behavior of coarse-grained shale rockfill material. Using the parallel grading technique, they defined three samples with different maximum particle sizes: STV0 with $d_{max} = 10$ mm and tested in a triaxial sample of 70 mm in diameter; STV1 with $d_{max} = 40$ mm and a sample of 250 mm; and STV2 with $d_{max} = 160$ mm and a sample of 1000 mm. They ensured the sample diameter was around six times $d_{\max}$ in each case. The study found a grain size-shape correlation, where fine particles were more elongated and platy, while coarse particles had a higher I/L ratio and were less elongated, as shown in Figure 7.8(a). Figure 7.8(b) indicated that the correlations between particle size and shape influenced shear strength.Finer and more elongated particles tend to exhibit higher peak friction angles due to increased interlocking. This kind of behavior was observed in our numerical DEM tests [205, 214].

Hao and Pabst [48] characterized the shear strength of small-scaled samples of coarse-grained waste rocks from the Canadian Malartic Mine. The study found that shear strength increases as d_{max} increases. Visual inspection of this WR material suggests that fine particles are more rounded than coarse ones, which seem to have more angular and elongated shapes, as observed in Figure 7.9. This suggests that, as particles become coarser, their more elongated shapes

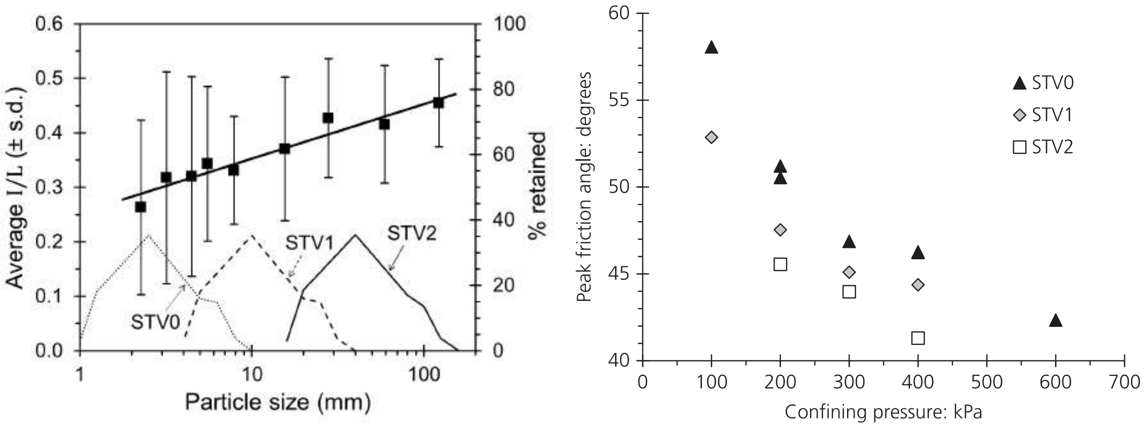

(a) (b)

Figure 7.8 Shale rockfill: (a) Characteristic dimensions of the particles, L=largest, I=shortest dimension. (b) particle shape-size correlation [19].

contribute to enhanced interlocking and interparticle contacts, thus improving the overall shear strength. However, it is unclear whether the observed trend is primarily due to the change in the characteristic shape of the particles in different samples, particle breakage, or the effect of the low aspect ratio (α) values used, ranging from 5 to 12 in such study.

Figure 7.9 View of the tested waste rock material of Canadian Malartic [48].

7.3 A recent implication of the study

We have previously discussed how size-shape correlations can help explain the apparent contradictions in the characterization of shear strength in small-scaled samples of coarse-grained materials. Here, we attempt to show some impact of this effect on other phenomena. For instance, Nie *et al.* [49] investigated the impact of fines on the mobility of dry granular flows using 2D DEM simulations, replicating the elongation-based size-shape correlations proposed in our previous work [205]. The study examined how different correlations between particle size and shape affect granular columns' flow characteristics and mobility.The results indicated that fines could either enhance or have a negligible influence on flow mobility, depending on the size-shape correlation (Figure 7.10). When particle size and elongation positively correlate, an increase in fine content leads to higher mobility, as our simulation demonstrated a decrease in ϕ_c. The study also examined how the grain size-shape correlation influences the mechanisms of energy dissipation and flow dynamics.

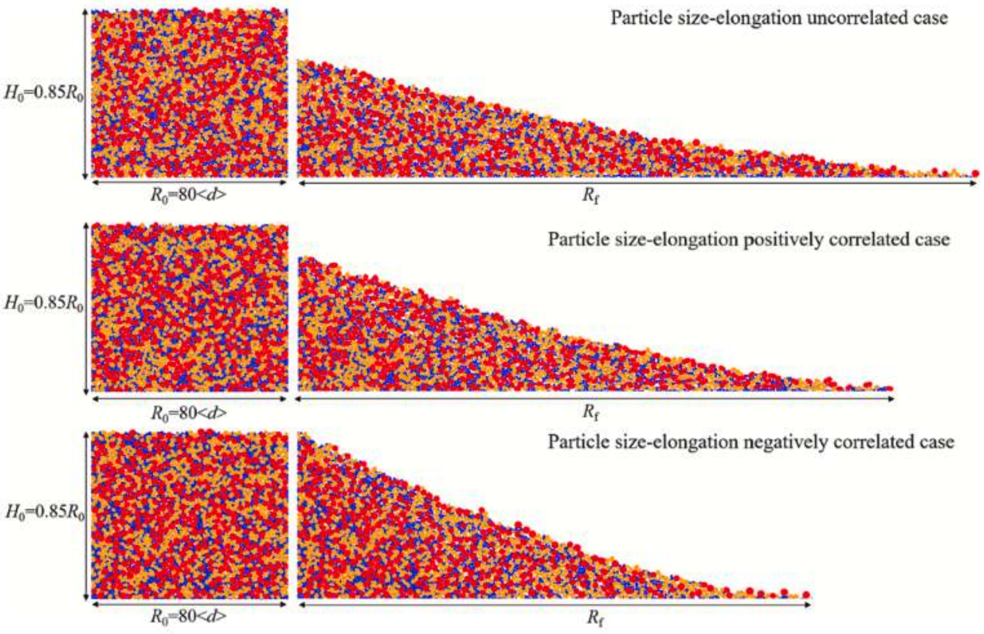

Figure 7.10 2D DEM dry flow simulation: initial configuration (left) and final deposit (right) of short granular columns for both particle size-elongation uncorrelated and correlated cases. [49]

7.4 Limitations

While this thesis presented a comprehensive numerical and theoretical investigation of the impact of size-shape correlations on the mechanical behavior of granular materials, the absence of experimental validation for these specific findings presents a notable limitation. Although the numerical model has been validated using spherical particles, confirming its accuracy under those specific conditions, further validation is necessary to determine its applicability to scenarios with grain size-shape correlations. To address this, a collaboration has been established with the LMGC research laboratory in France. This collaboration aims to create artificial granular materials with controlled size and shape variations, as shown in Figure 7.11, replicating the size-shape correlation in the 3D simulations studied in this thesis. It will enable future experimental investigations that directly correspond to the numerical simulations presented in this work. These planned experiments will be instrumental in validating the observed trends and conclusions related to size-shape correlations, ultimately reinforcing the impact and applicability of this research.

(a) (b)

Figure 7.11 Printed grains with dispersion in size and shapes.

Additionally, our numerical study simplifies reality in several key ways:

- **Particle shape:** we used geometrical figures (e.g. polygons or polyhedra) to describe particle shape, which deviates significantly from the complex morphology of real-world materials. This simplification may impact the accuracy of representing crucial aspects of granular behavior, such as particle interlocking and movement, influencing the simulated mechanical response [110].
- **Particle size distribution:** all our simulations assigned the same volume to each particle family. This approach neglects the naturally occurring variations in volume fractions within different particle sizes, potentially leading to an inaccurate representation of granular assembly. Furthermore, our model uses a maximum particle size dispersion of $d_{\max} \approx 20\ d_{\min}$, which, while broad, may not fully encompass the wider polydispersity observed in natural soils. This limited range, coupled with the model's inability to capture the fractal nature of psd often found in natural materials, could impact the realism of simulated particle packing and force distribution.
- **Particle breakage:** our study did not consider particle breakage. This omission could lead to overestimating the material's strength, especially under high stresses where particle breakage is more likely to occur [8,19,48,152,176]. When particles break, their size

and shape are altered, eventually influencing the size-shape correlations within the material. Therefore, shape-size correlations could also depend on the stress history of the material. Given that larger particles are more prone to breakage, the resulting smaller particles may exhibit altered shape properties, which could modify their interlocking potential and impact the overall shear strength of the granular assembly. If this leads to a reduction in shear strength, it could increase the risk of slope failures. To accurately characterize the long-term mechanical behavior of WRPs, it is crucial to understand the influence of particle breakage on size-shape correlations. Effective design strategies must account for the evolving particle size distribution and the associated changes in mechanical properties to mitigate potential risks and maintain the safety and integrity of WRPs over time.

7.5 Future research directions

For over six decades, research has focused on methods for testing coarse-grained materials. Techniques like scalping or parallel grading are the sole options for testing small-scale samples and characterizing the mechanical behavior of oversized material. Our numerical results demonstrate that a critical limitation of these small-scale techniques is their inability to replicate the mechanical behavior of materials with correlations between grain size and shape. The question of adequately testing coarse-grained materials remains unanswered and more research is needed.

The first research direction involves experimental validation and incorporating more realistic particle shapes. While this study relies on numerical simulations, future work should prioritize experimental validation of the findings. This would involve collaboration, as mentioned in the previous section, where artificial granular materials with controlled size and shape variations are created to correspond directly to the parameters used in the simulations. Furthermore, research should also study natural materials that exhibit size-shape correlation, characterizing particle shape through techniques such as X-ray tomography. Thus, the complex morphology of real-world grains could be incorporated into DEM numerical models.

Another potential research area is replicating analogous DEM simulations while using diverse functions for the psd. In our work, the number of particles per shape family was linked to the constant volume constraint per particle size. However, this approach favored a significant proportion of finer particles. Exploring different shapes of psds remains key to validating, or the contrary, the observations in this study.

The current study neglects particle breakage, a crucial aspect of soil behavior, especially under high stresses. Moreover, the grain size-shape correlation of a material can change due to the breakage of its particles. Future research should incorporate particle breakage mechanisms into the numerical models to improve the accuracy of strength predictions and better simulate the behavior of granular materials under realistic loading conditions.

These directions seek to propose small-scaling laws based on the grain's geometrical properties to obtain a representative small-scaled sample in terms of the shear strength of a given coarse granular prototype.

CHAPTER 8 CONCLUSION

Through DEM granular simulations under quasi-static shearing conditions, this thesis investigated the mechanical behavior of granular assemblies characterized by size-shape correlations across various scenarios. We used the Contact Dynamics DEM method, implemented in the LMGC90 open-source code. In order to validate the numerical DEM tests carried out with the code, large strain shearing 3D simulations of spheres with varied particle size distribution were compared with the results of Ring Shear tests on glass beads having the same grading. The numerical results were in close agreement with the experiments, particularly regarding critical strength and volumetric strains.

Three 2D DEM cases were studied, involving (i) diverse elongated and circular grains, (ii) regular polygons with varied sharpness, and (iii) pentagons with diversified irregularity. Additionally, 3D models were used with mixed angular polyhedral grains and spheres. The study found that the grain size-shape correlations profoundly affect the mechanical behavior of granular assemblies. In the first case, coarse elongated particles combined with fine circular particles exhibited a drop in shear strength as the range of particle sizes increased. In comparison, the opposite combination of coarse circular and fine elongated particles showed a slight increase in shear strength. In the second case, the correlation between particle sharpness significantly modified the mechanical response, with coarse less sharp particles and fine sharper grains increasing critical shear strength; at the same time, the inverse combination results in decreasing shear strength as the grain size span increases. The third case demonstrated that size-shape correlations involving regular and irregular pentagons did not significantly impact the mechanical behavior as the particle size span varied. In the fourth case, as grading broadened in 3D samples, they exhibited constant shear strength when the fine fraction was angular and decreased strength when the fines were rounded. Overall, the results of this numerical study are consistent with experimental observations, where the angularity of the fine fraction is varied to assess its effects on shear strength. Namely, Yang & Wei [45] showed that the strength of angular sand decreases if the fine fraction is replaced by rounded grains, while it slightly increases if more angular grains are used instead. Anyhow, further experimental validations are needed to confirm our findings.

Micro-mechanical analyses revealed diverse evolution patterns for the coordination number and the proportion of floating particles across the cases examined:

- **(i)** In samples with coarse elongated particles and fine circular grains, the coordination number Z decreased as the grain size span increased, which is consistent with critical strength decreasing. Also, the proportion of floating particles c_0 increased, indicating fewer contacts per grain and more particles not contributing to the force chain network. Comparatively, the opposite size-shape correlation exhibited a gradual increase in Z.

- **(ii)** In samples where fine grains were sharper than coarse ones, Z increased with the diversity of grain sizes. However, it decreased when fines were less sharp, due to ineffective interlocking between fines, leading to fewer floating particles.
- **(iii)** When testing regular and irregular pentagons, the impacts on Z and c_0 were minimal as grading evolves, indicating that pentagon irregularity did not significantly affect the assemblies' mechanical behavior or connectivity.
- **(iv)** In 3D assemblies with fine angular grains versus coarse rounded ones, shear strength was stable for varied grading, which was consistent with a constant Z. When testing fine rounded grains versus coarse angular ones, Z increased with grain size span but did not enhance shear strength, as coarse angular particles created voids for finer grains to roll.

In general, connectivity was higher in samples where larger grains contributed more to shear strength as the grain size span increased, particularly when these large grains were more rounded. This suggests that the strength of the granular assembly is enhanced when coarser particles have more surface area to establish contact with neighboring particles, forming a more robust contact network. Finer grains were angular or elongated in those cases, promoting interlocking and thus significantly contributing to the macromechanical strength.

Microstructural anisotropies in normal and tangential forces were crucial in understanding variations in mechanical behavior. In assemblies of mono-shaped grains with varied grading, it is well known that the critical shear strength remains constant due to compensation between normal force anisotropy and contact anisotropy. Nevertheless, this did not happen in our samples with polydispersity in particle size and shape. On the one hand, in assemblies involving elongated and circular grains, the anisotropy of tangential forces was a primary factor contributing to the variations observed in critical strength. In samples with fine elongated particles, a_{ft} increased with the diversity of grain sizes. In contrast, in samples with coarse elongated grains a_{ft} decreased as size span increased, due to promoted rolling in fine grains. On the other hand, in samples containing both angular and rounded grains, the anisotropy of normal forces dominated the variation in strength. In samples with fine angular grains and coarse rounded ones, a_{fn} increased as grading broadened due to the preferential force transmission pathways created by fine angular grains. Conversely, a_{fn} decreased when fine grains were more rounded than coarse particles, due to ineffective interlocking among finer grains. These results indicated that the orientation and magnitude of contact forces within the granular assembly are influenced by the shape and size of the particles, which in turn affects the overall mechanical response.

These findings underscore the importance of considering size-shape correlations when employing small-scaling techniques in geotechnical engineering. For decades, research on coarse-grained materials has utilized techniques like scalping and parallel grading to investigate small-scale samples and characterize mechanical properties. Our results indicate that these methods have a significant limitation: they fail to replicate the mechanical behavior of materials where particle size and shape are correlated. However, validation of these numerical observations through experimental tests is also needed. To address this issue, future research should prioritize experimental validation and incorporate more realistic particle geometries. Studies on natural materials using techniques such as X-ray tomography are also essential.

Additionally, replicating DEM simulations with varying psd could provide new insights into the behavior of granular assemblies. Developing theoretical or empirical equations to predict critical friction angles based on different psds is a promising research direction. Furthermore, incorporating particle breakage mechanisms into numerical models is necessary to improve strength predictions and simulate realistic loading conditions. These efforts aim to establish small-scaling laws based on grain geometry to create representative small-scale samples that accurately reflect the shear strength of coarse granular materials.

REFERENCES

[1] A. Deiminiat *et al.*, “Determination of the shear strength of rockfill from small-scale laboratory shear tests: A critical review,” *Adv. Civ. Eng.*, vol. 2020, pp. 1–18, 11 2020.

[2] A. B. Cerato and A. J. Lutenegger, “Specimen size and scale effects of direct shear box tests of sands,” *Geotech. Test. J.*, vol. 29, no. 6, pp. 507–516, 2006.

[3] A. Deiminiat, L. Li, and F. Zeng, “Experimental study on the minimum required specimen width to maximum particle size ratio in direct shear tests,” *CivilEng*, vol. 3, no. 1, pp. 66–84, 2022.

[4] V. Angelidakis, S. Nadimi, and S. Utili, “Shape analyser for particle engineering (shape): Seamless characterisation and simplification of particle morphology from imaging data,” *Comput. Phys. Commun.*, vol. 265, p. 107983, 2021.

[5] J. Zeller and R. Wullimann, “The shear strength of the shell materials for the goschenenalp dam, switzerland,” in *4th International Conference on Soil Mechanics and Foundation Engineering*, vol. 2, 1957, pp. 399–415.

[6] M. Al-Hussaini, “Effect of particle size and strain conditions on the strength of crushed basalt,” *Can. Geotech. J.*, vol. 20, no. 4, pp. 706–717, 1983.

[7] N. D. Marachi *et al.*, *Strength and Deformation Characteristics of Rockfill Materials*, ser. Report No. TE-69-5. Berkeley, CA: Department of Civil Engineering, University of California, Berkeley, 1969.

[8] C. Ovalle *et al.*, “The effect of size on the strength of coarse rock aggregates and large rockfill samples through experimental data,” *Acta Mech.*, vol. 225, pp. 2199–2216, 2014.

[9] A. Deiminiat and L. Li, “Experimental study on the reliability of scaling down techniques used in direct shear tests to determine the shear strength of rockfill and waste rocks,” *CivilEng*, vol. 3, no. 1, pp. 35–50, 2022.

[10] H. Wadell, “Sphericity and roundness of rock particles,” *J. Geol*, vol. 41, no. 3, pp. 310–331, 1933.

[11] M. Aubertin, M. Maknoon, and C. Ovalle, “Waste rock pile design considerations to promote geotechnical and geochemical stability,” *Can. Geotech. – The CGS Magazine: Fall*, vol. 2, no. 3, pp. 44–47, 2021.

[12] M. Hawley and J. Cunning, *Guidelines for mine waste dump and stockpile design.* CSIRO Publishing, 2017.

[13] C. Ovalle *et al.*, "Data compilation from large drained compression triaxial tests on coarse crushable rockfill materials," *J. Geotech. Geoenviron.*, vol. 146, p. 06020013, 9 2020.

[14] E. Bard, M. E. Anabalón, and J. Campaña, "Waste rock behavior at high pressures: dimensioning high waste rock dumps," in *Elementary mechanics of soil behaviour.* Wiley Online Library, 2012, pp. 83–112.

[15] S. Linero, C. Palma, and R. Apablaza, "Geotechnical characterisation of waste material in very high dumps with large scale triaxial testing," in *Proceedings of the 2007 International Symposium on Rock Slope Stability in Open Pit Mining and Civil Engineering.* Australian Centre for Geomechanics, 2007, pp. 59–75.

[16] N. Barton and B. Kjærnsli, "Shear strength of rockfill," *J. Geotech. Eng.*, vol. 107, no. 7, pp. 873–891, 1981.

[17] S. Linero *et al.*, "Trends in the evolution of particle morphology with size in colluvial deposits overlying channel iron deposits," in *EPJ Web Conf.*, vol. 140. EDP Sciences, 2017, p. 14005.

[18] S. Linero-Molina *et al.*, "Design of a 720-mm square direct shear box and investigation of the impact of boundary conditions on large-scale measured strength," *Geotech. Test. J.*, vol. 43, no. 6, pp. 1463–1480, 2020.

[19] C. Ovalle and C. Dano, "Effects of particle size–strength and size–shape correlations on parallel grading scaling," *Géotech. Lett.*, vol. 10, no. 2, pp. 191–197, 2020.

[20] L. Valenzuela *et al.*, "High waste rock dumps–challenges and developments," in *Proceedings of 1st International seminar on the management of rock dumps, stockpiles and heap leach pads*, 2008, pp. 65–78.

[21] K. L. Lee and H. B. Seed, "Drained strength characteristics of sands," *J. Mech. Found.*, vol. 93, no. 6, pp. 117–141, 1967.

[22] S. K. Razavi, "Constitutive modeling of flow liquefaction of tailings," Thèse de doctorat, École Polytechnique de Montréal, 2023.

[23] M. Lings and M. Dietz, "An improved direct shear apparatus for sand," *Géotechnique*, vol. 54, no. 4, pp. 245–256, 2004.

[24] G. E. Blight, *Geotechnical engineering for mine waste storage facilities.* CRC Press, 2009.

[25] C. Ovalle, "Contribution à l'étude de la rupture des grains dans les matériaux granulaires," Thèse de doctorat, École centrale de Nantes, Nates, France, 2013.

[26] J. Yang and X. D. Luo, "The critical state friction angle of granular materials: does it depend on grading?" *Acta Geotech.*, vol. 13, pp. 535–547, 6 2018.

[27] O. Polanía *et al.*, "Grain size distribution does not affect the residual shear strength of granular materials: An experimental proof," *Phys. Rev. E*, vol. 107, no. 5, p. L052901, 2023.

[28] D. Muir Wood and K. Maeda, "Changing grading of soil: effect on critical states," *Acta Geotech.*, vol. 3, pp. 3–14, 2008.

[29] D. Cantor *et al.*, "Rheology and structure of polydisperse three-dimensional packings of spheres," *Phys. Rev. E*, vol. 98, no. 5, p. 052910, 2018.

[30] D. Cantor, E. Azéma, and I. Preechawuttipong, "Microstructural analysis of sheared polydisperse polyhedral grains," *Phys. Rev. E*, vol. 101, p. 062901, Jun 2020.

[31] G. C. Cho, J. Dodds, and J. C. Santamarina, "Closure to "particle shape effects on packing density, stiffness, and strength: Natural and crushed sands" by gye-chun cho, jake dodds, and j. carlos santamarina," *J. Geotech. Geoenviron.*, vol. 133, no. 11, pp. 1474–1474, 2007.

[32] I. Cavarretta, M. Coop, and C. O'sullivan, "The influence of particle characteristics on the behaviour of coarse grained soils," *Géotechnique*, vol. 60, no. 6, pp. 413–423, 2010.

[33] E. Azéma and F. Radjai, "Force chains and contact network topology in sheared packings of elongated particles," *Phys. Rev. E*, vol. 85, no. 3, p. 031303, 2012.

[34] H. Shin and J. C. Santamarina, "Role of particle angularity on the mechanical behavior of granular mixtures," *J. Geotech. Geoenviron.*, vol. 139, no. 2, pp. 353–355, 2013.

[35] S. Linero *et al.*, "Impact of grading on steady-state strength," *Géotech. Lett.*, vol. 9, no. 4, pp. 328–333, 2019.

[36] E. Becker, C. K. Chan, and H. B. Seed, *Strength and Deformation Characteristics of Rockfill Materials in Plane Strain and Triaxial Compression Tests*, ser. Report No. TE-72-3. Berkeley, CA: Department of Civil and Environmental Engineering, University of California, Berkeley, 1972.

[37] A. Varadarajan *et al.*, "Testing and modeling two rockfill materials," *J. Geotech. Geoenviron.*, vol. 129, no. 3, pp. 206–218, 2003.

[38] P. A. Cundall and O. D. L. Strack, "A discrete numerical model for granular assemblies," *Géotechnique*, vol. 29, no. 1, pp. 47–65, 1979.

[39] C. O'Sullivan, "Particle-based discrete element modeling: geomechanics perspective," *Int. J. Geomech.*, vol. 11, no. 6, pp. 449–464, 2011.

[40] C. O'Sullivan, *Particulate discrete element modelling: a geomechanics perspective.* CRC Press, 2011.

[41] F. Dubois, V. Acary, and M. Jean, "The contact dynamics method: A nonsmooth story," *Comptes Rendus Mécanique*, vol. 346, no. 3, pp. 247–262, 2018.

[42] D. H. Nguyen *et al.*, "Effects of shape and size polydispersity on strength properties of granular materials," *Phys. Rev. E*, vol. 91, p. 032203, 3 2015.

[43] C. Voivret *et al.*, "Space-filling properties of polydisperse granular media," *Phys. Rev. E*, vol. 76, no. 2, p. 021301, 2007.

[44] G. T. Systems, *Ring Shear Testing Machine TORSHEAR EmS: User Manual*, GCTS Testing Systems, Phoenix, AZ, 2020.

[45] J. Yang and L. Wei, "Collapse of loose sand with the addition of fines: the role of particle shape," *Géotechnique*, vol. 62, no. 12, pp. 1111–1125, 2012.

[46] R. Alias, A. Kasa, and M. R. Taha, "Particle size effect on shear strength of granular materials in direct shear test," *Int. J. Civil and Env. Eng.*, vol. 8, no. 11, pp. 1144–1147, 2014.

[47] P. Cao, M.-J. Jiang, and Z.-J. Ding, "Effects of particle size on mechanical behaviors of calcareous sand under triaxial conditions," *JGS Special Publication*, vol. 8, no. 5, pp. 182–187, 2020.

[48] S. Hao and T. Pabst, "Mechanical characterization of coarse-grained waste rocks using large-scale triaxial tests and neuroevolution of augmenting topologies," *J. Geotech. Geoenviron.*, vol. 149, no. 6, p. 04023039, 2023.

[49] J. Nie *et al.*, "Dem study on role of fines in mobility of dry granular flows considering particle size-shape correlation," *Comput. Geotech.*, vol. 166, p. 105980, 2024.

[50] J. Nowotny *et al.*, “Towards global sustainability: Education on environmentally clean energy technologies,” *Renew. Sustain. Energy Rev.*, vol. 81, pp. 2541–2551, 2018.

[51] M. Aubertin, B. Bussière, and L. Bernier, *Environnement et gestion des rejets miniers: Manuel sur cédérom.* Presses Internationales Polytechnique, 2002.

[52] ASTM, “D2488–17e1: Standard practice for description and identification of soils (visual-manual procedures),” American Society for Testing and Materials, West Conshohocken, PA, Standard, 2004.

[53] ASTM., “D3080–04: Standard test method for direct shear test of soils under consolidated drained conditions,” American Society for Testing and Materials, West Conshohocken, PA, Standard, 2004.

[54] W. Hu *et al.*, “Effect of sample size on the behavior of granular materials,” *Geotech. Test. J.*, vol. 34, no. 3, pp. 186–197, 2011.

[55] A. N. Schofield and P. Wroth, *Critical state soil mechanics.* McGraw-hill London, 1968, vol. 310.

[56] K. H. Roscoe, “The influence of strains in soil mechanics,” *Géotechnique*, vol. 20, no. 2, pp. 129–170, 1970.

[57] G. Li *et al.*, “Influence of grain size distribution on critical state of granular materials,” in *Constitutive modeling of geomaterials.* Springer, 2013, pp. 207–210.

[58] C. Voivret *et al.*, “Space-filling properties of polydisperse granular media,” *Phys Rev. E*, vol. 76, p. 021301, 8 2007.

[59] C. Voivret, F. Radjai, and J. Y. Delenne, “Multiscale force networks in highly polydisperse granular media,” *Phys. Rev. Lett.*, vol. 102, p. 178001, 2009.

[60] E. Azéma *et al.*, “Shear strength and microstructure of polydisperse packings: The effect of size span and shape of particle size distribution,” *Phys. Rev. E*, vol. 96, 8 2017.

[61] F. Radjai and F. Dubois, *Discrete-element modeling of granular materials.* Wiley-Iste, 2011.

[62] F. Dubois *et al.*, “LMGC90,” in *10e colloque national en calcul des structures.* 10e colloque national en calcul des structures, 2011, p. 8 p.

[63] C. Ovalle *et al.*, “Population balance in confined comminution using a physically based probabilistic approach for polydisperse granular materials,” *Int. J. Numer. Anal. Methods Geomech.*, vol. 40, no. 17, pp. 2383–2397, 2016.

[64] H. Leussink, *Der Neubau des Institutes für Bodenmechanik und Grundbau: Bau eines grossen dreiaxialen Schergerätes zur Untersuchung grobkörniger Erdstoffe.* Institut f. Bodenmechanik u. Grundbau d. Techn. Hochschule Fridericiana, 1960, vol. 1.

[65] R. Marsal, “Soil properties-shear strength and consolidation,” in *Proc., 6th Int. Conf. on SMFE*, 1965, pp. 310–316.

[66] R. J. Marsal, “Mechanical properties of rockfill,” *Publication of: Wiley (John) and Sons, Incorporated*, 1973.

[67] N. D. Marachi, C. K. Chan, and H. B. Seed, “Evaluation of properties of rockfill materials,” *J. Mech. Found.*, vol. 98, no. 1, pp. 95–114, 1972.

[68] M. Aubertin, “Waste rock disposal to improve the geotechnical and geochemical stability of piles,” in *Proceedings of the 23rd World Mining Congress (WMC 2013), Montreal, Canada*, 2013.

[69] R. L. Quine, “Stability and deformation of mine waste dumps in north-central nevada,” Ph.D. dissertation, University of Nevada, Reno, 1993.

[70] V. T. McLemore *et al.*, “Literature review of other rock piles: characterization, weathering, and stability,” *Questa Rock Pile Weathering Stability Project. New Mexico Bureau of Geology and Mineral Resources. New Mexico Tech, USA*, 2009.

[71] W. Wahler, “A perspective–mine waste disposal structures–mine dumps, and mill and plant impoundments,” in *Proceedings of the 6th Panamerican Conference on Soil Mechanics and Foundation Engineering*, vol. 3, 1979.

[72] R. B. Burnley, “Mine reclamation and waste dump stability,” Thèse de doctorat, University of Nevada, Reno, 1993.

[73] B. Bussière, “Colloquium 2004: Hydrogeotechnical properties of hard rock tailings from metal mines and emerging geoenvironmental disposal approaches,” *Can. Geotech. J.*, vol. 44, no. 9, pp. 1019–1052, 2007.

[74] O. Fala, “Analyses des conditions d’ecoulement non sature dans les haldes a steriles,” Thèse de doctorat, École Polytechnique de Montréal, 2008.

[75] E. Prema, "Solid waste management in the construction sector: A prerequisite for achieving sustainable development goals." *IOP Conference Series: Earth and Environmental Science*, vol. 850, no. 1, 2021.

[76] British Columbia Mine Dump Committee and Piteau Engineering Ltd, *Investigation and design of mine dumps: Interim guidelines.* The Committee, 1991.

[77] R. F. Dawson, N. R. Morgenstern, and A. W. Stokes, "Liquefaction flowslides in rocky mountain coal mine waste dumps," *Can. Geotech. J.*, vol. 35, no. 2, pp. 328–343, 1998.

[78] O. Hungr *et al.*, "Rapid flow slides of coal-mine waste in british columbia, canada," *Catastrophic landslides: Effects, occurrence, and mechanisms*, vol. 15, p. 191, 2002.

[79] N. R. Barton, "Shear strength of rockfill, interfaces and rock joints, and their points of contact in rock dump design," in *Proceedings of the First International Seminar on the Management of Rock Dumps, Stockpiles and Heap Leach Pads.* Australian Centre for Geomechanics, 2008, pp. 3–17.

[80] R. Nichols, "Rock segregation in waste dumps," in *Flow-through rock drains: Proceedings of the International symposium convened at the Inn of the South, Cranbrook, BC*, 1986.

[81] S. L. Barbour *et al.*, "A research partnership program in the mining industry for waste rock hydrology," *University of Saskatchewan, Canada*, 2001.

[82] M. Arrieta and Z.-X. Zhang, "Particle size distribution (psd) estimation using unmanned aerial vehicle (uav) photogrammetry for rockfill shear strength characterization," *Acta Geotech.*, pp. 1–20, 2024.

[83] T. M. Leps, "Review of shearing strength of rockfill," *J. Mech. Found.*, vol. 96, no. 4, pp. 1159–1170, 1970.

[84] Y. Huillca *et al.*, "Modelling size effect on rock aggregates strength using a dem bonded-cell model," *Acta Geotech.*, vol. 16, no. 3, pp. 699–709, 2021.

[85] Y. Xiao *et al.*, "Evolution of particle shape produced by sand breakage," *Int. J. Geomech.*, vol. 22, no. 4, p. 04022003, 2022.

[86] R. D. Holtz, W. D. Kovacs, and T. C. Sheahan, *An introduction to geotechnical engineering.* Prentice-Hall Englewood Cliffs, 1981, vol. 733.

[87] D. J. Williams, “Assessment of embankment parameters,” Society of Mining, Metallurgy and Exploration, Technical Report, 2001.

[88] S. Azam *et al.*, “Hydrogeological behaviour of an unsaturated waste rock pile: a case study at the golden sunlight mine, montana, usa,” *B. Eng. Geol. Environ.*, vol. 66, no. 3, pp. 259–268, 2007.

[89] K. Essayad, “Migration des résidus à travers les inclusions de roches stériles et effet sur leur comportement hydrogeotechnique,” Thèse de doctorat, École Polytechnique de Montréal, Montreal, QC, Canada, 2020.

[90] A. Peregoedova, “Étude expérimentale des propriétés hydrogéologiques des roches stériles à une échelle intermédiaire de laboratoire,” Thèse de doctorat, École Polytechnique de Montréal, 2012.

[91] M. Maknoon, “Slope stability analyses of waste rock piles under unsaturated conditions following large precipitations,” Thèse de doctorat, École Polytechnique de Montréal, Montreal (Canada), 2016.

[92] K. Terzaghi, *Theoretical soil mechanics.* John Wiley and Sons, 1943.

[93] Z. Liu, “Measuring the angle of repose of granular systems using hollow cylinders,” Ph.D. dissertation, University of Pittsburgh, 2011.

[94] A. W. Bishop, “The stability of tips and spoil heaps,” *Quarterly Journal of Eng. Geol. and Hydrogeology*, vol. 6, no. 3-4, pp. 335–376, 1973.

[95] R. Ulusay *et al.*, “Engineering geological characterization of coal mine waste material and an evaluation in the context of back-analysis of spoil pile instabilities in a strip mine, sw turkey,” *Eng. Geol.*, vol. 40, no. 1-2, pp. 77–101, 1995.

[96] S. Sharma and I. Roy, “Slope failure of waste rock dump at jayant opencast mine, india: a case study,” *Int. J. Appl. Eng. Res.*, vol. 10, no. 13, 2015.

[97] S. García-Torres *et al.*, “Stability assessment of an open-pit waste rock backfilling: field monitoring and numerical back analysis,” in *GeoMontreal 2024*, Montreal, Canada, September 15–18 2024.

[98] S. Ouellet, S. Chapuis, and C. Ovalle, “Le projet de co-déposition dans la fosse canadian malartic,” in *Symposium Rouyn-Noranda 2021 sur l’environnement et les mines*, Université du Québec en Abitibi-Témiscamingue (UQAT), 2021.

[99] T. W. Lambe, “Methods of estimating settlement,” *J. Mech. Found.*, vol. 90, no. 5, pp. 43–67, 1964.

[100] C. Ovalle, C. Dano, and P.-Y. Hicher, “Experimental data highlighting the role of surface fracture energy in quasi-static confined comminution,” *Int. J. Fract.*, vol. 182, pp. 123–130, 2013.

[101] C. Dano *et al.*, “Behavior of granular materials affected by grain breakage,” in *Advances in multi-physics and multi-scale couplings in geo-environmental mechanics.* Elsevier, 2018, pp. 95–132.

[102] K. H. Roscoe, A. Schofield, and A. P. Wroth, “On the yielding of soils,” *Géotechnique*, vol. 8, no. 1, pp. 22–53, 1958.

[103] K. Roscoe, A. Schofield, and A. Thurairajah, “Yielding of clays in states wetter than critical,” *Géotechnique*, vol. 13, no. 3, pp. 211–240, 1963.

[104] D. Reid *et al.*, “Results of a critical state line testing round robin programme,” *Géotechnique*, vol. 71, no. 7, pp. 616–630, 2021.

[105] X. S. Li and Y. Wang, “Linear representation of steady-state line for sand,” *J. Geotech. Geoenviron.*, vol. 124, no. 12, pp. 1215–1217, 1998.

[106] C. Ovalle *et al.*, “Experimental framework for evaluating the mechanical behavior of dry and wet crushable granular materials based on the particle breakage ratio,” *Can. Geotech. J.*, vol. 52, no. 5, pp. 587–598, 2015.

[107] R. Osses *et al.*, “Testing and modelling total suction effects on compressibility and creep of crushable granular material,” *Soils and Foundations*, vol. 61, no. 6, pp. 1581–1596, 2021.

[108] C. Ovalle, “Role of particle breakage in primary and secondary compression of wet and dry sand,” 2018.

[109] Eurocode 7, “Geotechnical design—part 1: General rules: En 1997-1,” European Union, Brussels, Belgium, Standard, 2007.

[110] D. C. Wijeyesekera, A. J. L. M. Siang, and A. S. B. Yahaya, “Advanced statistical analysis for relationships between particle morphology (size and shape) and shear (static and dynamic) characteristics of sands,” *Int. J. Geosciences*, vol. Vol.4 no.10A, 2013.

[111] ASTM, “D7181–20: Method for consolidated drained triaxial compression test for soils,” American Society for Testing and Materials, West Conshohocken, PA, Standard, 2020.

[112] W. G. Holtz and H. J. Gibbs, “Triaxial shear tests on pervious gravelly soils,” *J. Mech. Found.*, vol. 82, no. 1, pp. 867–1, 1956.

[113] W. J. Drugan and J. R. Willis, “A micromechanics-based nonlocal constitutive equation and estimates of representative volume element size for elastic composites,” *J. Mech. Phys. Solids*, vol. 44, no. 4, pp. 497–524, 1996.

[114] T. Kanit *et al.*, “Determination of the size of the representative volume element for random composites: statistical and numerical approach,” *Int. J. Solids Struct.*, vol. 40, no. 13-14, pp. 3647–3679, 2003.

[115] R. Wen *et al.*, “Grain size effect on the mechanical behavior of cohesionless coarse-grained soils with the discrete element method,” *Adv. Civil Eng.*, vol. 2018, 2018.

[116] D. E. Jacobson, J. R. Valdes, and T. M. Evans, “A numerical view into direct shear specimen size effects,” *Geotech. Test. J.*, vol. 30, no. 6, pp. 512–516, 2007.

[117] J. Wang and M. Gutierrez, “Discrete element simulations of direct shear specimen scale effects,” *Géotechnique*, vol. 60, no. 5, pp. 395–409, 2010.

[118] AS1289.6.2.2, “Soil strength and consolidation tests-deter- mination of the shear strength of a soil-direct shear test using a shear box,” Standards Australia, Sydney, Australia, Standard, 1998.

[119] BS1377, “Methods of test for soils for civil engineering purposes. shear strength tests (total stress),” British Standard, London, UK, Standard, 1990.

[120] F. Dubois, M. Jean, and et al, “LMGC90 wiki page,” https://git-xen.lmgc.univ-montp2.fr/lmgc90/lmgc90_user/wikis/home, 2020, [Online; accessed 02-Jul-2024].

[121] F. N. Altuhafi, M. R. Coop, and V. N. Georgiannou, “Effect of Particle Shape on the Mechanical Behavior of Natural Sands,” *J. Geotech. Geoenviron.*, vol. 142, no. 12, p. 04016071, 2016.

[122] D. Sarkar, M. Goudarzy, and D. König, “An interpretation of the influence of particle shape on the mechanical behavior of granular material,” *Granul. Matter*, vol. 21, no. 3, pp. 1–24, 2019.

[123] Y. Xiao *et al.*, “Effect of particle shape on stress-dilatancy responses of medium-dense sands,” *J. Geotech. Geoenviron.*, vol. 145, no. 2, p. 04018105, 2019.

[124] Y. Deng *et al.*, “Influence of particle size on the drained shear behavior of a dense fluvial sand,” *Acta Geotech.*, vol. 16, no. 7, pp. 2071–2088, 2021.

[125] A. Pena, R. Garcia-Rojo, and H. J. Herrmann, “Influence of particle shape on sheared dense granular media,” *Granul. Matter*, vol. 9, no. 3, pp. 279–291, 2007.

[126] E. Azéma and F. Radjai, “Stress-strain behavior and geometrical properties of packings of elongated particles,” *Phys. Rev. E*, vol. 81, no. 5, p. 051304, 2010.

[127] T. Matsushima and C. S. Chang, “Quantitative evaluation of the effect of irregularly shaped particles in sheared granular assemblies,” *Granul. Matter*, vol. 13, no. 3, pp. 269–276, 2011.

[128] E. Azéma, F. Radjai, and F. Dubois, “Packings of irregular polyhedral particles: strength, structure, and effects of angularity,” *Phys. Rev. E*, vol. 87, no. 6, p. 062203, 2013.

[129] M. Xu, N. Guo, and Z. Yang, “Particle shape effects on the shear behaviors of granular assemblies: irregularity and elongation,” *Granul. Matter*, vol. 23, no. 2, pp. 1–15, 2021.

[130] P. Barrett, “The shape of rock particles, a critical review,” *Sedimentology*, vol. 27, no. 3, pp. 291–303, 1980.

[131] S. J. Blott and K. Pye, “Particle shape: a review and new methods of characterization and classification,” *Sedimentology*, vol. 55, no. 1, pp. 31–63, 2008.

[132] K. A. Alshibli and M. I. Alsaleh, “Characterizing surface roughness and shape of sands using digital microscopy,” *Civ. Eng. J*, vol. 18, no. 1, pp. 36–45, 2004.

[133] C. Clayton, C. Abbireddy, and R. Schiebel, “A method of estimating the form of coarse particulates,” *Géotechnique*, vol. 59, no. 6, pp. 493–501, 2009.

[134] C. K. Wentworth, “A laboratory and field study of cobble abrasion,” *J. Geol.*, vol. 27, no. 7, pp. 507–521, 1919.

[135] M. Panien, G. Schreurs, and A. Pfiffner, “Mechanical behaviour of granular materials used in analogue modelling: insights from grain characterisation, ring-shear tests and analogue experiments,” *J. Struct. Geol.*, vol. 28, no. 9, pp. 1710–1724, 2006.

[136] J. Gong *et al.*, “Effects of angularity and content of coarse particles on the mechanical behaviour of granular mixtures: a dem study,” *Granul. Matter*, vol. 26, no. 1, p. 17, 2024.

[137] M. Wu, F. Zhou, and J. Wang, “Dem modeling of mini-triaxial test on soil-rock mixture considering particle shape effect,” *Comput. Geotech.*, vol. 153, p. 105110, 2023.

[138] M. Meng *et al.*, “Influence of particle gradation and morphology on the deformation and crushing properties of coarse-grained soils under impact loading,” *Acta Geotech.*, vol. 18, no. 11, pp. 5701–5719, 2023.

[139] R. Hennes, “The strength of gravel in direct shear,” in *Symposium on Direct Shear Testing of Soils*. ASTM International, 1953.

[140] D. J. Williams and L. Walker, “Laboratory and field strength of mine waste rock,” *Civil Eng Tran*, vol. 27, no. 3, pp. 299–304, 1985.

[141] A. Hamidi, E. Azini, and B. Masoudi, “Impact of gradation on the shear strength-dilation behavior of well graded sand-gravel mixtures,” *Scientia Iranica*, vol. 19, no. 3, pp. 393–402, 2012.

[142] M. N. Islam *et al.*, “Effect of particle size on the shear strength behavior of sands,” *arXiv preprint arXiv:1902.09079*, 2019.

[143] J. Lowe, “Shear strength of coarse embankment dam materials,” in *Proc., 8th Int. Congress on Large Dams*, vol. 3. International Commission on Large Dams Paris, 1964, pp. 745–761.

[144] G. Thiers and T. Donovan, “Field density, gradation, and triaxial testing of large-size rockfill for little blue run dam,” in *Laboratory shear strength of soil*. ASTM International, 1981.

[145] R. Verdugo and K. de la Hoz, “Strength and stiffness of coarse granular soils,” in *Soil stress-strain behavior: Measurement, modeling and analysis*. Springer, 2007, pp. 243–252.

[146] J. C. Santamarina and G.-C. Cho, “Soil behaviour: The role of particle shape,” in *The Skempton conference, London, UK, on 29–31 March 2004*. Thomas Telford Publishing, 2004, pp. 604–617.

[147] G. Girumugisha, C. Ovalle, and S. Ouellet, “Sample size effect on shear strength of mine waste rock using the scalping method,” in *Geo-Congress 2024*, 2024, pp. 313–320.

[148] D. Cantor and C. Ovalle, “Sample size effects on the critical state shear strength of granular materials with varied gradation and the role of column-like local structures,” *Géotechnique*, pp. 1–12, 2023, published Online: December 04, 2023. [Online]. Available: https://doi.org/10.1680/jgeot.23.00032

[149] C. Ovalle *et al.*, “Size effects assessment of mine waste-rock shear strength combining numerical, laboratory and in situ approaches,” in *SSIM 2023: Third International Slope Stability in Mining Conference.* Australian Centre for Geomechanics, 2023, pp. 291–300.

[150] P. Quiroz-Rojo *et al.*, “Rev assessment of granular materials with varied grading based on macro- and micro-mechanical statistical data,” *Submitted to Acta Geotecnica*, 2024.

[151] S. Amirpour H. *et al.*, “Influence of particle size and gradation on shear strength–dilation relation of granular materials,” *Can. Geotech. J.*, vol. 56, no. 2, pp. 208–227, 2019.

[152] A. K. Gupta, “Effect of particle size and confining pressure on breakage and strength parameters of rockfill materials,” *Electronic J. Geotech. Eng.*, vol. 14, no. Bund. H, pp. 1–12, 2009.

[153] Y. Xiao *et al.*, “Particle size effects in granular soils under true triaxial conditions,” *Géotechnique*, vol. 64, no. 8, pp. 667–672, 2014.

[154] J. J. Moreau, “Unilateral contact and dry friction in finite freedom dynamics,” in *Nonsmooth mechanics and Applications.* Springer, 1988, pp. 1–82.

[155] R. Rorato *et al.*, “Image-based calibration of rolling resistance in discrete element models of sand,” *Comput. Geotech.*, vol. 131, p. 103929, 2021.

[156] J. Zhao, S. Zhao, and S. Luding, “The role of particle shape in computational modelling of granul. matter,” *Nat. Rev. Phys.*, vol. 5, no. 9, pp. 505–525, 2023.

[157] B. Yan and R. Regueiro, “Large-scale dynamic and static simulations of complex-shaped granular materials using parallel three-dimensional discrete element method (dem) on dod supercomputers,” *J. Comput. Eng.*, vol. 35, no. 2, pp. 1049–1084, 2018.

[158] R. D. Mindlin, “Compliance of elastic bodies in contact,” *J. Appl. Mech.*, vol. 16, no. 3, pp. 259–268, 1949.

[159] M. Jean and J. J. Moreau, “Unilaterality and dry friction in the dynamics of rigid body collections,” in *1st Contact Mechanics International Symposium*, 1992, pp. 31–48.

[160] C. Nouguier *et al.*, “Force fluctuations in a pushed granular material,” *Granul. Matter*, vol. 2, no. 4, pp. 171–178, 2000.

[161] M. Renouf, F. Dubois, and P. Alart, “A parallel version of the non smooth contact dynamics algorithm applied to the simulation of granular media,” *J. Comput. Appl. Math.*, vol. 168, no. 1-2, pp. 375–382, 2004.

[162] L. Staron, F. Radjai, and J.-P. Vilotte, “Multi-scale analysis of the stress state in a granular slope in transition to failure,” *European Phys. J. E.*, vol. 18, no. 3, pp. 311–320, 2005.

[163] A. Taboada *et al.*, “Rheology, force transmission, and shear instabilities in frictional granular media from biaxial numerical tests using the contact dynamics method,” *J. Geophys. Res. Solid Earth*, vol. 110, no. B9, 2005.

[164] A. Ries, D. E. Wolf, and T. Unger, “Shear zones in granular media: three-dimensional contact dynamics simulation,” *Phys. Rev. E*, vol. 76, no. 5, p. 051301, 2007.

[165] J. C. Quezada *et al.*, “Stability, deformation, and variability of granular fills composed of polyhedral particles,” *Phys. Rev. E*, vol. 86, no. 3, p. 031308, 2012.

[166] B. Saint-Cyr *et al.*, “Cohesive granular materials composed of nonconvex particles,” *Phys. Rev. E*, vol. 87, no. 5, p. 052207, 2013.

[167] P. Schuhmacher, F. Radjai, and S. Roux, “Wall roughness and nonlinear velocity profiles in granular shear flows,” in *EPJ Web Conf.*, vol. 140. EDP Sciences, 2017, p. 03090.

[168] I. Bratberg, F. Radjai, and A. Hansen, “Dynamic rearrangements and packing regimes in randomly deposited two-dimensional granular beds,” *Phys. Rev. E*, vol. 66, no. 3, p. 031303, 2002.

[169] G. Saussine *et al.*, “Modelling ballast behaviour under dynamic loading. part 1: A 2d polygonal discrete element method approach,” *Comput. Methods Appl. Mech. Eng.*, vol. 195, no. 19-22, pp. 2841–2859, 2006.

[170] V. Topin *et al.*, “Collapse dynamics and runout of dense granular materials in a fluid,” *Phys. Rev. Letters*, vol. 109, no. 18, p. 188001, 2012.

[171] M. Cárdenas-Barrantes *et al.*, “Micromechanical description of the compaction of soft pentagon assemblies,” *Phys. Rev. E*, vol. 103, no. 6, p. 062902, 2021.

[172] D. Cantor, M. Cárdenas-Barrantes, and L. F. Orozco, "Bespoke particle shapes in granular matter," *Papers in physics*, vol. 14, pp. 140 007–140 007, 2022.

[173] S. Nezamabadi *et al.*, "Mpm with frictional contact for application to soft particulate materials," *Procedia Eng.*, vol. 175, pp. 141–147, 2017.

[174] B. Cambou, M. Jean, and F. Radjaï, *Micromechanics of granular materials.* John Wiley & Sons, 2013.

[175] D. Cantor, E. Azéma, and C. Ovalle, "Failure of an effective stress approach in polydisperse wet granular materials," *Phys. Rev. Res.*, vol. 6, no. 2, p. L022008, 2024.

[176] D. Cantor, "Compaction des matériaux granulaires fragmentables en 3d," Thèse de doctorat, Université Montpellier, 2017.

[177] D. Cantor, C. Ovalle, and E. Azéma, "Microstructural origins of crushing strength for inherently anisotropic brittle materials," *Int. J. Solids Struct.*, vol. 238, p. 111399, 2022.

[178] N. Estrada and W. F. Oquendo, "Microstructure as a function of the grain size distribution for packings of frictionless disks: Effects of the size span and the shape of the distribution," *Phys. Rev. E*, vol. 96, no. 4, p. 042907, 2017.

[179] N. Estrada *et al.*, "Identification of rolling resistance as a shape parameter in sheared granular media," *Phys. Rev. E*, vol. 84, no. 1, p. 011306, 2011.

[180] R. Jullien, A. Pavlovitch, and P. Meakin, "Random packings of spheres built with sequential models," *J. Phys. A Math. Theor.*, vol. 25, no. 15, p. 4103, 1992.

[181] W. M. Visscher and M. Bolsterli, "Random packing of equal and unequal spheres in two and three dimensions," *Nature*, vol. 239, pp. 504–507, 1972.

[182] G. M. gdrmidi@ polytech. univ-mrs. fr http://www. lmgc. univ-montp2. fr/MIDI/, "On dense granular flows," *European Phys. J. E.*, vol. 14, pp. 341–365, 2004.

[183] R. J. Bathurst and L. Rothenburg, "Micromechanical aspects of isotropic granular assemblies with linear contact interactions," *J. Appl. Mech.*, vol. 55, pp. 17–23, 1988.

[184] B. Andreotti, Y. Forterre, and O. Pouliquen, *Granular media: between fluid and solid.* Cambridge University Press, 2013.

[185] F. Nicot *et al.*, "On the definition of the stress tensor in granular media," *Int. J. Solids Struct.*, vol. 50, no. 14-15, pp. 2508–2517, 2013.

[186] J.-N. Roux, “Geometric origin of mechanical properties of granular materials,” *Phys. Rev. E*, vol. 61, pp. 6802–6836, Jun 2000.

[187] V. Richefeu *et al.*, “Force transmission in dry and wet granular media,” *Powder Technol.*, vol. 190, no. 1-2, pp. 258–263, 2009.

[188] F. Radjai *et al.*, “Bimodal character of stress transmission in granular packings,” *Phys. Rev. letters*, vol. 80, no. 1, p. 61, 1998.

[189] L. Rothenburg and R. Bathurst, “Analytical study of induced anisotropy in idealized granular materials,” *Géotechnique*, vol. 39, no. 4, pp. 601–614, 1989.

[190] M. Oda, “Fabric tensor for discontinuous geological materials,” *Soils Found.*, vol. 22, no. 4, pp. 96–108, 1982.

[191] N. Guo and J. Zhao, “The signature of shear-induced anisotropy in granular media,” *Comput. Geotech.*, vol. 47, pp. 1–15, 2013.

[192] ASTM, “D6467-21: Standard test method for torsional ring shear test to determine drained residual shear strength of fine-grained soils,” American Society for Testing and Materials, West Conshohocken, PA, Standard, 2021.

[193] S. Amirpour Harehdasht *et al.*, “Influence of particle size and gradation on the stress-dilatancy behavior of granular materials during drained triaxial compression,” *Int. J. Geomech.*, vol. 17, no. 9, p. 04017077, 2017.

[194] L. Oger *et al.*, “Yield and deformation of an assembly of disks subjected to a deviatoric stress loading,” *Mech. Materials*, vol. 27, no. 4, pp. 189–210, 1998.

[195] M. M. Sazzad and M. S. Islam, “Macro and micro mechanical responses of granular material under varying interparticle friction,” *J. Civil Eng.*, vol. 36, no. 2, pp. 87–96, 2008.

[196] T. Binaree *et al.*, “Combined effects of contact friction and particle shape on strength properties and microstructure of sheared granular media,” *Phys. Rev. E*, vol. 102, no. 2, p. 022901, 2020.

[197] N. Estrada, A. Taboada, and F. Radjai, “Shear strength and force transmission in granular media with rolling resistance,” *Phys. Rev. E*, vol. 78, no. 2, p. 021301, 2008.

[198] S. Luding, “Introduction to discrete element methods: basic of contact force models and how to perform the micro-macro transition to continuum theory,” *European J. Environ. Civil Eng.*, vol. 12, no. 7-8, pp. 785–826, 2008.

[199] C. Thornton, “Numerical simulations of deviatoric shear deformation of granular media,” *Géotechnique*, vol. 50, no. 1, pp. 43–53, 2000.

[200] C. Thornton and Z. Ning, “A theoretical model for the stick/bounce behaviour of adhesive, elastic-plastic spheres,” *Powder Technol.*, vol. 99, no. 2, pp. 154–162, 1998.

[201] M. D. Bolton, “The strength and dilatancy of sands,” *Géotechnique*, vol. 36, no. 1, pp. 65–78, 1986.

[202] P. Schuhmacher, “Rhéologie des écoulements granulaires : variables internes et effets d’échelle,” Thèse de doctorat, Université Montpellier, 2016.

[203] R. J. Marsal, “Large scale testing of rockfill materials,” *J. Mech. Found.*, vol. 93, no. 2, pp. 27–43, 1967.

[204] E. Frossard *et al.*, “Size effects due to grain crushing in rockfills shear strength,” in *18th International Conference for Soil Mechanics and Geotechnical Engineering*, 2013.

[205] S. Carrasco, D. Cantor, and C. Ovalle, “Effects of particle size-shape correlations on steady shear strength of granular materials: The case of particle elongation,” *Int. J. Numer. Anal. Met.*, vol. 46, no. 5, pp. 979–1000, 2022.

[206] T. L. Youd *et al.*, “Liquefaction potential of unconsolidated sediments in the southern san francisco bay region, california,” US Geological Survey, Tech. Rep., 1973.

[207] J. Zheng and R. D. Hryciw, “Index void ratios of sands from their intrinsic properties,” *J. Geotech. Geoenviron.*, vol. 142, no. 12, p. 06016019, 2016.

[208] P. V. Lade, J. A. Yamamuro, and P. A. Bopp, “Significance of particle crushing in granular materials,” *J. Geotech. Eng.*, vol. 122, no. 4, pp. 309–316, 1996.

[209] B. O. Hardin, “Crushing of soil particles,” *J. Geotech. Eng.*, vol. 111, no. 10, pp. 1177–1192, 1985.

[210] C. Nouguier-Lehon, “Effect of the grain elongation on the behaviour of granular materials in biaxial compression,” *Comptes Rendus Mécanique*, vol. 338, no. 10-11, pp. 587–595, 2010.

[211] Y. Liu *et al.*, “The perpetual shearing of granular soils under low stresses using the stadium shear device,” *Open Geomechanics*, vol. 3, pp. 1–19, 2022.

[212] R. Kawamoto *et al.*, “All you need is shape: Predicting shear banding in sand with ls-dem,” *J. Mech. Phys. Solids*, vol. 111, pp. 375–392, 2018.

[213] S. E. Cho, “Effects of spatial variability of soil properties on slope stability,” *Eng. Geol.*, vol. 92, no. 3-4, pp. 97–109, 2007.

[214] S. Carrasco *et al.*, “Shear strength of angular granular materials with size and shape polydispersity,” *Open Geomechanics*, vol. 4, pp. 1–14, 2023.